Quantitative Dynamic Contrast Enhanced Magnetic Resonance Imaging for Evaluation of the Myocardium in Ischaemic Heart Disease

David Andrew Broadbent

Submitted in accordance with the requirements for the degree of
Doctor of Philosophy

The University of Leeds

School of Medicine

October 2015

The candidate confirms that the work submitted is his own, except where work which has formed part of jointly-authored publications has been included. The contribution of the candidate and the other authors to this work has been explicitly indicated below. The candidate confirms that appropriate credit has been given within the thesis where reference has been made to the work of others.

Specifically work contained in the following paper is referred to and sections reproduced (with permission from the publishers John Wiley and Sons) in Chapters 7 and 8. Contributions of the candidate and co-authors are detailed below:

> **David A. Broadbent,** John D. Biglands, David P. Ripley, David M. Higgins, John P. Greenwood, Sven Plein, David L. Buckley. 2016. *Sensitivity of quantitative myocardial dynamic contrast-enhanced MRI to saturation pulse efficiency, noise and T_1 measurement error: Comparison of nonlinearity correction methods*. Magnetic Resonance in Medicine. **75** pp1290-1300

David A. Broadbent (Candidate) Lead author. Study conception and design. Simulation work and analysis of volunteer data, including implementation of existing analysis techniques and novel application of bookend T_1 based approach. Interpretation of results. Production and revision of initial manuscript, revisions and final version.
John D. Biglands (Leeds Teaching Hospitals NHS Trust) Assistance with methods implementation and interpretation of results.
David P. Ripley (University of Leeds) Co-ordination and acquisition of data for volunteer scanning aspect of study.
David M. Higgins (Philips Healthcare) Implementation of dual sequence method on the scanner. Provision of details of implementation of sequences.
John P. Greenwood and Sven Plein (University of Leeds) Supervisory (clinical). Assistance with interpretation of results.
David L. Buckley (University of Leeds) Supervisory (physics). Assistance with methods development and interpretation of results.
All authors Critical review of drafts and approval of the final manuscript.

Additional Publications and Conference Abstracts

Simulation results and preliminary volunteer data from the study described on the previous page were also presented as a conference abstract:

David A. Broadbent, John D. Biglands, David P. Ripley, Sven Plein, David L. Buckley. 2015. *Comparison of non-linearity correction methods for quantitative myocardial perfusion MRI.* EuroCMR/Society for Cardiovascular Magnetic Resonance Joint Scientific Sessions. Nice, France

Results from the acute visit of the STEMI study (Chapter 9) were presented as a conference abstract (and at the meeting of the ISMRM Cardiac MR Study Group during the same conference):

David A. Broadbent, Ananth Kidambi, Sven Plein, David L. Buckley. 2015. *Quantitative Dynamic Contrast Enhanced MRI in Acute ST-Elevated Myocardial Infarction: Blood Flow, Microvascular Permeability and Interstitial Volume in Infarct and Peri-Infarct Edema.* International Society for Magnetic Resonance in Medicine Scientific Meeting and Exhibition. Toronto, ON, Canada.

The following publications and abstracts relate to work completed during this PhD, or as prior pilot work, but do not form part of this thesis.

Journal articles (* indicates pilot work accepted for publication prior to PhD)

*** David A. Broadbent**, John D. Biglands, Abdulghani Larghat, Steven P. Sourbron, Aleksandra Radjenovic, John P. Greenwood, Sven Plein, David L. Buckley. 2013. *Myocardial blood flow at rest and stress measured with dynamic contrast-enhanced MRI: comparison of a distributed parameter model with a Fermi function model*. Magnetic Resonance in Medicine **70**(6) pp1591-7

Darius Dabir, Nicholas Child, Ashwin Kalra, Toby Rogers, Rolf Gebker, Andrew Jabbour, Sven Plein, Chung Y. Yu, James Otton, Ananth Kidambi, Adam McDiarmid, **David Broadbent**, David Higgins, Bernhard Schnackenburg, Lucy Foote, Ciara Cummins, Eike Nagel, Valentina Puntmann. 2014. *Reference values for healthy human myocardium using a T1 mapping methodology: results from the International T1 Multicenter cardiovascular magnetic resonance study.* Journal of Cardiovascular Magnetic Resonance **16**:69

Ananth Kidambi, John Biglands, David Higgins, David Ripley, Arshad Zaman, **David Broadbent**, Adam McDiarmid, Peter Swoboda, Tarique A. Musa, Bara Erhayiem, John Greenwood, Sven Plein. 2014. *Susceptibility-weighted cardiovascular magnetic resonance in comparison to T2 and T2 star imaging for detection of intramyocardial hemorrhage following acute myocardial infarction at 3 Tesla.* Journal of Cardiovascular Magnetic Resonance **16**:86

Adam K. McDiarmid, Peter P. Swoboda, Bara Erhayiem, David P. Ripley, Ananth Kidambi, **David A. Broadbent**, David M. Higgins, John P. Greenwood. 2015. *Single bolus versus split dose gadolinium administration in extra-cellular volume calculation at 3 Tesla.* Journal of Cardiovascular Magnetic Resonance **17**:6

Adam K. McDiarmid, **David A. Broadbent**, David M. Higgins, Peter P. Swoboda, Ananth Kidambi, David P. Ripley, Bara Erhayiem, Tarique Al Musa, Laura Dobson, John P. Greenwood, Sven Plein. 2015. *The effect of changes to MOLLI scheme on T1 mapping and extra cellular volume calculation in healthy volunteers with 3 tesla cardiovascular magnetic resonance imaging.* Quantitative Imaging in Medicine and Surgery **5**(4) pp503-10

<u>Conference abstracts</u> (* indicates pilot work presented prior to PhD)

*** David Broadbent**, John Biglands, Abdulghani Larghat, Steven Sourbron, Sven Plein, David Buckley. 2012. *Myocardial microvascular function at rest and stress measured with dynamic contrast-enhanced MRI.* Society for Cardiovascular Magnetic Resonance Scientific Sessions. Orlando, FL, USA

David A. Broadbent, David M Higgins, Vanessa Ferreira, Alexander Liu, Claudia Marini, Christopher M Kramer, Sven Plein, Stefan Neubauer, Stefan K Piechnik. 2014. *Pilot Data on Inter-Centre and Inter-Vendor Comparison of MOLLI and ShMOLLI T1 Mapping Variants at 3T.* International Society for Magnetic Resonance in Medicine Scientific Meeting and Exhibition. Milan, Italy.

Adam K. McDiarmid, David M. Higgins, **David A. Broadbent**, David P. Ripley, Peter P. Swoboda, Ananth Kidambi, Bara Erhayiem, Tarique A. Musa, Laura E. Dobson, Pankaj Garg, John P. Greenwood, Sven Plein. 2015. *Split dose versus single bolus gadolinium administration in ecv calculation at 3 Tesla CMR*. EuroCMR/Society for Cardiovascular Magnetic Resonance Joint Scientific Sessions. Nice, France

Ananth Kidambi, John D. Biglands, David M. Higgins, David P. Ripley, Arshad Zaman, **David A. Broadbent**, Adam K. McDiarmid, Peter P. Swoboda, Tarique A. Musa, Bara Erhayiem, John P. Greenwood, Sven Plein. 2015. *Clinical validation of susceptibility-weighted cardiovascular magnetic resonance in comparison to T2 and T2* imaging for detection of intramyocardial hemorrhage following acute myocardial infarction.* EuroCMR/Society for Cardiovascular Magnetic Resonance Joint Scientific Sessions. Nice, France

Ananth Kidambi, Manish Motwani, Akhlaque Uddin, David P. Ripley, Adam K. McDiarmid, Peter P. Swoboda, **David A. Broadbent**, Tarique A. Musa, Bara Erhayiem, Josh Leader, John P. Greenwood, Sven Plein. 2015. *Myocardial extracellular volume estimation by CMR predicts functional recovery following acute myocardial infarction.* EuroCMR/Society for Cardiovascular Magnetic Resonance Joint Scientific Sessions. Nice, France

John D. Biglands, David P. Ripley, **David A. Broadbent**, David M. Higgins, Peter P. Swoboda, Adam K. McDiarmid, Pankaj Garg, Sven Plein, David L. Buckley. 2015. *A comparison of dual-bolus and dual-sequence quantitative myocardial perfusion techniques.* EuroCMR/Society for Cardiovascular Magnetic Resonance Joint Scientific Sessions. Nice, France

Ananth Kidambi, Manish Motwani, Akhlaque Uddin, David P. Ripley, Adam K. McDiarmid, Peter P. Swoboda, **David A. Broadbent**, Tarique A. Musa, Bara Erhayiem, Joshua Leader, John P. Greenwood, Sven Plein. 2015. *Myocardial Extracellular Volume Estimation by Cardiovascular Magnetic Resonance Predicts Functional Recovery Following Acute Myocardial Infarction.* British Cardiovascular Society Annual Conference. Manchester, UK

Acknowledgements

I am grateful to Professor David Buckley and Professor Sven Plein for their supervision and advice throughout this PhD. Additionally I would like to acknowledge and thank the numerous other people who have supported me both personally and professionally during this project.

- My collaborators and colleagues from medical physics (Dr David Higgins from Philips Healthcare and Dr John Biglands from Leeds Teaching Hospitals NHS Trust) and cardiology (Dr Ananth Kidambi and Dr David Ripley), with whom I have worked closely throughout this project.
- Colleagues both in the medical physics group of the Division of Biomedical Imaging and the Leeds Teaching Hospitals NHS Trust MRI Physics Group, in particular Dr John Ridgway for continuously supporting my career development
- The radiographers, assistants, clinicians, scientists and research nurses who have welcomed me into the Clinical CMR Research Group in Leeds
- The National Institute for Health Research for funding my fellowship the Research Design Service for their assistance in preparing my doctoral research fellowship application.

Research Team Contributions

The research described in this thesis has been carried out by a team which has included several members of the Leeds CMR Clinical Research Group.

The patient and volunteer data described in this thesis has been acquired from studies incorporating comprehensive scan protocols in order to collect data sufficient to answer both the research questions discussed in this thesis as well as other clinical questions of interest to Drs Kidambi and Ripley.

My own contributions have been informing aspects of scan protocol design relevant to the work within this thesis, assisting with volunteer recruitment, developing methods for and performing post-acquisition analysis and interpreting findings of these analyses. Simulation experiments were set up fully by the author with information on the sequence implementation gathered using

viewing tools from the Philips pulse sequence programming environment and provided by Dr David Higgins as detailed below.

Dr Kidambi and Dr Ripley contributed to the work in this thesis by performing patient and volunteer recruitment and assisting with clinical interpretation of findings. They also designed and performed independent analyses relating to other elements of data collected in the patient and volunteer studies, which are not included in this work. Drs Kidambi and Ripley have been supervised by Profs Plein and Greenwood.

Dr John Biglands has provided advice and shared ideas relating to myocardial perfusion analysis. He has also provided software used for data importing, handling and visualisation, but not for quantitative analysis, used in this research.

Dr David Higgins, of Philips Healthcare, has implemented the dual sequence protocol on the scanner used for the research included in this thesis, as well as provided information, and resources for accessing further information, on details of the on-scanner implementation of all of the applied sequences.

Specific contributions of the above individuals to published work are described earlier. Additional members of the Clinical CMR Group have performed and assisted with patient and volunteer recruitment, scanning and image contouring, but have not provided intellectual input to this thesis.

Abstract

Background: Use of contrast enhanced cardiac magnetic resonance imaging (MRI) for identification of focal pathology (perfusion deficit and scar) is widespread. Quantitative analysis of dynamic contrast enhanced (DCE) MRI data may allow objective assessment of focal and diffuse disease. However it is a complex process and not widely adopted outside the research domain. For accurate quantification temporal variation in relative contrast agent concentration in the myocardium and feeding blood supply must be measured. While MRI signal intensity can be used as a probe of contrast agent concentration its response is non-linear.

Aims: In this thesis non-linearity correction methods for quantitative myocardial DCE-MRI are compared, the feasibility of a novel bookend T_1 based correction is tested and the method is used in clinical studies to assess myocardial characteristics in health and ischaemic disease.

Methods: Signal non-linearity correction methods were compared using simulation, phantom experiments and a volunteer study. Methods compared were independent sampling strategies (dual-bolus and dual-sequence), previously proposed model based correction (native T_1 or proton density weighted image based) and bookend T_1 based correction which is proposed as a method to account for imperfect magnetisation preparation. The feasibility of the bookend T_1 method was tested and characteristics of heathy and diseased myocardium were assessed in clinical studies of ischaemia and infarction.

Conclusions: Native T_1 based correction has been found to be highly sensitive to imperfect magnetisation preparation, and is thus recommended against. Model based correction using proton density weighted images or bookend T_1 data have been found to be more accurate and precise than dual-sampling methods. The clinical studies have demonstrated the feasibility of the bookend T_1 based method and have yielded insights into myocardial characteristics in a range of conditions.

Table of Contents

Acknowledgements vii

Abstract ix

Table of Contents i

List of Tables xvi

List of Figures xviii

Abbreviations xxxiii

Chapter 1 Introduction 1

1.1 Structure of thesis 1

1.2 Equipment used 3

1.3 Ethics 3

1.4 Chronology of project and resulting limitations 3

1.5 Additional work completed during PhD 4

Chapter 2 Background Theory 7

2.1 Clinical and biological background 7

2.1.1 Normal myocardial structure, function and perfusion 7

2.1.2 The myocardium in disease 11

2.1.3 Clinical Imaging Modalities for Ischaemic Heart Disease 15

2.1.4 Relationship of Pathophysiology to Contrast Enhanced Magnetic Resonance Imaging 16

2.2 Magnetic resonance imaging signal contrast in magnetisation prepared spoiled gradient echo sequences 17

2.2.1 T_2^* weighting 20

2.2.2 T_1 weighting 21

2.2.3 Magnetisation preparation 23

2.2.4 Controlling weighting in MRI 30

2.3 Action of gadolinium based contrast agents (GBCAs) 31

2.4 Distribution of extracellular gadolinium based contrast agents 32

2.4.1 Temporal variation of contrast agent concentrations 34
2.4.2 The partition coefficient and distribution volumes 47
2.5 Conclusions.....49
Chapter 3 Outline of a Clinical Cardiac DCE-MRI Protocol.....51
3.1 Typical perfusion CMR protocol 51
3.1.1 Pharmacological stress.....53
3.2 Sequences 54
3.2.1 Cardiac perfusion sequence 54
3.3 Conclusions.....60
Chapter 4 Literature Review – Technical 61
4.1 Introduction.....61
4.2 Clinical motivation 61
4.3 Contrast enhanced MRI methods.....62
4.3.1 Delayed enhancement MRI 62
4.3.2 Dynamic contrast enhanced MRI.....64
4.3.3 Contrast equilibrium ECV imaging 76
4.4 T_1 measurement techniques.....84
4.4.1 Multi-point inversion or saturation recovery techniques 85
4.4.2 Inversion recovery Look-Locker based techniques.....88
4.4.3 Saturation recovery Look-Locker based techniques 99
4.4.4 Two-point saturation recovery method.....101
4.4.5 Segmented inversion recovery techniques 102
4.5 Conclusions.....105
Chapter 5 Literature Review - Clinical.....109
5.1 Early studies.....109
5.2 Further clinical studies in ischaemic heart disease.....110
5.2.1 Partition coefficient and extracellular volume fraction 110
5.2.2 Perfusion CMR 112

5.3 Proliferation of contrast equilibrium ECV estimation and expansion into assessment of diffuse fibrosis 114
5.4 Conclusions 116
Chapter 6 T_1 Mapping – Simulations and Phantom Validation 117
6.1 Methods 117
6.1.1 Simulations 117
6.1.2 Phantom validation 119
6.2 Results 119
6.3 Discussion 121
6.3.1 Limitations 123
6.4 Conclusions 123
Chapter 7 Signal Non-Linearity Correction – Simulation and Phantom Scanning 125
7.1 Introduction 125
7.1.1 Aims 128
7.2 Methods 128
7.2.1 Model-based non-linearity correction methods 132
7.2.2 Dual-sampling methods 138
7.2.3 Simulation study 140
7.2.4 Phantom study 140
7.3 Results 142
7.3.1 Simulation study 142
7.3.2 Phantom study 172
7.4 Discussion 175
7.4.1 Signal enhancement based analysis 175
7.4.2 Model-based non-linearity correction 176
7.4.3 Influence of image noise 185
7.4.4 Slice dependence 185

7.4.5 Practical implications 187
7.4.6 Limitations 188
7.5 Conclusions 190
7.6 Appendix 1 - Detailed methods for forward signal simulation 193
7.6.1 Starting condition 193
7.6.2 Events 193
7.6.3 Scope of events 195
7.6.4 Event timing 195
7.6.5 Signal simulation 196
7.6.6 Repetition 197
7.7 Appendix 2 - Examination of behaviour of signal models in comparison to forward simulation 199
7.7.1 Conventional saturation recovery sequence 200
7.7.2 Interleaved AIF sequence (dual-sequence) 205
7.7.1 PDw sequence 206
7.7.2 Justification for signal model choice 208
7.8 Appendix 3 - Optimisations with non-monotonic functions 125
7.8.1 Determination of saturation efficiency 211
7.8.2 Determination of T_1 from DCE signal intensity 212
7.8.3 Implications for results in this thesis and future work 214
Chapter 8 Volunteer Study - Comparison of Non-Linearity Correction Methods and Contrast Equilibrium MRI 215
8.1 Introduction 215
8.1.1 Aims 215
8.2 Methods 216
8.2.1 Acquisition 216
8.2.2 Analysis 218
8.3 Results 219

8.3.1 Non-linearity correction comparison 222
8.4 Discussion 225
8.4.1 Limitations 229
8.5 Conclusions 229
Chapter 9 Clinical Study – ST-segment Elevation Myocardial Infarction 231
9.1 Clinical background 231
9.1.1 Distributed parameter model constrained analysis of myocardial DCE-MRI data 232
9.1.2 Aims 232
9.2 Methods 233
9.2.1 Subjects 233
9.2.2 Acquisition protocol 233
9.2.3 Analysis 234
9.3 Results 242
9.4 Discussion 248
9.4.1 Limitations 249
9.5 Conclusions 250
Chapter 10 Clinical Study – Hyperoxaemia in Coronary Artery Disease 253
10.1 Clinical background 253
10.1.1 Aims 253
10.2 Methods 254
10.2.1 Subjects 254
10.2.2 Acquisition protocol 254
10.2.3 Analysis 255
10.3 Results 256
10.4 Discussion 264
10.4.1 Limitations 268
10.5 Conclusions 268

Chapter 11 Conclusions....271
11.1 Current research....271
11.1.1 Signal non-linearity correction....271
11.1.2 T_1 mapping in quantitative CMR....275
11.1.3 Myocardial characteristics in ischaemic disease....275
11.2 Future related research directions....277
11.2.1 Signal model derivation....277
11.2.2 Motion correction....278
11.2.3 Acquisition improvements – resolution, noise and anatomical coverage....278
11.2.4 Water exchange effects....280
11.2.5 Effect of saline flush....280
11.2.6 Deconvolution – model selection and robust fitting....280
11.2.7 Clinical studies and application....281
11.3 Conclusions....281
References....271

List of Tables

Table 7-1 – Parameters used for simulations. Imaging parameters are representative of local practice. a - Native MOLLI T1 values (septal region for myocardium) [14]. b - Relaxivity at 3 T for Gd-BT-D03A [186, 187]. c - Mean healthy volunteer values [1]. d - Mean healthy volunteer and chronic infarct core values (rounded to 2 significant figures) [189]. e - Middle of normal range [188]. 130

Table 7-2 – IR-SE, MOLLI and SR-GE T_1 results. 172

Table 7-3 – Example intermediate data for PDw image and native T_1 based correction methods (both for slice 1 using the full recovery signal model). Ground truth native T_1 and S_0 values were 1736ms and 1. 182

Table 7-4 – Estimated R_1 and ΔR_1 values for blood in the scenarios exemplified in Table 7-3. Without noise and with perfect saturation the native T_1 method performs ideally, so the values in the bottom 3 rows of the SE=1 column also reflect the ground truth values. 183

Table 8-1 - Imaging parameters for the volunteer study. 217

Table 8-2 – Haematocrit, T_1 values and ECV from the 18 volunteers. 220

Table 8-3 – Mean, standard deviation and coefficient of variation for MBF estimates from the different methods. 223

Table 8-4 – Mean, standard deviation and coefficient of variation for v_d estimates from the different methods. 223

Table 8-5 – Mean, standard deviation and coefficient of variation for MPR estimates from the different methods. 224

Table 9-1 – Results from the STEMI study for the acute visit (n indicates number of regions). 244

Table 9-2 – Results from the STEMI study for the follow-up visit (n indicates number of regions). 245

Table 9-3 – Paired t-test P values for the STEMI study (n indicates number of regions). 247

Table 10-1 – Fitting results for the volunteers in the hyperoxaemia study for data acquired at rest. 258

Table 10-2 – Fitting results for the volunteers in the hyperoxaemia study for data acquired under adenosine induced stress. 258

Table 10-3 – Paired t-test results for the volunteers in the hyperoxaemia study with successful fits for all physiological states..... 259

Table 10-4 – Results from patients with single vessel stable coronary artery disease. Results in this table are for the rest studies. The number of cases with stable fit results in at least 1 segment is indicated by n. 261

Table 10-5 – Results from patients with single vessel stable coronary artery disease. Results in this table are for the adenosine stress studies. The number of cases with stable fit results in at least 1 segment is indicated by n. 262

Table 10-6 – Myocardial perfusion reserve estimates for patients and volunteers from the CAD hyperoxaemia study. 264

List of Figures

Figure 2-1 – Left – Cross-sectional schematic of the structure of the heart showing the four chambers (RA – right atrium, RV – right ventricle, LA – left atrium and LV – left ventricle). Also shown are the major veins feeding the RA (SVC – superior vena cava and IVC – inferior vena cava) and the LA (PV – pulmonary veins) and major arteries draining the RV (PA – pulmonary artery) and LV (Ao – aorta).Ovals in the atria indicate inlets from the veins. Black arrows indicate direction of blood flow. Pink shaded regions show myocardium, with that forming the division between the LV and RV being the intraventricular septum. Right - Diagram of location of major coronary arteries in relation to structure of the heart. The major coronary arteries are indicated by RCA – right coronary artery, LCA – left coronary artery, Cx – circumflex and LAD – left anterior descending artery. 8

Figure 2-2 – Schematic of coronary circulation. Major coronary vessels lie on the epidcardial surface with smaller vessels penetrating the myocardium. Gas, nutrient and waste product exchange occurs across the thin wall of the capillaries. 9

Figure 2-3 – Simplified diagram of the microscopic structure of the myocardium. Blood (red) flows through the microvasculature (indicated by red arrows) to perfuse the tissue. Gas, nutrient and waste products exchange across the capillary walls (dashed lines), supporting metabolism in the cardiomyocytes (brown ovals) to allow contractile function. The cellular and vascular structure of the myocardium is supported by the interstitial extracellular matrix (blue) which predominantly consists of collagen. 10

Figure 2-4 – Diagram showing a healthy artery (left) and arteries with small (middle) and large (bottom) artherosclerotic plaques (mid-left and mid-right). Plaques may rupture (right) causing a blood clot to form, completely obstructing the lumen. 11

Figure 2-5 – The ischaemic cascade – figure reproduced from the original 1987 description by Nesto and Kowalchuk [25]. 12

Figure 2-6 – Indication of the short axis view (left, green dashed line) intersecting both ventricles and a schematic in this view (right) of potential myocardial tissue states in acute myocardial infarction. A region of infarcted myocardium (orange) may be surround by oedematous tissue (blue) and may contain a core with microvascular obstruction (black). The pink regions are the blood filled cavities of the respective chambers. 13

Figure 2-7 – Schematic of a 2D spoiled gradient echo MRI pulse sequence. Gradients (G) are applied in the slice selection (SS), phase encoding (PE) and frequency encoding (FE) in order to spatially localise received signals. Multiple signals (S) must be acquired with varying G_{PE} (indicated by striped pattern) in order to spatially encode signal in the PE direction, so the process is repeated multiple times (the RF pulse and slice select gradient for the subsequent repetition are shown on the right of this figure) with a repetition time TR. (Figure adapted from the Pocket Guide on Cardiovascular Magnetic Resonance Physics for Clinicians [19]) 19

Figure 2-8 - Variation of steady-state longitudinal magnetisation (for spoiled gradient echo sequences) with flip angle and T_1/TR ratio. The right hand figure is zoomed in to the low T_1/TR range. 23

Figure 2-9 – Comparison of a non-prepared and saturation prepared sequence. In the latter differences in longitudinal magnetisation depend predominantly on differential recovery after the preparation pulse. (Figure adapted from the Pocket Guide on Cardiovascular Magnetic Resonance Physics for Clinicians [19]).....24

Figure 2-10 – Longitudinal magnetisation recovery following an inversion pulse (left) and an example of how this can be exploited to visual pathological myocardial tissue using the LGE technique (right) in which infarcted tissue appears bright in comparison to healthy myocardium for which the signal is nulled (dark). (Figure adapted from the Pocket Guide on Cardiovascular Magnetic Resonance Physics for Clinicians [19]) 25

Figure 2-11 – Schematic of cardiac DCE-MRI in which images are acquired serially during and following the injection of a GBCA bolus. In this example three image slices are acquired per cardiac cycle using a saturation prepared

sequence. The images at the top show the temporal variation of contrast agent presence, with brighter signal corresponding to greater concentrations of GBCA. Contrast agent initially is seen in the right ventricular cavity, followed by the left ventricular cavity (after passing through the pulmonary circulation) before perfusing the myocardial tissue. (Figure adapted from the Pocket Guide on Cardiovascular Magnetic Resonance Physics for Clinicians [19]) 35

Figure 2-12 – Example data from myocardial DCE-MRI showing typical timescales of contrast agent variation in the blood (red) and myocardium (blue). (N.B. the myocardial data has been scaled up relative to the blood data for visualisation, as the signal variation in myocardium is generally much lower than in the blood, the signal is recorded in arbitrary units).....36

Figure 2-13 – Pre-contrast (left) and early post-contrast (right) phase images from a stress DCE-MRI series of a patient with an inferior perfusion defect visible as a region of myocardium showing reduced enhancement compared to normally perfused tissue after contrast agent arrival. Visual analysis of such data can allow identification of perfusion defects without quantitative or semi-quantitative analysis.....37

Figure 2-14 – One-compartment model with no leakage. A single well-mixed compartment with equal inlet and outlet flows (F_p) occupies a volume fraction v_d. 41

Figure 2-15 – Single-region plug-flow model. The contrast agent passes through a single tube with equal inlet and outlet flows (F_p) and occupying a total distribution volume fraction equal to v_d. To derive the residue function this tube is described mathematically as a series of communicating infinitesimal compartments. This model would typically be used for intravascular agents, in which case $v_d=v_p$.....42

Figure 2-16 – Two-region single barrier distributed parameter model. Contrast agent passes through a series of communicating infinitesimal regions, with equal inlet and outlet flows (F_p) and occupying a total distribution volume fraction equal to v_p. These regions communicate with a series of extravascular regions, which do not communicate with each other directly. The total distribution volume fraction of the extravascular regions is v_e and the transfer

between the two spaces is described by the permeability-surface area product (PS).....43

Figure 2-17 – Graphical representation of spaces making up the systemic blood and the myocardium. Only white regions are accessible to extracellular contrast agents. RBCs indicates red blood cells For the accessible areas the concentrations are defined as c_p for plasma (in both systemic and myocardial blood) and c_e for the extravascular-extracellular space. Relative volumes are defined as v_p and v_e for the same spaces respectively. For the systemic blood the plasma volume is equal to 1 – Hct, where Hct is the haematocrit. The ECV is the total extracellular volume fraction (v_e+v_p). 47

Figure 3-1 – Example protocol including stress/rest perfusion (DCE) MRI. Items in pink indicate DCE-MRI and include contrast agent administration. Those in blue relate to ECV measurement, T_1 mapping and/or non-linearity correction of DCE data. Items in green are additional sequences for tissue and function characterisation and the selection and ordering of these may vary depending on the clinical requirements. Additional elements, such as coronary artery imaging or flow encoded imaging, may also be included. Some of these sequences may be performed post-contrast during the delay periods (peach).....52

Figure 3-2 – “Three-of-five” approach for cardiac DCE-MRI imaging. Initially five equally spaced slices are prescribed (dashed lines). The outer two (red) are then discarded prior to acquisition of the inner three (green).....54

Figure 3-3 – Schematic of three slice, saturation recovery spoiled gradient echo, ECG triggered DCE-MRI sequence. Dark blue rectangles indicate non-slice selective saturation pulses. Bold blue lines indicate the position of the central line of k-space within the readout train (vertical blue striped rectangle). In proton density weighted variants the saturation pulses are omitted.....56

Figure 3-4 – Top – DCE-MRI images (cropped for clarity) acquired at each end of the respiratory cycle (left – inspiration, right – expiration). These images are from a volunteer who breathed deeply throughout acquisition. These images were acquired approximately 2 minutes after contrast agent administration and were 3 cardiac cycles (2.3 seconds) apart so little variation in contrast agent concentration would be expected. Despite this myocardial signal intensity varies

approximately 20% between the two images. Bottom – This variation leads to structured variation in the myocardial signal curve which is due to motion rather than contrast agent variation.....57

Figure 3-5 – Top - Schematic of three slice, saturation recovery spoiled gradient echo, ECG triggered DCE-MRI sequence with interleaved low spatial resolution image for measuring the AIF in the dual-sequence approach. Bold blue or red lines indicate the position of the central line of k-space within the readout trains (vertical blue or red striped rectangles) for the full resolution or interleaved low resolution sequences respectively. In proton density weighted variants the saturation pulses are omitted. Bottom – Example low-resolution (top row) and high resolution (bottom row, same slice location) images from different phases of enhancement (left – pre-contrast, middle - peak AIF, right – myocardial enhancement).....59

Figure 4-1 – Data collection for the MOLLI technique (for a single inversion). Images are acquired at the same cardiac phase and have differing contrast due to recovery of longitudinal magnetisation. (Figure adapted from the Pocket Guide on Cardiovascular Magnetic Resonance Physics for Clinicians [19]).....89

Figure 4-2 – Merging of data from multiple inversions (three in this case) in MOLLI. (Figure adapted from the Pocket Guide on Cardiovascular Magnetic Resonance Physics for Clinicians [19]).....90

Figure 4-3 – Comparison of MOLLI and ShMOLLI schemes in relation to the ECG trace at 60bpm. Bottom plots show evolution of longitudinal magnetisation. Adapted from [136]. 97

Figure 6-1 – Example MOLLI schemes indicating cardiac phases with data acquisition (black bars). Each epoch is preceded by an inversion pulse. For the heart rate of 70 bpm in this example an extra RR interval is introduced into each recovery period in the 3(3s)3(3s)5 scheme (bottom) compared to the 3(3)3(3)5 scheme (top) to achieve a recovery period of at least 3 seconds. 118

Figure 6-2 - Simulated MOLLI accuracy curves for the simulated schemes. In the left column recovery periods are specified in terms of cardiac cycles and in the right column in seconds. 120

Figure 6-3 - MOLLI accuracy curves from the phantom data. 121

Figure 7-1 – Illustrative signal-R_1 curves. The black line shows the relationship between signal and R_1 for ideal saturation with the blue and red curves showing that for over- and under-saturation. Native, post-contrast and peak R_1 values are indicated by blue, green and brown dashed vertical lines respectively. In the native T_1 approach the signal model is constrained to pass through the origin and so the relationships expected for over- and under-saturation cannot be described. In these scenarios the derived signal models would be as shown by the blue and red dotted lines, and thus large errors would occur for estimation of post-contrast arrival R_1 values. Use of the bookend T_1 approach allows the expected relationship for non-ideal saturation efficiency to be determined from the two measured points. 127

Figure 7-2 - Ground truth concentration-time curves used in the simulations. 129

Figure 7-3 – Simulation process. Simulations are repeated with varying SNR, ground truth physiological parameters and saturation efficiencies. Graphical representations show the AIF and myocardial concentration curves (dotted – healthy myocardium at rest, solid – healthy myocardium under stress, dashed – infarcted myocardium at rest).....132

Figure 7-4 – AIF signal-time curves assuming ideal saturation efficiency. Shading indicates one standard deviation. Top: AIF. The red line shows the standard AIF (normal acquisition, full dose), blue reduced dose pre-bolus for the dual-bolus method and black the AIF from the full dose using the lower sensitivity sequence for the dual-sequence method (N.B. the same AIF concentration curves were used for rest and stress). Bottom: Myocardial response. Each line shows a different tissue status. The same myocardial signal data is used for each analysis method. 142

Figure 7-5 – Errors in estimated parameters for healthy myocardium at rest (A – MBF and B – v_d) and stress (C – MBF and D – v_d) and for infarcted myocardium at rest (E – MBF & F – v_d) for deconvolution using signal-enhancement data without correction for non-linearity. Dashed lines show results in the absence of noise. Solid lines and shading show mean results +/- one standard deviation for data with noise. Results presented are from slice 1. 144

Figure 7-6 – Errors in estimated parameters for healthy myocardium at rest (A – MBF and B – v_d) and stress (C – MBF and D – v_d) and for infarcted myocardium at rest (E – MBF & F – v_d) for deconvolution using signal-enhancement data without correction for non-linearity. Dashed lines show results in the absence of noise. Solid lines and shading show mean results +/- one standard deviation for data with noise. Results presented are from slice 2. Results were similar between slices 2 and 3. 145

Figure 7-7 - Errors in estimated parameters for healthy myocardium at rest (A – MBF and B – v_d) and stress (C – MBF and D – v_d) and for infarcted myocardium at rest (E – MBF & F – v_d) for deconvolution using the dual-bolus method. Dashed lines show results in the absence of noise. Solid lines and shading show mean results +/- one standard deviation for data with noise. Results presented are from slice 1. 146

Figure 7-8 - Errors in estimated parameters for healthy myocardium at rest (A – MBF and B – v_d) and stress (C – MBF and D – v_d) and for infarcted myocardium at rest (E – MBF & F – v_d) for deconvolution using the dual-bolus method. Dashed lines show results in the absence of noise. Solid lines and shading show mean results +/- one standard deviation for data with noise. Results presented are from slice 2. Results were similar between slices 2 and 3. 147

Figure 7-9 - Errors in estimated parameters for healthy myocardium at rest (A – MBF and B – v_d) and stress (C – MBF and D – v_d) and for infarcted myocardium at rest (E – MBF & F – v_d) for deconvolution using native T_1 based correction. Dashed lines show results in the absence of noise. Solid lines and shading show mean results +/- one standard deviation for data with noise. Results presented are from slice 1. Results are identical for the two signal models as the two signal models are equivalent for assumed ideal saturation (Equation 7-6). 149

Figure 7-10 - Errors in estimated parameters for healthy myocardium at rest (A – MBF and B – v_d) and stress (C – MBF and D – v_d) and for infarcted myocardium at rest (E – MBF & F – v_d) for deconvolution using native T_1 based correction. Dashed lines show results in the absence of noise. Solid lines and shading show mean results +/- one standard deviation for data with noise.

Results presented are from slice 2. Results were similar between slices 2 and 3. Results are identical for the two signal models as the two signal models are equivalent for assumed ideal saturation (Equation 7-6). 150

Figure 7-11 - Errors in estimated parameters for healthy myocardium at rest (A – MBF and B – v_d) and stress (C – MBF and D – v_d) and for infarcted myocardium at rest (E – MBF & F – v_d) for deconvolution using bookend T_1 based correction and the full recovery signal model. Dashed lines show results in the absence of noise. Solid lines and shading show mean results +/- one standard deviation for data with noise. Results presented are from slice 1. ...151

Figure 7-12 - Errors in estimated parameters for healthy myocardium at rest (A – MBF and B – v_d) and stress (C – MBF and D – v_d) and for infarcted myocardium at rest (E – MBF & F – v_d) for deconvolution using bookend T_1 based correction and the full recovery signal model. Dashed lines show results in the absence of noise. Solid lines and shading show mean results +/- one standard deviation for data with noise. Results presented are from slice 2. Results were similar between slices 2 and 3. 152

Figure 7-13 - Errors in estimated parameters for healthy myocardium at rest (A – MBF and B – v_d) and stress (C – MBF and D – v_d) and for infarcted myocardium at rest (E – MBF & F – v_d) for deconvolution using bookend T_1 based correction and the steady-state signal model. Dashed lines show results in the absence of noise. Solid lines and shading show mean results +/- one standard deviation for data with noise. Results presented are from slice 1. ...153

Figure 7-14 - Errors in estimated parameters for healthy myocardium at rest (A – MBF and B – v_d) and stress (C – MBF and D – v_d) and for infarcted myocardium at rest (E – MBF & F – v_d) for deconvolution using bookend T_1 based correction and the steady-state signal model. Dashed lines show results in the absence of noise. Solid lines and shading show mean results +/- one standard deviation for data with noise. Results presented are from slice 2. Results were similar between slices 2 and 3. 154

Figure 7-15 – Errors introduced in analysis due to errors in measured T_1 used for model-based correction. Data is for the native T_1 based conversion for slice

1. Results are identical for the two signal models as the two signal models are equivalent for assumed ideal saturation (Equation 7-6). 155

Figure 7-16 – Errors introduced in analysis due to errors in measured T_1 used for model-based correction. Data is for the native T_1 based conversion for slice 2. Results are identical for the two signal models. Results are similar between slices 2 and 3. 156

Figure 7-17 – Errors introduced in analysis due to errors in measured T_1 used for model-based correction. Data is for the bookend T_1 based conversion with the full recovery signal model for slice 1. 157

Figure 7-18 – Errors introduced in analysis due to errors in measured T_1 used for model-based correction. Data is for the bookend T_1 based conversion with the full recovery signal model for slice 2. Results are similar between slices 2 and 3. 158

Figure 7-19 – Errors introduced in analysis due to errors in measured T_1 used for model-based correction. Data is for the bookend T_1 based conversion with the steady-state signal model for slice 1. 159

Figure 7-20 – Errors introduced in analysis due to errors in measured T_1 used for model-based correction. Data is for the bookend T_1 based conversion with the steady-state signal model for slice 2. Results are similar between slices 2 and 3. 160

Figure 7-21 - Errors in estimated parameters for healthy myocardium at rest (A – MBF and B – v_d) and stress (C – MBF and D – v_d) and for infarcted myocardium at rest (E – MBF & F – v_d) for deconvolution using proton density weighted image based correction and the full recovery signal model. Dashed lines show results in the absence of noise. Solid lines and shading show mean results +/- one standard deviation for data with noise. Results presented are from slice 1 with 3° flip angle. 162

Figure 7-22 - Errors in estimated parameters for healthy myocardium at rest (A – MBF and B – v_d) and stress (C – MBF and D – v_d) and for infarcted myocardium at rest (E – MBF & F – v_d) for deconvolution using proton density

weighted image based correction and the full recovery signal model. Dashed lines show results in the absence of noise. Solid lines and shading show mean results +/- one standard deviation for data with noise. Results presented are from slice 2 with 3° flip angle. Results were similar between slices 2 and 3. ..163

Figure 7-23 - Errors in estimated parameters for healthy myocardium at rest (A – MBF and B – v_d) and stress (C – MBF and D – v_d) and for infarcted myocardium at rest (E – MBF & F – v_d) for deconvolution using proton density weighted image based correction and the steady-state signal model. Dashed lines show results in the absence of noise. Solid lines and shading show mean results +/- one standard deviation for data with noise. Results presented are from slice 1 with 3° flip angle. 164

Figure 7-24 - Errors in estimated parameters for healthy myocardium at rest (A – MBF and B – v_d) and stress (C – MBF and D – v_d) and for infarcted myocardium at rest (E – MBF & F – v_d) for deconvolution using proton density weighted image based correction and the steady-state signal model. Dashed lines show results in the absence of noise. Solid lines and shading show mean results +/- one standard deviation for data with noise. Results presented are from slice 2 with 3° flip angle. Results were similar between slices 2 and 3. ..165

Figure 7-25 - Errors in estimated parameters for healthy myocardium at rest (A – MBF and B – v_d) and stress (C – MBF and D – v_d) and for infarcted myocardium at rest (E – MBF & F – v_d) for deconvolution using the dual-sequence method and the full recovery signal model. Dashed lines show results in the absence of noise. Solid lines and shading show mean results +/- one standard deviation for data with noise. Results presented are from slice 1. Results were similar between all slices.....166

Figure 7-26 - Errors in estimated parameters for healthy myocardium at rest (A – MBF and B – v_d) and stress (C – MBF and D – v_d) and for infarcted myocardium at rest (E – MBF & F – v_d) for deconvolution using the dual-sequence method and the steady-state signal model. Dashed lines show results in the absence of noise. Solid lines and shading show mean results +/- one standard deviation for data with noise. Results presented are from slice 1. Results were similar between all slices.....167

Figure 7-27 - Box-and-whisker plots comparing non-linearity correction methods for realistic levels of saturation efficiency and SNR for resting MBF and normal v_d values. Outliers (individual points) are identified as data more than two times the inter-quartile range above/below the upper/lower quartiles. These results show errors in MBF when the full recovery signal model is used for model based conversions. 168

Figure 7-28 - Box-and-whisker plots comparing non-linearity correction methods for realistic levels of saturation efficiency and SNR for resting MBF and normal v_d values. Outliers (individual points) are identified as data more than two times the inter-quartile range above/below the upper/lower quartiles. These results show errors in MBF when the steady-state signal model is used for model based conversions. 169

Figure 7-29 - Box-and-whisker plots comparing non-linearity correction methods for realistic levels of saturation efficiency and SNR for resting MBF and normal v_d values. Outliers (individual points) are identified as data more than two times the inter-quartile range above/below the upper/lower quartiles. These results show errors in v_d when the full recovery signal model is used for model based conversions. 170

Figure 7-30 - Box-and-whisker plots comparing non-linearity correction methods for realistic levels of saturation efficiency and SNR for resting MBF and normal v_d values. Outliers (individual points) are identified as data more than two times the inter-quartile range above/below the upper/lower quartiles. These results show errors in v_d when the steady-state signal model is used for model based conversions. 171

Figure 7-31 - Bland-Altman plot of phantom T_1 values by two MOLLI schemes and SR-GE in comparison to IR-SE. The large errors observed for the 4s(1s)3s(1s)2s scheme at long T_1 are expected is this sequence is designed for use only with contrast enhanced tissues and does not allow for sufficient recovery of longitudinal magnetisation between inversion pulses to accurately quantify the native T_1 values of blood or myocardium. 173

Figure 7-32 – Normalised SR-GE signal intensity (crosses) and model fits (lines) from the phantom study (bottom panel shows zoomed view). Absolute

values are plotted and for each gel the fitted curve has a null point at TS>0, indicating over-saturation. For ideal saturation curves would recover from the origin, and for under-saturation curves would not reach the x-axis for TS>0. .174

Figure 7-33 – Correlation of ΔR_1 values from data acquired by imaging gels of differing T_1 using a DCE-MRI sequence (estimated using with native (blue) or bookend (red) T_1 based conversion with the full recovery model) to MOLLI T_1 values. The black dashed line shows ideal agreement and the red vertical dashed lines intersect the points used in estimating S_0 and (for bookend T_1) SE. For the native T_1 based approach only the point at ΔR_1=0 was used to constrain the model. The legend shows results of linear fits, and estimated SE for the bookend T_1 based correction. 175

Figure 7-34 – Signal models derived from the results of Table 7-3. The S_0 values for the PDw method are very similar so the three curves are not visibly distinguishable on this plot. 183

Figure 7-35 – Comparison of analytical models to the approximated steady-state in forward simulations of the conventional SR sequence. At SE = 0 (centre panel) the models and simulations overlie each as prior magnetisation evolution is irrelevant. This is also true for all of the SR data presented in the following three figures. 201

Figure 7-36 – Comparison of analytical models to the approximated steady-state in forward simulations of the conventional SR sequence. This figure is identical to the previous figure, except the x-axis is limited to a narrower range to better show deviations in behaviour. 202

Figure 7-37 – Comparison of analytical models to the first dynamic phase from forward simulations for the conventional SR sequence. The results for slice 1 overlie those for the full recovery model exactly, while those for the latter slices are close to the steady-state model due to the effect of the previous saturation pulse (or pulses). 204

Figure 7-38 – Comparison of analytical models to approximated steady-state from forward simulations for the interleaved AIF sequence. Due to the short

saturation times larger relative deviations exist for this sequence than for the conventional sequence. 206

Figure 7-39 – Comparison of analytical models to forward simulations for the 3° flip angle PDw sequence as implemented for the conventional and dual-sequence method. The vertical dashed lines indicate the native R_1 of blood. The top row shows the first dynamic phase while the bottom row shows the 100^{th}, approximating the steady-state. The middle row shows the 5^{th} dynamic phase, at which point the steady-state is still being approached. The three slices of the conventional sequence exhibit identical behaviour to each other and overlie the full-recovery model for the first dynamic phase and the steady-state model for the 100^{th}. For the AIF interleaved sequence the results of the forward simulation for the first dynamic phase overlie the full recovery model. 207

Figure 7-40 – Plots showing the approach to the steady-state for the longest T_1 relevant to the simulation study (that of native blood). Plots are shown for both flip angles simulated. 208

Figure 7-41 – ratio of baseline to post-contrast SI of blood modelled using the full-recovery model and parameters as in Table 7-1. Top: SE=0 to SE=2. Bottom: limited to SE range included in simulations. For the steady-state model the null point and singularity occur at higher SE values. 212

Figure 7-42 – Relative signal intensity variation with R_1 for ideal saturation and various over-saturation values for the full recovery (top) and steady-state (bottom) model. As larger degrees of over-saturation are required for signal nulling in the latter a broader range of SE values is plotted. 213

Figure 8-1 – Example contours from the hyperoxaemia volunteer study. Red and green contours show endocardial and epicardial layer contours respectively. The anterior right ventricular insertion point is marked (blue cross) and the myocardium segmented into 6 with equally spaced radial divisions although the full circumferential extent was averaged over these segments for this volunteer study as no focal disease was present. The yellow contour marks the region used for the AIF. Left – full field of view. Right – zoomed section showing left and right ventricles and contours. 218

Figure 8-2 – Example post-contrast T_1 map (left: individual images, right: T_1 map) with artefact in the LV and RV blood pool. Images are cropped to the heart.....219

Figure 8-3 – Example signal-time data from one volunteer including one compartment model fits to signal enhancement data.....220

Figure 8-4 – Example stress DCE-MRI images. Top to bottom: interleaved AIF scan (dual-sequence) followed by slices 1-3. Left to right: pre-contrast, peak AIF contrast and approximately 2 minutes post-contrast.....221

Figure 8-5 – Example rest DCE-MRI images. Top to bottom: interleaved AIF scan (dual-sequence) followed by slices 1-3. Left to right: pre-contrast, peak AIF contrast and approximately 2 minutes post-contrast.....222

Figure 8-6 - Mean parameter estimates for 18 volunteers (error bars show one standard deviation) showing systematic differences in results dependent on analysis method used. In 2 cases data from the native T_1 based method is excluded as this conversion failed due to peak AIF signal exceeding estimated S_0. These cases had the highest estimated over-saturation (saturation efficiencies of 1.037 and 1.045) by the bookend T_1 based method. Dual-bolus data for resting v_d is based on 13 of the volunteers as in the other 5 the parameter estimate was unstable due to low SNR in the AIF. 224

Figure 9-1 - Example images (acute visit) from a patient with persistent MVO and peri-infarct oedema. Left – T_2 weighted image showing contoured bright region which includes infarct and oedema. Centre – LGE image showing contoured bright region of infarct with a core of MVO, also contoured in blue is a region of remote myocardium. Right – DCE-MRI image showing regions used for MVO (cyan), infarct (magenta), peri-infarct oedma (yellow) and left-ventricular blood pool (blue, for AIF). In all images the endocardial and epicardial layers are delineated in red and green respectively.....235

Figure 9-2 - Example images (acute visit) from a patient without MVO and with substantial myocardial salvage. Left – T_2 weighted image showing contoured bright region which includes infarct and oedema. Centre – LGE image showing contoured bright region of infarct which is substantially smaller than the bright

region on T_2 weighted imaging. Right – DCE-MRI image showing regions used for infarct (magenta), peri-infarct oedma (yellow) and left-ventricular blood pool (blue, for AIF). In all images the endocardial and epicardial layers are delineated in red and green respectively. 235

Figure 9-3 – Follow-up images from the same patient and slice location as Figure 9-1. Left – LGE. Right – DCE with contours (infarct in red, remote myocardium in green). Note that in the LGE image the core of MVO is no longer present, nor is the region of slightly enhanced signal in the region contoured as peri-infarct oedema at the first image. 236

Figure 9-4 - Example AIF. Vertical lines indicate timing of MOLLI acquisitions and red circles indicate the SI used for this time point in saturation correction (derived from the baseline for pre-contrast or from the bi-exponential fit for post-contrast).....242

Figure 9-5 – Example myocardial signal-time curves from one patient (cropped to main-bolus administration and first DCE-MRI series). 244

Figure 9-6 – Results from the STEMI study. 246

Figure 10-1 – Example DCE-MRI images and contours from the hyperoxaemia study. Left – patient with severe occlusion of the right coronary artery with inferior perfusion defect visible. Right – healthy volunteer image. Images shown are at peak myocardial enhancement. 257

Figure 10-2 – Results from the volunteers in the hyperoxaemia study. 259

Figure 10-3 – Results from the patients with single vessel stable coronary artery disease in the hyperoxaemia study. 263

Abbreviations

Abbreviations used commonly throughout this thesis are defined below. Less frequently used abbreviations are defined where they are introduced.

$[CA]/C_i$	Contrast agent concentration in tissue or fluid "i"
AIF	Arterial Input Function
BAT	Bolus Arrival Time
bpm	Beats Per Minute
CAD	Coronary Artery Disease
CMR	Cardiovascular Magnetic Resonance
CNR	Contrast to Noise Ratio
CVF	Collagen Volume Fraction
DCE	Dynamic Contrast Enhanced
DP	Distributed Parameter
E	First pass extraction fraction
ECG	Electrocardiograph
ECV	Extracellular Volume Fraction
FA/α/θ	Flip Angle/Readout Pulse Flip Angle/Preparation Pulse Flip Angle
F_b/F_p	Blood Flow/Plasma flow
GBCA	Gadolinium Based Contrast Agent
H(t)	Transit Time Probability Distribution Function
Hct	Haematocrit
IR	Inversion Recovery
λ	Partition Coefficient
LGE/DE	Late Gadolinium Enhancement/Delayed Enhancement
LV	Left ventricle/ventricular
$M/M_z/M_{xy}$	Magnetisation/Longitudinal Magnetisation/Transverse Magnetisation
M_0/M_{SS}	Equilibrium Magnetisation/Steady-State Magnetisation
MBF	Myocardial Blood Flow
MI	Myocardial Infarction
MOLLI	Modified Look-Locker Inversion Recovery
MPR	Myocardial Perfusion Reserve

MRI	Magnetic Resonance Imaging
PDw	Proton Density Weighted
PET	Positron Emission Tomography
PPD	Pre-Pulse Delay
R(t)	Residue Function
R_1	Longitudinal Relaxation Rate
r_1	Longitudinal Relaxivity
RF	Radiofrequency
S0	Equilibrium Signal Intensity
SE	Saturation Efficiency
SI	Signal Intensity
SNR	Signal to Noise Ratio
SR	Saturation Recovery
STEMI	ST-segment Elevated Myocardial Infarction
$T/T_c/T_e$	Mean Transit Time/Mean Capillary Transit Time/Mean Extracellular-Extravascular Transit Time
T_1/T_1^*	Longitudinal Relaxation Time/Apparent Longitudinal Relaxation Time
T_2/T_2^*	Transverse Relaxation Time (irreversible spin-spin component only/ observed value including magnetic field inhomogeneity and susceptibility effects)
TD	Delay Time/Trigger Delay
TE/TR	Echo Time/Repetition Time
TI/TS	Inversion Time/Saturation Time
v_b/v_p	Blood Volume Fraction/Plasma Volume Fraction
v_d	Distribution Volume Fraction
v_e	Extracellular-Extravascular Volume Fraction

Chapter 1
Introduction

This thesis details work carried out between October 2012 and September 2015 investigating the clinical application of quantitative analysis of contrast enhanced cardiac MRI data to probe myocardial tissue status.

Prior to the period of the PhD I worked with my supervisors to retrospectively analyse dynamic contrast enhanced (DCE) magnetic resonance imaging (MRI) data acquired from a previous study in order to gain understanding of the applicability of the distributed parameter model to such data. This work resulted in the publication of a paper [1] and informs the work carried out during the PhD, but does not form part of this thesis. The structure of the work that is contained in the following chapters is detailed below.

1.1 Structure of thesis

Cardiovascular magnetic resonance (CMR) is an established tool for the evaluation of the structure and function of the human heart and vasculature and is employed routinely in clinical practice for a wide range of indications [2]. The work of this thesis focuses on a specific area of CMR, the quantitative assessment of myocardial tissue status using gadolinium based contrast agent (GBCA) enhanced MRI techniques.

The use of GBCAs in CMR has become ubiquitous in the assessment of the myocardium in both ischaemic heart disease and various cardiomyopathies. This is based largely on work in the 1990s by Wilke *et al* [3, 4] and Kim *et al* [5, 6] who demonstrated that the techniques allows identification of regions of suppressed perfusion and myocardial damage respectively. In addition to allowing visual identification of abnormal myocardium the technique affords the potential to perform quantitative analysis to determine absolute or relative physiological properties which may allow more objective assessment of focal pathology, and assessment of diffuse disease processes in which the lack of image contrast between myocardial segments or areas limits the usefulness of direct visual interpretation of acquired images.

The techniques discussed in this thesis rely on the underlying theory of the biodistribution of the contrast agents used, the physical effect of the contrast agent and its impact upon magnetic resonance signal intensity, and the biology and physiology of the heart. The theory of these areas is discussed in Chapter 2. As discussed in the technical and clinical literature reviews in Chapters 3 and 4 the majority of research on quantitative CMR for assessment of myocardium has focussed on the use of DCE-MRI to quantify myocardial perfusion or the use of contrast equilibrium MRI to estimate the distribution volume of the contrast agents used.

Contrast equilibrium based estimates of contrast agent distribution volume rely on accurate quantification of the longitudinal relaxation time of magnetisation of water and proteins both the myocardium and blood, and such measurements may also be used in the quantitative analysis of DCE-MRI. Simulation and phantom based studies assessing the performance of variants of the commonly used modified Look-Locker inversion recovery (MOLLI) approach [7] are discussed in Chapter 5.

The remainder of the thesis focusses on the assessment of multiple physiological parameters from the analysis of DCE-MRI using deconvolution analysis. Further background theory on this approach is discussed in Chapter 2. Chapter 6 describes the general methodology used for this approach in clinical studies, including those described in the subsequent chapters. For absolute quantification of physiological parameters from DCE-MRI it is necessary to be able to accurately relate magnetic resonance signal intensity to relative contrast agent concentration. Chapter 7 describes simulation and phantom studies performed to assess and compare the performance of several previously proposed methods and a novel proposal for this analytical stage.

Chapters 8 and 9 describe results of clinical studies performed using the methodology described in earlier chapters. The former focusses on results from a control group of healthy volunteers using a one-compartment tracer kinetic model to assess the methods described in Chapter 7 *in vivo*, while the latter compares results from cohorts of patients with ischaemic heart disease to these volunteers using distributed parameter model constrained deconvolution. Finally

in Chapter 10 overall conclusions are described and areas in which further study are warranted are discussed.

1.2 Equipment used

All experimental work described in this thesis used data acquired using a 3 Tesla Philips system or simulations of the sequences as implemented on this system. The system was upgraded from an Achieva TX system, as initially installed, to receive dSTREAM radiofrequency (RF) system architecture and updated software (from release 3.2 to 5.1) during the course of the PhD (December 2014).

1.3 Ethics

This thesis includes work involving the collection of data from healthy volunteers and patients including acquisition of image data, injection of adenosine and gadolinium based contrast agents, administration of oxygen and sampling of venous blood. The study protocols were approved by the local research ethics committee (12/YH/0169 STEMI study and 13/YH/0013 CAD hyperoxaemia study, the latter including volunteer and patient scanning) and complied with the Declaration of Helsinki. All patients and volunteers gave written informed consent.

1.4 Chronology of project and resulting limitations

The work presented in this thesis includes analyses of data collected during clinical studies led by different members of the research team as described in the acknowledgements.

Data acquisition for the ST-Elevation Myocardial Infarction (STEMI) study commenced near the outset of the PhD project and so the protocol was defined while naïve to the results of the work described in chapters 7 & 8. Indeed the concept of using bookend T_1 based non-linearity correction was arrived at during analysis of the STEMI data and identification of the fact that several cases in this study could not be analysed using native T_1 based correction. While the aim of this study was initially to measure myocardial characteristics post-STEMI the work also led to the development of the aim to compare non-

linearity correction methods, including those identified in the literature review (section 4.3.2.2) and the proposed bookend T_1 based approach. Additionally the original modified Look-Locker inversion recovery (MOLLI) T_1 mapping scheme was used in this study, rather than optimised schemes identified through later work both in this thesis and reported in the literature.

The scanner upgrade referred to in section 1.2 occurred after data acquisition for the STEMI study was completed. Part of the software upgrade included addition of the Philips interleaved scanning capability which allows instantaneous switching between multiple scans. This functionality allowed the dual-sequence approach, which was not possible before upgrade, to be performed on the scanner. This was implemented by Dr David Higgins of Philips Healthcare (see acknowledgements on page viii) and used in the subsequent hyperoxaemia study protocol. The simulation and phantom studies occurred concurrently with this clinical study. Consequently acquisition protocols for the clinical study were finalised prior to the outcomes of the simulation and phantom studies being known.

A resulting limitation of the work in this thesis is thus that the optimal sequences and techniques identified in the phantom and simulation work have not always been used in the clinical protocols. In particular a low-flip angle proton density weighted sequence was not included in the hyperoxaemia study protocol so that correction method was not used for analysis for the patient studies and the data in the volunteer non-linearity correction methods comparison study was acquired with a sub-optimal proton density weighted sequence. However the clinical aims and the test of the feasibility of the bookend T_1 approach in clinically usable protocols have been achieved through both patient studies.

1.5 Additional work completed during PhD

Beyond the work described in the following chapters I have supported additional research in cardiac MRI which has led to co-authorship on conference abstracts and papers in the following topics; comparing bolus administration strategies [8, 9] and T_1 mapping techniques [10] for contrast equilibrium based myocardial extracellular volume (ECV) fraction estimation, application of ECV mapping to develop understanding of myocardial adaption to exercise [11], analysis

strategies for myocardial perfusion MRI data [12], inter-vendor comparison of *in vivo* longitudinal relaxation time (T_1) measurements [13] and establishment of reference values for T_1 and ECV in an international multi-centre study [14]. Further analysis of data from the cohort of ST-elevation myocardial infarction (STEMI) patients described in Chapter 9 has led to co-authorship on abstracts and publications relating to the application of non-contrast enhanced susceptibility weighted MRI [15, 16] and the prognostic value of extracellular volume mapping in comparison to measurement of the extent of late gadolinium enhancement [17, 18].

I have also supported an international cardiac MRI study investigating hypertrophic cardiomyopathy by authoring sections of the imaging manual relating to T_1 mapping quality control. Finally, with colleagues from the Leeds Clinical CMR Group I authored a Pocket Guide on Cardiovascular Magnetic Resonance Physics for Clinicians which is endorsed by the European Association of Cardiovascular Imaging (EACVI) CMR Section of the European Society of Cardiology (ESC) [19].

Chapter 2
Background Theory

In this chapter aspects of biological, medical and physical theory relevant to the topic of the thesis are described.

The first section describes briefly the structure, function and physiology of the myocardium in health, and introduces common disease pathways and consequences.

The following two sections describe first the underlying physics of MRI signal intensity and subsequently how it varies in the presence of MRI contrast agents. These sections are not intended to provide a comprehensive overview of MRI physics but serve to describe the theory relevant to the contents of this thesis.

Finally the bio-distribution of extracellular contrast agents following intra-venous injection is described. This pattern of distribution informs the techniques used to quantitatively assess the physiological status of the myocardium that are employed in this thesis.

The combined process of detection of the presence of these contrast agents, quantification of their concentration, and interpretation of these data to assess physiological status depends on the theory outlined in the four sections of this chapter.

2.1 Clinical and biological background

In this section a brief description of the clinical and biological background relating to the structure, function and perfusion of the myocardium both in health and disease, as relevant to this thesis, is provided.

2.1.1 Normal myocardial structure, function and perfusion

The basic function of the heart is to pump blood around the body through the pulmonary and systemic circulation. The mechanical force to drive this circulation is produced by cardiomyocytes, the muscle fibres which are the major constituent of the myocardium that forms the walls of the four chambers of the heart. The pulmonary circulation is driven by the right side of the heart

and the systemic by the left. Each side consists of two chambers, the atria into which blood arrives before passing into ventricles from where it is driven into either the pulmonary artery or the aorta respectively (Figure 2-1, left). This thesis focusses on assessment of the left ventricular myocardium, which normally has the greatest myocardial thickness of the four chambers as it is required to generate the largest pressures in order to drive the systemic circulation.

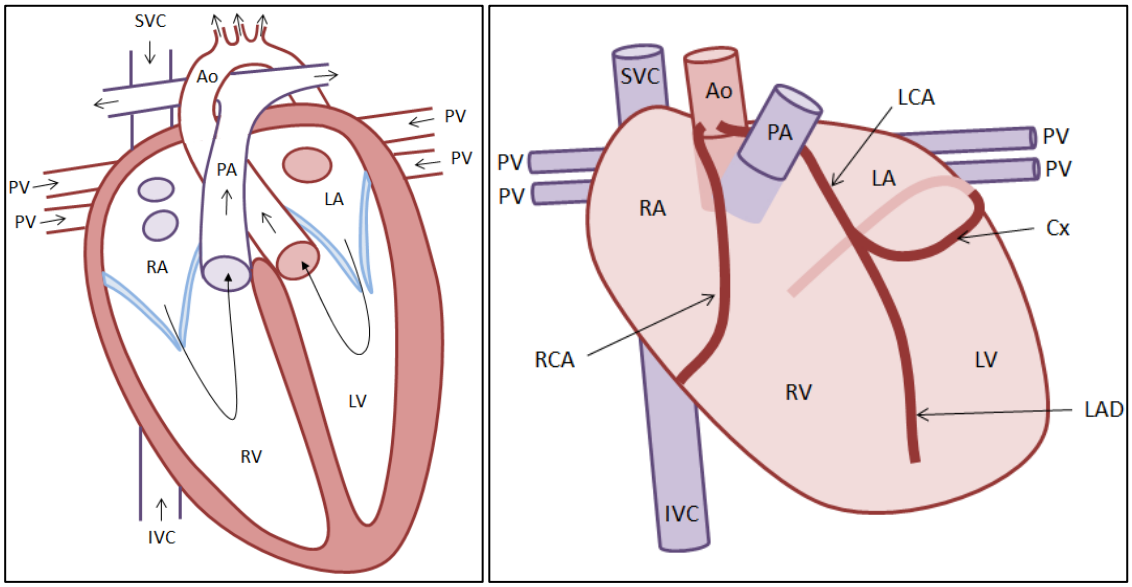

Figure 2-1 – Left – Cross-sectional schematic of the structure of the heart showing the four chambers (RA – right atrium, RV – right ventricle, LA – left atrium and LV – left ventricle). Also shown are the major veins feeding the RA (SVC – superior vena cava and IVC – inferior vena cava) and the LA (PV – pulmonary veins) and major arteries draining the RV (PA – pulmonary artery) and LV (Ao – aorta).Ovals in the atria indicate inlets from the veins. Black arrows indicate direction of blood flow. Pink shaded regions show myocardium, with that forming the division between the LV and RV being the intraventricular septum. Right - Diagram of location of major coronary arteries in relation to structure of the heart. The major coronary arteries are indicated by RCA – right coronary artery, LCA – left coronary artery, Cx – circumflex and LAD – left anterior descending artery.

The myocardium is perfused by the coronary arteries, the right and left coronary arteries being the most proximal branches of the aorta (Figure 2-1, right). These arteries branch sequentially into smaller arteries (the two major branches of the left coronary artery being the circumflex and the left anterior descending arteries), arterioles and then the capillary bed of the myocardium.

The walls of the capillaries consist of a single layer of endothelial cells and across these walls nutrient, gas and waste product exchange occurs to support the metabolism of the cardiomyocytes. Deoxygenated blood returns to the right atrium through the coronary venous system. The major vessels usually lie outside the epicardial surface of the heart and smaller branches permeate the myocardium to perfuse the full transmural thickness of the tissue (Figure 2-2).

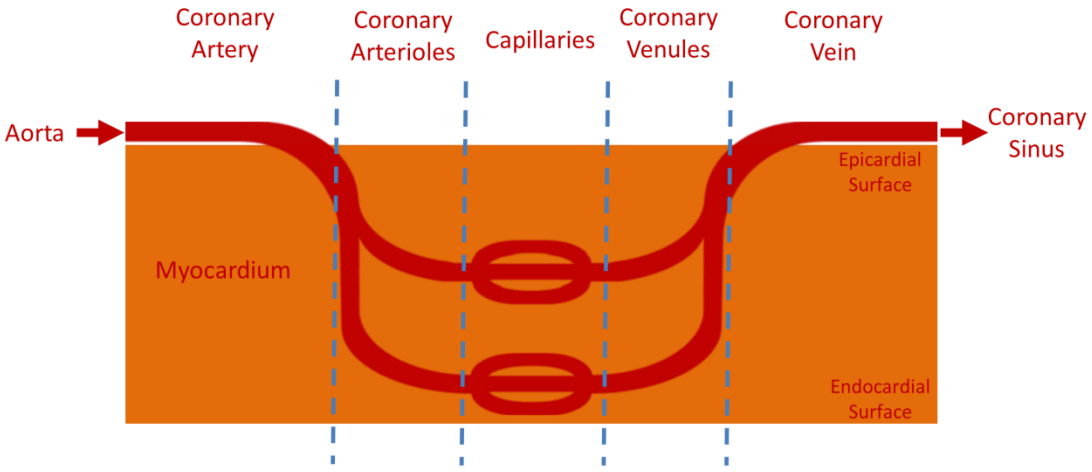

Figure 2-2 – Schematic of coronary circulation. Major coronary vessels lie on the epidcardial surface with smaller vessels penetrating the myocardium. Gas, nutrient and waste product exchange occurs across the thin wall of the capillaries.

It should be noted that while the description above implies a linear structure in which each region of myocardium is perfused through a single route from the aorta in reality the network of macro- and micro-vasculature is more complex with regions perfused by multiple pathways potentially overlapping and links between parallel vessels existing. Following myocardial injury or in the presence of vascular disease this network may undergo a process of remodelling to maintain sufficient perfusion to affected myocardium or flow through healthy regions may increase to compensate for reduced perfusion through affected vasculature.

At a microscopic level the myocardium consists of three major components, the cardiomyocytes and the microvasculature, supported within the extracellular matrix of the interstitium. This is depicted in Figure 2-3.

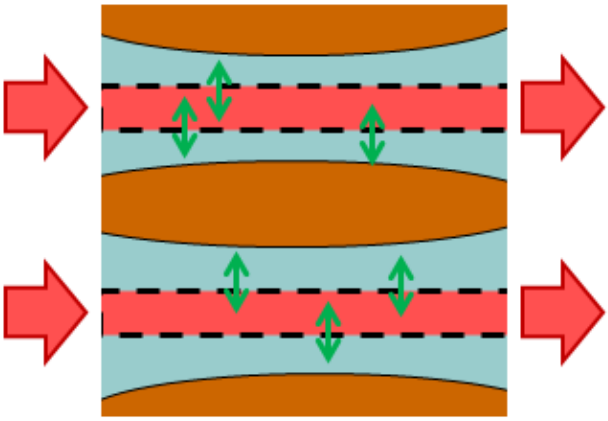

Figure 2-3 – Simplified diagram of the microscopic structure of the myocardium. Blood (red) flows through the microvasculature (indicated by red arrows) to perfuse the tissue. Gas, nutrient and waste products exchange across the capillary walls (dashed lines), supporting metabolism in the cardiomyocytes (brown ovals) to allow contractile function. The cellular and vascular structure of the myocardium is supported by the interstitial extracellular matrix (blue) which predominantly consists of collagen.

The structure of the myocardium is regular, with sheets of parallel fibres of varying orientations throughout the layers of the heart [20] to facilitate the shortening, thickening and twisting of the ventricle which occurs during the cardiac cycle. Capillaries are arranged in parallel to the fibres [21] with a high density of almost one capillary per cardiomyocyte fibre in the adult heart [22]. However not all capillaries are open at all times [23]. The individual capillaries have a small lumen diameter, narrower than the typical red blood cell diameter, and so the red blood cells have to deform to pass through the microvasculature.

Myocardial function responds autonomically to regulate systemic supply of oxygenated blood. Cardiac output can be increased either by increasing heart rate or the volume of blood ejected per cardiac cycle (or a combination of both). To facilitate the increased energy demand required for the cardiomyocytes to achieve this, myocardial perfusion can adapt and increases during periods of increased cardiovascular function, for example during exercise, emotional stress or after heavy meals. Myocardial stress can also be induced pharmacologically, as is used for stress perfusion studies in this thesis. For the work described in this thesis adenosine is used as a stress agent. This agent leads to dilation of the coronary vessels, with a lesser effect in stenosed vessels (see section 2.1.2) leading to a differential increase in blood velocity and flow

rate in vessels depending on their pathological status as well as decreased blood pressure and increased heart rate [24]. Similarly abnormalities in the function (i.e. the wall motion) that are not present at rest may also be induced by exercise or pharmacological stress. Increased myocardial blood flow is associated with a combination of increased arterial blood pressure and decreased microvascular resistance, the latter of which may arise due to a combination of dilation of small arteries and arterioles as well as the opening of additional capillaries (capillary recruitment) [23].

2.1.2 The myocardium in disease

Diseases of the myocardium can broadly be classified into ischaemic and non-ischaemic categories. Ischaemic heart disease arises due to limited perfusion through the coronary circulation arising from partial or complete occlusion of one or more of the coronary arteries or their sub-branches. Such occlusions arise due to atherosclerosis, in which fatty and fibrous materials are deposited on the arterial walls forming plaques (Figure 2-4).

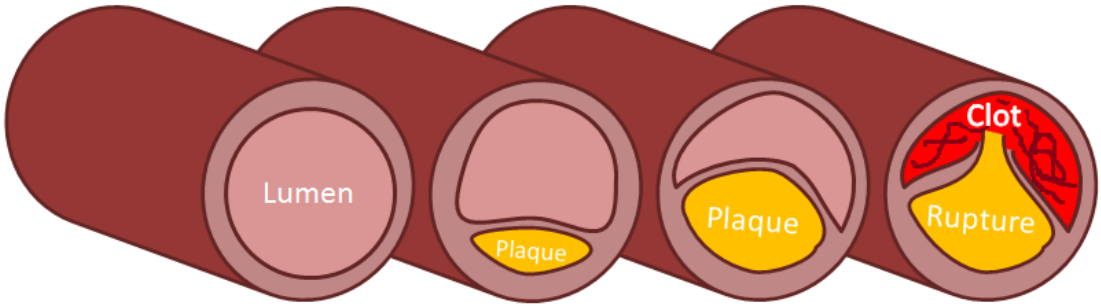

Figure 2-4 – Diagram showing a healthy artery (left) and arteries with small (middle) and large (bottom) artherosclerotic plaques (mid-left and mid-right). Plaques may rupture (right) causing a blood clot to form, completely obstructing the lumen.

Early phases of atherosclerosis may not lead to the presentation of symptoms as the plaques may not limit flow sufficiently to hinder myocardial metabolic activity. Eventually occlusions may advance such that adequate perfusion for normal myocardial metabolism levels may persist but without the capacity to increase sufficiently during periods of increased cardiovascular activity. This can lead to stress induced angina where symptoms of chest pain arise only during periods of increased cardiovascular demand. The series of processes that occur during ischemia have been described as the ischeamic cascade [25]

and initially consists of sub-clinical presentations which may not be detected before progressing to abnormalities in wall motion abnormalities and electrocardiographical findings as well as symptoms experienced by patients. This cascade is shown schematically in Figure 2-5.

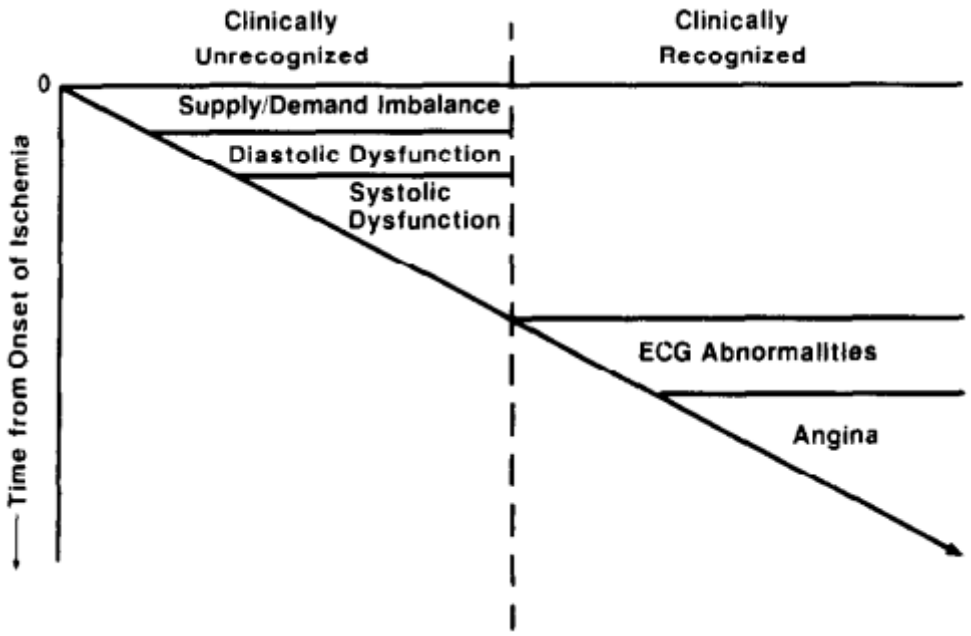

Figure 2-5 – The ischaemic cascade – figure reproduced from the original 1987 description by Nesto and Kowalchuk [25].

Coronary atherosclerotic disease can be stable, where the lumen narrowing plaque limits maximal blood flow but is at lower risk of rupture. However when a plaque ruptures thrombus (blood clot) may occlude the artery or fragments may occlude vessels downstream, cutting off blood supply to a region of myocardium. This leads to ischaemia-induced damage to cardiomyocytes, including necrosis, in a process referred to as myocardial infarction. Over time the space previously occupied by the viable cells is replaced by a collagen network through the mechanism of replacement fibrosis [26].

Treatment for myocardial infarction may include physical intervention (“revascularisation”) in which blood supply to the affected myocardium is restored through mechanical means by opening the arterial lumen. Following infarction and revascularisation the myocardium may exist in several physiological states as shown in Figure 2-6. Example clinical MRI images showing these regions are presented in Chapter 9.

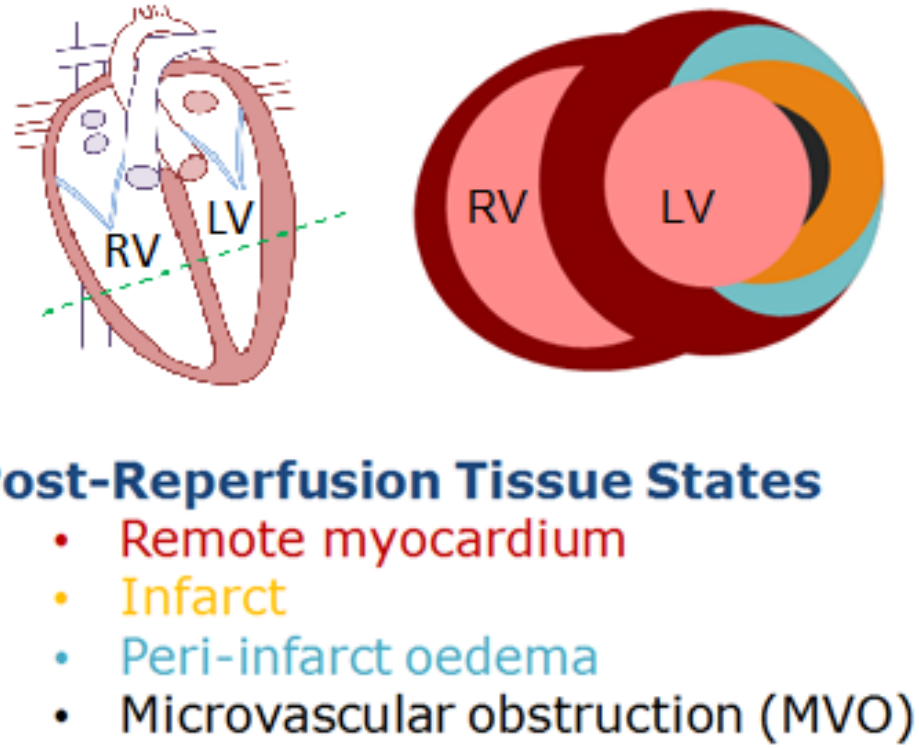

Figure 2-6 – Indication of the short axis view (left, green dashed line) intersecting both ventricles and a schematic in this view (right) of potential myocardial tissue states in acute myocardial infarction. A region of infarcted myocardium (orange) may be surround by oedematous tissue (blue) and may contain a core with microvascular obstruction (black). The pink regions are the blood filled cavities of the respective chambers.

Regions of reperfused infarcted myocardium have restored blood flow but consist predominantly of non-viable myocardium and so contractile function is not expected to be restored. This region may contain a core in which perfusion has not been fully restored due to obstruction of the microvasculature downstream of the major occlusion which was targeted during therapy, and its presence has negative prognostic implications [27]. This obstruction may occur as a consequence of reperfusion, which can cause narrowing of the microvascular lumina through swelling of endothelial cells in the capillary walls or compression of the capillaries by swollen cardiomyocytes [28, 29]. Such regions of microvascular obstruction may appear only transiently in imaging studies (being detectable in the first few minutes after contrast agent administration) or be persistent over a longer period of time, with a poorer prognosis being associated with the latter (e.g. in the study by de Waha *et al* [30] the presence of microvascular obstruction on imaging 15 minutes after contrast injection was independently associated with negative outcomes

following myocardial infarction in contrast to presence only at 1 minute post-injection). MVO was present in the majority of patients in this study (78%), and of those it was persistent in the majority (90%) of cases.

Finally peri-infarct regions of oedematous myocardium may surround the infarct in an inflammatory response to the process of ischaemia and reperfusion. As these regions contain viable cardiomyocytes contractile function can be recovered.

The spatial extent of these regions, and in particular the transmurality (extent throughout the thickness of the myocardium) of the infarct have been shown to have high prognostic significance [31, 32] and so imaging techniques with sufficient resolution to characterise the spatial distribution of these tissue types offer valuable clinical information. Quantitative analysis of image data can be performed on a pixel-wise basis allowing assessment of heterogeneity of disease. However this is limited by the need for robust compensation for both respiratory and cardiac motion and the fact that data from single pixels are noisier than that averaged over larger regions. Consequently analysis is commonly (including in work described in this thesis) performed on a regional or segmental basis, or on data averaged over the full extent of the myocardium within the imaging field of view.

As described earlier (p10) vessels with atherosclerotic disease exhibit a reduced response to stress compared to healthy vessels. When disease is present that limits perfusion only at stress imaging findings (and symptoms) may only present at stress with normal findings at rest while abnormalities present at both rest and stress indicate myocardial damage (infarction) is likely [33] which has implications for patient treatment as contractile function is not expected to be recovered for the latter even if perfusion is restored.

While this thesis focusses on ischaemic heart disease cardiomyopathies also arise due to a range of non-ischaemic aetiologies, including genetic predisposition, drug (e.g. chemotherapeutic agent) exposure, inflammatory response or as a secondary consequence of systemic or other diseases. Changes in structure and composition of the myocardium may occur during cardiomyopathy in response to chemical or mechanical influences. A common

pathological pathway is interstitial fibrosis, in which the interstitial portion of the myocardium increases due to collagen deposition [26]. This can lead to impaired contractility of the myocardium leading to limited cardiovascular function and morbidity or mortality. Some changes to the myocardium, including interstitial fibrosis, may be partially or wholly reversible through medical intervention or reduction of physical load on the myocardium. However replacement fibrosis is considered irreversible [26].

2.1.3 Clinical Imaging Modalities for Ischaemic Heart Disease

In clinical practice several imaging modalities are available for evaluation of cardiac disease processes, each with different strengths and weaknesses as summarised in the review article by Schuijf *et al* [33] amongst other literature. As described in this review imaging can serve two purposes, functional assessment of the consequential outcomes of ischaemic heart disease and anatomical imaging of the coronary vasculature itself. Functional information can include assessment of changes to myocardial perfusion, structure and physiology as well as changes to the motion of the heart chamber walls which can arise due to such pathology. Dependent on the tissue or vascular properties being examined different imaging modalities, and different methods within those modalities, can be sensitive to different stages of the ischaemic cascade. Due to the difference in behaviour of the myocardium at rest and stress, and specifically the fact that some abnormalities in perfusion or function may only be observable at stress due to the behaviour described earlier (p10) imaging with many of these modalities is commonly performed at both stress and rest.

Ultrasound (echocardiography) can allow visualisation of wall motion abnormalities and, through the use of echogenic microbubble contrast agents, myocardial perfusion and has the benefit of being relatively cheap and readily available as well as safe and well tolerated by patients. However the technique relies on availability of suitable acoustic windows and image quality can be compromised in some patients, particularly those of large body habitus.

Nuclear medicine techniques (including single photon emission computed tomography, SPECT, and positron emission tomography, PET) allow assessment of myocardial perfusion; albeit with limited spatial resolution and without the temporal resolution to allow assessment of wall motion. Contrary to

non-ionising imaging modalities (MRI and echocardiography) nuclear medicine techniques impart a radiation dose to the patient and so the risks associated with this must be minimised and justified against the benefit of the clinical information obtained from the scan.

MRI allows multi-parametric assessment of myocardial wall motion, perfusion and tissue structure (the latter two discussed throughout this thesis) with the benefits of high spatial and temporal resolution in comparison to nuclear medicine techniques and high soft-tissue/blood image contrast in comparison to echocardiography. Like echocardiography MRI imparts no ionising radiation risk. However the technique is contraindicated for patients with some medical implants or foreign bodies, and patients with severe renal dysfunction are contraindicated for contrast enhanced MRI using the most commonly used gadolinium based agents.

Anatomical imaging of the coronary vasculature is most commonly performed using x-ray angiography although both MRI and x-ray computed tomography (CT) based techniques have been developed. As this thesis focusses on functional assessment of the myocardium these techniques are not discussed further here.

2.1.4 Relationship of Pathophysiology to Contrast Enhanced Magnetic Resonance Imaging

As described later (sections 2.3 and 2.4) magnetic resonance imaging can be sensitive to the presence of injected contrast agents which locally shorten the longitudinal relaxation time of magnetisation (T_1, discussed in section 2.2). The pathological processes described above can affect the perfusion of the myocardium, and hence the delivery of contrast agent, as well as the relative volume fraction of the myocardium which is accessible to these agents (including extracellular spaces both within and outside the coronary microvasculature). Consequently contrast enhanced MRI can be sensitive to changes in myocardial structure and function that occur in ischaemic pathology, and so can be a useful probe for assessing such diseases.

2.2 Magnetic resonance imaging signal contrast in magnetisation prepared spoiled gradient echo sequences

In this section specific areas of magnetic resonance imaging physics relevant to this thesis are described. For detail on the underlying fundamental principles describing magnetic resonance signal generation, decay and recovery of magnetisation (as discussed in sections 2.2.1 and 2.2.2) and localisation readers are referred to textbooks such as MRI: The Basics [34] or Picture to Proton [35], or for a cardiac MRI focussed reference the review article by Ridgway [36].

Signal intensity in MRI scanning is equal to the magnitude of the product of the transverse magnetisation at the time of signal acquisition and a constant (Ψ) that depends on factors including receiver gain, coil sensitivity etc. The former is dependent on magnetic properties of the signal generating tissue or fluid, parameters of the image acquisition sequence and the prior evolution of the magnetisation.

Equation 2-1

$$S = \left|\Psi M_{x,y}\right|$$

For the work described in this thesis simplifying assumptions are made, namely that spoiling of transverse magnetisation is ideal (that is to say that no transverse magnetisation remains at the time of application of each readout pulse), that readout pulses are ideal and that recovery and decay curves exhibit mono-exponential behaviour. The latter point is valid where the exchange of detectable spins between regions of differing relaxation rates is fast in comparison to those rates and is discussed later in the context of water exchange. Additionally effects related to motion, such as in-flow, have been neglected. While these assumptions have been made here both imperfect spoiling [37-39] and slow water exchange [40-43] have been investigated by others and further investigation relating to the potential impact on quantitative cardiac MRI techniques may be warranted although are outside the scope of this thesis.

MR images are generated by acquiring a series of signals (echoes) in the presence of an applied magnetic field gradient to spatially encode signal in one in-plane direction (such that the precessional frequency varies with position – frequency encoding). Signals are generated by application of readout radiofrequency (RF) pulses which, for 2D acquisitions as are discussed in this thesis, are applied in the presence of a field gradient in the through-plane direction so that signal is only generated from within the slice of interest (slice selection). To encode a second in-plane direction additional gradients are applied between excitation and signal acquisition (so that position dependent phase differences are accrued – phase encoding), with the magnitude of this gradient varied between successive signal acquisitions. In spoiled gradient echo sequences residual transverse magnetisation after signal acquisition is destroyed by using a combination of gradients and/or RF pulses to dephase the magnetic moments in a process referred to as spoiling. This overall acquisition scheme is shown schematically in Figure 2-7;

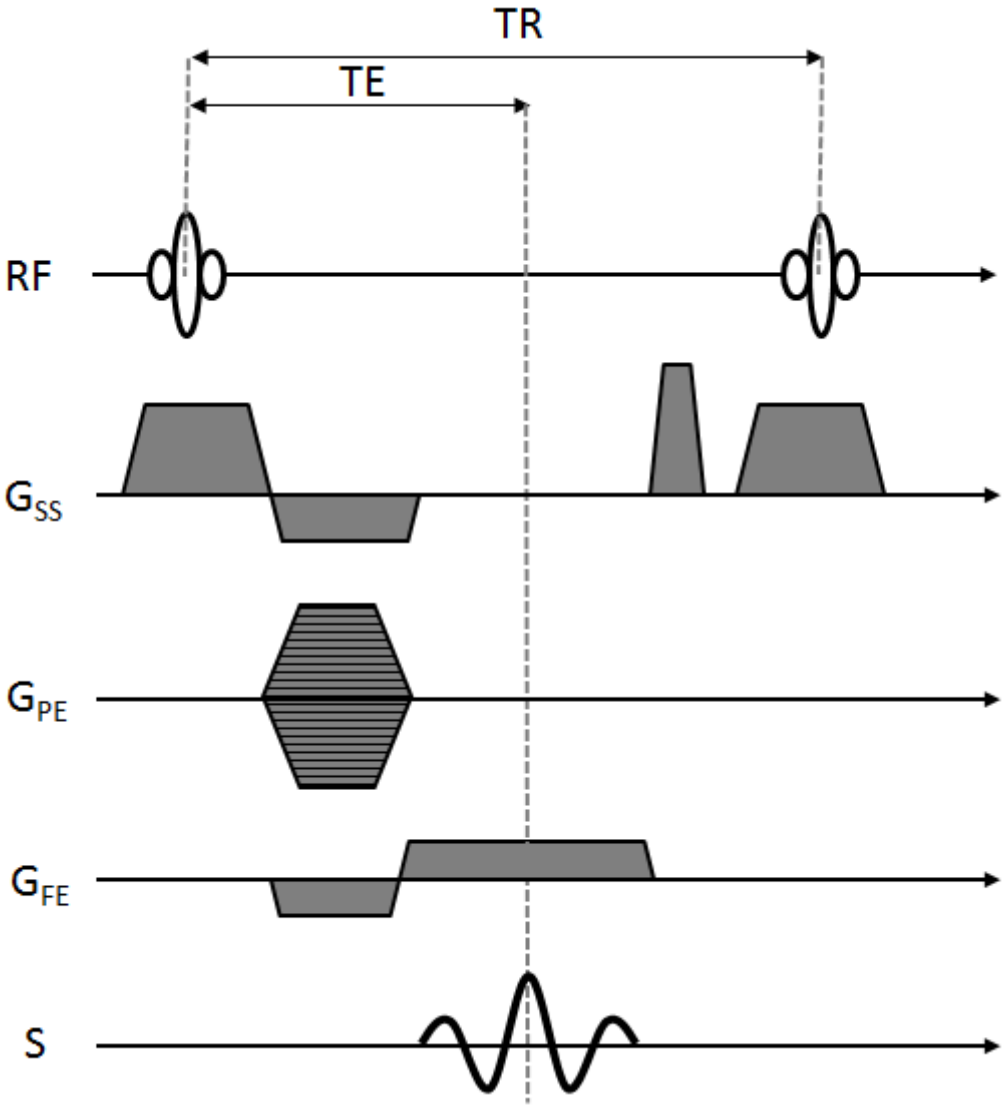

Figure 2-7 – Schematic of a 2D spoiled gradient echo MRI pulse sequence. Gradients (G) are applied in the slice selection (SS), phase encoding (PE) and frequency encoding (FE) in order to spatially localise received signals. Multiple signals (S) must be acquired with varying G_{PE} (indicated by striped pattern) in order to spatially encode signal in the PE direction, so the process is repeated multiple times (the RF pulse and slice select gradient for the subsequent repetition are shown on the right of this figure) with a repetition time TR. (Figure adapted from the Pocket Guide on Cardiovascular Magnetic Resonance Physics for Clinicians [19])

Raw acquired data in MRI describes image signal intensity in the spatial frequency domain, with the spatial frequency space traversed in one direction temporally throughout each acquired echo and traversed in the perpendicular direction in a step-wise fashion by repeating the acquisitions with differing phase encoding gradient moments. This raw data is stored in an array in the spatial frequency domain referred to as k-space. Data near the centre of k-space, i.e. data acquired near the centre of the echoes generated with low

gradient moments, represents low spatial frequency (and thus dominates the determination of large scale image contrast) while those towards the periphery contain high spatial resolution detail. Data in k-space is transformed into an image in the conventional spatial domain by application of 2D Fourier transformation.

2.2.1 T_2^* weighting

If a sufficient delay (for full transverse decay) or effective spoiling has been applied net magnetisation will exist only in the longitudinal axis. For signal generation a portion of the longitudinal magnetisation is tipped into the transverse plane using a readout RF pulse. The magnitude of the transverse magnetisation generated immediately after a readout pulse will depend on the prior longitudinal magnetisation and the flip angle as below.

Equation 2-2

$$M_{x,y}^{+} = M_{z}^{-} \cdot \sin \alpha$$

This magnetisation will then decay exponentially with a decay rate constant equal to the inverse of T_2^* (as described in standard textbooks including those referenced above [34, 35]). The signal is determined by the transverse magnetisation at time TE (echo time) after the readout RF pulse is applied.

Equation 2-3

$$M_{x,y} = M_{x,y}^{+} \cdot e^{-TE/T_2^*} = M_{z}^{-} \cdot \sin \alpha \cdot e^{-TE/T_2^*}$$

For a given prior longitudinal magnetisation the signal will therefore be maximal with a 90° flip angle and the shortest possible TE. For a given TE value magnetisation of species with shorter T_2^* values will decay more than those with longer values, thus giving reduced signal intensity. The relative signal differences between species with different T_2^* values but equal longitudinal magnetisation after excitation will not depend on the flip angle, as this simply scales the proportion of the longitudinal magnetisation that is tipped into the transverse plane and is thus detectable. Extending TE values can increase the relative differences in signal intensity between different T_2^* values, i.e. increase the T_2^* weighting. However this also decreases the absolute signal intensity for all species, thus reducing signal to noise ratio.

The above description relates to gradient echo based sequences, which are used for the majority of CMR imaging sequences and all sequences used for human scanning in this thesis. For spin-echo based imaging the application of a re-focussing pulse reverses the dephasing arising from static sources, and so the constant T_2^* is replaced by the longer T_2 value which describes the decay of transverse magnetisation due only to irreversible spin-spin interactions.

2.2.2 T_1 weighting

As described above MR signal intensity is dependent on the transverse magnetisation at the time of acquisition, which is dependent on both the longitudinal magnetisation prior to the application of the readout RF pulse and the transverse decay. The former will depend on the history of the evolution of the longitudinal magnetisation, which will depend on both the prior sequence of applied RF pulses and the T_1 of the tissue or fluid being scanned. Following a single RF pulse the longitudinal magnetisation will be reduced by a factor equal to the cosine of the flip angle of that pulse.

Equation 2-4

$$M_z^+ = M_z^- \cdot \cos\alpha$$

The longitudinal magnetisation then recovers at a rate dependent on the T_1 of the tissue or fluid (as described in standard textbooks including those referenced above [34, 35]).

Equation 2-5

$$M_z(t) = M_0 - (M_0 - M_z^+)e^{-t/T_1}$$

Most biological tissues and fluids have T_1 values of around 250-2000 ms at typical field strengths of clinical scanners (1.5 or 3T). This may be reduced to less than 100 ms in the presence of high concentrations of contrast agents (described in section 2.3). For cardiac imaging the T_1 relaxation time is thus commonly of the same order of magnitude as the typical cardiac cycle length which typically ranges from around 500-1500 ms (40-120bpm) during scanning. For a system that has been undisturbed for sufficient time to allow equilibrium to be attained the prior longitudinal magnetisation of an ensemble of spins will equal M_0, which is dependent on the spin density, temperature and magnetic

field strength. In MRI successive RF pulses are typically applied during image readout, with a regular temporal separation (TR, repetition time) which is not sufficient to allow full recovery to the equilibrium state. The prior longitudinal magnetisation for all RF pulses except the first applied will be less than M_0 and, based on Equation 2-5, will be:

Equation 2-6

$$M_z^{-,n} = M_0\left(1 - e^{-TR/T_1}\right) + M_z^{+,(n-1)} \cdot e^{-TR/T_1}$$

Substituting in Equation 2-4 and rearranging gives:

Equation 2-7

$$M_z^{-,n} = M_0\left(1 - \left(1 - \frac{M_z^{-,(n-1)}}{M_0} \cdot \cos\alpha\right) \cdot e^{-TR/T_1}\right)$$

As n increases from 1 the prior longitudinal magnetisation tends towards a steady-state which is reached in which the longitudinal magnetisation prior to pulse n is equal to that prior to pulse n-1. Substituting steady-state magnetisation, $M_z^{-,ss}$, for both $M_z^{-,n}$ and $M_z^{-,(n-1)}$ into the equation above and rearranging yields the following equation steady-state prior longitudinal magnetisation.

Equation 2-8

$$M_z^{-,ss} = M_0 \frac{\left(1 - e^{-TR/T_1}\right)}{1 - \cos\alpha \cdot e^{-TR/T_1}}$$

Signal intensity is dominated by low spatial frequency components of the acquired data, which are acquired at the middle of the readout train when using a fully-sampled Cartesian readout trajectory. Consequently by the time of the acquisition of the low spatial frequency components the steady-state will normally have been reached, although with under-sampling methods or alternative trajectories this may not be the case. Figure 2-8 shows steady-state M_z as a proportion of M_0 for flip angles up to 90° and T_1/TR from up to 100. As can be seen to maintain relatively large steady-state magnetisation at short TR (i.e. large T_1/TR) a low flip angle must be used.

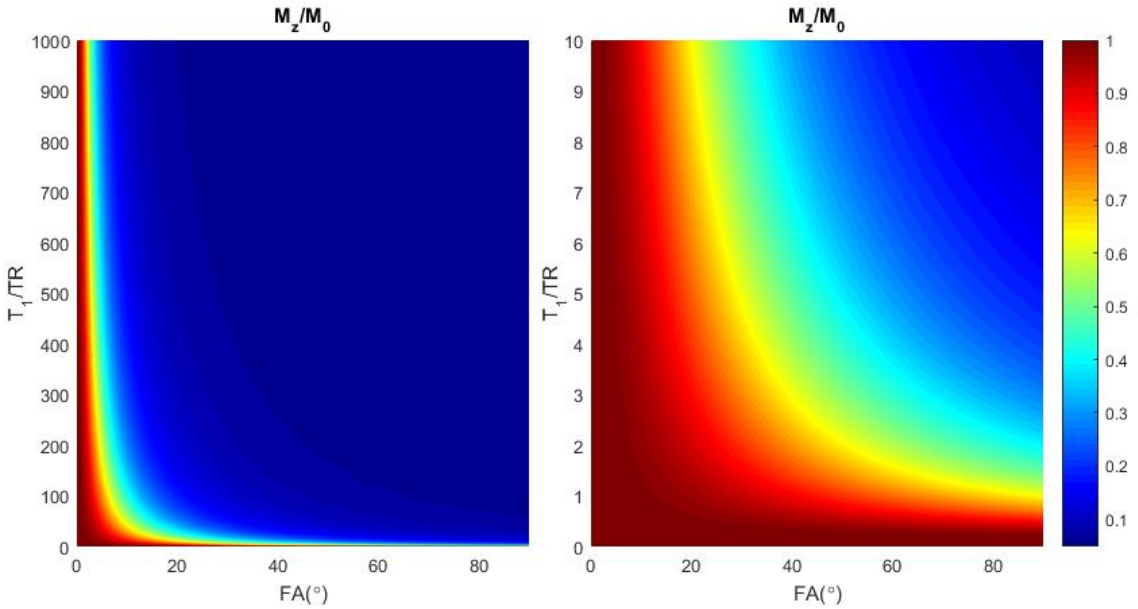

Figure 2-8 - Variation of steady-state longitudinal magnetisation (for spoiled gradient echo sequences) with flip angle and T_1/TR ratio. The right hand figure is zoomed in to the low T_1/TR range.

When the flip angle is low or T_1 is short compared to TR magnetisation is able to nearly fully recover between RF pulses, and so is close to M_0. Decreasing TR or increasing the flip angle reduces the steady-state magnetisation for a given T_1, and increases the rate of variation of relative steady-state magnetisation with T_1, thus yielding increased T_1 weighting at the expense of signal to noise ratio. As can be seen in the right panel unless TR is similar to T_1 (or longer) large flip angles result in very low steady-state M_z for this sequence.

2.2.3 Magnetisation preparation

Pulse sequences employed in cardiac MR scanning commonly employ a magnetisation preparation pulse followed by a delay prior to acquisition using a train of low flip-angle pulses. The preparation pulse may be a saturation pulse, which ideally nulls both longitudinal and transverse magnetisation, or an inversion pulse which ideally inverts the orientation of the longitudinal component of the magnetisation while maintaining its magnitude. These preparation pulses and delays are the predominant source of T_1 weighting in the sequences used both for T_1 mapping and dynamic contrast enhanced MRI discussed in the experimental chapters later in this thesis, in contrast to non-prepared sequences where T_1 dependent signal contrast is predominantly controlled by the flip angle of the readout pulses and the TR (Figure 2-9).

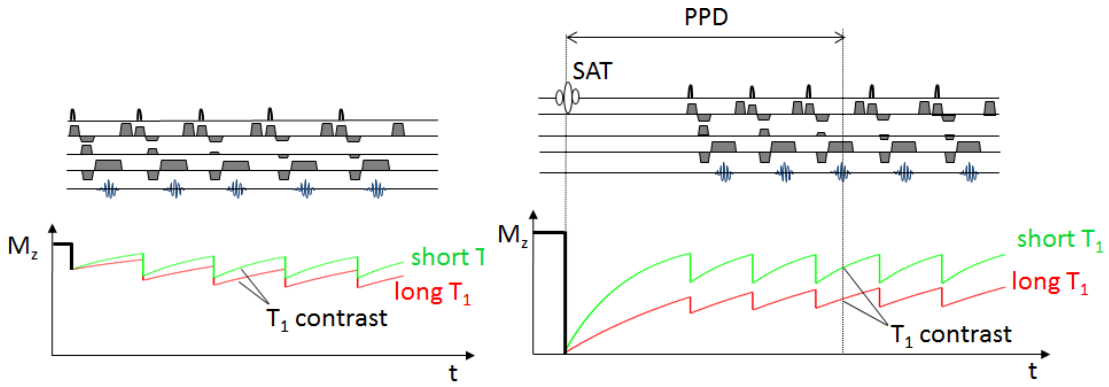

Figure 2-9 – Comparison of a non-prepared and saturation prepared sequence. In the latter differences in longitudinal magnetisation depend predominantly on differential recovery after the preparation pulse. (Figure adapted from the Pocket Guide on Cardiovascular Magnetic Resonance Physics for Clinicians [19])

The magnetisation prior to the readout of the central line of k-space (i.e. following a preparation pulse and a pre-pulse delay, PPD), assuming the system is in equilibrium prior to magnetisation preparation and neglecting the effect of the readout pulses, will be described by the equation below. This is based on Equation 2-4 and Equation 2-5.

Equation 2-9

$$M_z^{-,n_{k0}} = M_0\left(1 - (1 - \cos\theta) \cdot e^{-PPD/T_1}\right)$$

Note that PPD is used as a general term for the delay after a magnetisation preparation pulse. When referring specifically to inversion recovery sequences the term “Inversion Time (TI)” is commonly used and the term “Saturation Time (TS)” is used for saturation prepared sequences. For cases where magnetisation is inverted immediately after the preparation pulse it will then recover towards equilibrium. There will thus exist a T_1 dependent time PPD at which the magnetisation is nulled at the time of acquisition of the zero-spatial frequency data ($M_z^{-,nk0}$=0):

Equation 2-10

$$PPD_{null} = T_1 \cdot \ln(1 - \cos\theta)$$

This is shown graphically in Figure 2-10. In this example post-contrast healthy myocardium has the longest T_1 and is nulled while blood and infarcted myocardium have shorter T_1 and so have recovered past the null point. This is

the basis of late gadolinium enhancement (LGE) imaging discussed later in section 4.3.1.

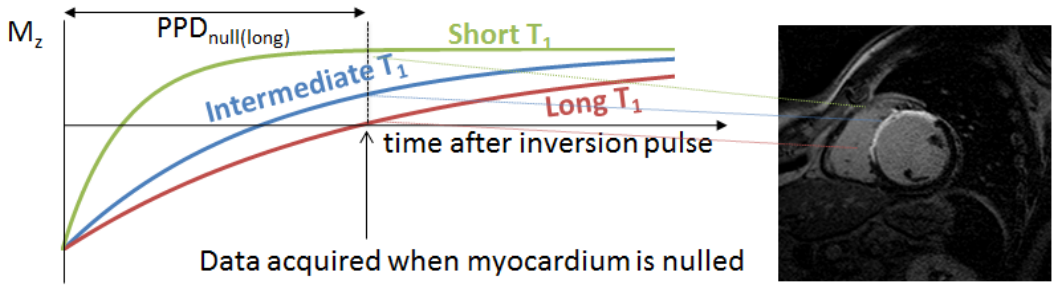

Figure 2-10 – Longitudinal magnetisation recovery following an inversion pulse (left) and an example of how this can be exploited to visual pathological myocardial tissue using the LGE technique (right) in which infarcted tissue appears bright in comparison to healthy myocardium for which the signal is nulled (dark). (Figure adapted from the Pocket Guide on Cardiovascular Magnetic Resonance Physics for Clinicians [19])

Equation 2-10 can be used to determine the PPD required to null signal from tissue with a given T_1. Equivalently, for a specified PPD a specific T_1 value will yield nulled myocardium, and so no signal.

Equation 2-11

$$T_{1,null} = \frac{PPD}{\ln(1 - \cos\theta)}$$

Typically magnitude data is recorded in MR images, so a non-zero signal intensity could correspond to either of two T_1 values, one shorter than $T_{1,null}$ for which longitudinal magnetisation has recovered to positive values prior to readout and the other longer than $T_{1,null}$ which has not reached the null point prior to readout. A reduction in T_1 of a tissue or fluid could therefore lead to either an increase or decrease in signal intensity, dependent on the original T_1 and the PPD used.

The above scenarios specifically describe a system in which M_z prior to the preparation pulse is equal to M_0.

For the case of repeated magnetisation preparation pulses with insufficient time for full recovery between preparation phases, the assumption of starting in the equilibrium state will not hold. However in the specific case of the application of ideal saturation pulses all magnetisation is nulled, and so the model below

(Equation 2-12) can be applied as an approximation (excluding the effects of readout RF pulses) regardless of prior magnetisation history. Consequently saturation pulses are commonly applied in ECG triggered cardiac MR sequences, to remove the dependence on prior history and variability that could arise due to inconsistency in preparation pulse spacing (due to variation in the subjects' heart rate).

Equation 2-12

$$M_z^{-,n_{k0}} = M_0\left(1 - e^{-PPD/T_1}\right)$$

For saturation prepared sequences with ideal saturation (i.e. cosθ=0) M_z is positive for all combinations of PPD and T_1, so T_1 and signal intensity vary monotonically with shortening T_1 (for a given T_2*) leading to increased signal intensity.

Models have been published that also incorporate the effect of the readout pulses. The following derivation is based on that by Larsson *et al* [44] with notation adapted to match that used in this thesis. In general the longitudinal magnetisation prior to the nth readout pulse ($M_z^{-,n}$) will depend on that after the prior pulse ($M_z^{+,n}$) as well as the T_1 and the delay (TR) according to Equation 2-6. $M_z^{+,n}$ will be determined by the magnetisation prior to the (n-1)th pulse and the cosine of the readout flip angle according to Equation 2-4. Therefore:

Equation 2-13

$$M_z^{-,n} = M_0\left(1 - e^{-TR/T_1}\right) + M_z^{-,n-1} \cdot cos\alpha \cdot e^{-TR/T_1}$$

Substituting $a = cos\alpha \cdot e^{-TR/T_1}$ and $b = 1 - e^{-TR/T_1}$ this recursive formula can be expressed:

Equation 2-14

$$M_z^{-,n} = M_z^{-,1} \cdot a^{n-1} + M_0 b \sum_{i=0}^{n-2} a^i$$

$$M_z^{-,n} = M_z^{-,1} \cdot a^{n-1} + M_0 b \frac{1 - a^{n-1}}{1 - a}$$

M_z^{-1} is the longitudinal magnetisation prior to the first readout pulse. Larsson assumed the preparation pulse was an ideal inversion pulse (θ=180°) and applied at equilibrium ($M_z=M_0$). Larsson used TI to indicate the delay from magnetisation preparation to the first pulse. In this thesis PPD is used to describe the delay to the acquisition of the central line of k-space. Therefore TI is equivalent to PPD-(n_{k0}-1)TR and thus, according to Equation 2-5:

Equation 2-15

$$M_z^{-,1} = M_0 - \left(M_0 - M_0 \cdot cos(180°)\right)e^{-(PPD-(n_{k0}-1)TR)/T_1}$$
$$= M_0\left(1 - 2e^{-(PPD-(n_{k0}-1)TR)/T_1}\right)$$

Therefore the longitudinal magnetisation after the nth pulse is:

Equation 2-16

$$M_z^{-,n} = M_0\left[\left(1 - 2e^{-(PPD-(n_{k0}-1)TR)/T_1}\right)\cdot a^{n-1} + b\frac{1-a^{n-1}}{1-a}\right]$$

The assumption of perfect inversion doesn't have to be made as Larsson *et al* did, and this equation can be kept more general for arbitrary magnetisation preparation as:

Equation 2-17

$$M_z^{-,n} = M_0\left[\left(1 - (1-cos\theta)e^{-(PPD-(n_{k0}-1)TR)/T_1}\right)\cdot a^{n-1} + b\frac{1-a^{n-1}}{1-a}\right]$$

While the above equation allows for arbitrary values of θ the assumption of the magnetisation being at equilibrium prior to the inversion pulse remains. Kershaw [45] derived an equation for the steady-state magnetisation following the nth pulse of this sequence when applied repetitively at regular intervals and at a constant T_1. As for the previous model notation is adapted to match that used in this thesis. The derivation for this model is identical to the prior model as far as Equation 2-14 but instead of assuming the magnetisation at the time of the preparation pulse is at equilibrium it is determined by first deriving the magnetisation at the end of the readout train ($M_z^{+,N}$, where N is the total number of pulses) and then applying Equation 2-5 for the remainder of the time until the

next magnetisation preparation pulse. According to Equation 2-4 and Equation 2-14:

Equation 2-18

$$M_z^{+,N} = M_z^{-,N} cos\alpha = \left[M_z^{-,1} \cdot a^{N-1} + M_0 b \frac{1 - a^{N-1}}{1 - a} \right] cos\alpha$$

Substituting F=b/(1-a) and $Q=M_z^{-1}/M_0$:

Equation 2-19

$$M_z^{+,N} = M_0[F + a^{N-1}(Q - F)]cos\alpha$$

With the time between magnetisation preparation pulses defined as the inter-shot delay (ISD) the recovery time after the final readout pulse to the next magnetisation preparation pulse is equal to ISD-(PPD+(N-n_{k0})TR). The longitudinal magnetisation at the end of this period and thus immediately before the preparation pulse ($M_z^{-,PP}$) is, according to Equation 2-5:

Equation 2-20

$$M_z^{-,PP} = M_0 \left[1 - (1 - [F + a^{N-1}(Q - F)]cos\alpha) e^{-\frac{(ISD - (PPD + (N - n_{ko}))TR)}{T_1}} \right]$$

In the steady-state the magnetisation at the end of this period is the same as that prior to the preparation pulse at the start. According to Equation 2-4 the magnetisation after the preparation pulse is:

Equation 2-21

$$M_z^{+,PP} = M_z^{-,PP} cos\theta$$

The magnetisation prior to the first readout pulse, $M_z^{-,1}$, according to Equation 2-5, is:

Equation 2-22

$$M_z^{-,1} = M_0 - \left(M_0 - M_z^{+,PP} \right) e^{-\frac{(PPD - (n_{k0} - 1)TR)}{T_1}}$$

Substituting $E_1 = e^{-(PPD - (n_{k0} - 1)TR)/T_1}$ and $E_D = e^{-(ISD - PPD - (N - n_{k0})TR)/T_1}$ then re-arranging yields:

Equation 2-23

$$M_z^{-,1} = M_0(1 - E_1) + M_0 cos\theta E_1[1 - E_D + [F + a^{N-1}(Q - F)]cos\alpha E_D]$$

Dividing by M_0, replacing $M_z^{-,1}/M_0$ with Q, and re-arranging gives:

Equation 2-24

$$Q = \frac{(1 - E_1) + cos\theta \cdot E_1(1 - E_D) + cos\theta \cdot E_1 \cdot cos\alpha \cdot E_D \cdot F(1 - a^{N-1})}{(1 - a^{N-1} \cdot cos\alpha \cdot E_D \cdot cos\theta \cdot E_1)}$$

Substituting:

$A=(1-a^{N-1})/(1-a)$

$B=a^{N-1}\cdot E_1$

$C= a^{N-1}\cdot(1-E_1)$

$D=E_D.\cos\alpha$

Then simplifying yields:

Equation 2-25

$$Q = \frac{M_z^{-,1}}{M_0} = \frac{cos\theta\left(bDE_1A + E_1\left(1 - \frac{D}{cos\alpha}\right) + BD(1 - E_1)\right)}{1 - BDcos\theta} + (1 - E_1)$$

Returning to Equation 2-14 and substituting in the above result:

Equation 2-26

$$M_z^{-,n} = M_0 Q \cdot a^{n-1} + M_0 b\frac{1 - a^{n-1}}{1 - a}$$

Finally substituting in Q from Equation 2-25 and simplifying yields:

Equation 2-27

$$M_z^{-,n} = M_0\left[\frac{b}{1 - a}(1 - a^{n-1}) + a^{n-1}(1 - E_1) + a^{n-1}cos\theta\frac{\left(bDE_1A + E_1\left(1 - \frac{D}{cos\alpha}\right) + BD(1 - E_1)\right)}{1 - BDcos\theta}\right]$$

Substituting A, B and D in from above and re-arranging yields:

Equation 2-28

$$M_z^{-,n} = M_0 \left[\frac{b}{1-a}(1-a^{n-1}) + a^{n-1}(1-E_1) + E_1 a^{n-1} cos\theta \frac{bcos\alpha E_D \frac{1-a^{N-1}}{1-a} + 1 - E_D + a^{N-1} cos\alpha E_D (1-E_1)}{1 - cos\theta a^{N-1} E_1 cos\alpha E_D} \right]$$

This can be further rearranged to the form used later in Equation 7-5:

Equation 2-29

$$M_z^{-,n} = M_0 \left[\frac{b}{1-a}(1-a^{n-1}) + (1-E_1)a^{n-1} - E_1 a^{n-1} cos\theta \left[\frac{-cos\alpha E_D \left(b\frac{1-a^{N-1}}{1-a} - \frac{1}{cos\alpha} + a^{N-1}(1-E_1) \right) - 1}{1 - cos\theta a^{N-1} E_1 cos\alpha E_D} \right] \right]$$

2.2.4 Controlling weighting in MRI

As described in the previous sections the signal in MR images is dependent on a range of parameters including magnetic properties of the material being imaged and parameters describing the imaging sequence. By appropriate selection of the latter images can be generated that are more or less sensitive to differences in the former. For example by using a high flip angle and short repetition time (potentially with the addition of a magnetisation preparation pulse) in the imaging sequence relative signal intensity across the image will depend strongly on differences in the T_1 of the imaged material. In such T_1 weighted images a short echo time is typically used to minimise T_2^* weighting. Conversely parameters that minimise the sensitivity of signal intensity to T_1 and maximise it to T_2^* may be chosen to achieve T_2* weighting. By selecting parameters that minimise both T_1 and T_2^* weighting images can be acquired in which the signal intensity is primarily determined by the relative density of MR

detectable spins. Such images are referred to as proton density weighted images.

2.3 Action of gadolinium based contrast agents (GBCAs)

Contrast agents for MRI are generally not visualised directly through imaging but instead affect signal intensities by altering the properties of the neighbouring hydrogen nuclei. The agents can both accelerate the recovery of longitudinal magnetisation to equilibrium values (i.e. shorten longitudinal recovery time, T_1) and accelerate dephasing of transverse magnetisation (i.e. shorten transverse decay time, T_2^*) of MR visible spins in the local vicinity of the contrast agent molecules. The effect on relaxation rates (reciprocal of T_1 and T_2^*) is linearly dependent on concentration of the contrast agent with a constant of proportionality defined as the relaxivity:

Equation 2-30

$$R_i = R_i^n + r_i \cdot [CA]$$

Where:

i = 1 for longitudinal recovery or 2 for transverse decay in gradient echo sequences*

R_i indicates relaxation rate (i.e. $R_i = 1/T_i$)

Superscript 'n' indicates native (i.e. in absence of contrast agent)

r_i indicates contrast agent relaxivity

[CA] indicates contrast agent concentration

GBCAs consist of a central gadolinium ion surrounded by a chelate molecule in order to make the agent safe (pure gadolinium is toxic). The effect of the paramagnetic gadolinium ion on relaxation rates is localised to a spatial region of roughly the same size of the chelate molecule. Consequently only small, mobile molecules are substantially affected by the presence of the contrast agent, resulting in the predominant effect of the agents in clinical MRI scanning being on the signal from water molecules with minimal effect on larger MRI visible molecules such as fat.

Gadolinium based contrast agents therefore influence local MR signal indirectly by shortening the T_1, T_2 and T_2^* of surrounding MR visible water. Depending on the sequence parameters used, and the consequential balance of T_1 and T_2 or T_2^* weighting, this can potentially lead to either increased or decreased local signal intensity as described in the previous sections. Typically however GBCAs are used in conjunction with T_1 weighted sequences (as described in section 2.2.4) where sequence parameters are chosen such that the predominant effect of the contrast agent will be to increase signal intensity (typically using either a short TR/high flip angle and/or a magnetisation preparation pulse to achieve strong T_1 weighting along with a short TE to minimise T_2^* weighting). Situations in which signal decrease may occur are in magnitude reconstructed inversion recovery sequences used for T_1 mapping, where the TI will typically be shorter than that required to null signal (i.e. signal will be acquired while magnetisation is still inverted) for some tissues in some of the acquired images, or in cases where high concentrations of contrast agent are encountered, in which case the signal loss due to T_2^* shortening may become dominant over signal increase due to T_1 shortening.

The majority of GBCAs in clinical use can pass through the capillary walls into extravascular spaces but remain outside cells with intact membranes. Such agents are described as extracellular agents and their distribution characteristics are described in the following section. Additionally some contrast agents have been developed which do not pass through capillary membranes and so remain in the intravascular space (except for through their clearance route, which is predominantly renal). These intravascular agents are not used in the work carried out in this thesis and so unless explicitly stated subsequent discussion of GBCAs refers to use of extracellular agents.

2.4 Distribution of extracellular gadolinium based contrast agents

In 1984 Weinmann *et al* [46] assessed the characteristics of a gadolinium chelate, diethylenetriaminepentaacetic acid (Gd-DTPA) as a contrast agent for MRI. Gadolinium, a rare earth element, exhibits the strongest effect on the longitudinal relaxation time (T_1) of protons of all elements and also shortens

transverse decay times (T_2^*), and so can alter MRI signal intensities. This work established the *in vivo* stability and high tolerance of Gd-DTPA in a rat model while demonstrating fundamentals of the pharmacokinetics of the agent, including the predominance of glomerular filtration as the excretion route. This, and other early work, established the value of such agents and Gd-DTPA was approved for clinical use in 1987.

Later work furthered understanding of the biodistribution of Gd-DTPA. Koenig *et al* [47] demonstrated that, in the blood, Gd-DTPA exists in the plasma volume but does not enter the blood cells. As the exchange of water between the intra- and extracellular spaces in the blood pool is rapid in comparison to the differences in R_1 relaxation rates which would exist between isolated plasma or intracellular regions, the overall longitudinal relaxation rate (R_1) can be modelled as the weighted average of that of the water, intra- and extracellular proteins and the exogenous contrast agents. This results in the fact that a mono-exponential function adequately describes the evolution of the longitudinal magnetisation of blood. Through comparison of Gd-DTPA (using the radioactive isotope ^{153}Gd) with other tracers these results were confirmed and further information on the biodistribution of the agent were determined.

Comparison of Gd-DTPA to manganese-54 DTPA in dogs [48] and technetium-99m DTPA in rats [49] demonstrated that the agent distributes to the interstitial space as well as the blood plasma, but does not penetrate intact cell membranes. Gd-DTPA can thus be described as an extracellular contrast agent as it only enters the extracellular spaces in both intra- and extravascular regions. The exchange of water between intra- and extracellular regions in the extravascular space is less rapid than between the equivalent regions in the blood. Consequently a model of fast-water exchange (and thus mono-exponential model of longitudinal magnetisation recovery) may not be adequate when relaxation rate differences between intra- and extracellular water become large in comparison to the water exchange rates (i.e. at high contrast agent concentrations). Some recent publications have investigated the effect of water exchange on ECV estimation [43] and the potential utility of markers of water exchange rates for identifying cardiomyocyte hypertrophy [50].

2.4.1 Temporal variation of contrast agent concentrations

In this section the basis of tracer kinetics is described qualitatively and in terms of specific mathematical models.

In many organs perfused tissue can be modelled as consisting of two regions accessible to extracellular contrast agents, the interstitium and the plasma volume. In such tissues transfer can occur between these two regions, as the contrast agent can cross capillary walls. This is not the case in healthy brain tissue, where the blood brain barrier constrains the contrast agent to the intravascular region.

The transfer of contrast agent molecules occurs in both directions, but predominantly from high concentration to low concentration regions. Consequently the concentration in the plasma will reduce and that in the interstitium increase until equilibrium is reached.

In addition to transfer between the interstitium and the plasma, the plasma volume in the perfused tissue also communicates with the systemic circulation and is thus subject to external effects. To fully describe the variation of contrast agent concentration in the interstitium it is therefore also required that the external drivers of plasma concentration are known. In a clinical application this is described by the administration method (e.g. bolus injection or infusion) as well as physiological parameters such as the blood plasma flow (F_p) to the tissue, dispersion of the contrast agent through the systemic vasculature and extraction of the contrast agent through the glomerular apparatus.

Following a bolus injection of contrast agent the concentration in the plasma volume of a region of perfused tissue will rise rapidly when the bolus first arrives. The concentration in the interstitium will then rise, with the early rise being determined by both the delivery of concentration to the microvasculature (i.e. F_p) and the extraction efficiency (E) from the plasma volume into the interstitial space.

At a later time, following a bolus injection, or following an infusion, the contrast agent will be well-mixed in the blood. In the absence of extraction of contrast agent from the system the concentration in the interstitium and the plasma

would reach a steady-state. In reality contrast agents are renally extracted from the blood (at a rate dependent on the individual's glomerular filtration rate) and so the concentration in the plasma and the interstitium will both gradually decrease.

2.4.1.1 Observing temporal variation of GBCA concentration

In clinical practice GBCAs can be used by observing the effect on signal intensity at a prescribed time after contrast agent injection (in order to allow distribution to the tissue of interest), often in comparison with pre-contrast images. Alternatively the temporal variation in the distribution of contrast agent can be measured dynamically by acquiring images serially during and following the injection of the contrast agent. This process of dynamic contrast enhanced MRI is shown schematically in Figure 2-11, which relates specifically to cardiac DCE-MRI as discussed throughout this thesis in which image acquisition is triggered by an electrocardiograph (ECG) trace in order to allow images to be acquired at a consistent cardiac phase.

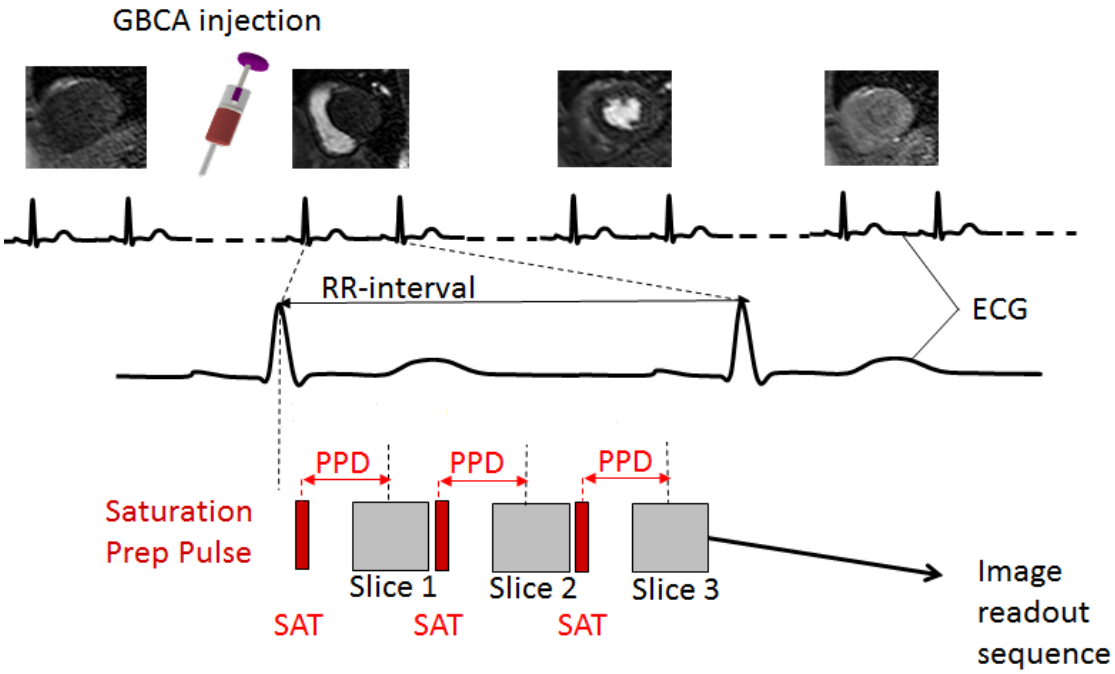

Figure 2-11 – Schematic of cardiac DCE-MRI in which images are acquired serially during and following the injection of a GBCA bolus. In this example three image slices are acquired per cardiac cycle using a saturation prepared sequence. The images at the top show the temporal variation of contrast agent presence, with brighter signal corresponding to greater concentrations of GBCA. Contrast agent initially is seen in the right ventricular cavity, followed by the left ventricular cavity (after

passing through the pulmonary circulation) before perfusing the myocardial tissue. (Figure adapted from the Pocket Guide on Cardiovascular Magnetic Resonance Physics for Clinicians [19])

In order to perform quantitative analysis on such data it is necessary that the data is acquired with a sufficient temporal resolution to sample the most rapid components of the GBCA concentration variation in both the blood pool and tissue [51], for which exemplar curves are shown in Figure 2-12 to demonstrate the typical temporal scales of contrast agent concentration during the first minute after bolus injection.

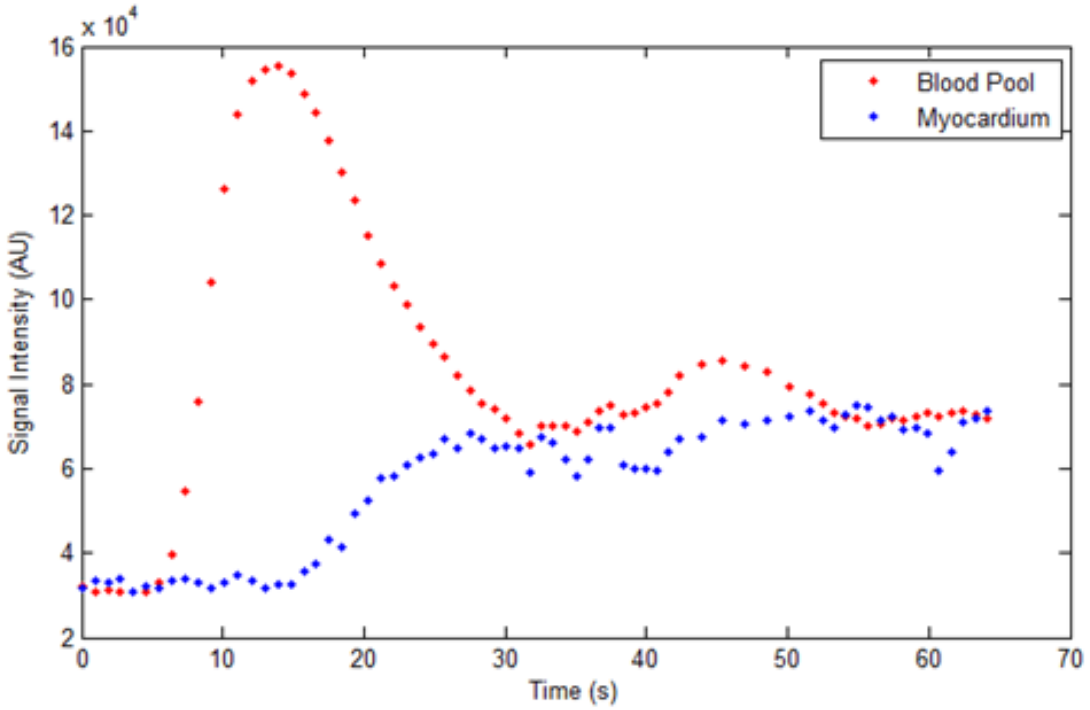

Figure 2-12 – Example data from myocardial DCE-MRI showing typical timescales of contrast agent variation in the blood (red) and myocardium (blue). (N.B. the myocardial data has been scaled up relative to the blood data for visualisation, as the signal variation in myocardium is generally much lower than in the blood, the signal is recorded in arbitrary units).

In the blood pool this occurs during the first pass of the GBCA, which has a typical width on the order of 20-30s (dependent on injection protocol and cardiovascular function) [52] while in tissues it is typically the transit through the capillary network which is shorter, and may be of similar order of magnitude to the cardiac cycle length [1], and hence the temporal resolution when images are acquired every heartbeat. Note that the width of the first pass in the blood pool is substantially longer than the typical injection duration (which would be 2.5s for a 0.05 mmol/kg dose at 3 ml/s injection rate for an 80kg patient using a 0.5

mmol/ml contrast agent) due to dispersion in the peripheral veins and pulmonary circulation.

Qualitative or semi-quantitative analysis

While this thesis focuses on fully quantitative methods DCE-MRI data can be assessed in a qualitative fashion (through visualisation of acquired data, typically viewed in a movie format to show temporal variation) or through semi-quantitative analysis. An example of the former, showing a selection of images from a DCE-MRI series with a perfusion defect visible, is shown in Figure 2-13 below:

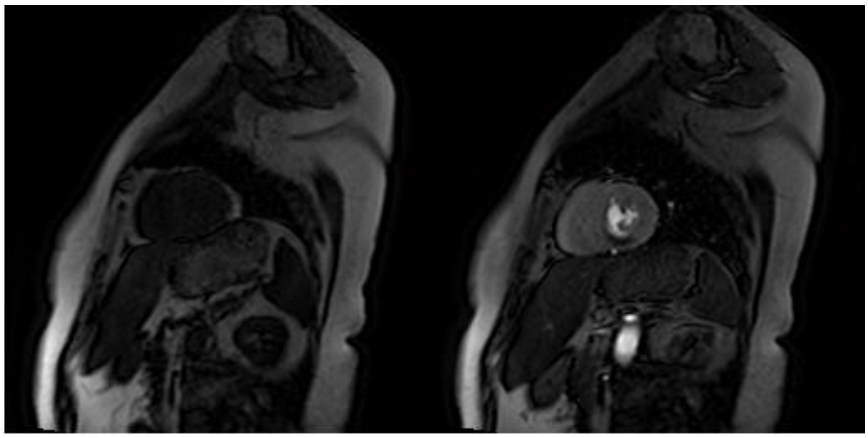

Figure 2-13 – Pre-contrast (left) and early post-contrast (right) phase images from a stress DCE-MRI series of a patient with an inferior perfusion defect visible as a region of myocardium showing reduced enhancement compared to normally perfused tissue after contrast agent arrival. Visual analysis of such data can allow identification of perfusion defects without quantitative or semi-quantitative analysis.

In particular comparison of regions of perfusion defects in DCE-MRI images as described above to regions of scar from late gadolinium enhancement imaging (used to assess viability of tissue, described later in section 4.3.1) can help guide the decision as to whether revascularisation therapy is appropriate as this therapy may restore function in tissue with stress-induced perfusion defects as long as the tissue remains viable [53].

Semi-quantitative analyses include calculation of parameters such as the initial rate of myocardial enhancement (“up-slope”) or area under the myocardial uptake curve up to the first-pass peak in the blood have been used as markers of perfusion [54]. As the signal intensity in MRI images is arbitrarily scaled such metrics require normalisation, typically by dividing stress and rest results to

obtain estimates of the myocardial perfusion reserve (MPR). While such parameters do not provide estimates of absolute physiological parameters they are dependent on physiological status, and so may provide sufficient diagnostic accuracy to be of clinical value while requiring less complex analysis than full quantification. However, as normalisation is required they provide less information than absolute quantification which may limit applicability in some settings. For example reduced MPR may be due to either increased resting perfusion (which may arise in hypertensive patients), reduced perfusion at stress due to coronary artery disease or otherwise impaired response to stress, or a combination of both [54]. Accurate absolute quantification of perfusion in each state would be able to identify the relative contributions of these sources to reduced MPR unlike semi-quantitative analysis.

2.4.1.2 Basis of deconvolution for DCE-MRI analysis

As described above contrast agent arriving in the myocardium distributes in the plasma and extravascular-extracellular regions of the tissue. A contrast agent molecule entering tissue via the coronary microvasculature will spend a finite amount of time in these regions of the tissue before exiting the system at the venous end of the capillary bed. The duration of this transit will vary randomly with a distribution of probabilities of a given transit time, H(t), the shape of which will depend on physiological conditions. If a large number of molecules arrive instantaneously the full proportion will exist in the tissue initially and then decrease as molecules leave the system. The rate of fractional loss of molecules from the system at any time after arrival will equal the value of H(t) at that time. The fraction of molecules that have exited the system by a given time will therefore equal the integral of H(t) over that time. The fraction remaining in the tissue, and thus detectable by imaging, is referred to as the residue function, R(t), as in Equation 2-31.

Equation 2-31

$$R(t) = 1 - \int_0^t H(t')\,dt'$$

This is a monotonically decreasing function, with R(0)=1, as all contrast agent is still present immediately after delivery.

In reality contrast agent delivery will be distributed over time, and contrast agent will re-circulate through the systemic and pulmonary circulation after leaving the tissue. The contrast agent delivery rate is thus variable, and is monitored by observing the arterial input function (AIF), that is the concentration of contrast agent in the feeding blood plasma supply. For an infinitesimal period of time (Δt) the number of contrast agent molecules delivered per unit volume tissue will equal the product of the blood plasma flow per unit volume tissue (F_p), the instantaneous concentration of contrast agent in the plasma and the duration of the time period. The concentration in the tissue at a given time, $C_t(t)$, will equal the sum of the residual concentration from all previous time periods (assuming the physiological parameters, and thus the value of F_p and the shape of R(t) are constant) as in Equation 2-32.

Equation 2-32

$$C_t(t) = \sum_{\tau=0}^{\infty} R(\tau) \cdot F_p \cdot AIF(t-\tau) \cdot \Delta t$$

In the limit of infinitesimally small Δt this becomes an integral, which in turn is equal to a convolution of the AIF and the residue function, scaled by the myocardial blood plasma flow (Equation 2-33).

Equation 2-33

$$C_t(t) = \int_0^{\infty} R(t') \cdot F_p \cdot AIF(t-t') \cdot dt' = F_p \cdot R(t) * AIF(t)$$

In DCE-MRI $C_t(t)$ and AIF(t) are measured through imaging and the aim of quantitative analysis is to determine the shape and amplitude of the product of F_p.R(t). This is the reverse process of the above equation, and is thus referred to as deconvolution. This problem is ill-posed, and so optimisation techniques are required to perform the deconvolution. As R(0)=1 the initial amplitude of the result of deconvolution can be interpreted as F_p. In performing deconvolution the shape of R(t) can be constrained only by conditions such as smoothness and a requirement to be monotonically decreasing. This process is referred to as model-free or model-independent deconvolution respectively. Alternatively R(t) can be constrained to follow a mathematical form determined by a set of

parameters (model-based or model-constrained deconvolution). This mathematical form can be chosen on a phenomenological basis by choosing a form of the anticipated shape, or be of a form derived from an underlying physiological model. In the latter case the additional parameters describing the shape of R(t) can be interpreted in order to estimate physiological parameters beyond F_p. An appropriate model must be chosen carefully to match the underlying physiology of the tissue being studied, as an over-simplified, inappropriate or over-parameterised model can lead to invalid parameter estimates.

2.4.1.3 Model choice

One-region models

A simple model of tissue structure from which a residue function can be derived is that of a single well-mixed compartment. In such a model the contrast agent concentration is assumed to be equal throughout the spatial extent of the region, and so the concentration at the venous outlet (C_v) is equal to that in the region. In DCE-MRI the observed quantity is the concentration in the tissue as a whole, which is equal to the concentration within the space accessible to the contrast scaled by the volume fraction of the tissue that the contrast agent distributes into (distribution volume fraction, v_d). For intravascular agents v_d is equal to the plasma volume fraction (v_p), but the one-compartment model can also be applied to extra-vascular agents if the microvascular permeability is sufficiently high that it presents a negligible barrier to extravasation. In the latter case the contrast agent concentration in the intra- and extra-vascular regions is assumed to be equal at all times, and v_d is the sum of v_p and the extravascular-extracellular volume fraction (v_e).

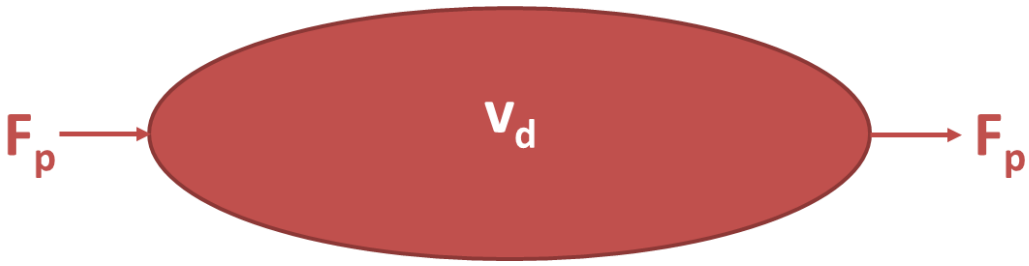

Figure 2-14 – One-compartment model with no leakage. A single well-mixed compartment with equal inlet and outlet flows (F_p) occupies a volume fraction v_d.

The rate of change of contrast agent concentration in the myocardium will, based on the principle of mass balance, equal the difference of the products of the plasma flow and contrast agent concentrations at the inlets and outlets. For a stationary system the flows will be equal. Consequently the rate of change of contrast agent will be described as in Equation 2-34.

Equation 2-34

$$\frac{dC_t}{dt} = F_p\left(AIF - \frac{C_t}{v_d}\right)$$

The solution to this is of the form of a mono-exponential function (Equation 2-35).

Equation 2-35

$$C_t(t) = \int_0^\infty F_p \cdot \left(e^{-F_p\tau/v_d}\right) \cdot AIF(t-\tau) \cdot d\tau$$

From inspection of Equation 2-33 it can be seen that the residue function for the one compartment model, $R_{1C}(t)$, is thus defined as in Equation 2-36.

Equation 2-36

$$R_{1C}(t) = e^{-F_p t/v_d}$$

From Equation 2-31 the distribution of transit times can be determined by taking the negative of the time-derivative of R(t), and the mean transit time is the expectation value of this function. For the one-compartment model it is thus defined as in Equation 2-37 (where E[H(t)] indicates the expectation value of H(t).

Equation 2-37

$$T = E[H(t)] = -\int_0^\infty t\frac{d}{dt}\left(e^{-F_p t/v_d}\right)dt = \frac{v_d}{F_p}$$

For intravascular agents which do not enter the extravascular spaces a one-region plug-flow model may better describe the tissue, especially for tissues with a linear capillary structure. This model consists of a tube in which axial variation of contrast agent is allowed. For derivation of the residue function this is described mathematically as a series of communicating infinitesimal compartments. Such a model gives rise to a residue function with a discontinuity both at t=0 (in common with most residue functions) and at a later time point. The form of the residue function for this model is a step-function equal to 1 for the duration of the capillary transit time and then falling instantaneously to zero as the contrast agent exits at the venous outlet.

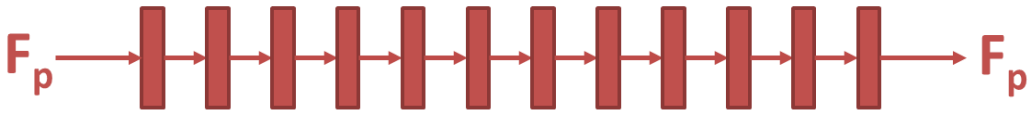

Figure 2-15 – Single-region plug-flow model. The contrast agent passes through a single tube with equal inlet and outlet flows (F_p) and occupying a total distribution volume fraction equal to v_d. To derive the residue function this tube is described mathematically as a series of communicating infinitesimal compartments. This model would typically be used for intravascular agents, in which case v_d=v_p.

Two-region models

In reality the capillary membranes may offer measurable resistance to extravasation and so a two-region model consisting of intra- and extravascular components may better describe the data. In such models the rate of contrast agent extravasation is dependent on both the permeability and surface area of the capillary walls, and is thus described by the product of these two parameters, PS. A variety of combinations of assumptions about the underlying nature of each of the two regions can be made leading to different models. For example both regions are assumed to be well-mixed compartments in the two-compartment exchange model, which results in a bi-exponential residue function, whereas other models incorporate spatial variation of contrast agent in one or both of the regions.

Choice of the appropriate model can be made based on statistical grounds regarding goodness of fit, *a priori* understanding of the underlying tissue structure, or a combination of the two. In pilot work completed prior to this PhD project [1] a two-region one-barrier distributed parameter model, which incorporates spatial variation in both regions, was used for deconvolution of myocardial DCE-MRI data based on the linear structure of the myocardial capillary bed. This model incorporates plug-flow in the intravascular space with communication along the axial length of the vascular region to a series of infinitesimal extravascular regions. In this model axial transport is allowed only in the vascular region, so there is no direct communication between the extravascular regions.

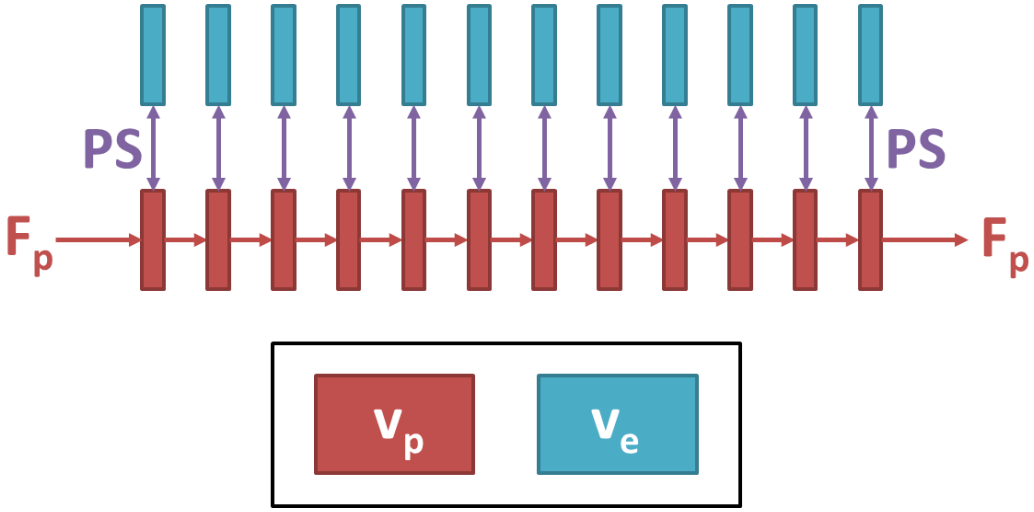

Figure 2-16 – Two-region single barrier distributed parameter model. Contrast agent passes through a series of communicating infinitesimal regions, with equal inlet and outlet flows (F_p) and occupying a total distribution volume fraction equal to v_p. These regions communicate with a series of extravascular regions, which do not communicate with each other directly. The total distribution volume fraction of the extravascular regions is v_e and the transfer between the two spaces is described by the permeability-surface area product (PS).

As transit is not allowed between the compartments of the extravascular regions in this model axial transport is limited to the intravascular compartment, and so, similar to the one-region plug-flow model, the residue function contains a second discontinuity with an initial plateau (of length determined by the mean capillary transit time, T_c). This is followed by a monotonically decreasing shape which is dependent on a combination of the mean transit times in the two regions separately (T_c and T_e) as well as the overall mean transit time (T). As

discontinuous residue functions can cause instability in the deconvolution process [55] Laplace domain fitting was used in this pilot work (as discussed in section 2.4.1.4 below) and in the analysis using this model described in Chapter 9. The Laplace domain solution for the residue function is defined in Equation 2-38 [51].

Equation 2-38

$$R_{DP}(s) = \frac{1 - e^{-s\frac{T + sT_cT_e}{1+sT_e}}}{s}$$

From the mean transit times further physiological parameters, which may be more intuitively interpreted, can be derived, as listed in equations 2-39 to 2-42 [51].

Equation 2-39

$$ECV = v_d = F_pT$$

Equation 2-40

$$v_p = F_pT_c$$

Equation 2-41

$$v_e = v_d - v_p = F_p(T - T_c)$$

Equation 2-42

$$PS = \frac{v_e}{T_e} = \frac{F_p(T - T_c)}{T_e}$$

From F_p and PS a further parameter, the first-pass extraction fraction (E) can be calculated. For the distributed-parameter model (or other models in which plug-flow is assumed in the intra-vascular region) this is defined as in Equation 2-43.

Equation 2-43

$$E = 1 - e^{-PS/F_p} \text{ (plug-flow capillary bed)}$$

For models in which the capillary bed is modelled as a well-mixed compartment (such as the two-compartment exchange model) the equation above is not valid and E is defined as in Equation 2-44.

Equation 2-44

$$E = \frac{PS}{F_p + PS} \text{ (compartmental capillary bed)}$$

Phenomenological models

The residue functions above are derived from underlying models of tissue structure. However a widely used model in myocardial DCE-MRI analysis is the Fermi function [56] which was chosen on a phenomenological basis as the shape of the function was observed to approximate that expected. The function is described in Equation 2-46 and is characterised by two shape-defining parameters as well as the overall scaling by F_p. It consists of an initially slow decrease in value (approximating the plateau at the start of the distributed parameter model residue function), followed by a smooth transition into a roughly exponential decay. As it contains no discontinuity it can be utilised robustly in the temporal domain and, in terms of complexity (based on the number of shape defining parameters), lies between the one and two-region models described above. The model does not accurately describe washout of contrast-agent in the latter phases of enhancement and so analysis using this model is typically limited to data collected during the first-pass of the contrast agent.

Equation 2-45

$$R_{Fermi}(t) = \frac{1 + b}{1 + be^{at}}$$

As the shape of the function is not derived from a physiological model typically only the initial amplitude is interpreted (as F_p) and the parameters a and b are discarded.

2.4.1.4 Deconvolution process

The relationship described in Equation 2-33 relates the variation of the contrast agent in the tissue of interest to that in the blood directly at the inlet of the

tissue. In practice this is rarely measurable and the AIF is measured in a large vessel (or in the case of myocardial DCE-MRI typically in the left ventricular cavity) upstream of the tissue. The delay in arrival of contrast agent at the tissue relative to the blood sampled for the AIF (bolus arrival time, BAT) must be accounted for during or prior to deconvolution analysis. Several strategies exist to account for this including performing multiple fits with varying fixed BAT candidates and selecting the fit with the lowest residuals, including BAT as an additional continuous free parameter in the deconvolution process [57] or identifying the delay between the onset of the upslope of the tissue and AIF curves either manually or using an automated process [58, 59]. As the deconvolution process is ill-posed limiting the number of free parameters is preferable to avoid decreased precision, and so the increased number of procedural steps involved in estimating BAT prior to deconvolution may be preferable.

Optimisation is commonly performed in a least-squares sense, by identifying a set of residue function defining parameters which optimally minimise the sum of the square of the residual values between the observed concentration in the tissue and the result of Equation 2-33. Several algorithms exist to perform this optimisation process and their precise application can be controlled by several parameters (such as initialisation values and termination tolerances). Generally these algorithms adjust the parameter set iteratively (from a user defined starting value) to find the set which gives the lowest sum of square of residuals, with different algorithms employing different methods to determine how the parameter sets are changed between each iteration. The optimisation terminates once specified limits are reached, for example when the parameter estimates change by less than specified values between each iteration. One limitation of these methods is that local minima can be found where a parameter set gives the lowest sum of square of residuals of the surrounding region of the parameter space which the algorithm searches, but that where the true minimum is elsewhere. Dependent on the nature of the optimisation problem and the quality of the data used different approaches may thus result in different optimal parameters sets being identified. This can be a particular problem in cases where several local minima exist as algorithms may not find the global minimum across the entire parameter space. A robust optimisation algorithm

and appropriate choice of initialisation values, constraints and termination tolerances is thus required for reliable estimation of these parameters.

The above formulation is defined in the temporal domain. Alternatively data can be transformed into the frequency domain prior to optimisation. Such an approach can reduce the sensitivity of the optimisation process to the initialisation values and allow use of models for which there is no known temporal domain solution such as the tissue homogeneity model [55]. This process involves performing a Fourier transform on the AIF, multiplying by the Laplace domain solution of the residue function for the tracer kinetic model and then performing an inverse Fourier transform prior to calculating the residual difference compared to tissue data. As well as the advantages described above this can be computationally more efficient than direct convolution in the temporal domain in some circumstances.

2.4.2 The partition coefficient and distribution volumes

As described above the concentrations in the interstitium and the blood plasma will equalise over time following contrast agent administration. However, these volumes form part of a macroscopic system in which other regions are inaccessible to the contrast agent. In general it is the concentration within this macroscopic environment that is measurable. For example, the concentration in the whole blood is generally measured, rather than the concentration within the plasma alone. This is demonstrated graphically in Figure 2-17.

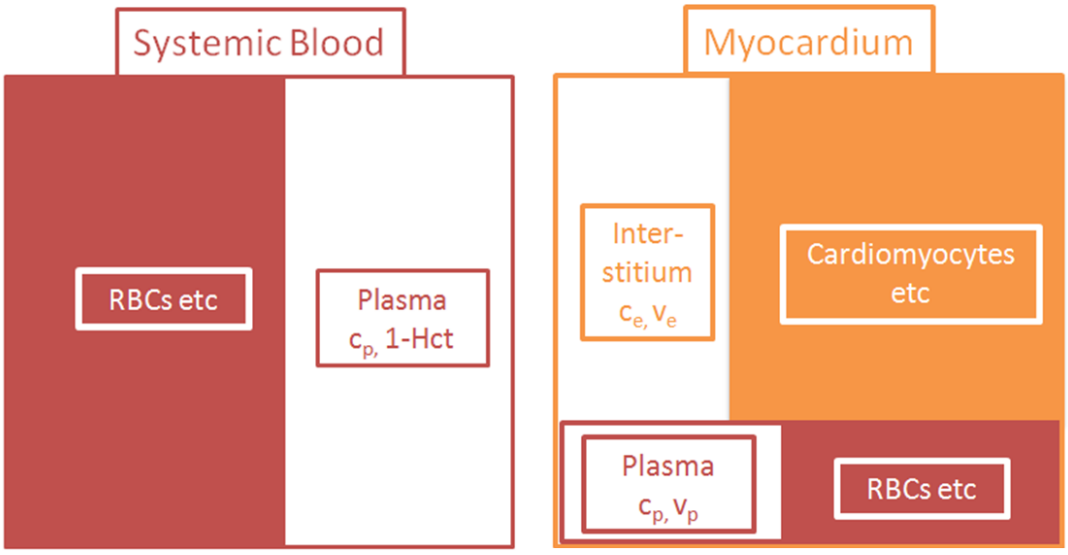

Figure 2-17 – Graphical representation of spaces making up the systemic blood and the myocardium. Only white regions are accessible to

extracellular contrast agents. RBCs indicates red blood cells For the accessible areas the concentrations are defined as c_p for plasma (in both systemic and myocardial blood) and c_e for the extravascular-extracellular space. Relative volumes are defined as v_p and v_e for the same spaces respectively. For the systemic blood the plasma volume is equal to 1 – Hct, where Hct is the haematocrit. The ECV is the total extracellular volume fraction (v_e+v_p).

In this figure it can be seen that in the systemic blood there exists a space accessible to the contrast agent which has a relative volume equal to 1-Hct, i.e. the plasma volume. In the myocardium a given section of tissue will contain capillaries, interstitial space and cells (predominantly cardiomyocytes). The accessible space is thus composed of both the extravascular-extracellular space (relative volume = v_e) and the plasma volume (v_p). Once equilibrium has been reached the concentrations in these regions (c_e and c_p respectively) are by definition equal. The following equations define the measurable concentrations, c_b and c_m (i.e. blood and myocardial concentrations):

Equation 2-46

$$c_b = (1 - Hct) \cdot c_p$$

Equation 2-47

$$c_m = c_e \cdot v_e + c_p \cdot v_p$$

As c_e=c_p at equilibrium Equation 2-47 can be re-written as:

Equation 2-48

$$c_m = c_p \cdot (v_e + v_p) = c_p \cdot v_d$$

(at equilibrium only)

Assuming that the contrast agent distributes in the entire extracellular space (i.e. that v_d is equivalent to ECV), re-arranging the above yields the following definition:

Equation 2-49

$$ECV = v_d = \frac{c_m}{c_p} = \frac{c_m}{c_b} \cdot (1 - Hct)$$

(at equilibrium only)

Defining the partition coefficient (λ) as the ratio of myocardial to blood concentration at equilibrium ECV can thus be calculated if λ and Hct are measured thus:

Equation 2-50

$$ECV = \lambda \cdot (1 - Hct)$$

2.4.2.1 Measuring the partition coefficient using MRI

As described in Equation 2-30, R_1 varies linearly with contrast agent concentration. Consequently the relative contrast agent concentration in myocardium and blood can be estimated from the relative change in R_1 from the pre-contrast state to that after contrast agent administration once equilibrium has been achieved (Equation 2-51).

Equation 2-51

$$\lambda = \frac{c_m}{c_b} = \frac{\Delta R_{1,m}}{\Delta R_{1,b}} = \frac{\left(\frac{1}{T_{1,m,equilib}} - \frac{1}{T_{1,m,pre}}\right)}{\left(\frac{1}{T_{1,b,equilib}} - \frac{1}{T_{1,b,pre}}\right)}$$

Note that the above relationship is valid only where the assumption of fast water exchange between regions can be assumed, as discussed previously.

2.5 Conclusions

In this chapter the relevant biological, clinical and physical theory that informs the subsequent content of this thesis has been introduced and described. This theory is required to inform the acquisition, analysis and interpretation of quantified contrast enhanced MRI as applied to the assessment of the myocardium.

Chapter 3

Outline of a Clinical Cardiac DCE-MRI Protocol

In this chapter the generic structure of a clinical DCE MRI protocol is described, including details of the sequences used for quantification of perfusion and distribution volume in the left ventricular myocardium. Variants of this generic structure using these established sequences are used in the later chapters describing clinical studies.

3.1 Typical perfusion CMR protocol

CMR is a highly flexible imaging tool and so protocols are tailored to the clinical questions being addressed. A protocol will begin with localiser scans to identify positioning for the standard cardiac views, including the short-axis view typically used for perfusion imaging and T_1 mapping. This will be followed by a series of imaging sequences designed to assess the structure, function and status of the heart. Commonly this will include a variety of the following: cine images, tagged images, velocity encoded images, T_2 weighted images, T_2^* maps, T_1 maps, and images of the coronary arteries. An example protocol including stress/rest perfusion is shown in Figure 3-1, such a protocol may take around 40-60 minutes to acquire.

The ordering and selection of some sequences in the protocol will vary based upon clinical indication or research questions with some constraints imposed due to the fact that some data should be acquired either before or after contrast agent administration (either as an absolute necessity or a preference, e.g. tagged images can be acquired at any time but may be best acquired pre-contrast as tag patterns persist longer when T_1 is longer). To account for both cardiac and respiratory motion the majority of scans are triggered or retrospectively gated by ECG and many are acquired in either one or several breath-holds.

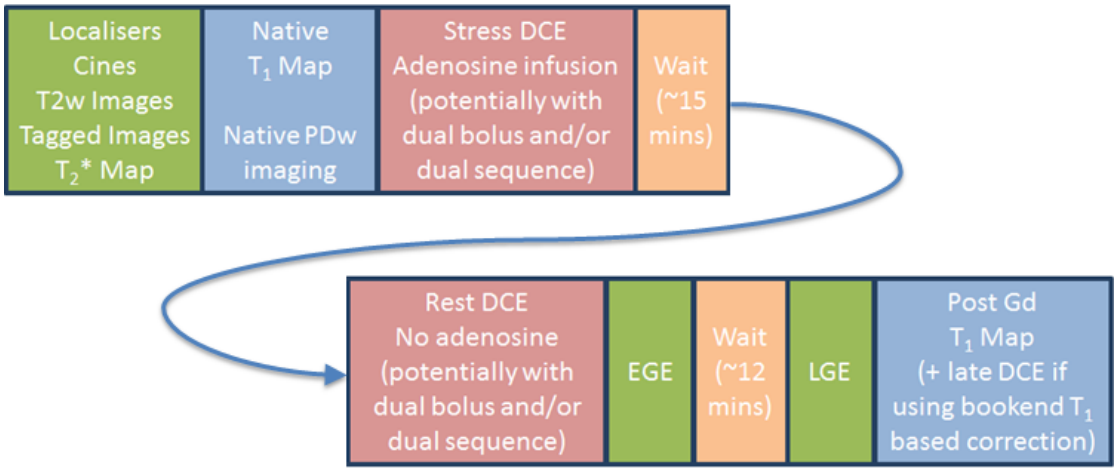

Figure 3-1 – Example protocol including stress/rest perfusion (DCE) MRI. Items in pink indicate DCE-MRI and include contrast agent administration. Those in blue relate to ECV measurement, T_1 mapping and/or non-linearity correction of DCE data. Items in green are additional sequences for tissue and function characterisation and the selection and ordering of these may vary depending on the clinical requirements. Additional elements, such as coronary artery imaging or flow encoded imaging, may also be included. Some of these sequences may be performed post-contrast during the delay periods (peach).

For myocardial DCE-MRI, images are acquired regularly (typically every heartbeat) for a period of time which will be chosen based on the intended post-acquisition analysis. During this time contrast agent is administered as a bolus administration at a high injection rate (typically 3-5 ml/s) followed by a saline flush (typically around 20 ml at the same injection rate as the contrast agent). For dual-bolus studies a reduced dose of contrast agent will be administered prior to the main bolus with either a reduced volume or the same volume of diluted contrast agent, also with a saline flush. For such studies the acquisition duration is extended to accommodate the two bolus administrations. Depending on the clinical indication perfusion studies may be repeated under different physiological conditions, for example under stress and at rest. As well as the perfusion series themselves additional sequences may be acquired to allow correction of the non-linear signal response to contrast agent concentration, as discussed later in this thesis.

Following perfusion imaging additional contrast-enhanced studies may be acquired at prescribed times after the final contrast agent administration. These include inversion recovery early and late gadolinium enhancement images at around 1-3 and >10 minutes respectively, and T_1 maps for fibrosis assessment (typically ~15 minutes). Inclusion of both early and late gadolinium

enhancement allows distinction of non-persistent (which can also be identified on perfusion imaging) MVO and persistent MVO (with the latter appearing at both time points and the former appearing only at the early phase). As discussed in section 2.1.2 the presence of persistent MVO implies a poorer prognosis than non-persistent or completely absent MVO. It has been postulated [30] that in cases with non-persistent MVO the residual blood flow is low but contrast agent does reach the tissue slowly through collateral flow and diffusion while persistent MVO reflects severely disturbed microvasculature, leading to the differential appearance at delayed phases after contrast agent administration.

Finally, in addition to acquisition of MRI data it may be necessary to collect blood samples prior to scanning to provide patient specific haematocrit measurements, which are necessary for determining some physiological parameters (for example estimation of plasma flow and ECV requires knowledge of haematocrit, but that of blood flow and partition coefficient does not).

3.1.1 Pharmacological stress

As described above it is common to acquire perfusion images both at rest and under stress. Stress is achieved using pharmacological agents such as the vasodilators adenosine, regadenoson or dipyramidole, or the inotropic agent dobutamine. For the studies described in this thesis adenosine was used to achieve maximal hyperaemia (typically using a 140 μg/kg(bodyweight)/min dose infusion although in the absence of symptoms or substantial (10%) increase in heart rate after two minutes this was increased to 210 μg/kg(bodyweight)/min). This infusion is continued throughout the perfusion study to maintain hyperaemia, and terminated at the end of the acquisition at which point the effects subside rapidly due to the short blood half-life of adenosine [60]. Consequently for stress perfusion studies two cannulae are required, one for contrast agent delivery and one for stress agent infusion.

3.2 Sequences

The following sections describe the sequences used for the DCE-MRI acquisition in the studies described in later chapters, as well as details of associated sequences used in the quantitative analysis.

3.2.1 Cardiac perfusion sequence

Cardiac DCE-MRI data in the studies described later in this thesis were acquired using an ECG triggered saturation recovery prepared 2D spoiled gradient echo sequence. Acquisitions consist of three slices aligned to provide short-axis views evenly spread through the longitudinal extent of the left ventricle, adopting the commonly used “three-of-five” approach to ensure reproducible positioning [61]. In this approach five short-axis slices are initially specified, equally spaced from the apex to the base of the left ventricle, the outer two are then discarded prior to imaging (see Figure 3-2).

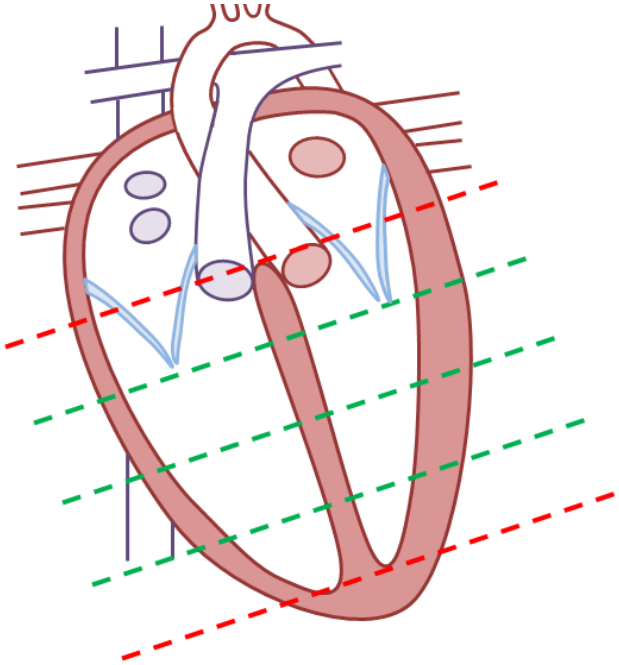

Figure 3-2 – “Three-of-five” approach for cardiac DCE-MRI imaging. Initially five equally spaced slices are prescribed (dashed lines). The outer two (red) are then discarded prior to acquisition of the inner three (green).

The acquisition process for each slice consists of a non-slice selective saturation pulse followed by a delay and then a train of slice-selective readout pulses. Each readout consists of a Cartesian k-space trajectory accelerated with partial Fourier acquisition and parallel imaging to reduce the number of

lines of data that need to be acquired. Approximately 40 readout pulses (depending on resolution and field of view) are therefore acquired (N_{PE}≈40), with the central line of k-space acquired early in the readout train (typically at around the 12th readout, n_{k0}≈12). This line of k-space is acquired a specified delay, TS, typically around 100ms. Data is acquired with short TR and TE to minimise acquisition duration and T_2^* weighting respectively. These are typically around 2.7 ms and 1.1 ms respectively. As a spoiled readout technique is used a low flip angle (FA≈15°) is used. The duration of the readout train (acquisition duration) is equal to the product of N_{PE} and TR, around 108ms, and the total duration required to image a single slice (shot duration) is equal to the sum of TS and the product of TR and the number of lines of k-space acquired after the central line (N_{PE}-n_{k0}), around 176 ms.

Image acquisition is triggered by ECG, with imaging starting at a delay after detection of the R-wave (trigger delay, TD) chosen to acquire images during diastole, when cardiac motion is minimal. The three slices are then acquired contiguously in time as shown in Figure 3-3. As the acquisition of all three slices takes a little over half a second there is an upper limit on the heart rate of around 110 bpm of the subject for which the sequence can be acquired without requiring a reduction in either resolution, number of slices or changing to triggering imaging every other heartbeat. This limit is typically not reached during scanning at rest but may be limiting when scanning subjects under pharmacologically induced stress. Changes in heart rate will also affect the cardiac phase of each slice, as the duration of image acquisition will remain constant while cardiac cycle length changes.

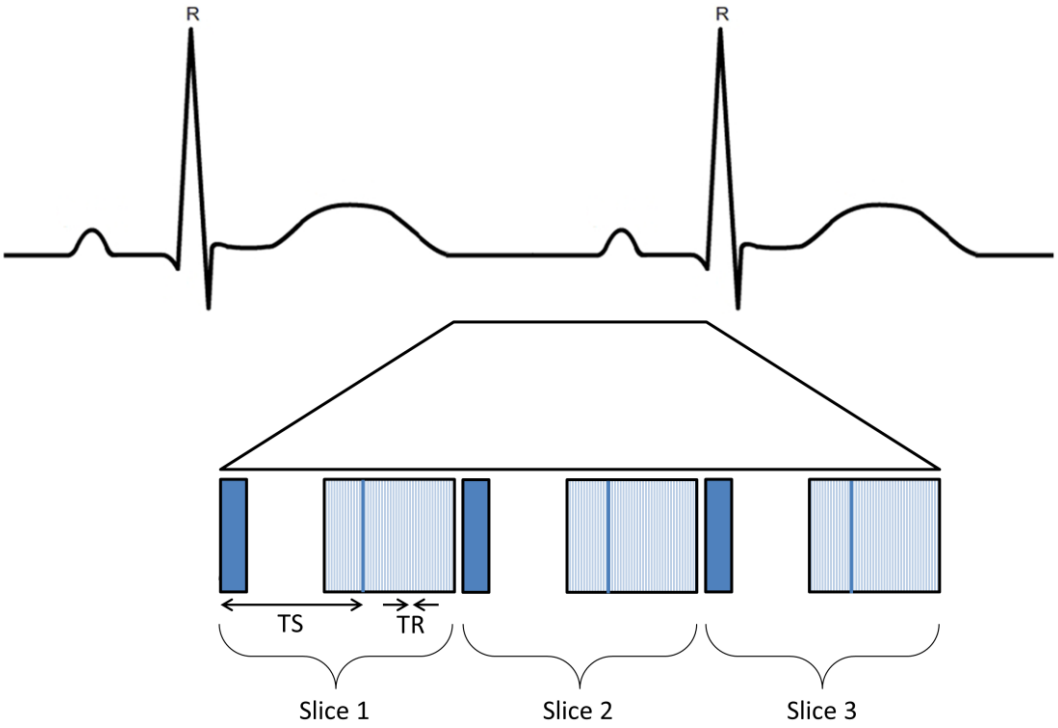

Figure 3-3 – Schematic of three slice, saturation recovery spoiled gradient echo, ECG triggered DCE-MRI sequence. Dark blue rectangles indicate non-slice selective saturation pulses. Bold blue lines indicate the position of the central line of k-space within the readout train (vertical blue striped rectangle). In proton density weighted variants the saturation pulses are omitted.

Respiratory motion

As well as the requirement to account for cardiac motion (typically achieved through ECG triggering as discussed above) the heart undergoes bulk motion due to breathing. For short DCE-MRI sequences this can be accounted for by the patient holding their breath during the acquisition. However this limits the maximum acquisition duration and may lead to severe motion if the patient takes a deep breath before imaging has finished. For longer acquisitions, or for patients who cannot easily hold their breath, shallow breathing throughout the acquisition may be preferable to a breath-hold followed by shallow breathing to reduce the likelihood of a deep breath leading to substantial motion taking place. In the latter case (breath-hold for initial part of acquisition) the variability in signal intensity may generally be more severe later in the DCE-MRI acquisition after the end of the breath-hold.

For analysis in-plane respiratory motion can be accounted for by image registration techniques or by moving region of interest contours to account for motion. However neither of these methods can account for through-plane

motion in 2D imaging. Furthermore if image uniformity is not ideal sensitivity may vary across the imaging field of view and so even with successful correction for motion (using either registration or adjustment of contours) respiratory motion may cause artefactual variation in signal intensity throughout the acquired DCE-MRI data as for example in Figure 3-4 below:

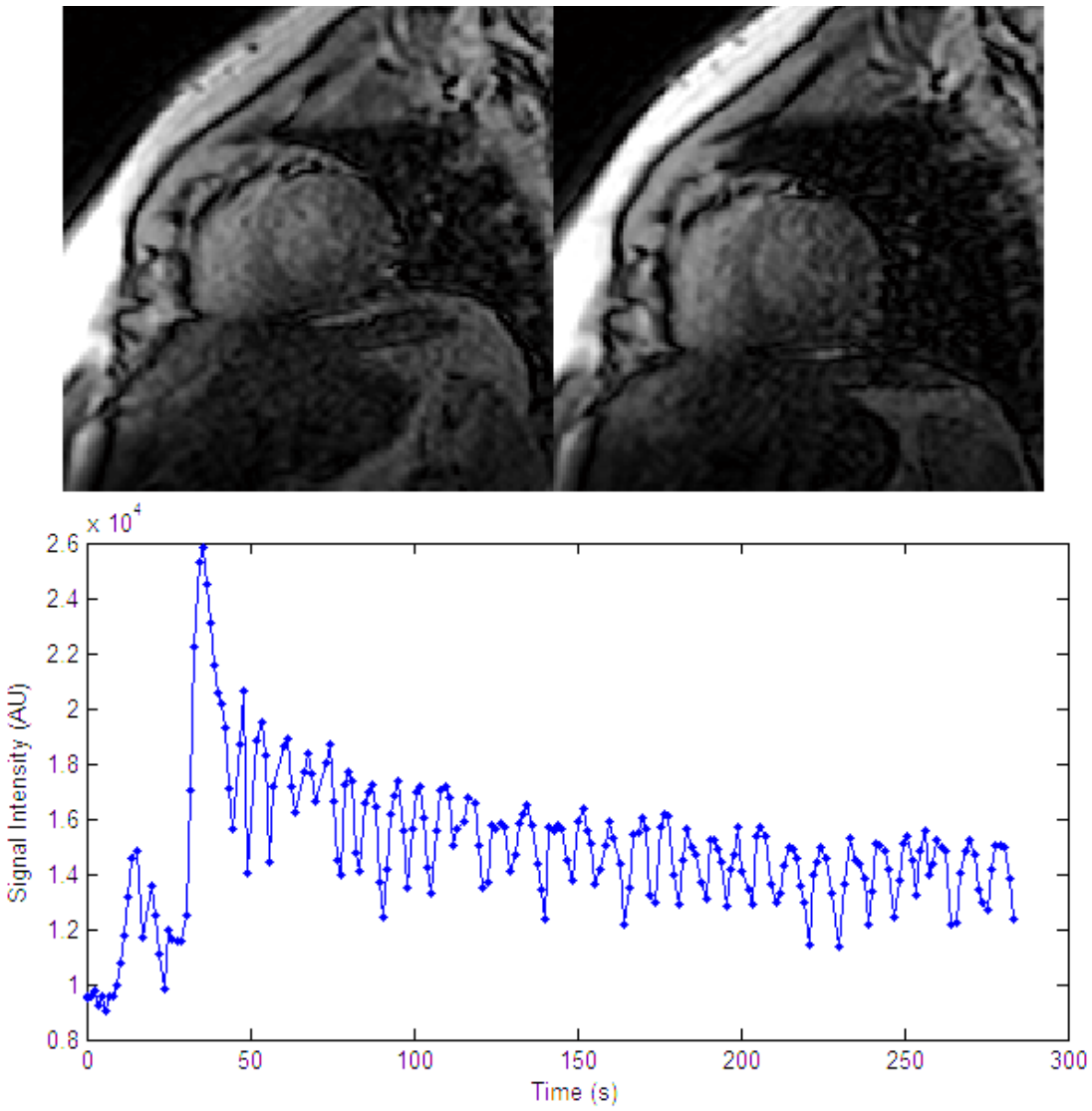

Figure 3-4 – Top – DCE-MRI images (cropped for clarity) acquired at each end of the respiratory cycle (left – inspiration, right – expiration). These images are from a volunteer who breathed deeply throughout acquisition. These images were acquired approximately 2 minutes after contrast agent administration and were 3 cardiac cycles (2.3 seconds) apart so little variation in contrast agent concentration would be expected. Despite this myocardial signal intensity varies approximately 20% between the two images. Bottom – This variation leads to structured variation in the myocardial signal curve which is due to motion rather than contrast agent variation.

3.2.1.1 Dual-sequence variant

The dual-sequence approach exploits the unused time between the saturation preparation pulse and image readout of the DCE-MRI sequence to acquire an additional image with reduced T_1 sensitivity, and thus linearity of signal response over a greater contrast agent concentration range. Due to the short time available (TS-n_{k0}TR) this additional image has very low spatial resolution, but can be used to measure signal variation in the blood pool, i.e. the arterial input function, as this is taken from the relatively large left ventricular blood pool. The sequence does not have sufficient spatial resolution to allow reliable measurement of myocardial signal intensity. Typical parameters for this sequence are TS≈24 ms N_{PE}≈24 and n_{k0}≈8 with FA, TR and TE similar to the full resolution acquisition. Figure 3-5 shows a schematic and example images for this approach.

The additional image acquisition is interleaved between the saturation pulse and image readout of one of the slices of DCE-MRI data. To avoid the extra readout pulses affecting the magnetisation evolution of the myocardium prior to acquisition of the full resolution image, a different slice position is used and slice-selective readout pulses are employed. For example a low-resolution image acquired at a position towards the base of the left ventricle would be acquired between the saturation pulse and readout of a slice towards the apex. As non-selective saturation pulses are used the magnetisation is saturated in the position of both slices. Additionally magnetisation in blood outside of the imaged slices (but within the region in the scanner bore over which the RF pulses are transmitted) which could flow into the slice by the time of image acquisition will also be saturated, although the saturation efficiency may be reduced away from the scanner isocentre, outside the imaging volume of the scanner. However, as this volume extends to around 40-50cm in the axial direction in a typical closed bore scanner, and saturation pulses are applied multiple times per cardiac cycle, it is unlikely that blood will be imaged that has not experienced multiple saturation pulses with similar saturation efficiency to those experienced by static tissue in the imaging slices.

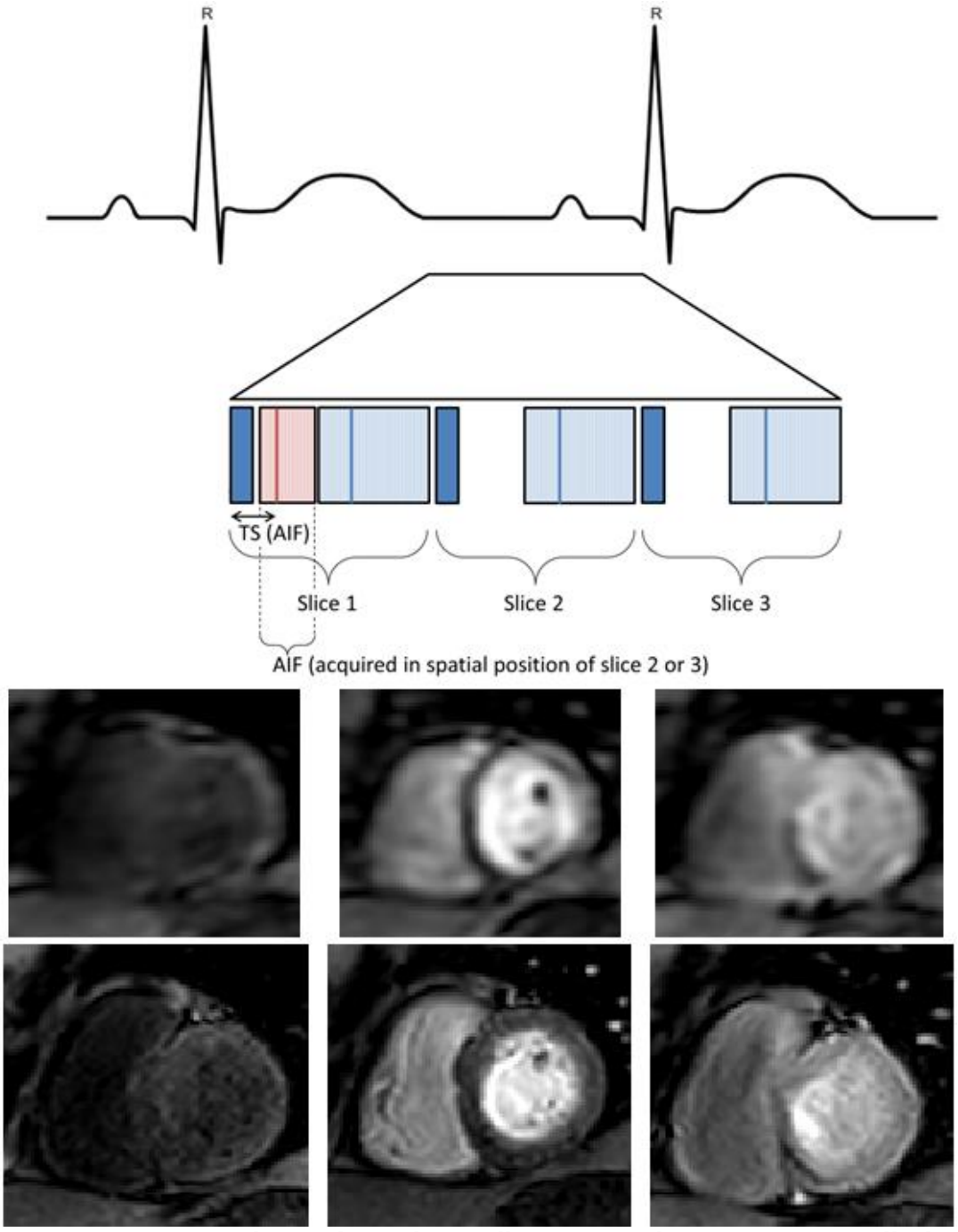

Figure 3-5 – Top - Schematic of three slice, saturation recovery spoiled gradient echo, ECG triggered DCE-MRI sequence with interleaved low spatial resolution image for measuring the AIF in the dual-sequence approach. Bold blue or red lines indicate the position of the central line of k-space within the readout trains (vertical blue or red striped rectangles) for the full resolution or interleaved low resolution sequences respectively. In proton density weighted variants the saturation pulses are omitted. Bottom – Example low-resolution (top row) and high resolution (bottom row, same slice location) images from different phases of enhancement (left – pre-contrast, middle - peak AIF, right – myocardial enhancement).

3.2.1.2 Non-SR proton density weighted variant

To perform signal non-linearity correction data from a proton density weighted sequence can be used to constrain a signal model. To acquire data for this a modified version of the DCE-MRI sequence is used, which is identical to the standard sequence except the saturation pulses are removed to reduce T_1 weighting. This sequence is acquired separately to the standard DCE sequence, typically over a small number of heart beats (~10) within a single breath-hold. A dual-sequence variant of this can also be acquired to provide proton density weighted images with resolution matched to the saturation recovery images acquired. As the readout pulse train is repeated every heart beat some T_1 weighting will remain and signal may vary between early images as a steady-state is reached. To reduce such effects it may be beneficial to reduce the readout pulse flip angle.

3.3 Conclusions

In this chapter the outline of a CMR protocol has been outlined and the sequences performed for perfusion CMR described in further detail. These sequences form the basis of the protocols used in the following chapters. Specific parameters used for those studies are introduced as they are used.

Chapter 4

Literature Review – Technical

This chapter provides a review of scientific literature relating to the technical aspects of quantitative contrast enhanced MRI, focussing on applications within the field of clinical cardiovascular imaging but also including relevant material from other clinical and pre-clinical fields.

4.1 Introduction

Changes to myocardial perfusion, structure and physiology are common to a range of ischaemic and non-ischaemic heart diseases. There is consequently a demand for techniques that are able to identify and characterise such changes in the clinical setting. Ideally such techniques should be non-invasive, safe and readily applicable in routine practice. Developments in MRI, along with other imaging modalities, have allowed increasingly detailed assessment of the myocardium, including through the application of exogenous contrast agents. This review details the development of quantitative cardiac MRI methods exploiting gadolinium based contrast agents for the measurement of perfusion, extracellular volume fraction (ECV) and other physiological parameters relating to myocardial tissue status.

4.2 Clinical motivation

Visual analysis of myocardial DCE-MRI data allows identification of perfusion defects and is thus commonly used in the assessment of ischaemic heart disease (being included in international standardised protocols [62]), both to identify regions of reduced perfusion and to assess response to therapy. Initially motivation for characterising changes in myocardial ECV was focussed on the assessment of viability of myocardium following infarction. In this setting the loss of cardiomyocyte cell membrane integrity associated with myocardial infarction was proposed as a mechanism for hyperenhancement observed in infarcted regions of myocardium in post contrast T_1 weighted imaging [5] described in section 4.3.1. More recently interest in assessment of this parameter has developed into assessment of both interstitial and replacement fibrosis in a range of cardiomyopathies. Due to the more diffuse distribution of

fibrosis in many of these settings, and the fact that severity as well as spatial extent is of interest, methods to quantitatively assess contrast agent distribution volumes have thus been desired and developed [26]. Similarly quantification of perfusion may allow more objective assessment of changes due to non-ischaemic diseases, or due to three-vessel disease where perfusion is limited throughout the myocardium and so localised deficits may not be visible [63]. As this chapter focusses on the technical development of quantitative contrast enhanced cardiac MRI a review of relevant clinical studies is presented in the following chapter.

4.3 Contrast enhanced MRI methods

Since the introduction of Gd-DTPA as a contrast agent its potential for use in a range of clinical applications has been investigated. Early investigations into cardiac applications were performed by assessing contrast between remote and infarcted myocardium, first in a canine model [64] and later in humans [65], and established the potential for this agent to be used to differentiate tissue states in acute myocardial infarction. Use of gadolinium based contrast agents in cardiac MRI is widespread and can broadly be classified into three categories which : DCE- MRI (also referred to as perfusion CMR), delayed enhancement (DE) MRI and contrast equilibrium MRI [66, 67]. These exploit different sections of the myocardial enhancement curves (as exemplified in Figure 2-12) to distinguish normal and pathological tissue. The development, theoretical background and application of these methods are discussed in the following sections.

4.3.1 Delayed enhancement MRI

The value of the use of gadolinium based contrast agents in assessing the viability of myocardium (as opposed to its perfusion status, discussed later) was first evaluated by Fedele *et al* in 1994 [68] . In this study the authors identified significant differences in signal intensities of T_1 weighted images acquired 12 and 30 minutes after contrast agent administration between normal, necrotic and hibernating myocardium (differences were not statistically significant at the earlier measured time points of 4 and 8 minutes). This provided the basis for the development of LGE MRI, in which T_1 weighted inversion recovery images (with an inversion time selected to null signal from normal myocardium, see Figure

2-10 and associated discussion in section 2.2.3) are acquired after a delay of around ten minutes after contrast agent administration [69]. Due to the enlarged distribution volume resulting from breakdown of cardiomyocyte membranes in infarcted myocardium (and hence increased accumulation of Gd-DTPA once equilibrium is reached), the T_1 at this delayed phase is shortened and strong contrast between normal and infarcted tissue can be achieved when the normal myocardium is nulled. This has since developed to become a gold standard technique for the identification of focal fibrosis and scar in a range of ischaemic and non-ischaemic heart diseases [70-75] and has been shown to provide great prognostic value in coronary artery disease [76].

The above techniques used to assess myocardial viability are commonly referred to as late gadolinium enhancement (LGE) MRI and are typically acquired 10 minutes or longer after contrast agent administration. Application of similar methods earlier (within around 5 minutes of injection) can allow identification of microvascular obstruction after infarction and reperfusion (as described in section 2.1.2) [66], referred to as early gadolinium enhancement (EGE).

Development is still ongoing to improve the utility of this method, for example through the use of double inversion sequences to supress signal from blood as well as viable myocardium, and hence increase contrast at the endocardial layer [77]. Notably the introduction of phase-sensitive inversion recovery techniques (in which the image data depends on the direction of the longitudinal magnetisation prior to the application readout pulse, as well as its magnitude) can reduce the scope for operator error as the technique is less sensitive to the choice of inversion time although a systematic bias between such techniques and conventional magnitude reconstructed LGE imaging has been observed [78].

There are, however, two limitations to this technique. Firstly; while being useful for identifying regions of disease it is not possible to determine the severity of damage to the tissue reliably. Secondly; the technique relies on contrast between injured and remote myocardium, and so is not suited to the assessment of diffuse fibrosis or other pathological processes that result in global changes to the extracellular matrix. Consequently there remains a need

for other methods to quantitatively assess the physiological status of the myocardium.

4.3.2 Dynamic contrast enhanced MRI

The potential use of Gd-DTPA as a tracer for quantitative assessment of both myocardial blood flow (MBF) and ECV was investigated in 1992 by Diesbourg *et al* [79]. This was the first study in which MBF and ECV were estimated along with T_1, T_2 and myocardial Gd-DTPA concentration in a canine model of ischemic heart disease. The study was also the first to compare simulations based on tracer kinetic modelling techniques using the modified Kety model [80] to simulate myocardial Gd-DTPA concentration following a bolus or infusion administration. For this study simulated myocardial Gd-DTPA concentration curves were compared to measurements from hearts excised following sacrifice immediately post infusion and both immediately and at five minutes post bolus administration.

The simulations from this study predicted that the physiological parameter which most influences myocardial Gd-DTPA concentrations changes throughout the period following bolus injection. Within the first minute MBF is the dominant effect whereas at later times ECV becomes dominant. Following a slow constant infusion to achieve a steady-state between the plasma and interstitial volumes, the concentration is primarily determined by ECV. At the time of this study MRI techniques for sampling the required concentration curves with the required temporal resolution were not available (as discussed in section 2.4.1.1 this must be sufficiently high to sample the contrast agent variation adequately, which in practice requires imaging at least every other cardiac cycle [81]). However the paper raised the theoretical possibility of measuring the product of MBF and E, the extraction efficiency (this product is also known as the unidirectional influx constant, K_i [82]), as well as the Gd-DTPA distribution volume in myocardium by using deconvolution methods if the technological obstacles could be overcome. For this T_1 estimates of blood and myocardium would be required every few seconds. The study also measured λ following a constant infusion administration. Measurement of this parameter, along with adjustment based on a haematocrit measurement, is another method to measure ECV.

Later studies by the same group [83, 84] proposed a method combining contrast enhanced MRI, microsphere based myocardial blood flow estimates and nuclear medicine based distribution volume estimates to allow local measurements of E in a canine model. However this technique could not be applied in a clinical setting, and the results showed that E varied between subjects and tissue status and so an assumed value could not be used to allow estimates of MBF from DCE-MRI using this model.

4.3.2.1 Acquisition techniques and estimation of physiological parameters

Concurrent with the work above developments in MRI technology were allowing the introduction of rapid T_1 weighted sequences to monitor the delivery of Gd-DTPA to the myocardium *in vivo* [85, 86], thus allowing DCE-MRI to be introduced into clinical cardiac MRI workflow. Semi-quantitative measures (see section 2.4.1.1) such as signal intensity slope, time-to-peak and time to reach steady-state can be straightforwardly derived from DCE-MRI data [85] and offer objective parameterisation, although without direct physiological interpretation.

Larsson *et al* [82] provided the first fully quantitative study using DCE-MRI to sample both myocardial and arterial Gd-DTPA concentration curves (validated against invasive arterial sampling). In this work the MRI derived AIF was scaled (to account for haematocrit and flow effects) using venous blood samples taken 6 minutes post injection, so the need for blood sampling was not fully alleviated. However the protocol could, in principle, allow a change from repetitive arterial sampling to a single venous sample (although repeated venous and arterial samples were performed in this study for comparison). In order to measure the curves through MRI a pre-contrast T_1 measurement (using an electrocardiograph (ECG) triggered inversion recovery (IR) spoiled gradient echo sequence (Fast Low Angle Shot, FLASH) with 12 inversion times (TI)) was performed (triggered every third RR interval). The same sequence was repeated with a single fixed TI to allow estimation of changes in R_1 with a temporal resolution equal to three times the cardiac cycle length ($T_{RR,}$ the time between successive R-waves on the ECG trace). A Gd-DTPA bolus was injected after the acquisition of 15 baseline images, with 127 images acquired in total. Curves were generated for a region of interest in the septum and in the

descending aorta and estimates of K_i and ECV were derived through deconvolution methods using both the MRI generated and directly sampled AIFs (applying the Kety model [80]). In this approach it is assumed that the exchange of water between the different regions of the myocardium is fast in comparison to the temporal resolution and the range of longitudinal relaxation times. Consequently the myocardium is assumed to act as an ensemble of spins with equal longitudinal relaxation rates equal to a weighted average of those in the various regions. In the small healthy volunteer component of this study (n = 4 for MRI derived AIF, 3 of which also had arterially sampled AIFs) agreement in ECV and perfusion between AIF measurement technique was moderate with lower estimates of K_i from the arterially sampled AIF. The authors note that it was necessary to shift the arterially sampled AIF temporally to account for the transit time between the heart and the brachial artery sampling point and suggest that this is a possible source of error. If this was the case then the MRI sampled AIF may be preferable not just because it is sampled non-invasively, but also because this error source is minimised as the sampling point is much closer anatomically to the myocardium. Furthermore this may reduce dispersion of the contrast agent bolus shape between the sampled AIF and the true input to the myocardium, as well as the temporal offset.

A subsequent study by the same group [87] utilised an extended model which assumed slow water exchange between the vascular and interstitial compartments, and thus also allows measurement of the fractional plasma volume (v_p) in addition to K_i, ECV and BAT. Additionally a model which included the extraction fraction was included to attempt to separate K_i into its constituent parts (E and F_p). In this work data acquisition methods were similar to those for the previous study. It was found (in simulation studies) that the four parameter model was robust to noise but that inclusion of E (to allow F_p, rather than K_i to be determined) led to significant errors being introduced for moderate noise levels. Consequently the authors analysed the *in vivo* data (collected from healthy volunteers) using the four parameter model. The results from this analysis agreed reasonably well with separate PET (2.1.3) studies although with slightly higher results from MRI. The authors acknowledge that absolute MBF quantification with PET imaging has some limitations, including limited spatial resolution and the need to correct for factors such as partial volume and

spillover effects. In particular it was noted that due to the relatively low spatial resolution in PET, and the lack of ECG triggering to compensate for cardiac motion, there is likely to be significant averaging of flow heterogeneity. However this comparison has demonstrated the feasibility of DCE-MRI as a method to quantitatively measure parameters related to both perfusion and compartmental volumes.

Vallée *et al* [88] later also used a one-compartment model (in which the interstitial and vascular compartments in the myocardium are not separated, as in the first study by Larsson *et al*). Consequently only the total distribution volume (ECV) and not its constituent parts can be assessed alongside the influx constant K_1. It should be noted that there has been some variability in the use of notation within DCE-MRI literature [89], with K_1, K_i and K^{trans} having been used to represent the transfer constant from blood to myocardium, and K_1 in this study is equivalent to K_i in the previous discussion. This study was performed in order to assess the change in measured parameters at rest and under dipyramidole induced stress in a canine model. The group later applied these methods in humans (n = 10) with normal resting cardiac function [90]. Distribution volumes measured averaged 15% in this study, which was similar to their animal study but considerably lower than those measured by Larsson *et al* in the study described above (around 30%) [87] suggesting that further work was necessary to elucidate the mechanisms responsible for the differences.

In the first study to apply these methods in the setting of acute myocardial infarction a one compartment model (as per Vallée *et al* [88]) was employed to analyse MRI derived concentration curves following the bolus injection of Gd-DTPA [91]. The study used an IR spoiled gradient echo (Turbo-FLASH) sequence, initially with varying TI to calculate pre-contrast T_1 and then with fixed TI to monitor contrast agent passage. This sequences employs a 180° pulse to initially invert longitudinal magnetisation followed by a spoiled gradient echo sequence (Figure 2-7) with low readout flip angles and short TR to reduce image acquisition duration. Signal intensities were converted to changes in R_1 and subsequently contrast agent concentrations using the pre-contrast T_1 measurement and the signal intensity equation for the imaging sequence. Data was collected for 5 slices, each of which was segmented radially into 60

regions. K_1 and ECV were calculated for each region and K_1 maps produced. In regions with infarct (identified through lack of enhancement in visual assessment of the images) K_1 was seen to fall dramatically. Converse to expectations the distribution volume was also significantly lower in infarcted regions. This contradicts results from other acute MI studies described more fully later in this review using both DCE and contrast equilibrium MRI (e.g. Flacke *et al* [92] and Pereira *et al* [93]). The reasons for this unexpected result are not clear but could relate to the distribution volume being underestimated in regions of microvascular obstruction where very little contrast agent reaches the myocardium, particularly if the duration of the image acquisition period was too short to allow precise estimation of distribution volumes.

A study by Pack *et al* [94] evaluated DCE-MRI for assessing the distribution volume in chronic infarction using a modified Kety model. Dynamic data acquisition was performed at rest and under adenosine induced stress. Results were compared to a contrast equilibrium derived ECV estimate (a technique described in section 4.3.3) based on signal intensity ratios pre-contrast and at the end of the full protocol (at 40 minutes following two 0.025 mmol/kg injections of Gd-DTPA at approximately 3 and 13 minutes and a further 0.15 mmol/kg injection at 20 minutes). In order to assess the length of dynamic data acquisition required simulations were performed. It was found that for normal myocardium, estimates of ECV were within 5% of the ground truth value when 30 s of data was acquired and for infarcted myocardium 90 s was required for the same accuracy. In both cases inclusion of later data points did not significantly affect accuracy. For patient studies acquisition durations of at least 3 minutes were used, and for healthy volunteers at least 1 minute was acquired, to ensure ECV could be accurately assessed. This highlights the importance of ensuring that the protocol is designed to collect data sufficient for the purpose, and that extended DCE protocols may be required for myocardium with reduced perfusion and increased ECV. Using these acquisition durations ECV measured by DCE-MRI was not significantly different to that measured by contrast equilibrium methods, and was observed to increase approximately two-fold in infarcted myocardium compared to normal myocardium.

The studies described above employed model-constrained deconvolution, in which the shape of the residue function is described by a mathematical function which is derived from an underlying model of the physiology and is described by a small (typically 2-4) number of physiological parameters. Alternatively the deconvolution can be performed using a function that is chosen on a phenomenological basis, such as the Fermi function as employed by Jerosch-Herold *et al* [56] or using model-free deconvolution (as later utilised later by same author [95]) in which the shape of the residue function is constrained only by shape defining parameters (such as smoothness and a requirement to be monotonically decreasing). In either case the amplitude of the residue function can be interpreted as the blood (or plasma depending on how data is scaled for haematocrit) flow while other physiological parameters are not readily interpretable.

Since the work of Pack *et al* [94] the majority of published research into ECV quantification by cardiac MRI has focussed on T_1 mapping based contrast equilibrium methods. However a 2009 abstract by Jerosch-Herold *et al* [96] described a study in which ECV measured by DCE-MRI in a sample of patients (11 congenital heart disease and 9 idiopathic dilated cardiomyopathy) and healthy volunteers (n = 20 was compared to that by obtaining the partition coefficient using one pre-contrast and three post-contrast T_1 measurements. The DCE analysis used a two-compartment model and the parameters v_e, F_p and PS parameters were optimised while an assumed value for the v_p was kept constant. Signal intensity data were used in the deconvolution process, with no correction for signal non-linearity effects. The results agreed well between the two methods with no significant overall bias and similar variability in results, although with some differences existing between methods for individual subjects (the 95% confidence limits for agreements being -8 to +6 %). The authors concluded that contrast-to-noise ratio is the dominant factor affecting precision in such measurements by DCE-MRI (although no evidence was provided to support this claim) and that the technique may prove to be an efficient alternative to T_1 mapping based techniques.

A later study [1][1] compared results of DCE-MRI analysis using deconvolution constrained by the widely used Fermi model to derive measures of F_b to model-based deconvolution using a distributed parameter (DP) model, in which plasma and interstitial volume fractions, as well as PS and F_b were determined. The acquisition was performed at rest and under adenosine stress allowing the myocardial perfusion ratio (MPR, the ratio of F_b at stress to rest) to be calculated. A subset (11/16) of the volunteers returned for a second visit allowing repeatability to be assessed. This study allowed the effect of measuring additional parameters on the flow measurement to be evaluated, although no independent means of measuring volume fractions were included to allow the accuracy of the technique for that purpose to be tested directly. The DP model could be applied in the majority of cases, although in 5 of 27 data sets acquired at rest the results were deemed to be unreliable (yielding non-physiological results). This was thought to be due to the model being over-parameterised in cases with high first-pass extraction fraction in which case the delivery of contrast agent to the interstitium is limited predominantly by myocardial blood flow and it becomes difficult to separately characterise the extra- and intra-vascular distribution of contrast agent. This may limit the applicability of some models which while providing potentially useful additional data in some cases may be less robust than simpler models for tissue with differing physiology. In the failed cases in this study a one-compartment model was used to arrive at estimates of F_b and ECV (i.e. the combined plasma and interstitial volume fractions). The F_b results showed no significant bias at rest but those from the DP model analysis were significantly lower than the Fermi model results. However without independent gold-standard verification it was not possible to assess the accuracy. The authors note, however, that similar findings were reported previously [97] and that differences could be due to the fact that the Fermi model was developed for use with intravascular contrast agents (for which the single region distribution assumption the model is based on would be valid). In the repeatability assessment F_b was found to have lower or equal test/retest variation when measured with the DP model than with the

[1] The author of this thesis is lead author on this paper. Methods and software developed for this paper were implemented in the work carried out during this PhD but the work contained within the paper does not directly form part of this thesis.

Fermi model. Additionally the interstitial and combined volume measurements from the DP analysis were also less variable than the Fermi model flow results, and were consistent with literature values lending support to this analysis method.

A lack of gold standard reference data is a common limitation to the above clinical studies as the most commonly accepted gold standard technique for non-invasive assessment of MBF is ^{15}O-water or ^{13}N-ammonia PET which are not widely available, largely due to the need for on-site isotope generating equipment [98]. Additionally PET based quantification is also limited by spatial and temporal resolution considerations as described earlier in this section (on p66) and so may not be an ideal reference standard, particularly for heterogeneous disease.

Further comparisons between tracer kinetic models used for myocardial DCE-MRI analysis has been performed by different groups. Handayani *et al* [99] compared the distributed parameter, Fermi, extended Tofts and Patlak constrained deconvolution and found similar estimates of MBF at rest, but significant differences between results for the Patlak model when compared to both distributed parameter and Fermi (but not when compared to the extended Tofts model). This comparison was performed in patients with either suspected or known coronary artery disease for whom coronary computed tomography was performed to identify coronary stenoses of more than 50% diameter reduction). For myocardium subtended by arteries with such stenoses perfusion estimates were only significantly reduced at stress when assessed by extended Tofts model or Fermi model based deconvolution, suggesting model choice could affect diagnostic accuracy.

In a separate study by Biglands *et al* [100] diagnostic accuracy of a different set of four techniques was compared. In this study model based deconvolution constrained by one compartment, Fermi and uptake models, in addition to model-independent deconvolution, were compared in terms of the diagnostic performance for identifying perfusion deficits with a reference standard of a combination of the detection of inducible ischaemia by single photon emission computed tomography and a luminal stenosis of 70% or more by x-ray angiography. Diagnostic accuracy was compared for measurement of both

absolute MBF under adenosine induced stress and of myocardial perfusion reserve (MPR, the ratio of MBF at stress to that at rest). For absolute stress MBF the diagnostic performance was similar for all four methods (area under curve on receiver operating characteristic (AUC ROC) analysis of 0.85-0.87). For MPR diagnostic accuracy was also similar between three of the methods (Fermi and uptake model constrained or model-independent deconvolution), and was slightly higher than for absolute stress MBF (AUC ROC 0.87-0.92). However it was lower for one-compartment model based deconvolution (AUC ROC = 0.80) suggesting that this model may not be appropriate at rest.

As described in the discussion above a range of techniques have been developed for both acquisition and quantitative analysis of myocardial DCE-MRI data. Systematic differences in results as well as variation in the physiological parameters estimated exist between many of these due to the differing underlying physiological assumptions in the models used. For these techniques to be useful in widespread application sufficient diagnostic or prognostic accuracy must be proven and the techniques must be robust enough to be applied in a routine clinical setting. The choice of the optimal method for this remains an open question and may depend on the clinical questions that are being addressed as well as the physiological status of the tissue and quality of the acquired data.

4.3.2.2 Non-linear response of signal to contrast agent concentration

As has been described above the DCE-MRI method relies on sampling concentrations of the contrast agent repeatedly with a high temporal resolution. This is done indirectly through serial measurement of the MRI signal intensity. Over a limited range of concentrations the signal response to contrast agent concentration is approximately linear, and such assumptions of linearity have been used in some studies (for example the study by Pereira *et al* described previously [93]). However, to make such assumptions use of a low contrast agent dose is required and this can be problematic as the signal to noise ratio of the measured curves is reduced. At higher concentrations the signal response becomes sub-linear, and eventually saturates as the longitudinal recovery of magnetisation becomes sufficiently fast to be effectively complete between preparation and image readout pulses. At high concentrations signal intensity

may decrease due to the T_2^* shortening effect of the contrast agent. As the contrast agent concentration range in the left ventricular blood is much higher than that in the myocardium if the assumption of signal linearity is made for a standard DCE-MRI protocol a compromise must be made between the extent of the validity of that assumption (which becomes less valid at higher doses, and affects the accuracy of derived parameters) and the contrast to noise ratio (which is poorer at low dose, and limits precision in quantification).

Model based correction

Signal non-linearity can be corrected for by using a mathematical model to describe signal intensity for the imaging sequence used and either assumed or measured additional data to constrain this model. However this relies on the relationship being monotonic (i.e. the contrast agent concentration being below that at which peak signal is achieved) and for the signal response to be sufficiently strong so that noise in the signal data does not lead to excessive errors in the conversion process. Use of either T_1 measurements [44, 101] or signal from a proton density weighted series [102] acquired pre-contrast have been proposed as data that can be used alongside baseline signal from the DCE-MRI series for this process. In this approach the signal model is determined entirely by pre-contrast data and then used to convert signal data across the full range sampled, from baseline to the peak of the AIF. Consequently inaccuracies in the conversion process could be introduced by any bias in the pre-contrast data (either the baseline DCE-MRI signal or the additional data) or limitations of the signal model equation.

The requirement to be in a regime of adequate contrast to noise ratio and below the levels of concentration that lead to signal saturation are complicated by the fact that a wide range of concentrations need to be measured, with considerably higher peak concentration in the blood pool (i.e. the peak of the AIF) compared to the peak concentration in the myocardium. Consequently dual-sampling techniques have been proposed to sample the AIF and myocardial data separately as discussed below.

Dual-sampling methods

Two such approaches to sampling AIF and myocardial data independently have been proposed. The dual-bolus technique (assessed in a canine model in 2004 [103] and later in humans [104]) employs administration of two injections of contrast agent. The first is a small dose used to measure the AIF, and the second a larger dose to measure the myocardial curve. This successfully allowed acquisition of an AIF in the approximately linear range while also acquiring a tissue response curve with sufficient signal to noise ratio. For analysis the measured curves are scaled by the ratio of the doses used prior to quantitative analysis. Similarly Köstler *et al* [105] observed in clinical studies that increasing the dose from 3-12ml of Gd-DTPA in a single bolus experiment led to increasing estimates of MBF. However when the myocardial data was taken from the varying dose studies but the AIF data from the 3ml dose study this trend was not observed. Furthermore, using a lower dose of 1ml for the AIF, in combination with an 8 or 12ml dose for myocardial data, led to reduced variability in their MBF estimates. While the benefit of this technique has been demonstrated for perfusion quantification using first-pass data, for example in a study demonstrating improved diagnostic performance compared to single-bolus DCE-MRI for the detection of significant coronary artery disease [106], its application to ECV quantification has not yet been studied. The work of Hsu *et al* [107] demonstrated that perfusion quantification using the dual-bolus method may potentially be improved by performing non-linearity correction of myocardial signal intensity data. Results from studies using two different saturation delay times (in order to give differing degrees of signal saturation) with a dual-bolus strategy employed were compared and differences in results demonstrated, indicating that despite the dual-bolus approach signal non-linearity effects were still present.

The requirement for two boluses to be injected introduces procedural complexity, including preparation and injection of the additional reduced volume or diluted dose. With current injector pump technology this typically requires staff presence within the scan room during scanning to perform. While future hardware changes to injector pumps may simplify this process the dual-bolus technique is currently cumbersome and single bolus techniques are thus preferable for ease of clinical implementation.

An alternative method utilises a single bolus administration, but a dual acquisition sequence. In this method images with two sets of acquisition parameters are acquired at each time point, one a lower spatial resolution image with lower T_1 weighting than the other. The first exhibits a lower degree of signal non-linearity across the contrast agent concentration range expected in the blood pool and so is suited to measurement of the AIF. As only an average signal from a relatively large volume (typically the left ventricular blood pool) is required, a low spatial resolution can be used to minimise acquisition duration. The higher resolution, more T_1 weighted sequence is more typical of a conventional myocardial DCE acquisition and is used to measure the myocardial curve. This was originally proposed by Gatehouse *et al* in 2004 [108] in a study in which a separate acquisition was performed with a short saturation time to capture the data for the AIF. The results were compared to a dual-bolus acquisition and a significant bias in myocardial perfusion reserve (MPR) measures between the methods was observed (11% overestimation by the dual-sequence approach compared to the dual-bolus method). This was unexplained in the paper, but may be explained by the findings of Hsu *et al* [107] described above, as non-linearity correction of the myocardial signal data was not performed in this study and so MBF may have been underestimated by the dual-bolus strategy with more severe underestimation expected under stress conditions. In the initial dual-sequence study only relative blood flow (MPR) was reported. In order to perform absolute quantification of MBF it is necessary not only to sufficiently limit the effect of signal non-linearity in both the myocardial signal data and the AIF, but also to account for the differential T_1 weightings between the sequences. Following further optimisation of the dual-sequence a study by Sánchez-González *et al* [109] demonstrated both good correlation (R^2=0.92) and low bias between estimates of absolute MBF using the dual-sequence approach and dual-bolus methods. To account for the different T_1 weighting in the acquisitions for the former signal intensity data were converted into contrast agent concentration data using a model-based approach constrained by a measurement of native T_1 using MOLLI T_1 mapping.

The dual-sequence technique is more appealing than dual-bolus methods as the same bolus is used, so variations in contrast agent administration, dispersion or distribution are not a concern. However it is limited to providing

relative estimates of physiological parameters unless combined with a model-based correction for the differential sensitivity of the two sequences. In terms of clinical practice the technique is thus also favourable as only a single injection is required, unlike the dual bolus technique. The technique was later refined, firstly by Kim *et al* [110] who developed a multi-slice variant to allow increased anatomical coverage, and later by Kholmovski *et al* [111] who modified the technique to use data from the same acquisition for the two image sets. In the latter a radial k-space sampling scheme was employed and a sub-set (one quarter of the 96 acquired projection) with the shortest effective saturation time were used to reconstruct low resolution images for the AIF, while the full data set was used to reconstruct higher, more T_1 weighted images to characterise the myocardial response. By using the same acquisition for both data sets the time penalty incurred by including a second acquisition is circumvented. This idea has been extended by utilising highly-constrained back projection reconstruction techniques with a sliding window by Chen *et al* [112] and Ge *et al* [113], further shortening the temporal footprint of the AIF acquisition.

While saturation effects in the AIF and methods to compensate for this have been in the research domain for the past decade, a consensus on the optimal strategy has yet to be reached. Although the techniques have been applied in research centres a method that is practically straightforward and widely available on commercial scanners will be required to allow widespread clinical adoption. Furthermore the assessment of these methods has focussed on perfusion quantification to date, and further studies will be required to evaluate their applicability in assessment additional parameters such as ECV.

4.3.3 Contrast equilibrium ECV imaging

As described previously, measurement of the partition coefficient, λ, of extracellular contrast agents along with measurement of the haematocrit can allow calculation of the distribution volume of the agent. This volume comprises the interstitial space and the plasma space within the capillary bed of the tissue of interest. As described in equation 2-30 the longitudinal relaxation rate, R_1, is linearly related to the contrast agent concentration, therefore measurement of the change in R_1 (ΔR_1) between pre- and post-administration in both the blood and myocardium can allow calculation of the partition coefficient, as long as the

post-contrast measurement is performed once contrast equilibrium is achieved. According to equation 2-49, the ECV can be straightforwardly calculated from this, if the haematocrit is known. This forms the basis of contrast equilibrium ECV imaging. Contrary to DCE-MRI this technique uses data acquired before and at a delayed time after contrast agent administration and uses a few (typically two) time points, rather than imaging at high temporal resolution during contrast agent administration (see Figure 3-1).

Arheden *et al* [114] applied this method *in vivo* in a rat model of myocardial infarction in 1999. In this study the distribution volume of Gd-DTPA measured by pre and post-contrast T_1 measurements (inversion-recovery echo-planar imaging, IR-EPI) was compared to radioisotope (^{99m}Tc-DTPA) measurements in both normal myocardium (remote in infarcted mice and myocardium in a control group) and reperfused infarcted myocardium. To determine the effect of post-contrast T_1 measurement time on distribution volume estimates the post-contrast measurement was repeated at 4, 14 and 29 minutes after contrast agent administration. The authors commented on the fact that one fundamental difference in these techniques is that the radioisotope experiment involves a direct measurement of tracer content whereas contrast enhanced MRI is inherently an indirect technique as it is the effect of the tracer on the local water molecules that is measured. Both techniques demonstrated a marked increase in infarcted myocardium compared to healthy myocardium (interpreted as the tracer gaining access to the intracellular space as the cardiomyocyte membrane is damaged). Agreement between the methods was excellent for the infarcted tissue but distribution volume fractions measured by MRI were significantly lower than radioisotope counterparts for both myocardium in the control rats and myocardium remote to infarction. Comparing post-contrast T_1 measurements at different delays following Gd-DTPA administration showed no temporal dependence, suggesting that contrast equilibrium in rats was achieved within 4 minutes of contrast agent administration in both healthy and infarcted myocardium.

A further study by Pereira *et al* [93] used signal intensity ratios as a substitute for ΔR_1 ratios in a canine model study of the variation of λ with time following reperfusion. This approach assumes a linear relationship between contrast

agent concentration and signal intensity, which is valid for low concentrations, as noted by the authors. At higher concentrations (dependent on pulse sequence parameters) the relationship deviates from a linear one and saturates to a maximal signal intensity. Consequently care must be taken with such an approach to ensure that measurements are performed in the linear range of contrast agent concentrations.

The first human clinical study applying contrast equilibrium techniques compared λ derived from ΔR_1 measurements (using a Look-Locker sequence) between acute and chronic myocardial infarction [92]. This study was the first to assess the clinical value of MRI derived partition coefficients to identify myocardial segments with acute or chronic ischaemic disease, and found high sensitivity and specificity for both when a threshold of 20% elevation above remote myocardium was applied. The study also looked at the regional variation of λ across the myocardium of healthy subjects and found that λ was generally uniform (with a non-significant trend for increased values towards the apex) but with significantly higher values measured in the septum. One explanation proposed for this was an increased tendency for partial volume effects with inclusion of mixed myocardium/blood pool voxels in the analysis. This highlights the importance of careful contouring and image registration, and the need for sufficient spatial resolution, when applying this technique.

In the decade following these early demonstrations of the feasibility and clinical value of the technique research in the field concentrated on three main strands, which form the basis of the following sections. Studies were performed to assess the approach to equilibrium and the impact of the contrast agent administration scheme, techniques were developed and assessed for the accurate measurement of T_1 required for measuring λ, and further clinical studies were performed assessing the technique within the context of myocardial infarction, in a range of other cardiomyopathies and in assessing variation across the healthy population (e.g. with age or gender).

4.3.3.1 Contrast agent administration

As described previously the contrast equilibrium method of measuring λ and ECV is reliant on the post-contrast measurement being performed once

equilibrium is obtained between the plasma and extravascular-extracellular space, i.e. the concentrations of contrast agent in the two compartments are equal. This can be achieved through a long infusion of the contrast agent. However, for the technique to find routine application it is necessary that equilibrium can be achieved using a method that is acceptable in clinical practice.

Simulations performed in the early development of the contrast equilibrium method showed that it could take longer than 1 hour of infusion to reach 90% of equilibrium for tissues with high λ and low perfusion [83] although previous work had shown that this can be accelerated through use of a bolus injection prior to infusion [79]. The former study investigated optimisation of this protocol and found that, with an optimal ratio of bolus dose to infusion dose rate and no intervening gap, 90% equilibrium could be obtained in most tissue states within 15 minutes and that 1 hour would be sufficient for even tissue with very low perfusion and highly increased distribution volumes.

A later study by Thornhill *et al* [115] assessed the feasibility of omitting the lengthy infusion and measuring λ (in the setting of myocardial infarction) after a single bolus. The study recruited 9 patients and for each performed measurements at 3-4 weeks and 6 months post-infarction, in each case performing the experiment with both a bolus and infusion strategy and using relative signal intensity ratios rather than ΔR_1 ratios as per the study by Pereira *et al* described previously in this review [93]. For the bolus strategy images were acquired serially at 3-5 minute intervals for up to 35 minutes after bolus injection. The study showed that for a delay time ≥ 4 minutes there was reasonable concordance (concordance coefficient > 0.83) between the two methods for both normal and infarcted myocardium at both time points. Concordance was significantly lower for the shortest delay time used (2 minutes). This work suggested that, with a suitable delay, a bolus injection of Gd-DTPA could therefore be used to determine λ without the requirement for a lengthy infusion.

The comparison of bolus and slow infusion contrast agent administration strategies was revisited in 2011 by Schelbert *et al* [116]. In this healthy volunteer study ΔR_1 was calculated using a MOLLI sequence (described later in

this review) rather than relying on the assumption of linearity between signal intensity and contrast agent concentration. This study also built upon the previous study by including subject specific haematocrit measurements to allow calculation of ECV from λ. Other differences included the use of a different (but still non-ionic, extracellular) contrast agent, gadoteridol. The study did not evaluate the early time points assessed by Thornhill *et al* [115] but acquired post-contrast T_1 measurements between 12 and 50 minutes post-injection. Results showed that while post-contrast T_1 of both blood and myocardium increase with time after bolus injection (due to renal clearance of the contrast agent), λ, and ECV, were largely stable. There was a very small but statistically significant trend identified with the bolus strategy, with measured ECV increasing by 0.6% over 30 minutes, but this change is less than the size of the 95% confidence intervals on the individual ECV measurements. This suggests that in healthy volunteers with normal renal function the glomerular clearance is sufficiently slow in comparison to exchange across the myocardial capillary walls that it does not have a detrimental effect on the ability to achieve contrast equilibrium. For patients with reduced renal function any effect would be expected to be lower, so it can be assumed that this would not produce problems for patients with renal impairment (although this was not tested in this study). However the result was reported with the caveat that for the specific case of patients with systemic amyloidosis rapid extra-renal clearance of Gd based contrast agents from the blood pool may impact the approach to equilibrium.

More recently Salerno *et al* [117] built upon the work of Schelbert *et al* and Thornhill *et al* by performing a healthy volunteer study which incorporated a bolus and infusion strategy, although with a delay in between of 15 minutes which allowed collection of data for assessment of the bolus injection method. Two key results were presented as a result of this. Firstly, the methods showed good agreement, supporting the results of the previous studies. Secondly, regression of post-bolus data points at 5, 10 and 15 minutes showed a linear relationship, suggesting that equilibrium was achieved within 5 minutes for this sample. This is in concordance with the results of Thornhill *et al* who reported that equilibrium was achieved in 4 minutes for normal and infarcted myocardium.

In clinical practice it is common to administer two boluses of contrast agent in order to perform perfusion CMR under both pharmacologically induced stress and resting conditions. McDiarmid *et al*[1] [8] compared ECV results obtained from T_1 maps acquired before and after a split dose contrast agent administration, as would be used in stress/rest perfusion studies, to those from single bolus studies. The study included 10 healthy volunteers as well as 4 ischaemic heart disease patients and 1 hypertrophic cardiomyopathy patient, all of whom were scanned at 3 Tesla with T_1 maps acquired before contrast agent administration and after a total administration of 0.15 mmol/kg Gd-BT-DO3A gadobutrol (Gadovist), either injected as a single bolus or two 0.075 mmol/kg boluses separated by 12 minutes. Post-contrast T_1 maps were acquired 15 minutes after either the single or the latter of the two split dose administrations. Each subject was scanned with the single bolus administration once and the split dose administration either once (patients) or twice (volunteers), with each study performed on separate days. The results demonstrated no significant bias between administration protocols, with similar coefficients of variability whether comparing between protocols (5.04%) or between the two split dose studies for the volunteers (5.67%). This study thus provides evidence to support the compatibility of contrast equilibrium based ECV estimation with a stress/rest perfusion protocol and also demonstrates good reproducibility of the technique.

The studies detailed above have demonstrated that a single or split dose bolus-injection strategy can be applied to measurements of λ (or ECV) by MRI. Across the studies this has been demonstrated for both healthy and infarcted myocardium and has thus been tested at both extremes of the expected range of ECV values.

4.3.3.2 Contrast agent choice

The majority of studies have employed solutions of the non-ionic extravascular Gd based contrast agent Gd-DTPA. A study by Kawel *et al* [118] compared results of T_1 mapping (MOLLI) and ECV calculation using Gd-DTPA and an ionic contrast agent, gadobenate dimeglumine (Gd-BOPTA). In this study post-contrast myocardial T_1 was systematically shorter when Gd-DTPA was used

[1] The author of this thesis is a co-author on this paper, but the work contained within the paper does not form part of this thesis.

compared to Gd-BOPTA, while there was no difference in blood T_1. This led to a small but statistically significant difference in ECV (1% higher for Gd-DTPA). The authors suggested that this could be due to the fact that Gd-BOPTA binds to albumin, which is found mainly in the blood, a process which could lead to differences between the distribution characteristics of the two agents. A secondary outcome of this study was identification of a trend for measured ECV to increase with the delay between injection and post-contrast T_1 mapping, as previously seen in the study by Schelbert *et al* [116] described earlier. Across the range studied (5 – 45 min) ECV increased by 3%. Additionally other contrast agents have been used in contrast equilibrium studies such as gadodiamide [119] or gadobutrol [8], with results comparable to other studies using different contrast agents but without direct comparison.

4.3.3.3 Additional confounding factors

A further study by Kawel *et al* [120] assessed a range of factors that may confound T_1 and ECV measurements. It is well established that T_1 demonstrates a field strength dependence and so pre- and post-contrast T_1 of both blood and myocardium would be expected to be longer at 3 T than 1.5 T. However, as ECV is a physiological parameter this would not be expected to vary with magnetic field strength. This was demonstrated in the study, in which 31 healthy volunteers (all aged under 40) were scanned once at 1.5 T (using Gd-DTPA) and twice at 3 T (using Gd-DTPA in one study and Gd-BOPTA in the other). Native T_1 of blood and myocardium was 31% and 28% higher respectively at 3 T compared to 1.5 T. T_1 remained higher post-contrast but to a lesser extent. Importantly differences in ECV were not significant.

In addition to comparing field strengths this study also performed measurements at two cardiac phases (systole and diastole) and compared the regional variation of ECV. T_1 was shorter at diastole than systole both pre- and post-contrast. The relative difference was larger post-contrast leading to a statistically significant difference in ECV between the cardiac phases, with systolic ECV being 0.01 lower than diastolic ECV on average. In assessing regional variation it was seen that septal myocardial ECV was significantly higher than non-septal myocardial ECV.

The results of this study and the comparison of Gd-DTPA to Gd-BOPTA demonstrate that a variety of factors can confound ECV measurement, even within the same patient. In comparing ECV results care should be taken to ensure that consideration is made of differences in protocol, contrast agent, cardiac phase and myocardial region. Differences arising from some of these factors are due to imperfections in the measurement technique (as the measurement technique does not change the ECV). Others (such as cardiac phase or myocardial region) could be due to genuine physiological differences, measurement technique imperfections, or a combination of both. For example T_1 and ECV could genuinely change throughout the cardiac cycle due to variations in the blood volume, or the apparent differences could be artefactual and arise due to varying degrees of impact of partial volume averaging with extra-myocardial tissue due to changes in the thickness of the myocardium.

For contrast equilibrium methods a current area of research relates to the rate of water exchange between the interstitium and intra-cellular space. Koenig *et al* [47] demonstrated that in the blood Gd-DTPA exists in the plasma volume but does not enter the blood cells. However, as the exchange of water between the intra- and extracellular spaces in the blood pool is rapid in comparison to the T_1 times, the overall longitudinal relaxation rate (R_1) can be modelled as the weighted average of that of the water, intra- and extracellular proteins and the exogenous contrast agents. This results in the fact that a single exponential function adequately describes the evolution of the longitudinal magnetisation of blood. In most contrast equilibrium studies to date a similar assumption has been made for the myocardium, and a single T_1 value measured for the tissue has been used in analysis. However evidence from Judd *et al* [121, 122] and Donahue *et al [40]* has shown that this may not be the case for water exchange between plasma and the interstitium and between the interstitium and intra-cellular spaces. In the first study by Judd *et al* [121] the change in R_1 when a known concentration of contrast agents was introduced to isolated canine hearts was observed to be less than expected under the assumption of fast water exchange, and this phenomenon and a subsequent underestimation of myocardial perfusion was also observed in a follow-up study in isolated rabbit hearts [122]. Donahue *et al* [40] compared measured T_1 changes in response to contrast agent concentrations in excised rat hearts to simulations under a range

of assumptions including fast and slow water exchange between the different regions. They concluded that the exchange between interstitial and intra-cellular regions could be considered fast while exchange between interstitium and intra-vascular plasma could not.

Coelho-Filho *et al* [43] suggested that the assumption of fast water exchange where it is not valid may lead to inaccuracy in ECV estimation. In the animal part of their study T_1 was measured at least 6 minutes after successive contrast agent administrations, until a cumulative dose of 0.5 mmol/kg was achieved. Under the fast exchange assumption a linear relation between myocardial and blood R_1 would be expected. However the results demonstrated a sub-linear relationship, consistent with the two-space slow exchange (2SX) model employed (where the two spaces are the intra and extracellular components of the myocardium). This was found to be the case in both control mice and those with fibrosis induced through Nω-nitro-L-arginine-metyl-ester administration. ECV by MRI was compared to histological connective tissue volume fraction measurements. Use of the 2SX model significantly improved correlation of ECV values with histological results compared to the fast exchange (FX) model. For the latter model significant underestimation was observed. In this study the two models were also compared in patients with hypertension and healthy volunteers where similar deviations from the linear relation predicted by the FX assumption were observed. This study suggests that the FX assumption in the myocardium is not necessarily valid for clinical doses of contrast agent, and so for accurate quantification of ECV the effect should be considered. This could complicate data acquisition and analysis, as multiple data points are required to allow use of the 2SX model, but could potentially lead to an increased sensitivity for diffuse fibrosis.

4.4 T_1 measurement techniques

In order to calculated ECV or λ maps using contrast equilibrium MRI it is usually necessary to acquire T_1 maps of the heart (unless the relative signal intensity method used by, for example, Pereira *et al* is adopted [93]). Cardiac MRI is complicated by the rapid motion of the heart throughout the cardiac cycle and the slower movement associated with breathing. To calculate T_1 maps it is necessary to collect multiple images with differing contrast weighting to allow

estimation of T_1 on a voxel-by-voxel basis. This is typically achieved through variation of a single scan parameter, and the majority of research into cardiac T_1 mapping involves the variation of the delay following magnetisation preparation (either saturation or inversion). Alternatively ECV can be calculated for specific regions of myocardium, for which voxel-by-voxel T_1 maps are not required but instead T_1 can be calculated for user-defined regions. This approach circumvents some of the difficulties associated with cardiac motion but does not allow as full an assessment of heterogeneity across myocardium.

4.4.1 Multi-point inversion or saturation recovery techniques

In early work developing cardiac DCE-MRI techniques by Larsson *et al* [82], pre-contrast T_1 was measured using an ECG triggered IR FLASH sequence acquired with 12 different TI values. By varying the trigger time the images were acquired at the same cardiac phase (mid-diastole). Images were acquired every third RR interval resulting in a total imaging time that is too long for acquisition within a breath-hold in the clinical setting. Consequently T_1 was not calculated on a voxel-by-voxel basis, but for a small region of interest that was shifted to account for respiratory motion between image acquisitions. Further limitations of this sequence (acknowledged by the authors) were the low dynamic range and susceptibility to signal saturation effects, the latter being cited as a potential cause of underestimation of T_1 seen by the authors in their phantom validation. Signal saturation effects arise as the readout pulses and spoiler gradients employed in this sequence perturb the recovery of longitudinal magnetisation. The authors postulated, and demonstrated through phantom experiments, that the effect of saturation on T_1 measurement errors could be reduced through positioning of the acquisition of central portions of k-space (which dominate image contrast) towards the start of the readout train. Additionally the three heart-beat recovery period between inversion pulses is not sufficient to allow full recovery of longitudinal magnetisation in native myocardium or blood, and so incomplete recovery is likely a significant contributor to the underestimation of T_1 observed in phantom experiments in this study. The authors did not identify this effect separately to the inherent saturation effects of a spoiled readout such as that employed by the FLASH sequence, and so this warrants further attention.

Use of a standard multi-point IR experiment, such as that described above, while allowing sufficient recovery between inversion pulses is not compatible with the requirement for imaging within a breath-hold in the clinical setting. The remainder of this section of this review focuses on ECG triggered sequences that exploit methods to allow them to be performed within a breath-hold, and are therefore suited to cardiac T_1 mapping as opposed to purely segmental or region-based analysis.

A study [123] including T_1 measurement to investigate the effect of pharmacological stress on perfusion also utilised an ECG triggered FLASH sequence to measure baseline T_1. However, for this a saturation preparation pulse was employed rather than an inversion pulse. In saturation recovery (SR) sequences the preparation pulses null the longitudinal magnetisation rather than negating it. Consequently the recovery periods required for IR methods are not necessary if saturation is ideal. This allows imaging to be performed in successive RR intervals and so shorter (breath-hold compatible) scan times can be achieved. In this approach nine images were acquired (saturation recovery time, TS, from 100-1400 ms). For the longer TS acquisitions it was necessary for the saturation pulse and readout module to be in consecutive RR intervals, whereas for short TS the two components were applied in a single RR interval. Consequently a single-slice T_1 map could be generated within a breath-hold. In conventional imaging linear k-space ordering is used, in which the gradient moment is incremented in a step-wise process so that the outer lines of k-space (containing the highest spatial frequencies) are acquired first and last and the central lines are acquired in the middle of the pulse train. In this sequence partial centric k-space reordering (in which the order of the application of the gradient moments is changed so that the central, low-spatial frequency, lines of k-space are acquired earlier) was used. This reduces saturation effects from the readout train as the number of RF pulses applied prior to acquisition of the contrast dominating central lines of k-space is reduced

A single breath-hold saturation recovery (SR) myocardial T_1 mapping technique capable of acquiring three slices was proposed later by Higgins *et al* [124], motivated by a requirement to perform multi-slice T_1 mapping during the first pass of a contrast agent. In the method (dubbed Short Acquisition Period T1,

SAP-T1) five images are acquired per slice (in successive RR intervals) using a single-shot spoiled gradient echo sequence (TurboFLASH). The nulling of longitudinal magnetisation at each preparation pulse, and use of an individual preparation pulse for each image, results in a sequence for which accuracy should have no heart rate dependence. However, as for all SR based methods, the maximal dynamic range is reduced as the longitudinal magnetisation can only vary between zero and its equilibrium value (M_{eq}), whereas in IR experiments the magnetisation can vary between $-M_{eq}$ and M_{eq}.

In SAP-T_1 the first image is acquired with no saturation pulse (equivalent to infinite TS) and later images are acquired with TS values of 60, 90, 120 and 160 ms (the authors refer to this parameter as preparation pulse delay, PD, but for consistency with the above study TS is used in this review). All images for a given slice are acquired at the same cardiac phase, although the authors propose that the trigger delay can be adjusted on a per-slice basis to allow T_1 maps to be generated corresponding in position and phase to a perfusion sequence. The short TS values allow the preparation pulse and image readout to be performed in the same RR interval for all images (unlike the previous study). This, and the reduced number of TS values used, allows a single slice to be acquired in 5 heart beats, and hence 3 slices to be acquired in a breath-hold. While SR methods do not suffer from effects of incomplete recovery between preparation pulses the longitudinal magnetisation evolution is still perturbed by the readout pulses. Simulations of the sequence used by the authors demonstrated that by including an offset time as free parameter in the fitting algorithm T_1 estimations can be improved, although a theoretical justification was not provided for this approach.

The proposed T_1 measurement and calculation method was validated by measurements of vials of Gd-DTPA solution with T_1 values covering the physiologically expected range (85 to 1716 ms). Multi-point IR spin-echo (SE) relaxometry was used as a reference standard, with a long repetition time (10 s) to avoid saturation effects. Results demonstrated a systematic overestimation of T_1 in comparison to IR-SE. The maximal error observed across all samples was 14%.

A major limitation of this method *in vivo* however is the limitation of TS to very short values (up to 160 ms). For tissues with short T_1 (e.g. post-contrast administration) there is sufficient recovery of longitudinal magnetisation to allow acquisition of images with sufficient signal-to-noise ratio (SNR) to generate T_1 maps. However, for native blood and myocardium SNR is severely impaired in all but the image with no saturation preparation. Consequently, while the method is applicable to the purpose intended by the authors, it cannot be extended to be applied to pre-contrast T_1 mapping.

4.4.2 Inversion recovery Look-Locker based techniques

A later clinical study [92] by Flacke *et al* used a Look-Locker (LL) [125, 126] approach to perform pre and post-contrast T_1 mapping. In this method a train of images is acquired following a single inversion pulse to reduce image acquisition times. For this study 50 images were acquired using an EPI readout for each of four short-axis slices during free-breathing. As images were acquired at different cardiac phases and with respiratory motion, T_1 maps could not be readily generated on a voxel-by-voxel basis. Instead the authors calculated T_1 on a segmental basis (8 circumferential sectors). In this method, as with all LL methods, the signal intensity measured at later time points is not equal to that which would be acquired at the same time point in a conventional IR experiment. This is due to the impact of the preceding readout pulses on the evolution of the longitudinal magnetisation. Deichmann and Haase [127] described this phenomenon, and the means to allow calculation of the true T_1 from a series of spoiled gradient echo images acquired consecutively and with a small readout flip angle. In this method a three parameter model (equation 4-1) is fitted to the recorded signal intensities to estimate A, B and an apparent longitudinal recovery time, T_1^*. This value differs from the true T_1 value as the longitudinal recovery is disturbed by the application of the readout pulses, but T_1 can be calculated from the estimated parameters (equation 4-2).

Equation 4-1

$$M(t) = A - Bexp(-t/T_1^*)$$

Equation 4-2

$$T_1 = T_1^*(B/A - 1)$$

4.4.2.1 Modified Look-Locker inversion recovery (MOLLI)

A modification to this approach (Modified Look-Locker Inversion Recovery, MOLLI) which allows high resolution T_1 mapping of the heart was proposed by Messroghli *et al* [7]. In this method data is acquired only during a specified cardiac phase and following multiple inversion pulses. The timing of image acquisition in relation to an ECG trace and longitudinal magnetisation recovery for the imaging that is performed following a single inversion is shown in Figure 4-1 and the merging of data from multiple inversion epochs in Figure 4-2 below.

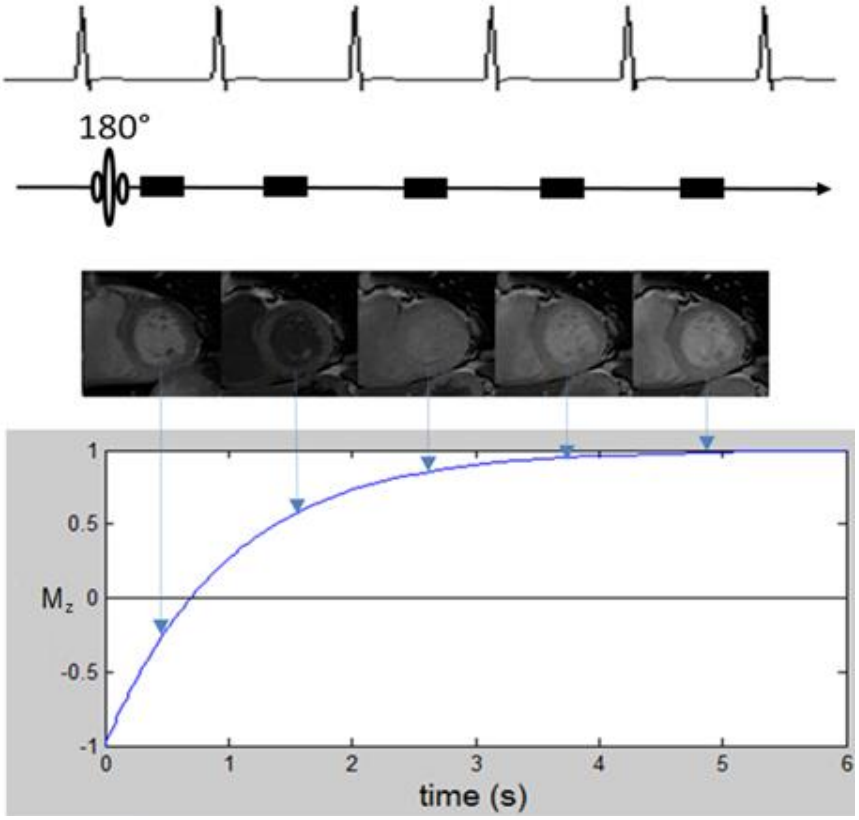

Figure 4-1 – Data collection for the MOLLI technique (for a single inversion). Images are acquired at the same cardiac phase and have differing contrast due to recovery of longitudinal magnetisation. (Figure adapted from the Pocket Guide on Cardiovascular Magnetic Resonance Physics for Clinicians [19])

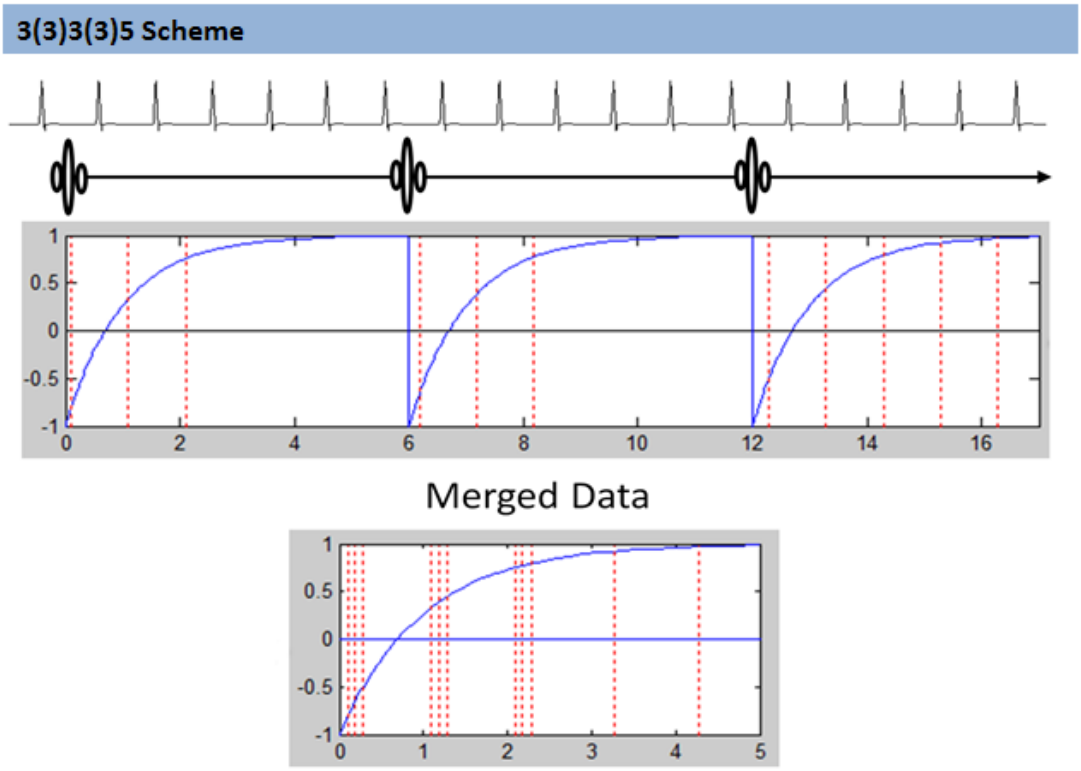

Figure 4-2 – Merging of data from multiple inversions (three in this case) in MOLLI. (Figure adapted from the Pocket Guide on Cardiovascular Magnetic Resonance Physics for Clinicians [19])

For the original proposed scheme an initial image acquisition is performed with data collected at an effective TI of 100 ms, and then at the same cardiac phase in the subsequent two RR intervals. Three images with TI values of 100, $100+T_{RR}$ and $100+2xT_{RR}$ are thus collected, where T_{RR} is the RR interval of cardiac cycle (which will in practice exhibit some variability). Following a rest period of at least 4 seconds (to allow recovery of longitudinal magnetisation) another acquisition is performed to acquire a further three images with the shortest TI incremented to 200 ms. The trigger delay (TD) is adjusted to ensure the data is collected at the same cardiac phase as that in the first epoch. Finally, following a further rest period, a final acquisition is performed, this time with a shortest TI of 350 ms and five images acquired. This scheme is referred to as 3(4s)3(4s)5 in the nomenclature adopted for this thesis, referring to the number of readouts in each epoch with the recovery period defined in parentheses.

In total image data for 11 TI values was acquired in a period of 15.1 to 18.2 s (in a single breath-hold) for the volunteers in this study. Inversion times range from

100 ms to over 5 RR intervals providing sufficient data to characterise the longitudinal recovery of magnetisation for most biological tissues. This data is collated to provide a dataset with signal intensity values at 11 TI values before fitting to an appropriate equation in order to calculate T_1. This approach circumvents the problems of the low number of data points that can be acquired within a breath-hold using a conventional IR approach, and of the impact of cardiac motion which prevents data collected using a conventional LL experiment to perform T_1 mapping on a voxel-by-voxel basis. The readout method adopted for this protocol was a balanced steady-state free-precession (bSSFP) sequence, which minimises the effect of the readout train on the recovery of the longitudinal magnetisation recovery [128] as transverse magnetisation is not spoiled following readout.

The authors propose using the same fitting procedure as per Deichmann and Haase above [127] where an initial three-parameter fit yields T_1^* from which T_1 is then calculated. However this method was originally derived for a low flip angle spoiled gradient echo sequence, as opposed to a balanced sequence employed in the MOLLI sequence. Furthermore the correction was derived for a continuous train of readouts, as opposed to the selective approach where there are periods of free recovery adopted in MOLLI, and so it is not clear if its use in MOLLI fitting is justified theoretically.

Phantom studies performed in this study demonstrated a systematic underestimation of T_1, the magnitude of which is dependent on both heart rate (which affects the sampling times and recovery durations) and T_1. For moderate to long T_1 values (above around 500 ms) errors were seen to increase with increasing T_1, reaching 10% for T_1 of 1196 ms and a simulated heart rate of 40 beats per minute (bpm). A more pronounced error (up to 22%) was seen for the shortest T_1 tested (60 ms), although this is lower than would be seen *in vivo*. In the *in vivo* part of the study healthy myocardium in two volunteers and remote myocardium in a myocardial infarction patient was reported at around 1000 ms, and so within the range of T_1 values validated in the phantom experiment. However infarcted myocardium and blood both had T_1 values measured by MOLLI above the validated range and so the uncertainty for these tissues is

unclear. Underestimation is also likely to be more of a problem at higher field strengths where T_1 would be longer.

Following the original paper setting out the methods and phantom validation of MOLLI, a reproducibility study was performed in a sample of healthy volunteers [129]. MOLLI was performed in the volunteers for a single mid-cavity short axis slice in an initial study, followed by a second study on the same day with MOLLI data acquired for three slices at baseline and at several time-points (2-20 minutes, mid-cavity only) following a dual bolus injection of Gd-DTPA (0.05 mmol/kg followed one minute later by 0.1 mmol/kg). Eight randomly selected subjects returned for baseline and post-contrast mid-cavity T_1 mapping on a later day. Extraction of data was performed independently by two experienced cardiac MRI readers. Consequently both inter- and intra-subject and inter- and intra-observer reproducibility could be assessed in this study, all of which were reported as being favourable. Additionally, visually assessed image quality was scored as good in 93% of segments analysed with the remainder suffering some extent of artefact (predominantly motion induced). Finally results were compared to *in vivo* studies described previously in this review. Results were in agreement with the LL method [92] but lower than the SR TurboFLASH method [123]. This is consistent with the observation of systematic underestimation of T_1 made in the original MOLLI paper [7]. Assessment of the heart-rate dependence (due to effects described in the previous study) for the reproducibility study data demonstrated a linear dependence on heart-rate for T_1 values typical of baseline studies. This dependence was not seen for shorter T_1 values (post-contrast). Consequently the authors proposed and utilised a linear heart rate correction for baseline studies only. This was seen to reduce variability in baseline myocardial T_1 across their sample, but further evaluation would be needed to establish suitable correction methods for longer T_1 values (e.g. blood or myocardium at higher field strengths).

After the demonstration of reproducibility and reliability of MOLLI further work was undertaken to optimise the parameters of the pulse sequence [130]. MOLLI was performed in a phantom study with iterative changes to four key parameters (flip angle, minimum TI, TI increment and recovery period duration (number of heart cycles)), altered successively to optimise accuracy. The

optimal sequence from the phantom work was then applied to 20 healthy volunteers pre-contrast and at various times (1 minute to 20 minutes) after administration of 0.15 mmol/kg of Gd-DTPA. The optimised parameters were: flip angle = 35°, minimum TI = 100 ms, TI increment = 80 ms and length of recovery period = 3 cardiac cycles). With the change to a recovery period defined as a fixed number of cardiac cycles this scheme is defined as 3(3)3(3)5. The results of the volunteer study were compared to those from the reproducibility study described above [129]. The results demonstrated comparable mean T_1 values and less variability pre-contrast in comparison to the earlier study, and evidence of heart-rate dependence was no longer present. This suggests that the optimisation procedure had successfully improved some attributes of the protocol, although the results could have been strengthened by direct comparison of the original and optimised protocols in the same volunteer group.

Further evaluation of MOLLI was performed by Nacif *et al* [131], who compared the sequence to a conventional LL protocol (with bSSFP readout) in healthy volunteers. Both sequences were performed pre-contrast and at various time points post-contrast. As a single-examination was performed there was a 1.5 minute offset between the post-contrast times used for the two sequences. The results demonstrated good agreement pre-contrast but a systematic difference post-contrast, with T_1 measured by MOLLI to be approximately 60 ms greater than by LL. With the lack of a gold-standard for myocardial T_1 mapping *in vivo*, and of a direct comparison of these techniques in a phantom study, it is not possible to comment on the relative accuracy of these schemes. However the study did demonstrate a reduced variation in T_1 values as measured by MOLLI in comparison to LL. Consequently they recommended the use of MOLLI in future studies for ECV calculation, and correction of post-contrast T_1 values for retrospective analysis of LL data.

Reference values of native T_1 and ECV were determined at two field strengths (1.5 and 3 T) in an international study of 102 healthy subjects and 113 low-risk subjects, demonstrating the transferability of the technique between centres

[14][1]. In this study narrow variability in native myocardial T_1 was demonstrated, with coefficients of variation of 2.2% at both field strengths.

As discussed above the original MOLLI method uses a balanced gradient echo readout. This can lead to artefacts due to off-resonance effects, particularly at higher field strengths. An alternative method has been proposed in which the same acquisition scheme is used as MOLLI but using a spoiled gradient echo readout [132]. To account for the different readout type a modified fitting procedure, using a Bloch simulation of the sequence, was used. In this study, performed at 3 T, accuracy and precision compared favourably to conventional balanced readout based MOLLI sequences in phantom studies, and off-resonance artefacts were eradicated in volunteers.

Acquisition of data for MOLLI using the optimised scheme (3(3)3(3)5) requires a breath-hold of 17 heart-beats. This is generally achievable for healthy volunteers and for some patients. However patients with pulmonary compromise may not find this possible as maximal breath-hold time is reduced [133]. Consequently work has been completed to develop and evaluate shorter variants of the scheme as discussed below.

Several alternative MOLLI acquisition schemes have been proposed, the most commonly applied of which are discussed in the following paragraphs. A study by Salerno *et al* [117] compared 3(3)3(3)5) MOLLI to two shortened versions (as well as comparing bolus and continuous infusion methods for determining partition coefficients, as discussed earlier in this review). In one the first epoch was removed (3(3)5 MOLLI, 11 heart-beats) and in the second each epoch was shortened by one readout (2(3)2(3)4 MOLLI, 14 heart-beats). The techniques were tested in a phantom study for a range of T_1 values (447 – 1459 ms) at two simulated heart-rates (60 and 100 bpm). For the lower heart-rate maximal errors were 8.4% across all T_1 values and MOLLI variants, with little variation between the sequences. For the higher heart-rate 3(3)3(3)5) and 3(3)5) MOLLI were again comparable, and demonstrated larger underestimation than at lower heart-rate (consistent with previous studies). However large errors (up to 33%)

[1] The author of this thesis is a co-author on this paper, but the work contained within the paper does not form part of this thesis.

were observed for 2(3)2(3)4 MOLLI. Errors were most severe for the longest T_1 values. This is likely due to the reduction in the time between inversions in comparison to conventional MOLLI, which will exacerbate the effect of incomplete recovery of longitudinal magnetisation. In the healthy volunteer element of this study mean blood and myocardium values were comparable both pre- and post-contrast for 3(3)3(3)5 and 3(3)5 MOLLI. The standard deviation was larger for 3(3)5 MOLLI, due to the penalty of increased noise sensitivity incurred by using fewer data points in the fitting process. 2(3)2(3)4 MOLLI demonstrated comparable results post-contrast. However T_1 was lower pre-contrast, reaching statistical significance for blood (mean of 1379 ms compared to 1483 ms for 3(3)3(3)5MOLLI). This is as would be expected from the phantom study. This work has demonstrated that MOLLI can be shortened through the removal of the first epoch without affecting accuracy, although with a reduction in precision. This could prove beneficial for patient groups who struggle or find it impossible to hold their breath for the 17 heart-beat duration of conventional MOLLI.

A similar study [134] compared 11 heart-beat (3(3)5) MOLLI to 17 heart-beat (3(3)3(3)5) MOLLI in both phantoms and volunteers at 3 T (where T_1 of corresponding tissues would be expected to be longer than for the previously described study performed at 1.5 T). The phantom study compared both to an IR-SE reference standard, and results demonstrated the underestimation of longer T_1 values and heart rate sensitivity seen in other MOLLI studies. Similar to the work completed at 1.5 T, 3(3)5 and 3(3)3(3)5 MOLLI showed good agreement, even at long T_1, with no statistically significant bias reported. In the healthy volunteer component of this work agreement was also good between the two MOLLI variants for both blood and myocardium before and at various delays after bolus injection of Gd-DTPA. Consequently there was no significant difference in calculated ECV values. The results also showed no significant variation in calculated ECV from 8.5 minutes to 23.5 minutes post injection (differences were seen at 3.5 and 5 minutes), suggesting that dynamic equilibrium is reached (in healthy myocardium) within this time.

Further modifications to MOLLI schemes have included the use of specified minimum temporal durations for recovery (as in the original MOLLI publication

[7]) or acquisition periods to minimise the dependence of T_1 measurement accuracy on heart rate [135]. At high heart rates the acquisition duration of a conventional (fixed number of cardiac cycles) scheme is reduced, but systematic errors in T_1 estimation may be introduced as the time between inversion pulses becomes too short to allow sufficient recovery of longitudinal magnetisation. Instead if a time interval is specified the overall acquisition duration and time between inversion pulses can be approximately maintained. As the acquisitions are synchronised to the cardiac cycle the duration of each readout or recovery period must be a multiple of the RR interval, and so in practice a minimum time period is specified and the minimum number of cardiac cycles to achieve that is used. For example for a specified 3 second recovery period the number of cardiac cycles would be 3 for heart rates between 40 and 60 bpm but 4 for heart rates between 60 and 80 bpm. This study also introduced the idea of using different schemes for native and contrast-enhanced T_1 mapping. A 4(1s)3(1s)2 scheme is proposed for contrast-enhanced T_1 mapping in order to provide a greater density of data at short inversion times to improve the accuracy and precision of short T_1 value estimates. As the T_1 is short the reduced time between inversion pulses introduced through the inclusion of three inversion recovery epochs and short recovery periods does not lead to inaccuracies. For native T_1 mapping a 5(3s)3 scheme is proposed to increase the time between inversions, while sacrificing the density of sampling of short inversion times, which is less important for estimation of long T_1 values.

4.4.2.2 Shortened MOLLI (ShMOLLI)

Another shortened variant of MOLLI (ShMOLLI) was proposed by Piechnik *et al* in 2010 [136] which employs a 9 heart-beat scheme (5(1)1(1)1), as contrasted to the 3(3)3(3)5 MOLLI scheme in Figure 4-3.

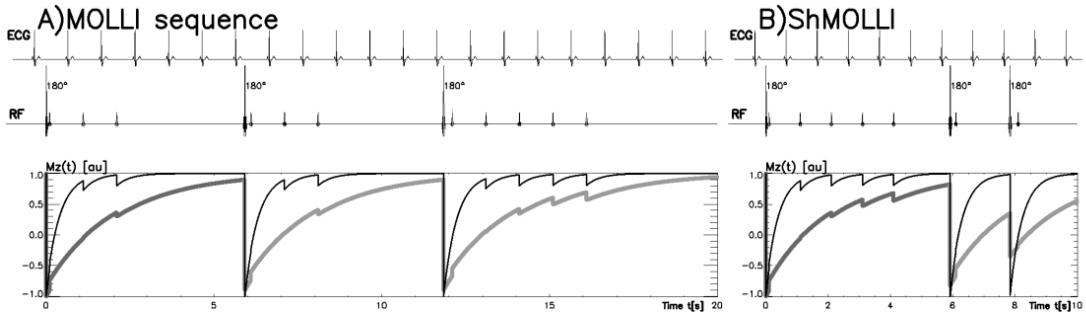

Figure 4-3 – Comparison of MOLLI and ShMOLLI schemes in relation to the ECG trace at 60bpm. Bottom plots show evolution of longitudinal magnetisation. Adapted from [136].

The proposed scheme does not allow sufficient recovery of longitudinal magnetisation for the full range of T_1 values expected. However, errors in T_1 estimation caused by this are avoided through selective use of the data as described below. For accurate T_1 mapping it is necessary to sample the recovery curve adequately. For a short T_1 it is therefore optimal to include a high density of short inversion times to characterise the shape of the curve, whereas for longer T_1 longer inversion times are required. In the first epoch of the ShMOLLI scheme data inversion times range from the shortest (100 ms) to longest ($5xT_{RR}$ + 100 ms) acquired. This is sufficient to characterise long T_1 recovery curves, and inclusion of data from later epochs would reduce accuracy as these data points would be affected by incomplete recovery. For intermediate T_1 values there is sufficient recovery between the first and second inversion (6 RR intervals later) to allow inclusion of the data from the single readout of the second epoch without adversely affecting T_1 accuracy. The final inversion pulse is applied just two RR intervals after the second, and so longitudinal recovery of magnetisation will only be adequate to allow inclusion of the data for calculation of very short T_1 values. However, it is these T_1 values for which the additional data at short inversion times is most valuable. The ShMOLLI fitting algorithm therefore differs to that for MOLLI in that it is performed in a conditional manner, with data from the second and third epochs only utilised when the fitted T_1 value is under a threshold that is dependent on T_{RR}.

Simulation and phantom studies performed in the study demonstrated that ShMOLLI is less susceptible to underestimation of long T_1 values, and demonstrates less heart rate dependence. This is due to the fact that, for long

T_1 values, all data that is used for the fit has been collected following a single inversion pulse, eradicating the effect of incomplete recovery. The penalty is an increase in noise, due to the use of fewer data points in the fit. Theoretically, the noise penalty, in comparison to MOLLI, would be more severe for longer T_1 values where fewer data points are used. This effect was demonstrated in the simulation, phantom and human volunteer experiments making up the initial ShMOLLI study. One key advantage demonstrated in ShMOLLI was a much more linear relationship to T_1 measured by a reference standard technique than MOLLI. Both sequences demonstrated systematic underestimation, but for ShMOLLI this was consistent at 4% rather than demonstrating heart-rate or T_1 dependence. Correction is therefore more straightforward to apply.

Normal variation of T_1 in humans (at 1.5 T) was later assessed in a follow up study [137]. This multi-centre study (n = 342) allowed assessment of variation of myocardial and blood T_1 with a range of potential confounding factors. Mid-wall myocardial T_1 was found to be highly reproducible across individuals and scanners (<2% variability). Values were taken from the mid-wall to avoid partial volume effects (with blood or surrounding tissues). Age dependence was observed in females, with no difference between genders for volunteers over the age of 45 but slightly higher mid-wall myocardial T_1 observed in younger females. In contrast to the original ShMOLLI paper, small but statistically significant heart-rate dependence was also identified (following correction for age and gender), with T_1 increasing by 6 ms per 10 bpm. Similarly, small but statistically significant dependences on age, gender and heart rate were seen for blood T_1 (although in this case T_1 decreased with heart rate), as well as a small difference between measurements in the left and right ventricles. This study does not establish absolute values for population averages of myocardial and blood T_1 *in vivo* or the accuracy of the ShMOLLI method. This is due to the fact that there is no accepted gold standard for *in vivo* cardiac T_1 measurements and so accuracy can only be assessed in phantom studies, which do not fully replicate the complexities of the physiological system. However, the study does robustly demonstrate the reproducibility and stability of the ShMOLLI method.

A subsequent study [138] utilised ShMOLLI in ECV calculations for healthy volunteers and patients with a range of disease states (n = 100 in total, 50

healthy). The technique was compared to multi-point IR FLASH performed over multiple breath-holds. The techniques demonstrated good correlation and low bias with comparable inter-study reproducibility (the latter tended towards being greater for ShMOLLI but did not reach statistical significance). Patients with severe aortic stenosis (n = 18) underwent myocardial biopsy, which allowed comparison with histological collagen volume fraction (CVF) measures. ECV correlated with CVF for both methods, with stronger correlation demonstrated for ShMOLLI than multi-point IR FLASH. These results demonstrate that ShMOLLI is comparable or better than IR FLASH techniques, but importantly is better tolerated with a lower failure rate. This is due to the fact that only a single short breath-hold is required for each T_1 map.

4.4.3 Saturation recovery Look-Locker based techniques

The variants of MOLLI described above all utilised IR techniques. A method was proposed by Song *et al* [139] which employs the same modifications to conventional LL as MOLLI (selective data acquisition and use of data from multiple LL experiments) but uses a saturation preparation pulse. The technique, modified Look-Locker acquisition using saturation recovery (MLLSR), employed the same sequence architecture as MOLLI with three schemes investigated (2-2-4 and 1-3). Unlike IR variants, there is no need for recovery periods between epochs as the longitudinal magnetisation is nulled by each saturation pulse. This leads to greater efficiency as there are no RR intervals in which no data are acquired. Furthermore the sequence should be robust to arrhythmia and be heart-rate independent as the magnetisation at each readout should not depend on the history of the magnetisation in the preceding RR intervals if the saturation pulse nulls the longitudinal magnetisation effectively. A further advantage of SR over IR is that polarity restoration of magnitude reconstructed data (i.e. determining which signal intensities should be negative) is not required, thus removing a potential error source, although this can also be overcome in IR methods by using phase-sensitive reconstruction [140].

The two schemes proposed have durations of 8 and 4 RR intervals respectively. In comparison to a reference standard IR-SE method phantom measurement, 2-2-4 MLLSR results also systematically underestimated T_1 in comparison to

MOLLI. The maximal error (11.8%) was observed for the longest T_1 (1139 ms) and highest simulated heart rate tested (100 bpm) tested. The authors attribute this to the fact that the longest saturation time (2100 ms) for this heart rate is not long enough to allow accurate characterisation of the recovery curve of the longer T_1 values. It should also be noted that the authors chose not to employ T_1* to T_1 conversion as used in MOLLI and ShMOLLI studies as they report that the validity of the correction is dependent on the T_2/T_1 ratio of the material being examined, and this tends to be significantly higher in gadolinium based phantoms than in biological tissues. Consequently the results can only be compared to other studies which employed this correction with this difference in mind. The shorter 1-3 MLLSR scheme was evaluated in a subset of 20 subjects. The results demonstrated good correlation with the 2-2-4 MLLSR and so may offer a viable alternative for patients with a very low heart rate or those who are unable to hold their breath for the required time for other schemes. It would be expected that using only four data points would lead to a noise penalty and an increase in variability of T_1 measurements, but data to assess this was not presented.

More recently a saturation recovery single-shot acquisition (SASHA) sequence was proposed [141] which differs to MLLSR in that an independent saturation pulse is used for each of the nine saturation prepared images (the first image is acquired without magnetisation preparation) and a single-shot balanced steady-state free-precession readout. The TS values for the saturation prepared images chosen to uniformly span the RR interval, so the maximal value depends on the subject's heart rate. The technique was validated by Bloch simulations and comparison to a reference standard IR-SE sequence, in which it was demonstrated that the method exhibited accuracy that is independent of heart rate, flip angle T_1 and T_2 but may exhibit bias due to off-resonance and imperfect saturation efficiency, and both bias and limited precision due to low signal to noise ratio.

These findings were confirmed in a subsequent comparison study [142] in which SASHA was compared to MOLLI and ShMOLLI as well as an IR-SE reference and a combined saturation/inversion recovery sequence (SAPPHIRE [143]). In this study it was shown that the techniques using saturation

preparation exhibited higher accuracy than MOLLI and ShMOLLI but lower precision, while reproducibility was similar across techniques. The optimal choice of T_1 mapping technique may therefore depend on the competing requirements for absolute accuracy or precision in addition to other factors. Additionally it was shown that while all methods had similar reproducibility in ECV the average values differed, implying that systematic biases exist in at least some of these techniques and that normal or disease ranges for ECV values should be appropriate to the T_1 mapping technique used to derive them.

4.4.4 Two-point saturation recovery method

A method has been proposed to allow arrhythmia insensitive rapid (AIR) T_1 mapping [144]. The technique utilises saturation recovery rather than inversion recovery for the reasons set out above. The technique described in this study does not employ a Look-Locker based method but instead uses just two images, one T_1 weighted and one proton density weighted. The PDw image is used to normalise the T_1 weighted image (correcting for variation in equilibrium magnetisation, coil sensitivity and radio-frequency uniformity) allowing the Bloch equation to be solved to establish T_1. The T_1 weighted image uses a TS of 600 ms. This allows the T_1 weighted image to be acquired in the same RR interval as the saturation pulse for heart rates up to 73 bpm. For higher heart rates two RR intervals are required for the T_1 weighted image. The PDw image is acquired in the RR interval before the saturation pulse, so the total imaging time is two or three RR intervals (dependent on heart rate). The technique was compared (at 3 T) to MOLLI and a reference standard IR fast spin echo (FSE) sequence in phantoms and to MOLLI alone in human and animal studies. Of the nine human subjects one was a healthy volunteer and the others were patients with a history of atrial fibrillation (AF) but in normal sinus rhythm during the scan. Chronic AF was induced in goats and dogs (n = 9 and 8 respectively) in the animal study with an implanted pacemaker.

The phantom study demonstrated smaller errors and variability in T_1 measured by AIR compared to MOLLI. Most significantly the accuracy and precision of MOLLI was severely reduced at a simulated high (100 bpm) heart rate and in arrhythmia whereas AIR showed minimal variation. The human and animal studies combined demonstrated a strong correlation between the two methods

but with AIR consistently providing higher T_1 estimates. For pre-contrast myocardium the results were 1501 and 1198 ms for AIR and MOLLI respectively. The authors note that the AIR result is closer to a published rigorous measurement of the T_1 of an excised heart [145] but it should be noted that there is no accepted gold standard technique for *in vivo* myocardial T_1 mapping so it is difficult to assess the accuracy of any method *in vivo*. Inter-scan repeatability was assessed (without repositioning) and was poorer (7% of mean compared to 5% of mean) for AIR compared to MOLLI. This is an expected consequence of the use of a small number of data points in the T_1 determination, and the authors note that this could be remedied through acquisition of additional T_1 weighted images (at the expense of scan duration). Other acknowledged limitations include the fact that the original version of MOLLI rather than the optimised version was used. However both versions are known to be sensitive to heart rate and arrhythmia so the proposed method still offers an insensitive alternative.

4.4.5 Segmented inversion recovery techniques

Segmented data acquisition is performed routinely in cardiac MRI in order to acquire cine MR data sets, in which the motion of the heart can be evaluated through acquisition of images acquired at different cardiac phases. In this technique a subset of the data required for each image is acquired in each RR interval and then combined after all of the data is collected. Goldfarb *et al* [146] employed a similar technique, with the addition of an inversion pulse, to allow T_1 calculations. In this technique data for 19 images is acquired in alternate RR intervals (to allow recovery of longitudinal magnetisation). Data is acquired contiguously over an 800 ms period, with 15 lines of k-space data per segment acquired each time. The acquisition of the 15 lines of data took 39 ms, so images with inversion time (TI) increasing in 39 ms steps were acquired.

The authors performed this protocol (using bSSFP readout) in phantoms consisting of Gd-doped water, and calculated T_1 using three different signal intensity equations describing the magnetisation evolution with different levels of complexity. The first describes only the variation of longitudinal magnetisation and neglects incomplete recovery between inversions. The second includes the variation of transverse magnetisation and the effect of the readout train, while

the third is a further refinement of the second, also including incomplete recovery between inversions. The phantom study showed that all three models were sufficient for short T_1 (yielding good accuracy in comparison to IR-SE results) but the simpler two models quickly diverged above around 500 ms, with severe underestimation of T_1. The authors concluded that it is therefore necessary to use the full signal equation to yield accurate T_1 estimates.

The protocol was also performed in four patients with myocardial infarction (two chronic, two acute). As the images are acquired at different cardiac phases it is not possible to calculate T_1 maps. Instead T_1 was calculated for regions drawn in normal and injured myocardium and the left ventricular blood pool. T_1 was calculated before and approximately every two minutes for one hour after a bolus injection of gadodiamide. Blood and both injured and normal myocardial T_1 demonstrated recovery during the 1 hour observed period as the contrast agent is renally extracted. However the authors noted a slower variation in infarct than in normal myocardium, and differences between chronic and acute cases, suggesting differences in the kinetics of the contrast agent between these tissues.

A modified version of this technique was later applied by Milanesi *et al* [119] in which the readout was extended over multiple heart-beats. This increases the maximum TI and increases the time between inversion pulses. This should allow better characterisation of slower recovery curves and more complete recovery of longitudinal magnetisation between inversion pulses, both of which should improve the accuracy of the technique for longer T_1 values. However the technique also assumes that the T_1 is constant throughout the cardiac cycle, yet small but significant variation in native myocardial T_1 between systole and diastole which may reflect temporal changes in microvascular volume fraction have since been reported [147]. The protocol was first performed in phantoms (at 1.5 T) and compared to an IR-SE reference standard. The number of simulated RR intervals between inversions was varied, to vary the repetition time (TR) from 2000 to 7000 ms in order to determine the required TR for *in vivo* studies. Good agreement was found at short T_1 for all TR values, but T_1 was underestimated for longer T_1 values with short TR. Consequently a TR of

2000 ms was used in subsequent post-contrast *in vivo* studies, and 5000 ms for pre-contrast studies, chosen to achieve accuracy of 2% or better.

The protocol (with the TR values determined from the phantom study) was applied in a cohort of healthy (n = 11) volunteers as well as patients with dilated cardiomyopathy (DCM, n = 22) and myocardial infarction (MI, n = 4). Data for T_1 calculations were acquired before and at 5, 10 and 15 minutes after bolus injection of gadodiamide. The number of RR intervals between inversions was adjusted on a per-subject basis (dependent on heart rate) to use the minimum number to achieve the required TR. LGE images were also acquired to identify regions of fibrosis. Examination of the results for healthy volunteers demonstrated no heart rate dependence suggesting that the use of a fixed minimum time between inversions successfully mitigated variations in the amount of longitudinal recovery affecting results. In comparing tissue types the authors found that T_1 in areas of delayed enhancement in MI patients was significantly higher than the other myocardial tissue states assessed (healthy, delayed enhancement in DCM and remote). The T_1 for healthy pre-contrast myocardium was reported as agreeing well with literature values for 1.5 T. Conversely T_1 post contrast is lower than the other groups in MI (significant only at 10 and 15 minutes post injection). From pre and post-contrast blood and myocardial T_1 measurements the authors calculated λ for the three time points. No significant differences were observed at 5 minutes but at 10 and 15 minutes λ was significantly higher for LGE regions in MI patients. LGE positive regions in DCM patients showed a trend for increased λ that did not reach statistical significance.

This study has demonstrated an alternative method for T_1 calculation (albeit one not suited to T_1 mapping) with a proven lack of heart rate dependence. Furthermore the human subject results further support the clinical value of pre and post-contrast T_1 mapping. However it should be noted that while the acquisition technique could be applied readily in clinical practice, the post-processing would be labour intensive as corresponding regions would need contouring on images at different cardiac phases to allow T_1 calculation on a segmental basis.

4.5 Conclusions

Since the introduction of gadolinium based contrast agents into clinical use there has been much investigation of their potential utility for assessing the physiological status of human myocardium. The biodistribution of Gd-DTPA and other extracellular agents has been studied and has been confirmed to be suitable for application to probe the tissue status of the myocardium in health and a range of pathological states. Consequently such agents can be a valuable tool for assessing the myocardial interstitium (both qualitatively and quantitatively) as well as myocardial perfusion. Development of quantitative methods has formed two strands, assessment of dynamic data acquired with a high temporal resolution, or comparison of data acquired before contrast administration and once equilibrium between the blood and interstitium has been reached (or approached).

Recent development has focussed primarily on contrast equilibrium methods, aided by the evidence supporting the fact that equilibrium can be approximated sufficiently well within a few minutes following a bolus injection, rather than requiring a clinically impractical lengthy infusion. There have been a range of techniques developed to allow T_1 mapping to be performed within a single breath-hold, generally with coverage limited to a single slice but some with potential to allow up to three slices to be acquired. This allows the potential for mapping extracellular volumes but robust image registration between the pre and post-contrast image is required for this.

While there has been much development in this field there are still a range of factors that must be considered when designing or evaluating contrast equilibrium data. The contrast agent administration regime and delay time are potential confounding factors, and some of the most widely adopted techniques are known to exhibit inaccuracy (particularly for long T_1, which is a greater issue at higher field strengths) and heart rate dependence. Additionally there is variation in the analysis measures used, with various correction methods proposed but not universally adopted. With a lack of an accepted gold standard for measuring myocardial T_1 *in vivo* direct validation of T_1 mapping techniques remains difficult and is likely to continue relying on phantom based surrogates and comparison to existing techniques. With a wide variation in T_1 mapping

techniques currently being investigated and used in clinical studies, each with differences in terms of precision, accuracy and heart rate dependence across the clinically applicable T_1 range, it is important that current research results are evaluated with this in mind. There is consequently still a need to optimise these sequences and identify the optimal protocols for clinical application, considering both the performance of the techniques as well as suitability for use in non-specialist MRI centres and with patients with limited breath-hold capability. In later chapters MOLLI schemes will be compared through simulations and phantom work (Chapter 6) although due to limitations as to the sequences and fitting algorithms available on the scanner used and the chronology of the project (section 1.4) the choice of T_1 mapping technique used for the experimental chapters was limited.

Despite the recent dominance of T_1 mapping based ECV measurements in the literature there remains interest in dynamic imaging. As technological developments drive image quality improvements this may be a viable and efficient alternative which can provide multi-parametric assessment of the myocardium. Pilot work prior to this PhD [1] investigated the use of a distributed parameter model to perform such multi-parametric assessment, although was limited by the fact that the data was not acquired with this analysis planned and consequently the length of the DCE-MRI acquisition may have been sub-optimal. This work is furthered in the clinical studies (Chapter 9 and Chapter 10) in this thesis firstly by prospectively acquiring data with this analysis technique planned and secondly by including ischaemic heart disease patients as well as volunteers. Furthermore limitations in non-linearity correction methods have been identified in this literature review, and these techniques are investigated further through both simulations and experimental work (Chapter 7 and Chapter 8) in which the techniques discussed here are compared to a novel application of bookend T_1 based correction.

Further validation of this technique and determination of the optimal analysis still needs to be performed. The demand for accurate and reliable methods that can readily be applied in the clinical setting to assess myocardial fibrosis quantitatively remains strong. This is evident from the large number of abstracts presented at recent cardiovascular and general MRI conferences which have

used the methods described above in clinical studies to assess ranges and variability in both the normal population and a wide range of pathological states. This review has focussed on the development of the techniques employed, rather than the clinical studies employing them, and so these recent studies have not been discussed here.

Chapter 5

Literature Review - Clinical

This chapter provides a review of clinical studies employing quantitative contrast enhanced cardiac MRI techniques. It serves to highlight and exemplify the key clinical areas which these techniques have provided insights into and may offer clinical value rather than describe the technical developments discussed in the previous chapter. Some of the studies described in the previous chapter are re-visited, but here the clinical observations rather than the technical developments are discussed.

5.1 Early studies

Early work investigating the use of quantitative analysis of contrast enhanced CMR data focussed on canine models of ischaemic heart disease with a series of studies by Pereira *et al* [93, 148, 149] demonstrating that the contrast agent partition coefficient in the infarcted territory is elevated after either temporary (two hour) occlusion followed by reperfusion or after permanent occlusion of a coronary artery. For temporary occlusion this increase was observed within the first minute following reperfusion, increased during the subsequent hours and showed a trend for a reduction (without returning to normal) over the following 8 weeks. This work established the potential use of quantification of the partition coefficient as a non-invasive means to establish extent of myocardial damage following infarction.

Concurrently studies investigating the application of contrast enhanced CMR in humans were ongoing. Fedele *et al* [68] measured MR signal intensity from a non-magnetisation prepared spin echo sequence prior to and at several time points (4, 8, 12 and 30 minutes) after administration of Gd-DTPA. This study was performed on 19 patients with chronic coronary artery disease and left ventricular dysfunction. The imaged myocardium was divided into 11 segments, with each segment defined as normal, hibernating or necrotic based on iodine 123-phenylpentadecanoic acid (IPPA) scintigraphy. Significant signal intensity differences were observed between each tissue type at each post-contrast time point (except for between normal and hibernating myocardium at 12 minutes)

suggesting differences exist in tracer kinetic properties of these tissues. Notably the time point with the maximum signal intensity was most frequently the first time point (4 minutes) for normal and hibernating myocardium but the final time point (30 minutes) for necrotic myocardium suggesting the contrast agent delivery is substantially slower in necrotic myocardium.

A study by Kim *et al* [6] demonstrated in canine models of both chronic and acute myocardial infarction that regions of hyperenhancement in inversion recovery prepared spoiled gradient echo sequences acquired 30 minutes after Gd-DTPA administration corresponded very closely with regions of necrosis in the acute phase or collagenous scar in the chronic phase by comparison with post-sacrifice histology. This observation held only for acute and chronic infarction, and not for induced reversible ischaemic injury in which signal intensity did not differ significantly from that in remote myocardium. Subsequent clinical studies from the same group demonstrated that the transmural extent of the region of hyperenhancement was highly predictive of recovery of contractile function in patients with both acute myocardial infarction treated by successful revascularisation [31] and chronic coronary artery disease [32]. These studies have led to the widespread adoption of late gadolinium enhanced (LGE) MRI for the assessment of myocardial viability in ischaemic heart disease. Additionally the technique has proven prognostic value [150, 151] for assessment of localised fibrosis or infiltrative disease processes in several non-ischaemic cardiomyopathies, for which the spatial distribution of enhancement is different to that for ischaemic disease.

5.2 Further clinical studies in ischaemic heart disease

Following the preliminary work described above clinical studies focussed on ischaemic heart disease, in which regions of myocardium affected by the temporarily or permanently restricted blood supply typically exist alongside regions of myocardium which have maintained normal blood supply. This leads to heterogeneity of tissue status within each case.

5.2.1 Partition coefficient and extracellular volume fraction

Flacke *et al* [92] measured the partition coefficient of gadopentetate dimeglumine in five patients with acute and five with chronic myocardial

infarction, as well as twelve healthy subjects, by measuring T_1 before and after a 30-40 minute infusion of the contrast agent. The partition coefficient was elevated in both acute (0.91±0.11 ml/g) and, to a lesser extent, chronic infarct (0.78±0.09 ml/g) in comparison to normal myocardium (0.56±0.10 ml/g). Using a 20% increase in partition coefficient cut-off yielded high diagnostic performance for identifying segments of both acute infarct (100% sensitivity and 98% specificity in comparison to a combination of identification of wall motion abnormality on angiography and echocardiography) and chronic infarct (88% sensitivity and 96% specificity in comparison to identification of wall motion and thickening abnormalities by CMR).

A study by Klein *et al* [152] further investigated the delayed tracer kinetics of Gd-DTPA in ischaemic heart disease by measuring T_1 of blood and myocardium both before and at several time points from 2-50 minutes after bolus contrast agent administration, as well as by measuring absolute myocardial blood flow by PET, in patients with ischaemic heart failure. T_1 was observed to be similar in both viable myocardium and scar before, but differ significantly (with shorter T_1 in scar) after contrast agent administration. It was also noted that T_1 of blood and scar is similar between 5 and 15 minutes post-contrast. This yields low contrast on T_1 weighted images (including late gadolinium enhancement images) in this situation, including at the endocardial border in segments with subendocardial scar which can lead to difficulty identifying this border. This problem has been identified and a potential solution addressed in a paper by Peel *et al* [77] in which a dual inversion recovery sequence was proposed to suppress blood signal. In the study by Klein *et al* [152] the partition coefficient measured in viable myocardium was consistent from 2-50 minutes, whereas in scar it increased with time until a plateau from 20 minutes. This agrees with the observations of slower contrast agent delivery in infarcts described by Kim *et al* [6] and discussed above. MBF (measured by PET) was observed to be lower in segments displaying delayed enhancement (scar) on MRI compared to unenhanced segments (viable myocardium), and to correlate moderately with the rate of the increase of the partition coefficient over the period from 2-20 minutes after contrast agent administration. The latter observation suggests that the slower enhancement in regions of scar is in part due to reduced wash-in of contrast agent due to reduced MBF. However the

correlation improved when the partition coefficient increase rate was correlated with the ratio of the steady-state partition coefficient to MBF, suggesting that the larger distribution volume is also a contributing factor to the slower tracer kinetics in the scar regions.

5.2.2 Perfusion CMR

In addition to measuring myocardial damage through the techniques described above there has also been interest in quantifying perfusion to myocardium in ischaemic heart disease. Nielsen *et al* [91] investigated the diagnostic ability of quantitative perfusion in the setting of acute myocardial infarction by model-based deconvolution using a mono-exponential residue function allowing estimation of both K_i (interpreted as the product of the myocardial blood flow and the extraction fraction across the capillary membranes) and v_e. The study recruited 7 patients presenting with acute myocardial infarction. Five of the patients received thrombolytic therapy, and of those 3 underwent MRI both before and 90 minutes after therapy. Reduced perfusion was demonstrated in regions of myocardium supplied by the occluded vessel, and in the patients scanned twice this was seen to recover partially following therapy. As discussed in the previous chapter, this study demonstrated unexpected findings in terms of estimated distribution volumes with lower results for regions of infarct. This casts some doubt on the validity of these results. However the perfusion estimates show that DCE-MRI can be sensitive to changes in the delivery of myocardial blood between healthy and pathological regions of myocardium, and also to changes induced by therapy.

A subsequent study my Selvanayagam *et al* [153] investigated resting blood flow in hibernating myocardium, that is non-infarcted myocardium that demonstrates impaired contractile function that can be recovered following revascularisation therapy. DCE-MRI data was acquired in 3 slices and segmented into 8 segments per slice. Late gadolinium enhancement and cine images were also acquired for identification of infarcted myocardium and assessment of function respectively. 27 patients with severe coronary artery disease were studied within 24 hours prior to and after percutaneous coronary intervention (PCI). 25 of the patients returned for a 3-month follow-up scan in which contractile function only was assessed. MBF in myocardial segments

perfused by stenosed arteries was significantly lower than in remote myocardium prior to PCI (1.2±0.3 ml/min/g vs 0.7±0.2 ml/min/g). Following PCI the MBF in the revascularised segments was similar to that in remote myocardium (1.2±0.2 ml/min/g) demonstrating that the therapy had successfully restored perfusion. Restoration of the function of this hibernating myocardium was also observed in these patients at 3-month follow-up, confirming that the dysfunctional myocardium identified pre-therapy was viable and not irreversibly damaged.

Hopp *et al* [154] utilised DCE-MRI to assess the development of myocardial infarction from the sub-acute (2-3 weeks post-revascularisation) to chronic (6 months post-revascularisation) phase. Both semi-quantitative parameters and parameters from model-constrained deconvolution using both an expanded two-compartment model including an intra- and extra-vascular volume fraction and model-independent deconvolution were determined. Semi-quantitative parameters showed that the initial upslope in both acute and chronic infarct is slower than in normal myocardium, and the signal persistently rises over the duration of the experiment (120 heart-beats acquisition in total) unlike the normal myocardium in which the slope is negative (i.e. signal decreases). Perfusion estimated by both model-constrained and model-independent deconvolution was decreased in infarct in the acute and chronic phases, with larger differences and lower absolute values at the chronic phase. At the acute phase only blood flow estimated by model-independent deconvolution, and not K^{trans}, was significantly lower in infarct than in normal myocardium. Extracellular volume fraction was also increased at both phases (26%±7% acute & 23%±9% chronic compared to 19±7% and 18±6% for normal myocardium at the two time points), with a greater difference in acute myocardial infarction. In both cases the relative increase in ECV was lower than the relative differences in partition coefficient observed in other studies, e.g. that by Flacke *et al* described in the previous section [92]. This study supports findings from previous studies investigating properties of myocardial infarction, however the assessment of the variation of properties following revascularisation was limited by the fact that the first study was acquired in the sub-acute, rather than acute phase.

Finally the study by Pack *et al* [94] discussed in the previous chapter compared estimates of extracellular volume fraction from DCE-MRI in chronic infarcts to remote myocardium in a small number (4) of patients. Extracellular volume was increased to a much greater extent (45.7±3.4% compared to 23.6±6.3% in normal myocardium) in this study than in the study by Hopp *et al* [154].

5.3 Proliferation of contrast equilibrium ECV estimation and expansion into assessment of diffuse fibrosis

The studies described above are focussed on ischaemic heart disease, in which myocardial damage is typically expected to be focal and substantial changes are expected. Since the facilitation of rapid myocardial T_1 mapping enabled by the introduction of MOLLI [7] and other techniques described in the previous chapter there has been a proliferation of studies investigating the use of equilibrium contrast based estimation of ECV for the evaluation of diffuse myocardial fibrosis in a range of both cardiac and systemic diseases, as well as other conditions and processes which may impact upon the structure of the myocardium. This includes dilated [155, 156] and hypertrophic cardiomyopathy [157-160], congenital heart disease [161], aortic stenosis [162], cardiotoxicity from chemotherapy [163, 164], diabetes mellitus [165, 166], heart [167] and non-cardiac [168] organ transplant, systemic amyloidosis [169], systemic sclerosis [170], chronic kidney disease [171] and ageing [172, 173].

Full discussion of these studies is beyond the scope of this literature review. However, a small number of these studies have included histological validation in human subjects, and thus warrant further discussion below.

Histological validation of ECV estimation techniques in humans is difficult as it requires analysis of tissue obtained from either myocardial biopsy, organ explant or autopsy. Consequently the number of studies that have performed histological validation are limited. Fontana *et al* [138] compared the single breath-hold ShMOLLI [136] T_1 mapping technique to a multiple (14) breath-hold technique for the estimation of ECV in 100 subjects including healthy volunteers and patients with hypertrophic cardiomyopathy, severe aortic stenosis and amyloid. A single bolus administration of contrast agent was used, with a 15 minute delay before post-contrast T_1 mapping. The patients with severe aortic

stenosis were additionally indicated for biopsy, allowing histological validation in comparison to collagen volume fraction (CVF) assessed by tissue staining. It should be noted in these studies that the two techniques are measuring different tissue properties, with CMR being sensitive to the total space accessible to the contrast agent and histology specifically measuring the volume fraction of collagen, and so they should not necessarily be expected to agree. However as the network of collagen fibres exists in the interstitial space which is accessible by the contrast agent an increase in CVF would be expected to be accompanied by an increased ECV while the absolute value of CVF would be expected to be lower than ECV.

ECV estimated by the multiple breath-hold technique and ShMOLLI both demonstrated moderate correlation with histological CVF (R^2 of 0.589 and 0.685 respectively) but with systematic differences. ECV was 27±6% and 31±5% for the two CMR techniques and CVF was 18±8% by histology.

A second study [174] performed a similar validation with six patients undergoing heart transplantation. ECV was measured by CMR using a bolus administration of gadolinium based contrast agent with pre and 10 and 15 minute post-contrast T_1 measurements by MOLLI T_1 mapping. Whole-heart CVF histology was performed post-explant using picrosirius red staining. Tissue samples were taken from 16 segments of the heart for each patient, corresponding to segments on CMR imaging. ECV by CMR using pre and 15 minutes post-contrast T_1 data showed strong correlation with CVF (R^2 = 0.555 within-subject, 0.893 between-subject) while post-contrast T_1 alone showed significant correlation with CVF only when tested within-subject. This study allowed validation across a wide range of fibrotic tissue states, with CVF ranging from 3.3-55.2% and ECV from 30.9-68.4%.

More recently de Meester de Ravenstein *et al* [175] performed a study similar to that of Fontana *et al* [138] comparing ECV from MOLLI based T_1 estimates to CVF from myocardial biopsy. Their patient cohort included patients with severe aortic stenosis, severe aortic regurgitation or severe mitral regurgitation, all free from coronary artery disease. CVF was lower than ECV as expected (6.1±4.3% vs 28.9±5.5%) but showed significant correlation (r=0.78). The study also examined correlation between CVF and native T_1 to assess the need for

contrast agent administration, as well as the spatial extent of late gadolinium assessment, but found no significant relationship for either.

The studies above have demonstrated that ECV estimation by equilibrium contrast CMR shows moderate to good correlation with CVF by histology, further supporting the use of the technique as a minimally invasive probe of myocardial tissue status. Additional components of these studies have suggested that acquisition of both pre- and post-contrast T_1 data to allow calculation of ECV is required, as neither in isolation demonstrated strong relationships to histologically derived markers of tissue status.

5.4 Conclusions

Contrast enhanced MRI has found widespread clinical application in the qualitative assessment of myocardial perfusion and viability. Alongside this research and development in to the clinical application of quantitative assessment of both dynamic and equilibrium contrast enhanced MRI data has been ongoing. With the advent of robust myocardial T_1 mapping methods that can be incorporated into routine protocols there has been a large growth in interest in quantifying extracellular volume fraction as a marker of both diffuse and focal pathological processes. Such techniques have been investigated in a wide range of diseases, including those of both ischaemic and non-ischaemic aetiology.

In subsequent chapters in this thesis clinical studies are performed in both healthy volunteers and patients with coronary artery disease (under different physiological conditions) and severe myocardial infarction (at two time points). Based on the literature discussed above these cohorts should provide a wide range of myocardial tissue status (both in terms of perfusion and tissue composition) in which to evaluate the performance of the techniques under investigation. Future work following on from this project could include expansion of the application of these techniques to the evaluation of diffuse myocardial disease in a range of conditions identified above for which changes to tissue status are expected to be smaller.

Chapter 6

T_1 Mapping – Simulations and Phantom Validation

In this section evaluation of Modified Look Locker Inversion Recovery based T_1 mapping is discussed, specifically with regards to acquisition scheme. The simulations have been limited to schemes that can be performed on the scanner used for the clinical studies described later in this thesis. While ShMOLLI data can be acquired on this scanner the mapping software lacks the conditional algorithm used for ShMOLLI, and so this scheme is not considered in this chapter.

6.1 Methods

6.1.1 Simulations

Simulated relative signal intensities were calculated for a range of MOLLI schemes, heart rates and T_1 values through Bloch simulation of the sequence. From these values T_1 was determined using published methods [7] and compared to the ground truth values used for the simulation. Software for this work was developed in MATLAB (Mathworks, Mattick, MA).

Throughout this thesis the following convention is adopted to describe MOLLI schemes (including the recovery period); $n_i(r_i)n_j(r_j)$... where n is the number of readouts (one per RR interval) for the *i*th, *j*th, ... epoch. The term “r” is the number of recovery RR intervals between the last readout and next inversion. The original optimisation of the MOLLI scheme [130] is thus represented as 3(3)3(3)5. A recently proposed modification to MOLLI is to use a minimum time rather than a prescribed number of RR intervals either for the readout cardiac cycles, the recovery period, or both [176]. This results in the number of RR intervals being increased for faster heart-rates. The suffix “s” after n_i or r_i is used to indicate recovery periods specified in this manner. This is demonstrated in Figure 6-1.

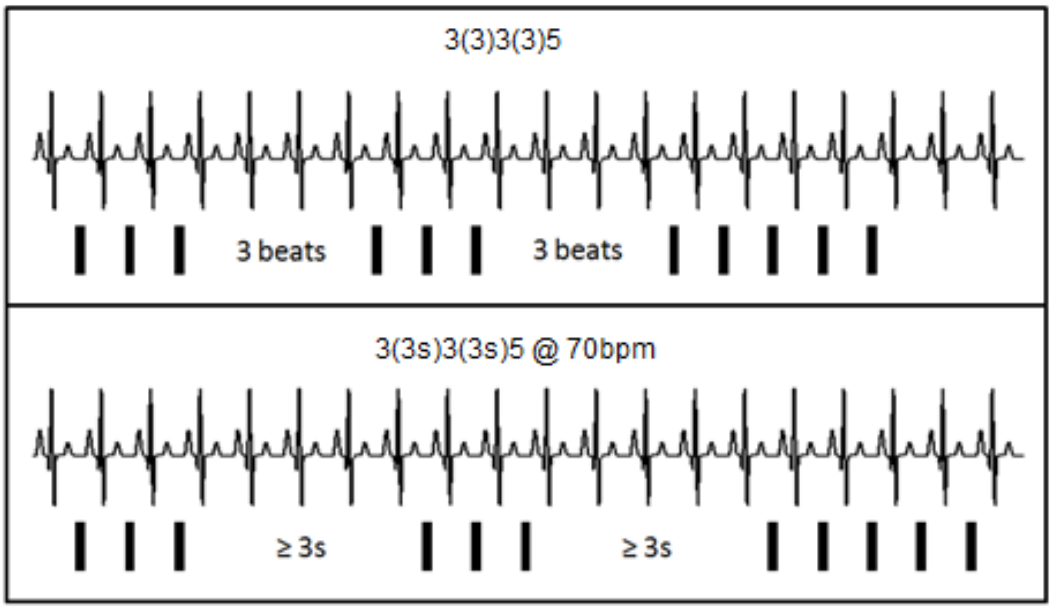

Figure 6-1 – Example MOLLI schemes indicating cardiac phases with data acquisition (black bars). Each epoch is preceded by an inversion pulse. For the heart rate of 70 bpm in this example an extra RR interval is introduced into each recovery period in the 3(3s)3(3s)5 scheme (bottom) compared to the 3(3)3(3)5 scheme (top) to achieve a recovery period of at least 3 seconds.

Simulations included the effect of all RF pulses in the version of MOLLI implemented on the scanner used for the experimental work in this thesis (Philips Achieva 3.0T TX, Philips Healthcare) and assumed a T_2 of 50 ms throughout. Signal intensity was assumed to derive entirely from the readout with zero phase-encoding gradient moment, which is the 47th readout of 83, following a 10 pulse linear ramp up in flip angle (up to 35°). The readout was a bSSFP sequence with TR/TE of 2.70/1.35 ms. TI for the first image after the inversion pulse was 146.46 ms for the first epoch, 350.00 ms for the last and 248.23 ms for the middle epoch where present. In practice the value for the final epoch is user-defined, that for the first epoch is automatically set at the shortest possible value (which will depend on the TR and number of phase-encoding lines acquired up to the acquisition of the zero-spatial frequency data) and the values for additional epochs (where present) are distributed evenly between these two values. Simulations were performed at heart rates of 40-100 bpm and T_1 from 50-2500 ms (50 ms increments). Conventional 3(3)3(3)5 MOLLI was simulated as well as a variant with the recovery period defined in seconds (3(3s)3(3s)5). Additionally shortened variants that have been proposed [135] were also simulated: 5(3)3 and 5(3s)3, and 4(1)3(1)2 and 4(1s)3(1s)2.

6.1.2 Phantom validation

A phantom containing doped agarose gels with a range of T_1 values was scanned to acquire MOLLI data with all schemes included in the simulation except 3(3s)3(3s)5. Data was acquired using the protocol from which the simulations were based at simulated heart rates of 40, 60 and 100 bpm. Results were compared to IR-SE reference T_1 values.

6.2 Results

Simulated errors in T_1 results are presented in Figure 6-2 in comparison to ground truth T_1 values used in the simulations, while Figure 6-3 compares MOLLI T_1 values to IR-SE reference values from phantom data.

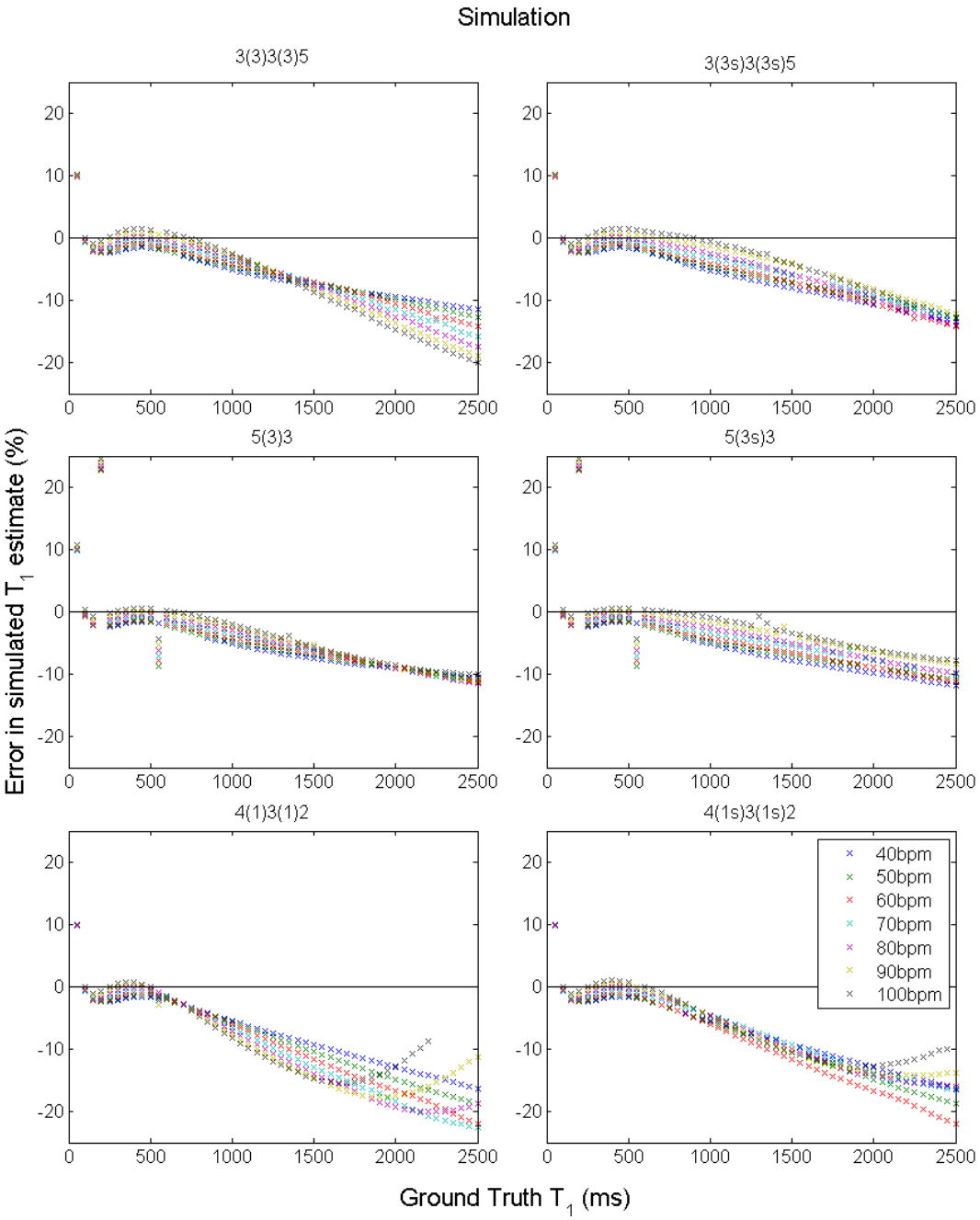

Figure 6-2 - Simulated MOLLI accuracy curves for the simulated schemes. In the left column recovery periods are specified in terms of cardiac cycles and in the right column in seconds.

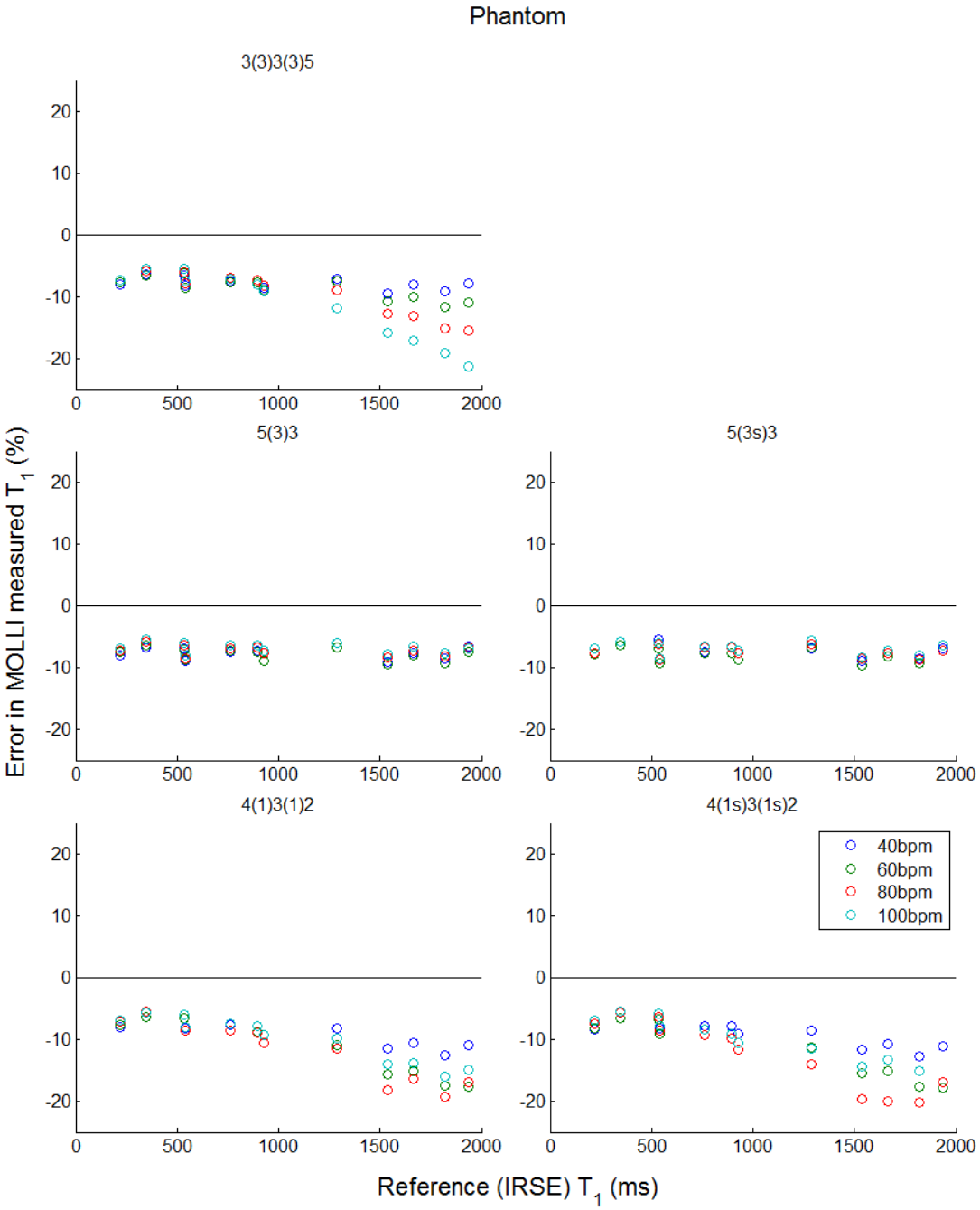

Figure 6-3 - MOLLI accuracy curves from the phantom data.

6.3 Discussion

For all schemes, underestimation of long T_1 values is observed in the simulation data. This arises from incomplete recovery of longitudinal magnetisation between inversion pulses as well as disturbance of the recovery caused by the readout pulses. Approximately 10% overestimation of the shortest T_1 (50 ms) occurs consistently as longitudinal magnetisation will have essentially fully recovered (TI=248.23ms corresponds to >99% recovery) for all but the image with the shortest TI. Consequently there is insufficient data at short TI to

characterise such fast recovery and the fitting is unstable. This is not of concern as this T_1 is outside the clinically relevant range which the techniques were designed to be able to characterise.

Examination of conventional MOLLI results (Figure 6-2 – top-left) shows that for this scheme underestimation of long T_1 is more severe at faster heart rates. This arises as the time between inversion pulses is proportional to the RR interval, so a faster heart rate is associated with less recovery time. This heart-rate variability at long T_1 values is reduced through the use of 3 s recovery periods (top-right) although variability is still present throughout the T_1 range. In this scheme an extra cardiac cycle is introduced into the recovery interval for heart rates above 60 bpm, and an extra two for heart rates above 75 bpm. However, breath-hold duration is also increased for heart rates above 60 bpm which may not be clinically acceptable.

A similar pattern is observed for 5(3)3 and 5(3s)3 MOLLI (Figure 6-2 middle row). However in this case underestimation of long T_1 values is less severe, likely because a smaller proportion (3/8 vs 8/11) of data points are affected by incomplete recovery and there is a greater time period between the first and second inversion pulses. In this sequence anomalies are observed at T_1 values of 200 and 550 ms. These occur due to incorrect assignment of polarity during the fitting process, which is more likely when signal intensity from one of the images is very low and when there are fewer unique data points informing the fit. Use of two rather than three inversion epochs may thus increase the likelihood of such polarity restoration errors.

4(1)3(1)2 and 4(1s)3(1s)2 MOLLI (Figure 6-2 – bottom) demonstrate comparable performance to the other shortened schemes at short T_1, but without evidence of polarity restoration errors in these data. Accuracy and heart rate dependence are worse at long T_1, as would be expected due to the shortened time between inversion pulses. However this sequence was only proposed for measurement of short, post-contrast T_1 values.

The phantom validation shows similar patterns to the simulation results, notably with a consistent error for 5(3)3 and 5(3s)3 but increasing errors and heart rate variability at longer T_1 values for the other schemes (Figure 6-3). Additionally

underestimation is generally greater for all schemes compared to the simulation results, which may arise due to inaccuracies in the IR-SE reference data, error sources in the MOLLI sequences that were not included in the simulations or systematic differences in T_1 caused due to a temperature difference between scans (discussed further in the limitations described below).

6.3.1 Limitations

Simulation work in this study is limited by omission of image noise, thus limiting the assessment to accuracy rather than precision and neglecting noise induced bias. Reducing the number of images acquired will tend to reduce precision and so a scheme that is identified as optimal in simulation and phantom studies (where images are generally SNR rich) may not be the optimal choice when imprecision arising from noise is considered.

Phantom work was compromised by the fact that reference T_1 maps were acquired on a different day to MOLLI T_1 maps, and so there may have been a temperature difference in the gels. While the dependence of the T_1 of these gels on temperature at 3 T is not known the datasheet accompanying the phantom indicates a typical change of 22% for an 8K change around room temperature (292-300K). For this experiment the phantom was stored in the scan room prior to scanning to equalise temperature, and the scan room temperature is controlled and maintained at 20°C for patient comfort so temperature differences, and consequently T_1 value differences, between the scanning sessions should have been low. Furthermore the most pertinent assessment related to comparison between MOLLI schemes and heart rates, rather than overall accuracy, and all MOLLI data was acquired during the same scanning session.

6.4 Conclusions

Simulations of MOLLI sequences have demonstrated underestimation of long T_1 compatible with literature reports. Choice of MOLLI scheme can significantly affect overall accuracy and heart rate dependence. Initial simulation results suggest that a 5(3s)3 scheme provides low heart rate variability and good accuracy, although with the potential for polarity restoration errors which can be avoided by including an additional inversion recovery epoch. While further *in*

vivo assessment is required to assess performance in the clinical setting these results suggest that the use of a 5(3)3 or 5(3s)3 scheme for native T_1 and a 4(1)3(1)2 or 4(1s)3(1s)2 scheme for contrast enhanced T_1 quantification can offer comparable or improved accuracy and heart rate variability to the conventional MOLLI scheme in a shorter breath-hold time.

Chapter 7

Signal Non-Linearity Correction – Simulation and Phantom Scanning

In this chapter a simulation study is presented in which the performance of signal non-linearity correction methods for myocardial DCE-MRI techniques is compared. Additionally a phantom study to measure the saturation efficiency and validate the proposed bookend T_1 based method is described. The simulation study was published as a paper [177] and conference abstract [178], although with the initial simulation of signal intensities described by an analytical approximation (the fully recovered model described later) rather than Bloch simulation. This publication also included results from a subset of the volunteer data from the following chapter. Contributions of the individual authors are described at the start of this thesis.

7.1 Introduction

Signal enhancement in saturation recovery DCE-MRI sequences is approximately proportional to contrast agent concentration for low concentrations and/or sequences with low T_1 sensitivity [179], and could be used in quantitative analysis under such conditions. In practice peak concentrations in the AIF are considerably larger than those in the myocardium, leading to a challenge for quantitative analysis. Consequently when an imaging sequence with sufficiently low T_1 sensitivity or contrast agent dose to obtain a linear response throughout the AIF is used the myocardial signal will vary only within a narrow range of the full dynamic range. The contrast-to-noise ratio (CNR) in the myocardium will thus be lower than if the protocol were optimised for myocardial contrast alone (which can be done for studies in which only visual analysis is performed) and this may limit the precision of quantification. Consequently a compromise must be made between signal linearity (which affects accuracy in quantitative analysis) and myocardial CNR (which affects quantitative precision, as well as the suitability of the images for visual analysis). As identified in section 4.3.2.2 several methods have been proposed to address this issue, including modelling the SI-concentration relationship [44,

101, 102, 107] or separating the AIF and tissue curve acquisition using the same (dual-sequence [108]) or an additional contrast agent administration (dual-bolus [103-105]).

In these methods perfect magnetisation saturation throughout the LV is generally assumed. However, even with pulses optimised for high-field cardiac MRI, a small fraction of equilibrium magnetisation may remain after saturation. This may be aligned with the equilibrium state or be inverted, and has been reported at around 2-3% using the original BIR-4 pulse train [180-182] and more recently at <1% using an optimised version [183]. Although further improvement in saturation pulse efficiency (SE) may arise this is likely to be limited by SAR and radiofrequency field homogeneity constraints. It has been identified that residual magnetisation could bias DCE-MRI SI [181] (particularly for native tissue or blood), and hence cause inaccuracy in quantification [102, 182]. While baseline subtraction can account for some degree of saturation imperfection in signal based analysis this may not be robust at higher levels, and the effect on baseline signal could affect model-based approaches. However the magnitude of such errors in physiological parameters has not previously been assessed.

In this chapter a novel application of bookend (native and post-contrast) T_1 data to estimate and account for imperfect saturation is introduced and assessed alongside established methods. Bookend T_1 measurements have been used to correct errors arising from various sources in breast DCE-MRI using non-magnetisation prepared sequences [184, 185], but have not been applied to SR sequences in myocardial DCE-MRI.

The combined use of signal and T_1 data in the bookend T_1 based technique was motivated by the observation that using native data may poorly define the signal-R_1 curve and be susceptible to bias, as discussed in section 4.3.2.2 and shown graphically in . In the native T_1 based method ideal saturation is assumed, which constrains the curve to pass through the origin. The curve shape is then defined by a single point which, under ideal circumstances of perfect T_1 measurement, ideal saturation and no noise bias, would be at the intersection of the blue dashed line (indicating native R_1) and the signal-R_1 curve (black curve). However, as indicated by the solid blue (over-saturation)

and red (under-saturation) curves this curve would not pass through the origin when saturation efficiency is not ideal.

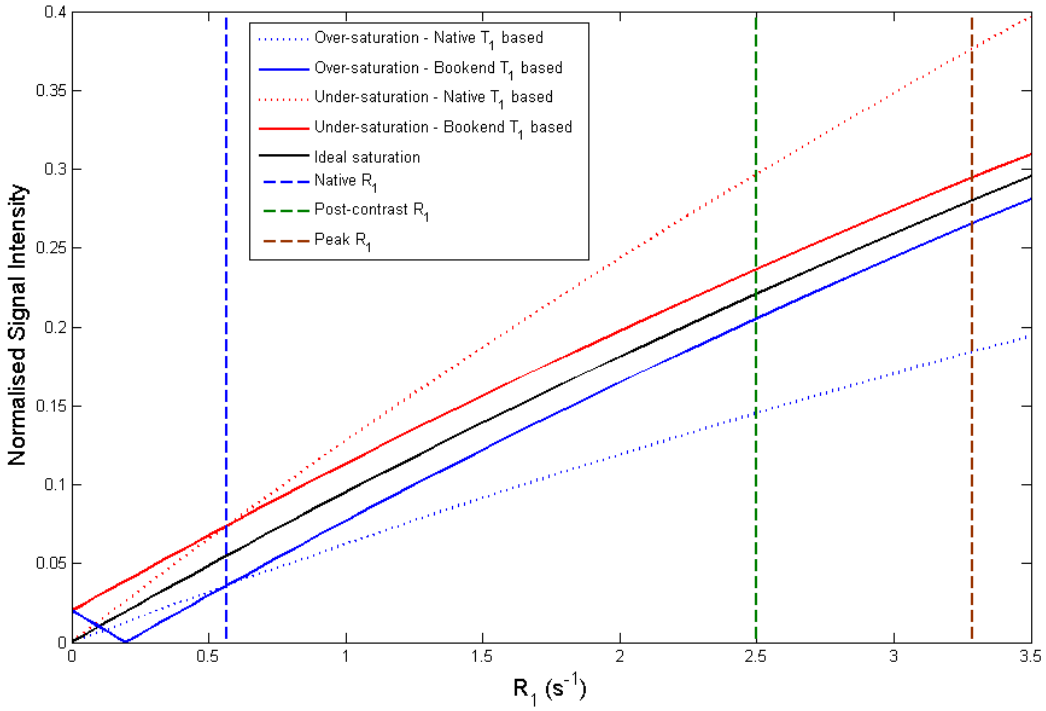

Figure 7-1 – Illustrative signal-R_1 curves. The black line shows the relationship between signal and R_1 for ideal saturation with the blue and red curves showing that for over- and under-saturation. Native, post-contrast and peak R_1 values are indicated by blue, green and brown dashed vertical lines respectively. In the native T_1 approach the signal model is constrained to pass through the origin and so the relationships expected for over- and under-saturation cannot be described. In these scenarios the derived signal models would be as shown by the blue and red dotted lines, and thus large errors would occur for estimation of post-contrast arrival R_1 values. Use of the bookend T_1 approach allows the expected relationship for non-ideal saturation efficiency to be determined from the two measured points.

As the single point constraining the model in the native T_1 approach is close to the origin small errors in the position of this point could lead to large deviations in the shape of the curve at higher R_1 values. In the examples shown over- or under-saturation indicated by the blue and red solid curves would yield estimated signal-R_1 relationships as indicated by the blue and red dotted curves. However similar errors could arise due to noise bias in the baseline signal or inaccuracy in measurement of R_1.

For accurate deconvolution it is sufficient for the relationship between the estimated R_1 values to have a linear relationship to the true concentration values. However the relationship between the erroneous dotted curves and the

true solid curves cannot be described solely by scaling and translation, and so the estimated R_1 values would still exhibit a non-linear response to concentration and thus yield inaccurate deconvolution results.

It was hypothesised that errors could be reduced by constraining the curve by using two measured points (native and post-contrast, the latter being the intersection of the green dashed line and the relevant solid curve). By doing this the curve is no longer constrained to pass through the origin, thus allowing non-ideal saturation, and data is only extrapolated over a smaller range of contrast agent concentrations (from the post-contrast value to the peak, corresponding to the R_1 values indicated by the green and red dashed lines).

7.1.1 Aims

The simulation study in this chapter aimed to assess the impact of imperfect saturation and T_1 measurement error on quantitative myocardial DCE-MRI using different non-linearity correction methods in the presence of realistic noise levels. Additionally a phantom study is described in which saturation efficiency is measured independently and the bookend T_1 based technique is validated.

7.2 Methods

Simulations were performed in MATLAB (Mathworks, Natick, MA, USA). A population representative AIF was generated with a form and mean parameters described previously [52]. This is derived for a 0.1 mmol/kg dose administered at 3 ml/s yielding peak blood [CA] of 6.04mM, so was scaled to peak blood [CA] of 3.02mM to reflect the 0.05 mmol/kg dose administered in the volunteer study described later (ground truth concentration curves are shown in Figure 7-2).

Longitudinal relaxivity (r_1) of 4.5 l/mmol/s for gadobutrol (Gadovist) at 3 T [186, 187] was assumed. Tissue concentration curves were generated by converting the AIF to concentration in plasma using a haematocrit value of 0.46 [188] and convolving with a one-compartment [88] residue function (a mono-exponential as defined in Equation 2-36). Equation 7-1, which is based on Equation 2-33), describes this process.

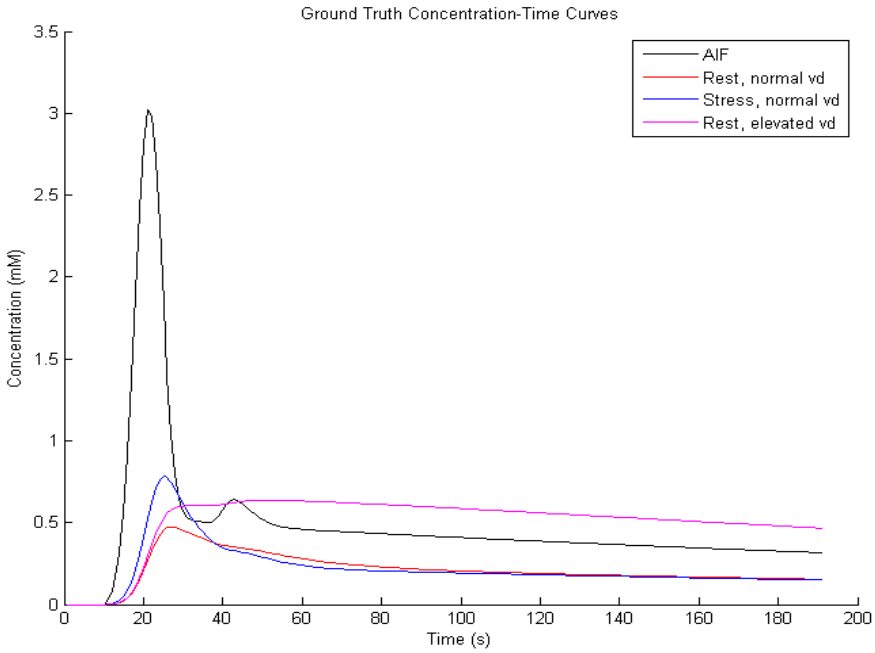

Figure 7-2 - Ground truth concentration-time curves used in the simulations.

Equation 7-1

$$C_t(t) = MBF \cdot (1 - hct) \cdot R(t) * AIF(t)$$

"Ground truth" MBF and distribution volume (v_d) were selected from published sources [1, 189]. GBCA concentration data were converted to longitudinal relaxation rate (R1) using Equation 7-2 (which is based on Equation 2-30) where $R_{1,n}$ is the native R_1 value (i.e. that in the absence of contrast agent).

Equation 7-2

$$R_1 = R_{1,n} + [CA] \cdot r_1$$

SI curves (assuming signal is determined entirely by the centre of k-space) were generated with a range of SE values using simulations based on Equation 2-2 and Equation 2-4 to describe the effect of each RF pulse on the magnetisation and Equation 2-5 to describe recovery between pulses. The sequences were as described in section 3.2.1 with parameters as in Table 7-1 (based on local practice and published values [14]).

Magnetic properties	
Baseline blood T_1[a]	1736 ms
Baseline myocardial T_1[a]	1052 ms
Post contrast blood T_1	400 ms
Post contrast myocardial T_1	550 ms
Contrast agent relaxivity, r_1[b]	4.5 l $mmol^{-1}$ s^{-1}
Physiological properties	
MBF (rest/stress)[c]	1.5/3.5 ml min^{-1} $100ml^{-1}$
v_d (healthy/infarct)[d]	25/69 %
Haematocrit[e]	0.46
Contrast agent dose	
Main bolus/pre-bolus	0.05/0.005 mmol kg^{-1} Gadovist
Main sequence parameters	
TS	95.94 ms
n_{k0} (steps to central line of k-space)	11
N (number of readout pulses per image)	42
FA	15°
TR	2.68 ms
Number of slices	3
Low T_1 sensitivity sequence parameters	
TS	24.3 ms
n_{k0} (steps to central line of k-space)	8
N (number of readout pulses per image)	19
FA	15°
TR	2.52 ms
Number of slices	1
PDw sequence parameters	
n_{k0} (steps to central line of k-space)	11
N (number of readout pulses per image)	42
FA	15° & 3°
TR	2.68 ms
Number of slices	3

Table 7-1 – Parameters used for simulations. Imaging parameters are representative of local practice. a - Native MOLLI T1 values (septal region for myocardium) [14]. b - Relaxivity at 3 T for Gd-BT-D03A [186, 187]. c - Mean healthy volunteer values [1]. d - Mean healthy volunteer and chronic infarct core values (rounded to 2 significant figures) [189]. e - Middle of normal range [188].

T_1 was calculated for the start of each cardiac cycle based on Equation 7-2, native T_1 and the contrast agent concentration at that time, and used for the simulation of each recovery period for that cycle (i.e. variation in T_1 within the readout of a single image or between slices acquired within the same cycle was neglected). The magnetisation at the end of each cardiac cycle was carried

forward to the next cycle so the full magnetisation history was simulated. SE is related to the effective flip angle of the saturation pulse, θ, by Equation 7-3, so SE of 1 corresponds to perfect saturation while 0 represents no preparation and 2 perfect inversion.

Equation 7-3

$$SE = 1 - \cos(\theta)$$

As described in section 2.2 perfect spoiling and mono-exponential recovery and decay of magnetisation were assumed. For each simulation the magnetisation was assumed to start in its equilibrium state at the start of imaging (i.e. for the first cardiac cycle) but the residual magnetisation following acquisition of each image and the subsequent recovery period was used for the later cardiac cycles (i.e. the signal intensity for each time point depended on the full prior history of magnetisation evolution accounting for variation in T_1 due to the variation in contrast agent concentration). Saturation pulses were modelled as non-selective whereas readout pulses were slice-selective (i.e. magnetisation for each slice was only affected by readout pulses for that slice), in agreement with the implementation on the scanner. Signal was recorded as being proportional to the magnitude of the transverse magnetisation, reflecting standard practice, with Rician noise added where required. Further details of this simulation process are presented in an appendix (section 7.6).

Deconvolution of resulting data with a one-compartment model was performed to estimate MBF and v_d using the non-linearity correction methods described below, and results were compared to ground truth. Deconvolution was performed using a multivariable constrained optimisation (fmincon) initialised with F_p at 0.4 ml/min/ml (limits of 10^{-6} - 10^{6} ml/min/ml) and v_d at 30% (limits of 10^{-6} - 100%)[1]. Figure 7-3 summarises the process.

[1] To avoid undefined numbers or invalid solutions lower limits several orders of magnitude lower than realistic values were used where physical lower limits were zero. Upper limits were several orders of magnitude higher than realistic values for F_p and 100% for v_d as values greater than that are not physically valid.

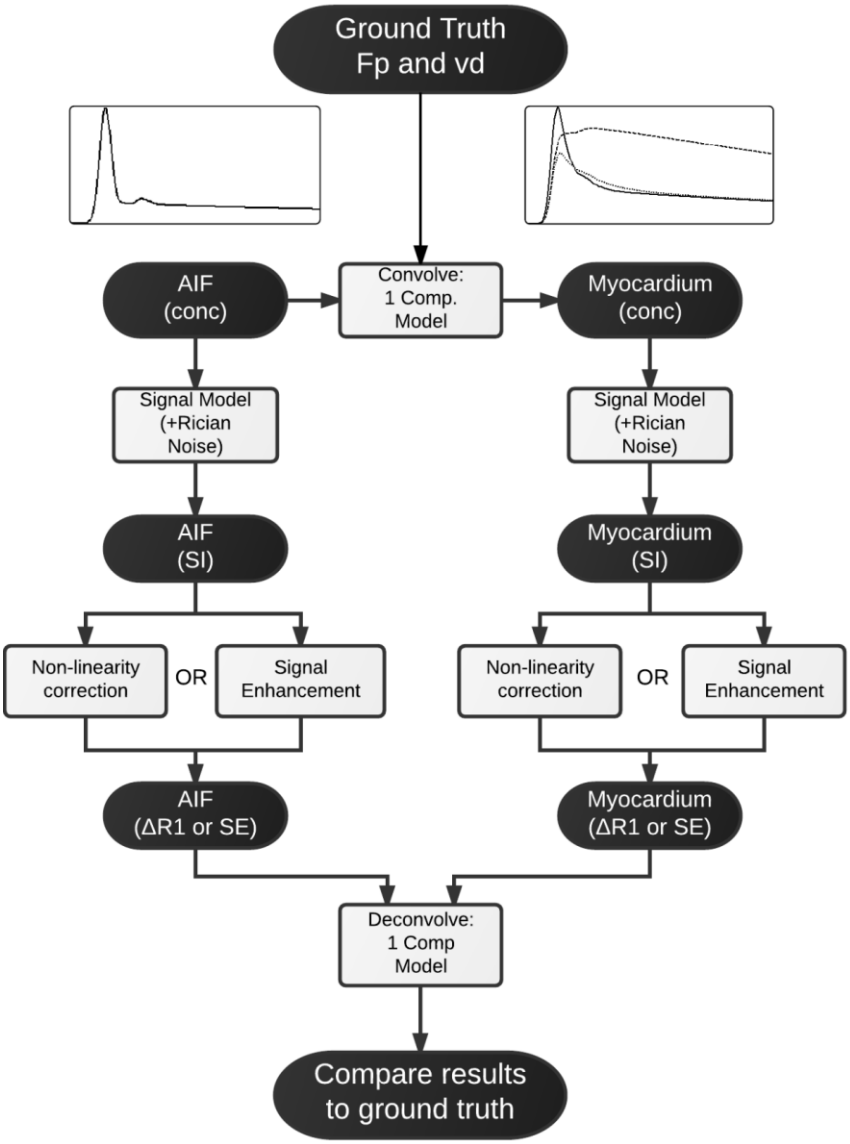

Figure 7-3 – Simulation process. Simulations are repeated with varying SNR, ground truth physiological parameters and saturation efficiencies. Graphical representations show the AIF and myocardial concentration curves (dotted – healthy myocardium at rest, solid – healthy myocardium under stress, dashed – infarcted myocardium at rest).

To assess errors introduced directly through deconvolution (due to factors including optimiser termination tolerances and discrete temporal sampling) noise-free concentration curves were analysed. Additionally deconvolution was performed using simulated signal enhancement data to assess errors incurred without non-linearity correction.

7.2.1 Model-based non-linearity correction methods

Model-based approaches involve the use of additional data and imaging parameters to constrain a signal model for the acquired data. This model is used to convert SI data into ΔR_1 throughout the DCE-MRI acquisition prior to

deconvolution. One potential model for this, Equation 7-4, is based on Equation 2-1 and Equation 2-17 ((for n=n_{k0} - based on Larsson *et al* [44], see section 2.2.3) with substitution of 1-SE for cos(θ) (as per Equation 7-4).

Equation 7-4

$$SI(t) = S_0 \cdot \left| f(T_1, SE) \right| \text{ where } f(T_1, SE) = \left(1 - SE \cdot e^{-(TS-(n_{k0}-1)TR)\cdot R_1(t)}\right) \cdot a^{n_{k0}-1} + b\frac{1-a^{n_{k0}-1}}{1-a}$$

Here $a = e^{-TR\cdot R_1(t)} \cdot \cos(\alpha)$, $b = 1 - e^{-TR\cdot R_1(t)}$ and R_1 is longitudinal relaxation rate ($1/T_1$). S_0 is the SI that would be acquired from a single readout pulse applied at equilibrium (i.e. $S_0 = |\Psi \cdot M_0 \cdot \sin\alpha \cdot \exp(-TE/T_2^*)|$), α is the readout pulse flip angle and n_{k0} is the number of RF pulses prior to the acquisition of the central k-space data.

In the above model magnetisation is assumed to be fully recovered immediately prior to the preparation pulse. An alternative, Equation 7-5, based on that derived in Kershaw's thesis [45], is to assume that the starting magnetisation is at a reduced steady-state value.

Equation 7-5

$$SI(t) = S_0 \cdot \left| g(T_1, SE) \right| \text{ where:}$$

$$g(T_1, SE) = \frac{b}{1-a}\left(1 - a^{n_{k0}-1}\right) + .\left(1 - E_1\right)a^{n_{k0}-1} + ..$$

$$...E_1 a^{n_{k0}-1}(SE-1)\left[\frac{-\cos(\alpha)E_D\left(b\frac{1-a^{N-1}}{1-a} - \frac{1}{\cos(\alpha)} + a^{N-1}(1-E_1)\right) - 1}{1 + (SE-1)a^{N-1}E_1\cos(\alpha)E_D}\right]$$

Here a and b are defined as above, $E_1 = e^{-(TS-(n_{k0}-1)TR)R_1}$ and $E_D = e^{-(ISD-TS-(N-n_{k0})TR)R_1}$ with ISD being the inter-shot delay, i.e. the time between saturation pulses and N being the total number of RF pulses in each readout train.

This model is based on Equation 2-1 and Equation 2-29 (for n=n_{k0}), see section 2.2.3. This model reflects a series of repeated epochs of magnetisation preparation and image readout is also an approximation to the true scenario in myocardial DCE-MRI and in the forward simulations here. Firstly the saturation

pulses are not regularly spaced temporally as the three slices are acquired contiguously after the ECG trigger, followed by a delay until the next trigger. Consequently there is an equal delay between the saturation pulses within the same cardiac cycle but a longer (and variable, due to natural variability in cycle length) delay between the final saturation pulse and the first saturation pulse of the next cycle. Secondly T_1 varies throughout the DCE-MRI acquisition. Both of these mean that steady-state will not be reached as described in this equation. Additionally a mixture of slice-selective (readout) and non-selective (saturation) pulses are used, so while stationary spins are affected by one saturation pulse for each slice during each cardiac cycle they will only be affected by readout pulses following one of these.

For these studies an approximation is made that the saturation pulses are equally spaced throughout the cardiac cycle, in which case the ISD used for the model is the cardiac cycle length divided by the number of slices. A further approximation that is made to allow this model to be used is to assume that all pulses (including the slice-selective readout pulses) affect all spins. Such an assumption was made for the SR sequences, where it was assumed that the effect of the saturation pulses would dominate. For the PDw sequences however, where only slice selective readout pulses are applied, the model was implemented with an ISD equal to the cardiac cycle.

Note that both of these models are approximations, and both differ to the forward simulation in that they use an analytical model of the signal intensity rather than a step-by-step simulation of the magnetisation evolution. The forward simulations thus account for the non-uniform spacing of slices throughout the cardiac cycle and for the variation in T_1 between cycles due to the varying contrast agent concentration. An appendix to this chapter (section 7.7) examines the behaviour of these analytical models in comparison to the forward simulations in further detail and explains the reasoning for inclusion of both models in this work.

These techniques can be sensitive to factors that lead to the signal not being fully described by the model. As well as the limitations of the models not fully describing the pulse sequences additional such factors include B_1 homogeneity, readout flip angle accuracy, motion and slice profile. These are not present in

either the forward or backward calculation in the simulation study but could explain additional errors in the experimental data.

In the following descriptions of model based correction methods f(T_1,SE) is used to describe the methods implemented with the fully-recovered model. In order to use the alternative model with steady-state prior magnetisation (as described in Equation 7-5) f(T1,SE) is replaced by g(T1,SE) in Equation 7-7 to Equation 7-12.

7.2.1.1 Native T_1 based

SI can be converted to ΔR_1 using measured or assumed baseline T_1 [101], a method that has also been employed in DCE-MRI using inversion recovery sequences [87, 190, 191]. In the model (Equation 7-4 or Equation 7-5), S_0 is initially unknown and SE is assumed to be ideal. For this approach as the model is only calculated with SE=1 the two signal models are equivalent, as f(T_1,SE) and g(T_1,SE) both simplify to exactly the same expression (Equation 7-6).

Equation 7-6

$$f\left(T_1, SE=1\right)=g\left(T_1, SE=1\right)=\left(1-e^{-TS\cdot R_1(t)}\right)\cdot a^{n_{k0}-1}+b\frac{1-a^{n_{k0}-1}}{1-a}$$

Consequently only one set of results valid for both models is presented. S_0 is determined using baseline SI and an independently derived native T_1 (Equation 7-7) and is assumed to be constant throughout the acquisition, allowing estimation of T_1(t) throughout the remainder of the DCE-MRI acquisition (Equation 7-8, evaluated using single variable optimisation (fzero) with limits of T_1 ranging from 10^{-6}-10^{6} ms. NB the fzero algorithm requires only a starting value or constraint range, the latter was used in its implementation in this study).

Equation 7-7

$$S_0=\frac{SI_{DCE,baseline}}{f\left(T_{1,baseline}, SE=1\right)}$$

Equation 7-8

$$T_1(t) = \underset{T_1(t)>0}{\arg\min}\left((S_0 \cdot f(T_1(t), SE=1) - SI(t))^2\right)$$

7.2.1.2 Native proton density weighted (PDw) based

An alternative model-based method to determine S_0 uses the acquisition of a proton density weighted (PDw) image (without saturation preparation) prior to DCE-MRI acquisition [102, 107]. In the absence of T_1 weighting S_0 would be sampled directly by that acquisition. In practice residual T_1 weighting is present in the PDw sequence (due to the read-out pulses). Estimates of baseline T_1 (Equation 7-9, evaluated using single variable optimisation (fzero) with limits of T_1 ranging from 10^{-6}-10^6 ms) and subsequently S_0 and $T_1(t)$ are therefore estimated using baseline DCE data and SI data from the PDw series, using the same approach as for the native T_1 based method. This approach is similar in principle to the two-point saturation recovery T_1 mapping method described in section 4.4.4 [144], although with the PDw and SR data acquired in separate series and a shorter saturation time used.

Equation 7-9

$$T_{1,baseline} = \underset{T_1(t)>0}{\arg\min}\left(\left(\frac{f(T_{1,baseline}, SE=1, \alpha_{DCE})}{f(T_{1,baseline}, SE=0, \alpha_{PDw})} - \frac{SI_{DCE,baseline}}{S_{PDw,baseline}}\right)^2\right)$$

Following estimation of the baseline T_1 the analysis proceeds as for native T_1 based correction, using Equation 7-7 and Equation 7-8. For this study the read-out flip angle was initially maintained at 15° for the PDw image. However, it is common to reduce the read-out flip angle in the PDw sequence [102, 107] to reduce T_1 weighting, in which case the appropriate value of α must be used in $f(T_1,SE)$ in the denominator of Equation 7-9. Simulations using PDw based conversion were repeated with α = 3°.

Note that while SE is assumed to be ideal for the saturation prepared sequence the two signal models are not equivalent for this method as the signal models are also used to describe the PDw sequence for which SE=0 and so the models are not equivalent (the models converge only at T_1=0).

7.2.1.3 Bookend T_1 based

The model-based methods described above sample SI only at native T_1 to define the signal model, under the assumption of ideal saturation efficiency. By sampling SI at two known T_1 values the relationship can be defined without this assumption by estimating SE (Equation 7-10, evaluated using single variable optimisation (fmincon) with a starting value of SE = 1 and limits of 0 and 2) and S_0 (Equation 7-11). $T_1(t)$ is estimated as before, but using a study specific SE estimate (Equation 7-12, evaluated using single variable optimisation (fzero) with limits of T_1 ranging from 10^{-6}-10^6 ms). For the bookend technique only the optimisations use functions that are non-monotonic. The implementation used in this work, and the implications of this, are discussed in the appendix (section Chapter 7). These issues are not relevant to the other techniques where the analytical functions used are monotonic (as ideal saturation is assumed in the analysis).

Equation 7-10

$$SE = \underset{0<SE<2}{\arg\min}\left(\left(\frac{\left|f\left(T_{1,baseline}, SE\right)\right|}{\left|f\left(T_{1,post-contrast}, SE\right)\right|} - \frac{SI_{DCE,baseline}}{SI_{DCE,post-contrast}}\right)^2\right)$$

Equation 7-11

$$S_0 = \frac{SI_{DCE,baseline}}{\left|f\left(T_{1,baseline}, SE\right)\right|} \text{ or, equivalently, } S_0 = \frac{SI_{DCE,post-contrast}}{\left|f\left(T_{1,post-contrast}, SE\right)\right|}$$

Equation 7-12

$$T_1(t) = \underset{T_1(t)>0}{\arg\min}\left(\left(S_0 \cdot \left|f\left(T_1(t), SE\right)\right| - SI(t)\right)^2\right)$$

To perform this method a T_1 measurement and DCE-MRI sequence are acquired at a delayed post-contrast time, as well as prior to contrast administration. Ideally the post-contrast data would be acquired while T_1 is stable, but this is not achievable in practice as T_1 will vary due to distribution and clearance of the contrast agent. However steps can be taken to approximate this including sampling post-contrast T_1 and SI as close together (temporally) as possible at a time where T_1 varies slowly (once equilibrium has been reached between blood and interstitium and variation is driven

predominantly by renal clearance). Measuring SI either side of T_1 and interpolating to estimate the former at the time of the latter (or vice-versa) could further reduce the impact of [CA] variation between measurements. In the clinical protocols described in later chapters the former approach (with T_1 maps and delayed DCE-MRI data acquired close together 10 minutes after the final contrast agent injection) was taken for the hyperoxaemia study. For the STEMI study this approach was not conceived at the time of protocol design (see section 1.4) and so the need to acquire late DCE-MRI data and T_1 maps close together had not been identified. However DCE-MRI data was available either side of a delayed T_1 map so the latter approach of interpolation could be employed as described in section 9.2).

7.2.2 Dual-sampling methods

The following methods allow independent measurement of an AIF that is minimally affected by non-linearity. These can be employed in isolation or in combination with model-based correction.

7.2.2.1 Dual-bolus

The dual-bolus approach [103-105] exploits the approximately linear response of SI to [CA] at the relatively low concentrations encountered in the myocardium from a standard dose, and in the AIF from a smaller diluted “pre-bolus” dose administered before the main bolus. Signal enhancement data from the pre-bolus AIF is scaled by the bolus:pre-bolus dose ratio and analysed with the tissue response from the main bolus. As linearity of SI response is assumed no conversion to [CA] is required.

This method was simulated by repeating simulation of the AIF signal data for a pre-bolus of equal duration with concentrations scaled by one-tenth. In practice residual contrast agent from the pre-bolus will affect the tissue curve. The details of this depend on physiological parameters and the delay between administrations. Additionally changes in AIF shape may occur between contrast agent administrations due to factors such as altered contrast agent volume or viscosity (depending on whether the pre-bolus is administered as a smaller volume or diluted dose) or cardiac output variation [192]. For simplicity it is assumed in these simulations that the pre-bolus is cleared entirely prior to main

bolus administration, and that the shape of the pre-bolus and bolus AIF and myocardial concentration curves are identical except for scaling.

7.2.2.2 Dual-sequence

The model-based methods described above can be combined with a dual-sequence acquisition (described in section 3.2.1.1) in which the AIF is acquired using a sequence with reduced T_1 sensitivity interleaved with the higher sensitivity sequences for myocardial curve acquisition [108]. This allows both curves to be acquired with a more linear signal response to [CA], while not introducing the additional procedural steps or concerns regarding bolus shape differences of the dual-bolus approach. For this study myocardial curves were generated using the same pulse sequence parameters employed for other methods. SI curves for the AIF were generated using the parameters described in the "Low T_1 sensitivity sequence parameters" section of Table 7-1. The latter is designed to result in a linear relationship between SI and T_1 over a wider range of concentrations, although yields reduced CNR and resolution.

The initial application of the dual-sequence approach [108] was for estimation of relative blood flow (myocardial perfusion reserve). If the technique achieves a linear signal response for both myocardial and AIF data then signal enhancement data can be used for this purpose despite the difference in the sensitivity of the two sequences, as this will lead to equal relative errors in the stress and rest results. Consequently the errors would cancel out when calculating MPR. For quantification of absolute parameters the differences must be accounted for and so signal enhancement cannot be used. For simplicity in this simulation study the PDw model-based conversion technique was adopted, although in practice any model-based conversion technique could be chosen. Calculated ΔR_1 is used in the deconvolution as for the other model-based approaches. Additionally, spatial resolution of the low T_1 sensitivity sequence is typically lower, which results in greater signal-to-noise ratio (SNR). In the simulations the noise standard deviation was halved for the low T_1 sensitivity sequence compared to the standard sequence. This is performed to achieve the approximate SNR that would be expected in this sequence, due to differences in the resolution and the number of lines of data read compared to the conventional sequence.

7.2.3 Simulation study

Using each of the methods described above MBF and v_d were estimated and compared to ground truth for a range of conditions (healthy myocardium at rest and under pharmacologically induced stress and chronically infarcted myocardium). In general MBF will be lower for infarcted myocardium at rest (one study reported regional blood flow in chronic infarct regions as being 16% lower than for remote myocardium [193]). For simplicity, and to allow comparison of results following alteration of individual parameters, the value of MBF used for infarct simulation was equal to that used for healthy myocardium. Similarly v_d was not altered between rest and stress. Parameter values used are presented in Table 7-1.

Simulations were performed in the absence of and including Rician noise with standard deviation equal to 0.5% of S_0. For healthy resting myocardium this corresponds to peak myocardial SNR of 14 which is similar to the data acquired in the volunteer study and that reported elsewhere [194]. Simulations with noise were repeated 100 times and mean and standard deviation of fitted parameters recorded. SE was varied in increments of 0.01 from 0.9-1.1, and at finer increments (0.005) in the central part of this range (0.97-1.03). SE is defined such that residual longitudinal magnetisation after saturation equals (1-SE)*M_z^- (where M_z^- is the prior longitudinal magnetisation) with positive values being aligned with the equilibrium state and negative values representing inverted magnetisation. Simulations were repeated with each model (Equation 7-4, full recovery, and Equation 7-5, steady-state).

Methods which utilise T_1 values were repeated assuming T_1 measurement errors of 5% (both under- and over-estimation).

7.2.4 Phantom study

In order to independently estimate the saturation efficiency for the pulse and scanner used in the volunteer and patient studies in the following chapters a phantom study was performed using the TO5 phantom from the Eurospin Test Object range [195]. This phantom consists of 18 gels of varying T_1 and T_2 values across a physiologically relevant range, of which up to 12 can be mounted in a supporting holder. For this experiment 12 gels were used but the

gels were bound together closely in a bundle rather than mounted in the holder, so that the spatial separation of the individual tubes was minimised.

Data were acquired using the DCE-MRI sequences described in the volunteer study in the following chapter. Additionally single slice MOLLI T_1 maps (using the shortened schemes of 5s(3s)3s and 4s(1s)3s(1s)2s) were acquired. For all ECG triggered imaging a simulated trace (implemented within the scanner software) with a heart rate of 60 bpm was used.

Additionally a reference standard IR-SE sequence was performed for T_1 measurement and a SR-GE for independent saturation efficiency estimation. Images were acquired with 11 TI (50-5000ms) values in the IR-SE experiment, with 15s between inversion pulses, and 15 TS values (30-5000ms) in the SR-GE experiment with 10s between saturation pulses. For the IR-SE experiment a single line of image data was acquired following each inversion pulse whereas for the SR-GE sequence a modified standard (i.e. not dual-sequence) cardiac perfusion sequence in which a single slice was acquired was used to ensure the same saturation pulse was used as is used for the clinical protocols.

MOLLI T_1 and DCE-MRI signal data were analysed using the methods described for the model-based non-linearity corrections methods described above with one gel identified to represent native tissue and a second to represent contrast enhanced tissue for the bookend T_1 method. Using the model parameters derived from that analysis T_1 is estimated from the signal intensity data in the other gels and compared to reference standard T_1. Signal intensity data from both IR-SE and SR-GE sequences were fitted to a three parameter model of longitudinal recovery, as in Equation 7-13.

Equation 7-13

$$S = S_0\left(1 - (1 - \cos\theta)exp^{PPD/T_1}\right)$$

In this equation PPD is the pre-pulse delay (inversion time (TI) for IR-SE and saturation time (TS) for SR-GE). S_0 is the signal that would be acquired in the absence of a preparation pulse and θ is the flip angle of the magnetisation preparation pulse.

7.3 Results

7.3.1 Simulation study

Simulated signal-time curves are presented in Figure 7-4.

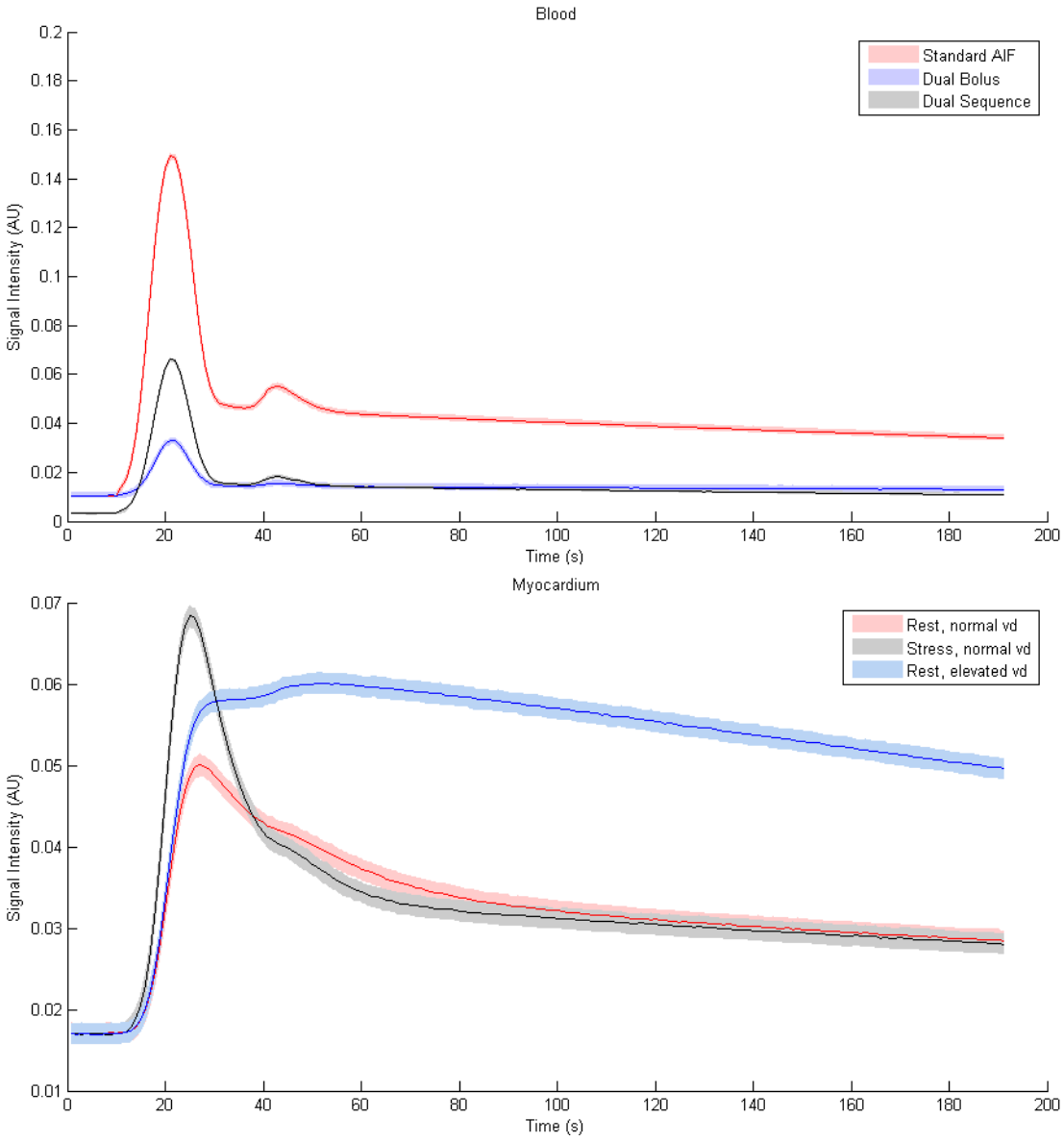

Figure 7-4 – AIF signal-time curves assuming ideal saturation efficiency. Shading indicates one standard deviation. Top: AIF. The red line shows the standard AIF (normal acquisition, full dose), blue reduced dose pre-bolus for the dual-bolus method and black the AIF from the full dose using the lower sensitivity sequence for the dual-sequence method (N.B. the same AIF concentration curves were used for rest and stress). Bottom: Myocardial response. Each line shows a different tissue status. The same myocardial signal data is used for each analysis method.

7.3.1.1 Signal enhancement methods

Deconvolving noise-free concentration curves directly yielded negligible errors (<0.0002%). However analysing signal enhancement data without non-linearity correction (Figure 7-5 and Figure 7-6) yielded systematic bias with 30-50% over-estimation of MBF and errors in v_d between -4% and +10% (for ideal saturation and in the absence of noise). Errors in both parameters showed an approximately linear dependence on saturation efficiency with larger variation in MBF accuracy and less variation for slices 2 and 3 in comparison to slice 1.

Use of the dual-bolus strategy led to underestimation rather than overestimation of MBF and v_d, but with lower absolute error than with the single bolus strategy at perfect saturation efficiency (Figure 7-7 and Figure 7-8). Precision, particularly in v_d, was substantially decreased. As for the single bolus strategy saturation efficiency dependency was lower for slices 2 and 3 than for slice 1.

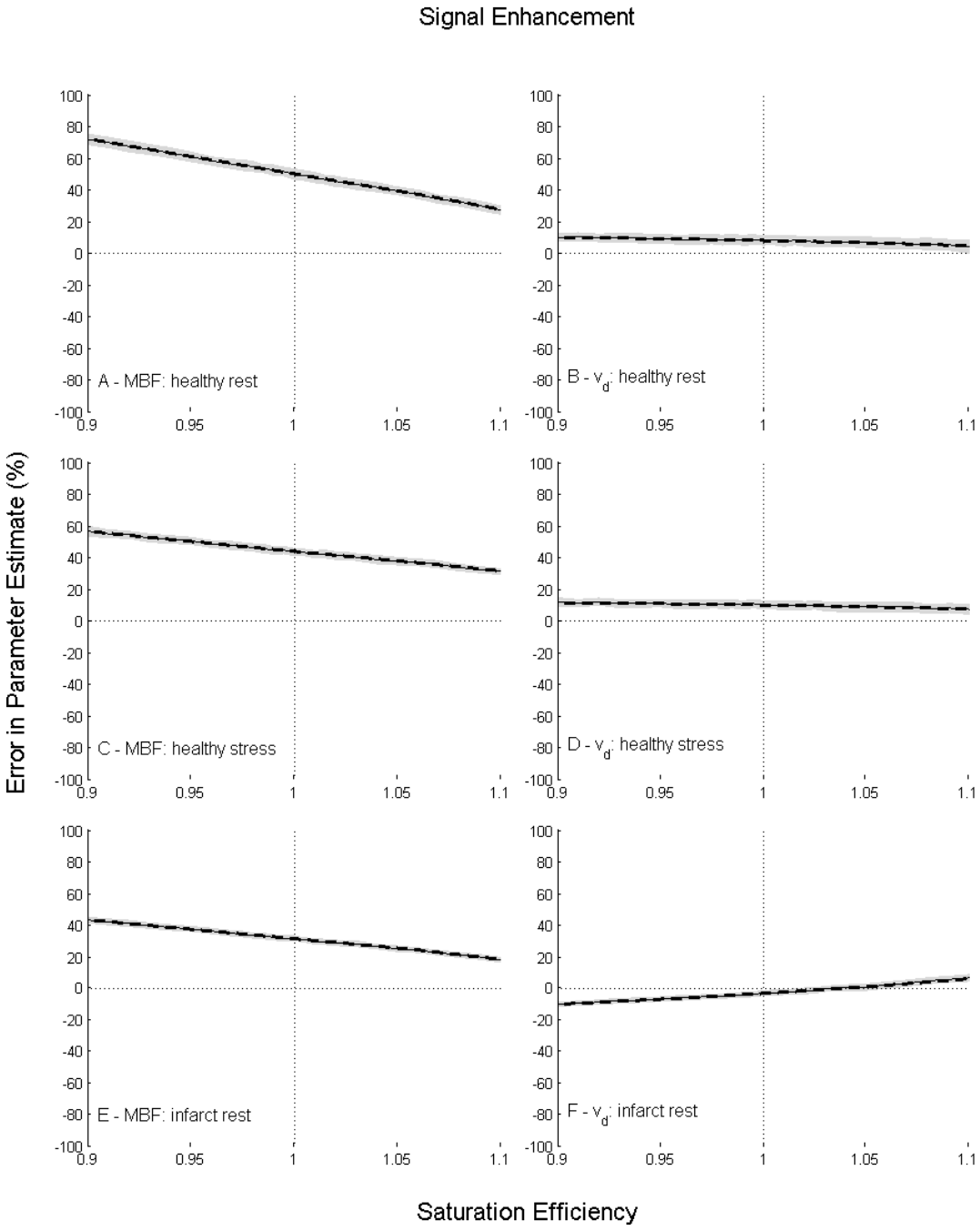

Figure 7-5 – Errors in estimated parameters for healthy myocardium at rest (A – MBF and B – v_d) and stress (C – MBF and D – v_d) and for infarcted myocardium at rest (E – MBF & F – v_d) for deconvolution using signal-enhancement data without correction for non-linearity. Dashed lines show results in the absence of noise. Solid lines and shading show mean results +/- one standard deviation for data with noise. Results presented are from slice 1.

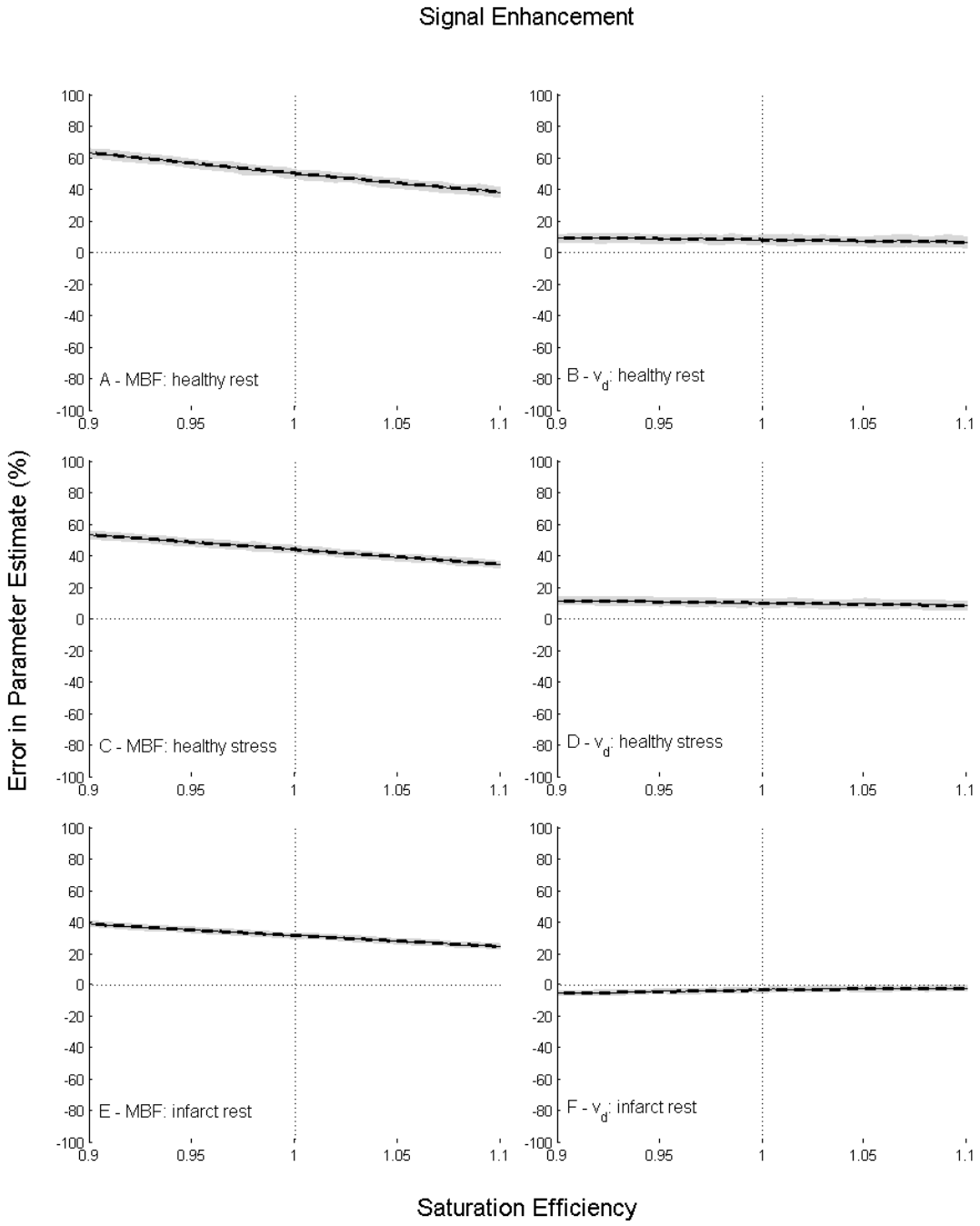

Figure 7-6 – Errors in estimated parameters for healthy myocardium at rest (A – MBF and B – v_d) and stress (C – MBF and D – v_d) and for infarcted myocardium at rest (E – MBF & F – v_d) for deconvolution using signal-enhancement data without correction for non-linearity. Dashed lines show results in the absence of noise. Solid lines and shading show mean results +/- one standard deviation for data with noise. Results presented are from slice 2. Results were similar between slices 2 and 3.

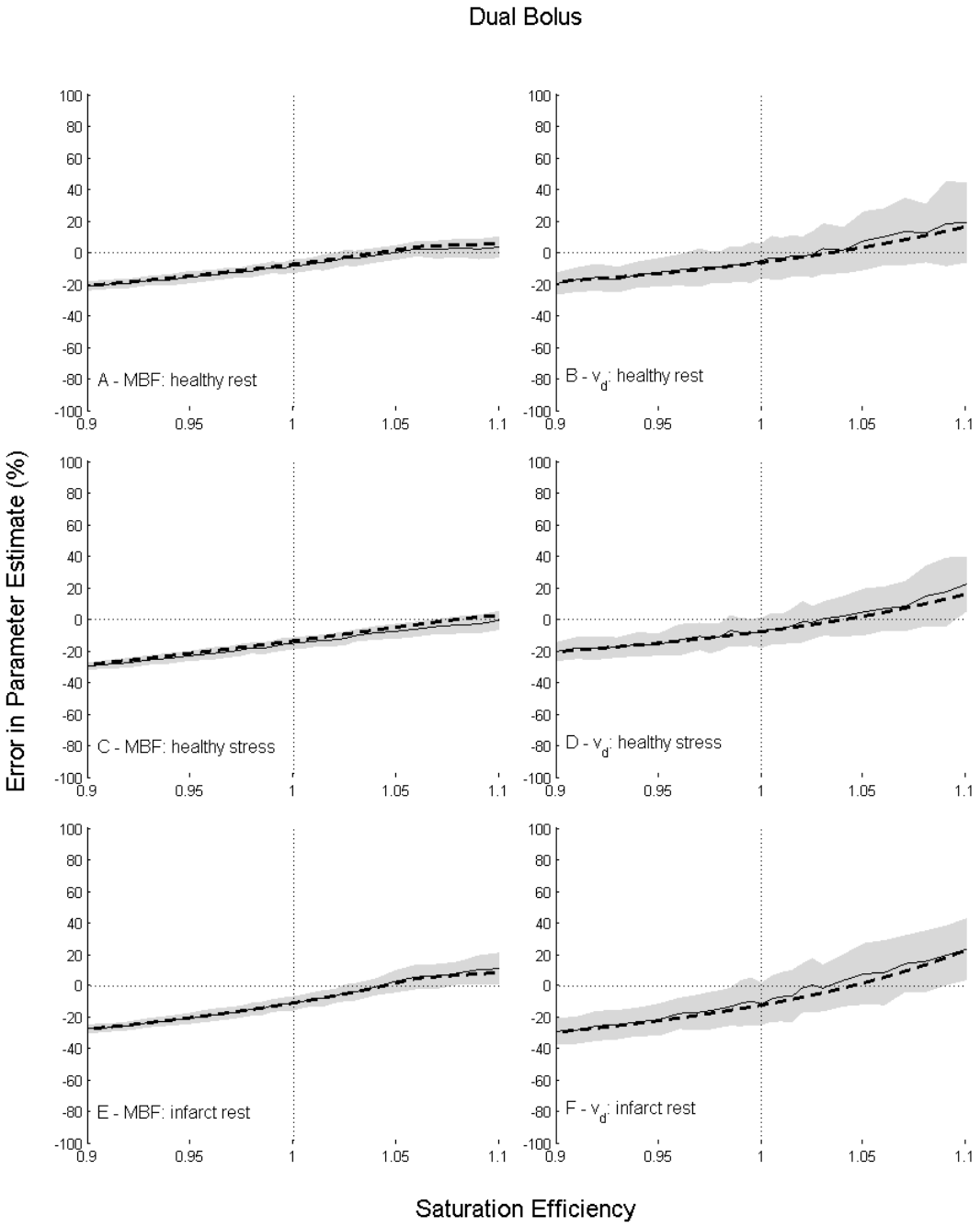

Figure 7-7 - Errors in estimated parameters for healthy myocardium at rest (A – MBF and B – v_d) and stress (C – MBF and D – v_d) and for infarcted myocardium at rest (E – MBF & F – v_d) for deconvolution using the dual-bolus method. Dashed lines show results in the absence of noise. Solid lines and shading show mean results +/- one standard deviation for data with noise. Results presented are from slice 1.

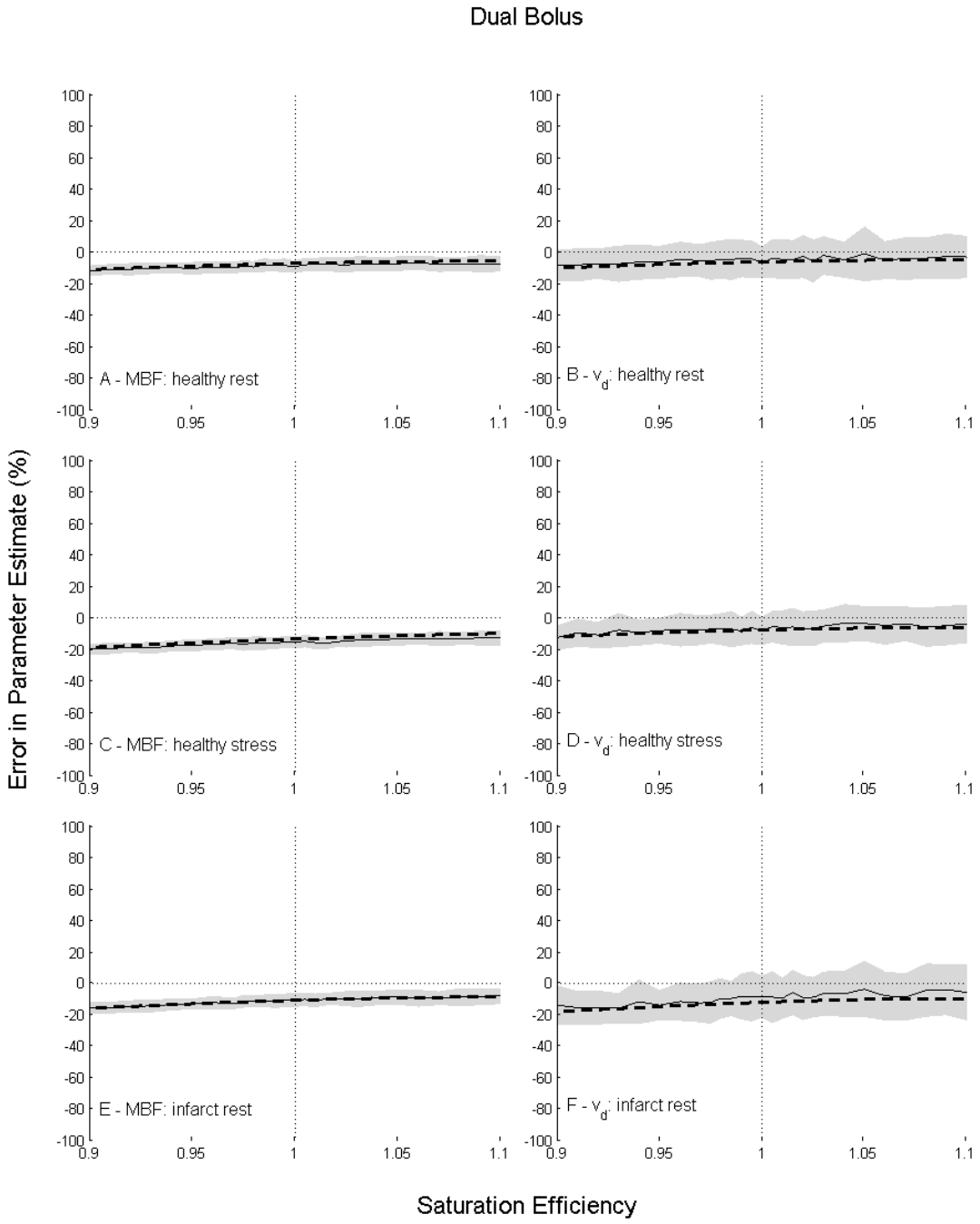

Figure 7-8 - Errors in estimated parameters for healthy myocardium at rest (A – MBF and B – v_d) and stress (C – MBF and D – v_d) and for infarcted myocardium at rest (E – MBF & F – v_d) for deconvolution using the dual-bolus method. Dashed lines show results in the absence of noise. Solid lines and shading show mean results +/- one standard deviation for data with noise. Results presented are from slice 2. Results were similar between slices 2 and 3.

7.3.1.2 Effect of saturation efficiency and non-linearity correction – T_1 based methods

Results using native T_1 based correction (Figure 7-9 and Figure 7-10) were identical for the two signal models, as the relevant signal model equation is only used under the assumption of perfect saturation in which case Equation 7-5 reduces to Equation 7-4 (i.e. $f(T_1,SE=1) \equiv g(T1,SE=1)$). Mean errors were negligible for ideal saturation but show strong dependence on saturation efficiency, particularly for slice 1 for which the method fails at high levels of over-saturation as the estimated S_0 value is less than the peak AIF signal. For slice 1 a marked decrease in precision and accuracy was observed above a saturation efficiency of around 1.06, where baseline signal is nulled due to the partial inversion.

For the bookend T_1 based method differences do arise between signal models (Figure 7-11 and Figure 7-12 (full recovery model) and Figure 7-13 and Figure 7-14 (steady-state model)). Errors at non-ideal saturation efficiency are smaller than for native T_1 based correction but saturation efficiency dependent errors persist as neither model fully describes the signal generation. Consequently for both models the degree of saturation pulse imperfection is underestimated (i.e. SE is overestimated when less than 1 but underestimated when greater than 1). These errors are larger when the full recovery model is used, but the steady-state model leads to poorer precision. As for native T_1 based correction a marked change in performance is observed above a saturation efficiency of 1.06 for slice 1 due to baseline signal nulling.

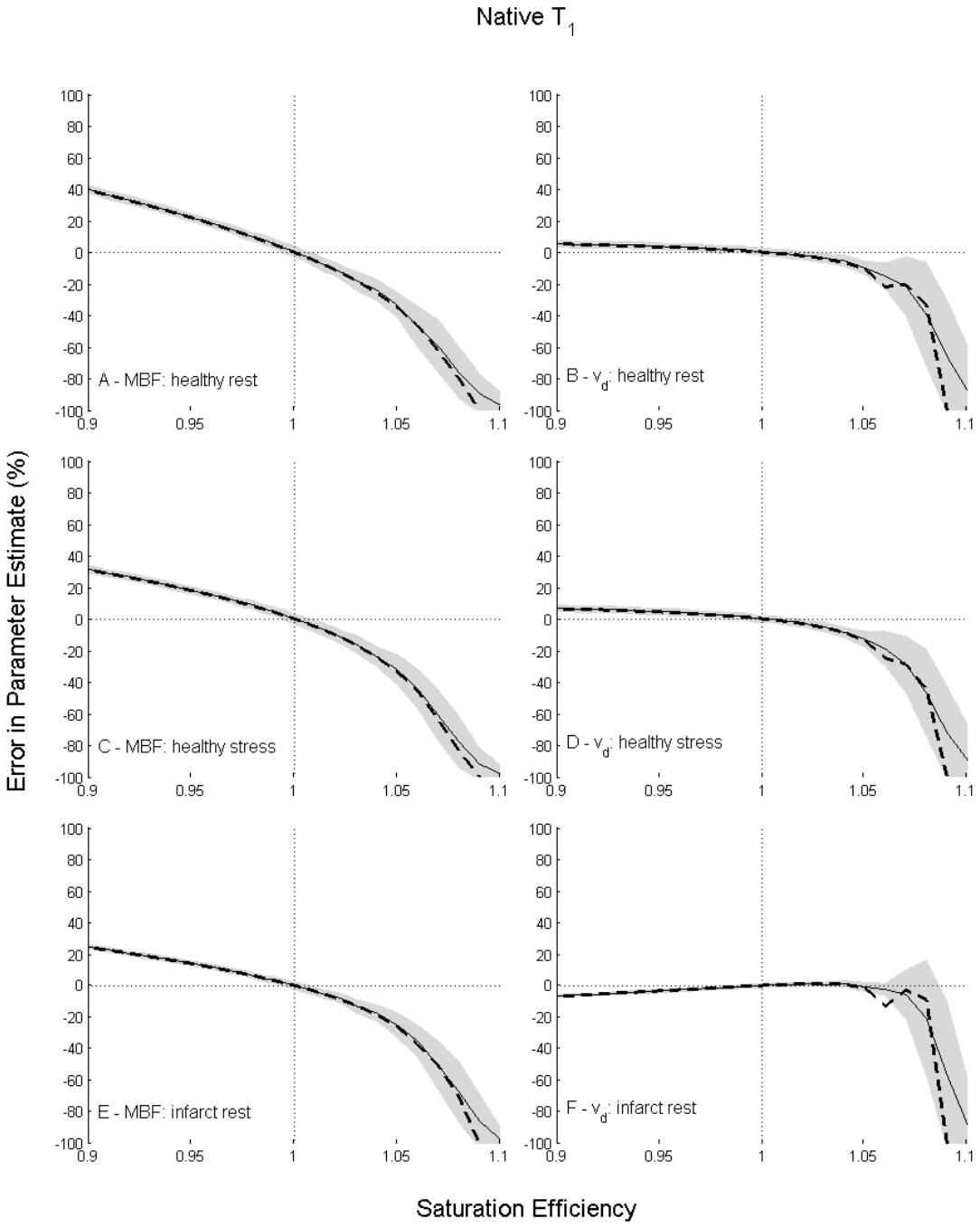

Figure 7-9 - Errors in estimated parameters for healthy myocardium at rest (A – MBF and B – v_d) and stress (C – MBF and D – v_d) and for infarcted myocardium at rest (E – MBF & F – v_d) for deconvolution using native T_1 based correction. Dashed lines show results in the absence of noise. Solid lines and shading show mean results +/- one standard deviation for data with noise. Results presented are from slice 1. Results are identical for the two signal models as the two signal models are equivalent for assumed ideal saturation (Equation 7-6).

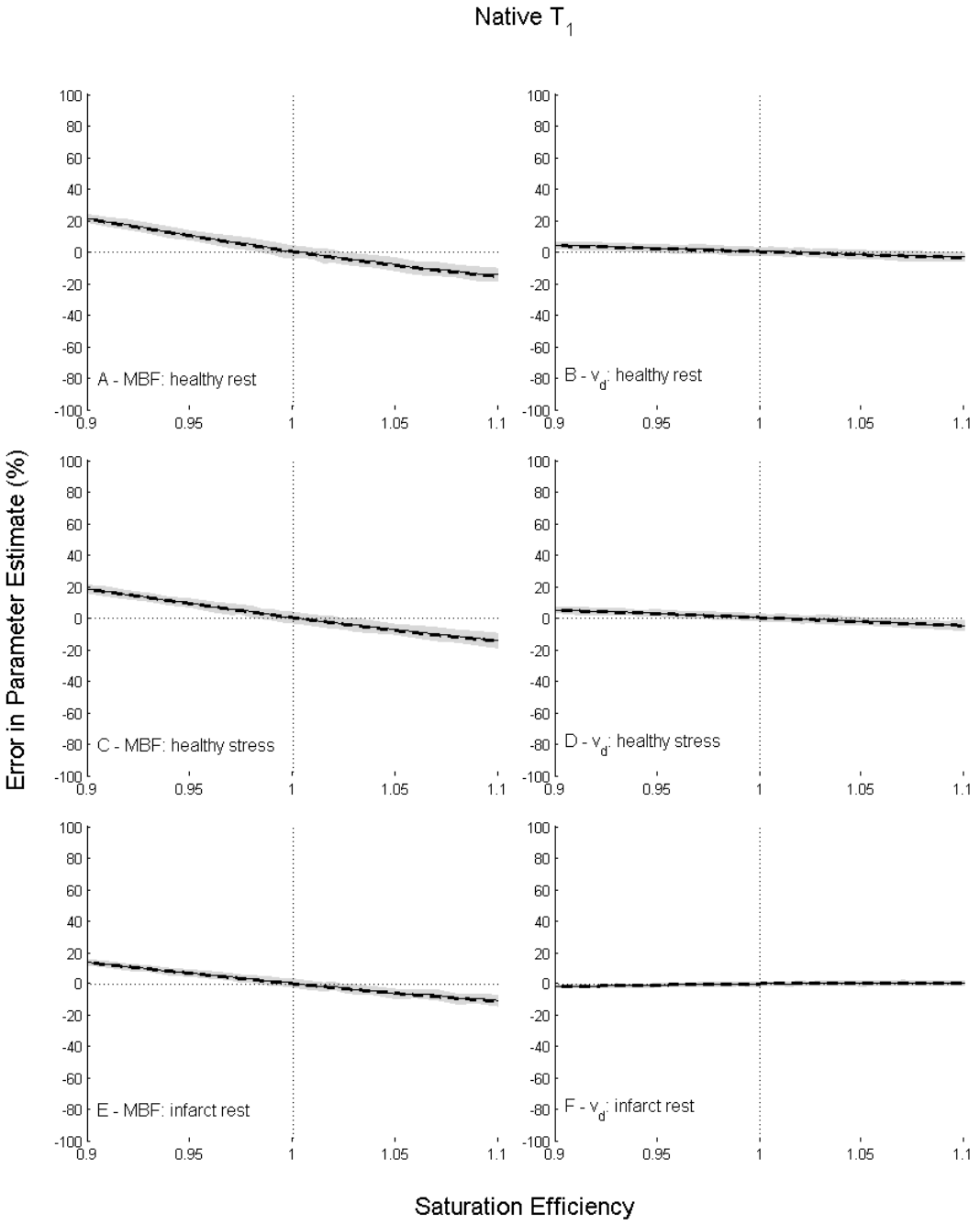

Figure 7-10 - Errors in estimated parameters for healthy myocardium at rest (A – MBF and B – v_d) and stress (C – MBF and D – v_d) and for infarcted myocardium at rest (E – MBF & F – v_d) for deconvolution using native T_1 based correction. Dashed lines show results in the absence of noise. Solid lines and shading show mean results +/- one standard deviation for data with noise. Results presented are from slice 2. Results were similar between slices 2 and 3. Results are identical for the two signal models as the two signal models are equivalent for assumed ideal saturation (Equation 7-6).

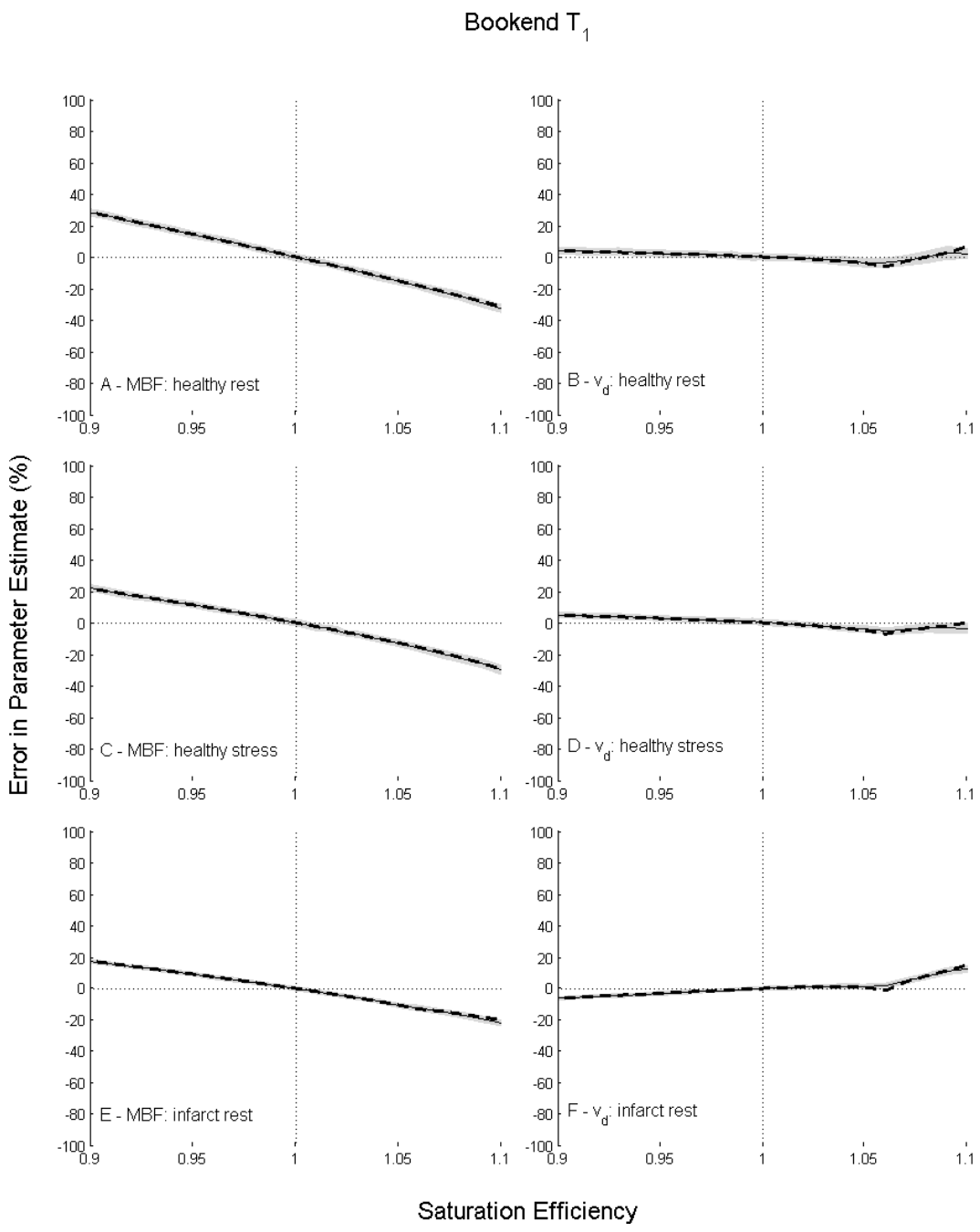

Figure 7-11 - Errors in estimated parameters for healthy myocardium at rest (A – MBF and B – v_d) and stress (C – MBF and D – v_d) and for infarcted myocardium at rest (E – MBF & F – v_d) for deconvolution using bookend T_1 based correction and the full recovery signal model. Dashed lines show results in the absence of noise. Solid lines and shading show mean results +/- one standard deviation for data with noise. Results presented are from slice 1.

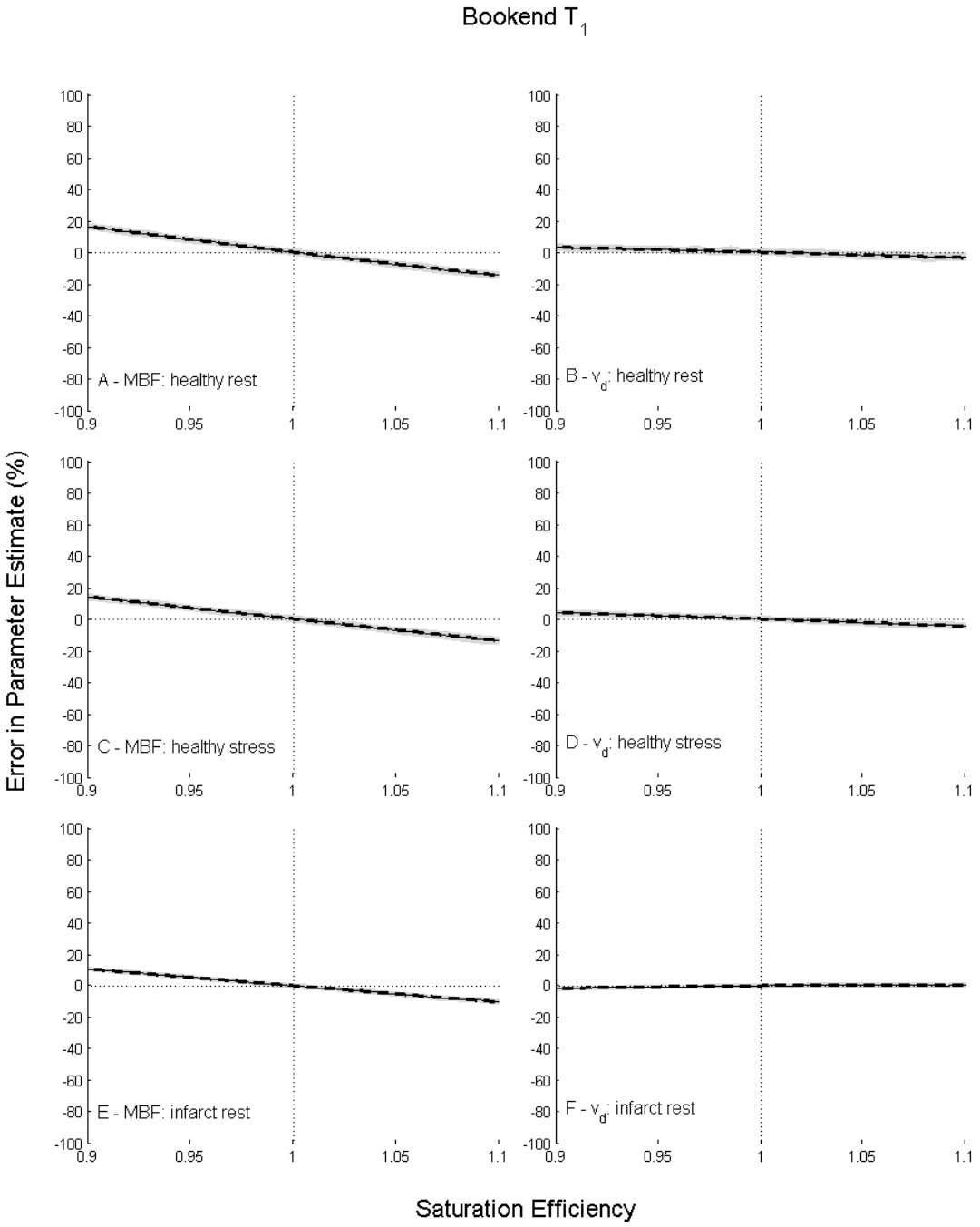

Figure 7-12 - Errors in estimated parameters for healthy myocardium at rest (A – MBF and B – v_d) and stress (C – MBF and D – v_d) and for infarcted myocardium at rest (E – MBF & F – v_d) for deconvolution using bookend T_1 based correction and the full recovery signal model. Dashed lines show results in the absence of noise. Solid lines and shading show mean results +/- one standard deviation for data with noise. Results presented are from slice 2. Results were similar between slices 2 and 3.

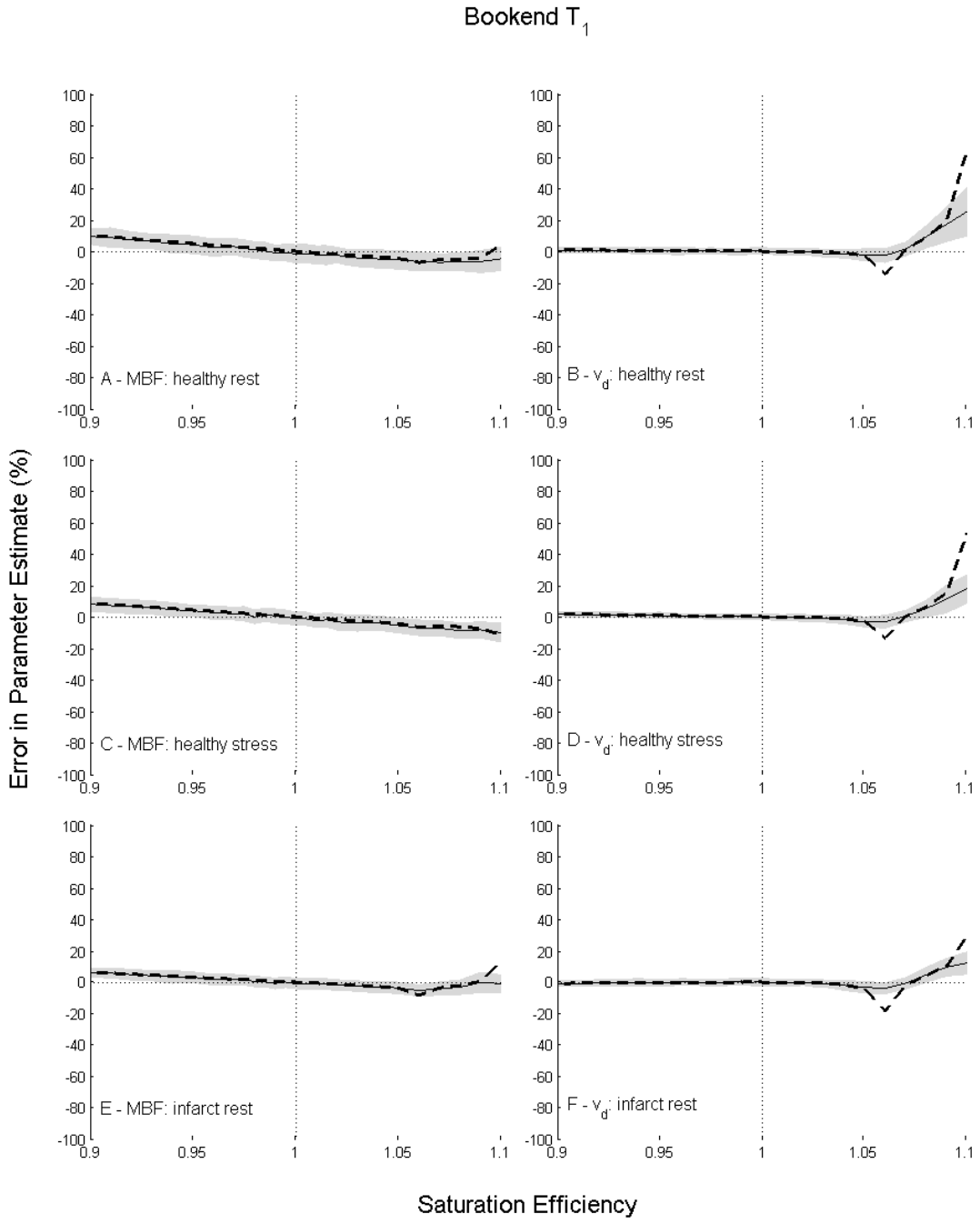

Figure 7-13 - Errors in estimated parameters for healthy myocardium at rest (A – MBF and B – v_d) and stress (C – MBF and D – v_d) and for infarcted myocardium at rest (E – MBF & F – v_d) for deconvolution using bookend T_1 based correction and the steady-state signal model. Dashed lines show results in the absence of noise. Solid lines and shading show mean results +/- one standard deviation for data with noise. Results presented are from slice 1.

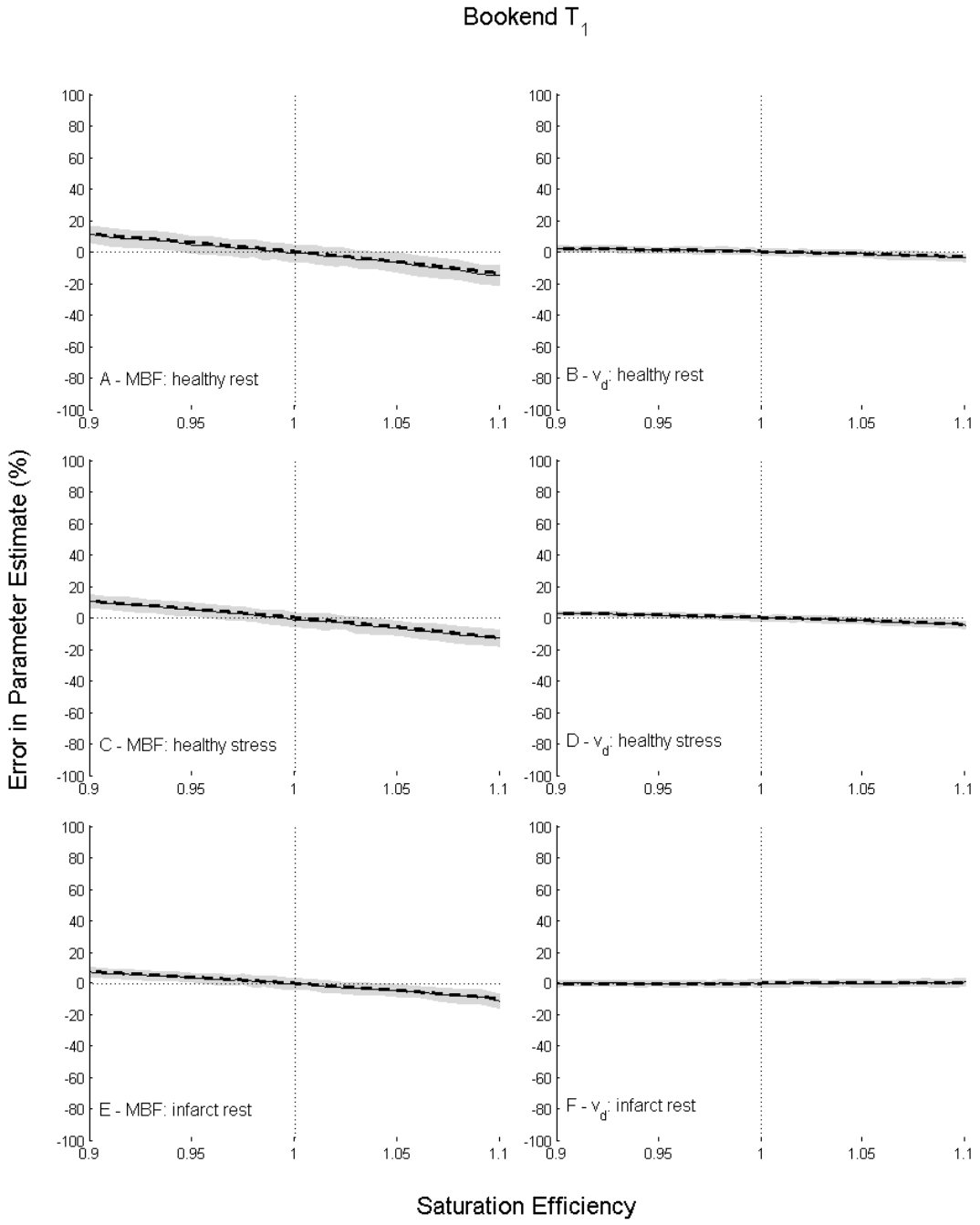

Figure 7-14 - Errors in estimated parameters for healthy myocardium at rest (A – MBF and B – v_d) and stress (C – MBF and D – v_d) and for infarcted myocardium at rest (E – MBF & F – v_d) for deconvolution using bookend T_1 based correction and the steady-state signal model. Dashed lines show results in the absence of noise. Solid lines and shading show mean results +/- one standard deviation for data with noise. Results presented are from slice 2. Results were similar between slices 2 and 3.

Effect of Errors in Measured T_1

In simulations of T_1 measurement dependent model-based methods errors in T_1 were found to introduce systematic errors in estimated physiological parameters. For model-based correction using native T_1 alone, underestimation

of T_1 led to a decrease in estimated S_0 for a given SE, and consequently lower estimates of both physiological parameters (Figure 7-15 and Figure 7-16). As described previously, the native T_1 method results are identical for both signal models, as the model equation is only ever used under the assumption of ideal saturation.

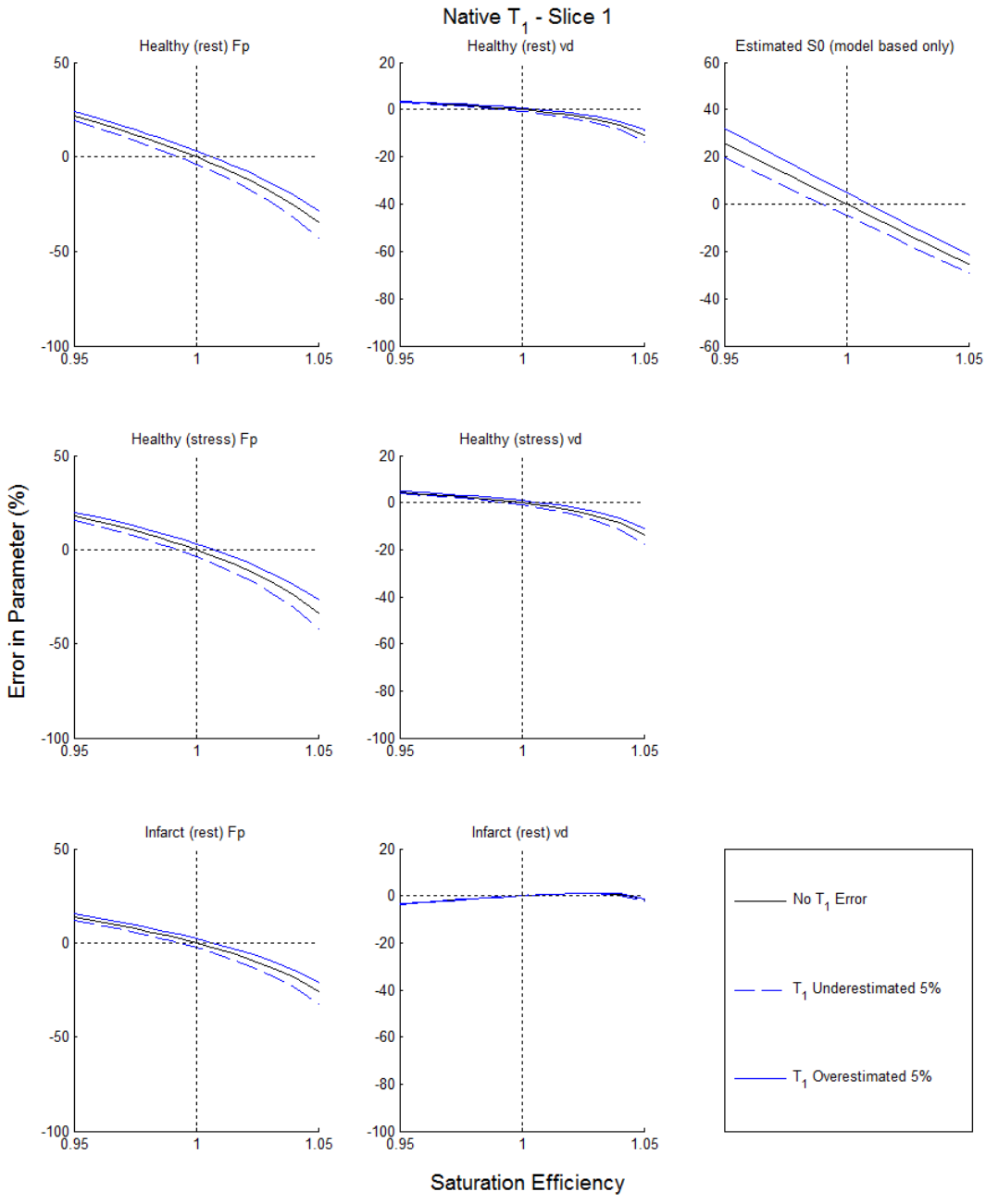

Figure 7-15 – Errors introduced in analysis due to errors in measured T_1 used for model-based correction. Data is for the native T_1 based conversion for slice 1. Results are identical for the two signal models as the two signal models are equivalent for assumed ideal saturation (Equation 7-6).

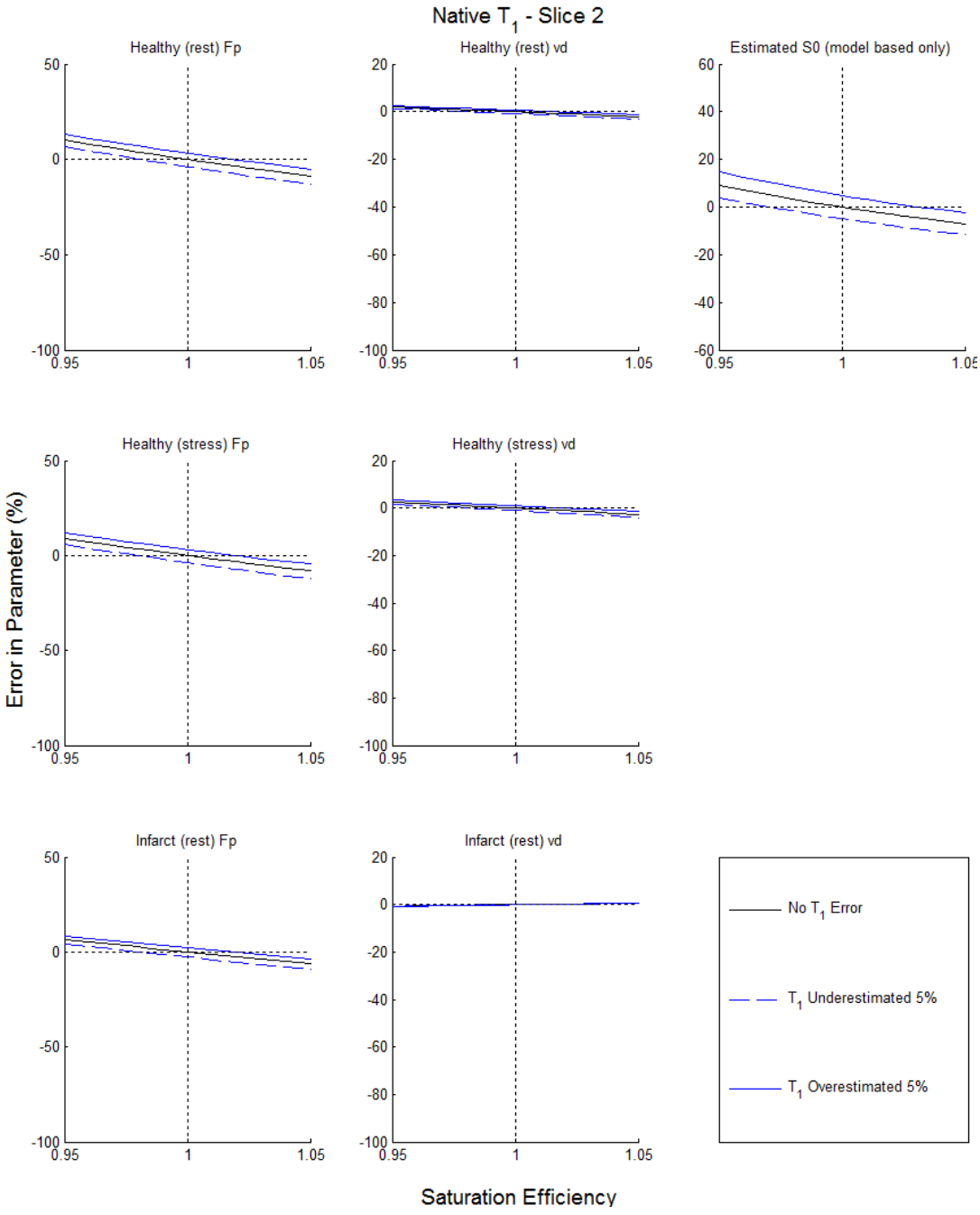

Figure 7-16 – Errors introduced in analysis due to errors in measured T_1 used for model-based correction. Data is for the native T_1 based conversion for slice 2. Results are identical for the two signal models. Results are similar between slices 2 and 3.

For the bookend method the direction of bias on physiological results depended on the T_1 measurement in error (Figure 7-17 and Figure 7-18 (full recovery model) and Figure 7-19 and Figure 7-20 (steady-state model)). Underestimation of native T_1 led to a slight overestimation of S_0 and SE. This resulted in increases in estimated physiological parameters. For overestimation of post-contrast T_1 the converse was true, and the sensitivity to a given relative T_1 error

was greater. Consequently when errors were simulated in both native and post-contrast T_1 simultaneously differences in SE, S_0, MBF and v_d were in the same direction as the T_1 error, unlike for the native T_1 based method.

For the bookend T_1 based method use of the steady-state model leads to larger T_1 error sensitivity than the full recovery model.

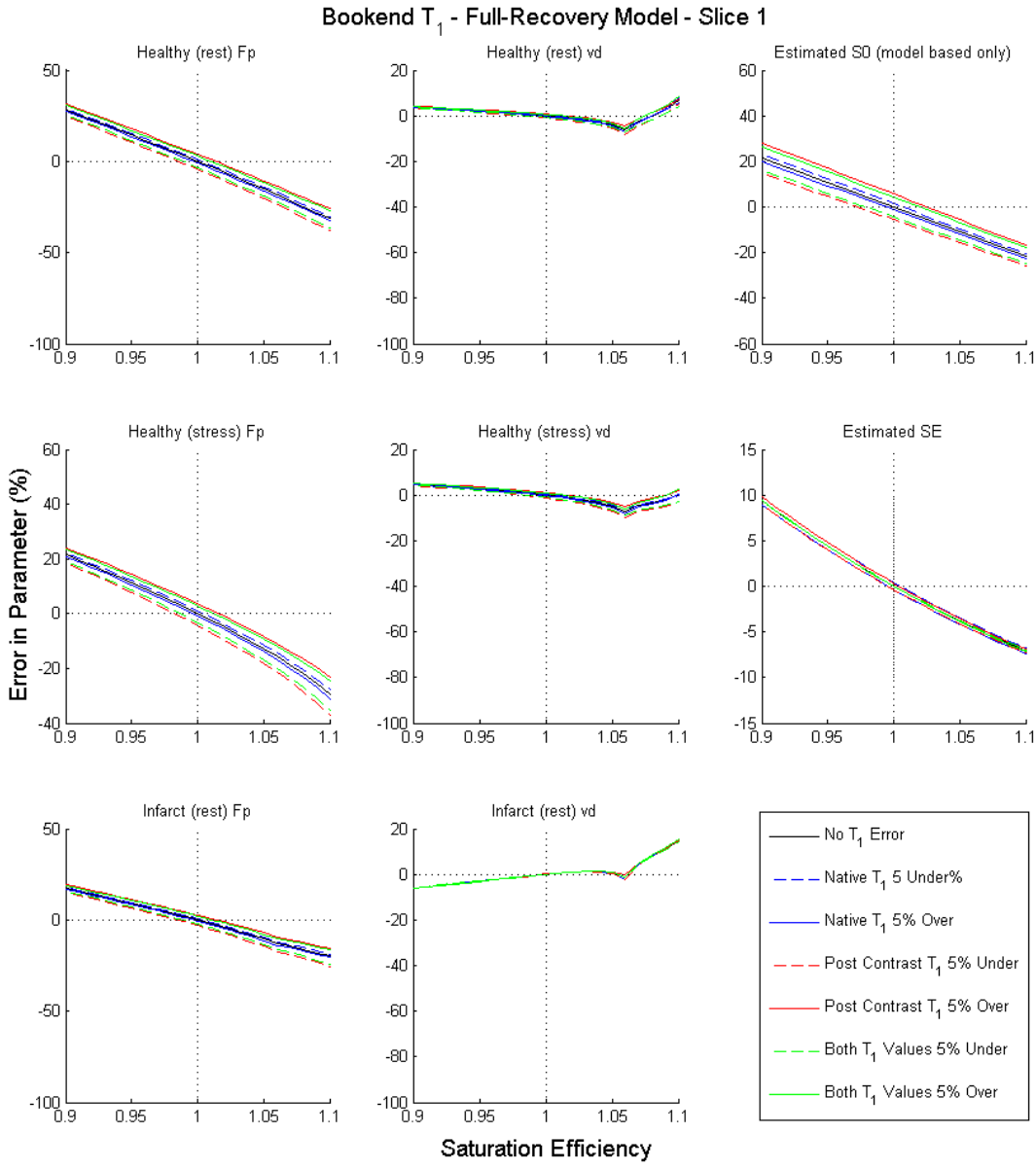

Figure 7-17 – Errors introduced in analysis due to errors in measured T_1 used for model-based correction. Data is for the bookend T_1 based conversion with the full recovery signal model for slice 1.

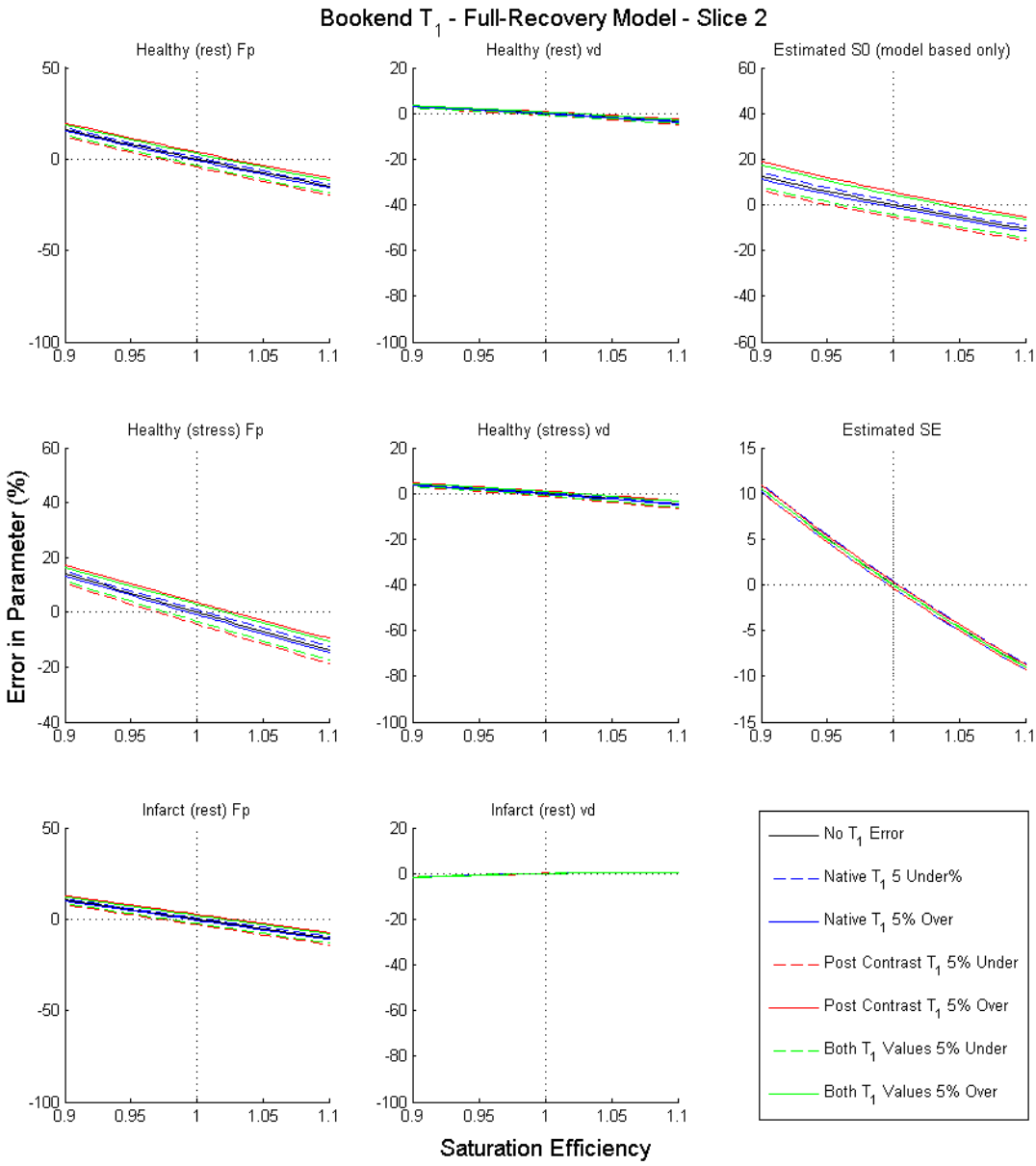

Figure 7-18 – Errors introduced in analysis due to errors in measured T_1 used for model-based correction. Data is for the bookend T_1 based conversion with the full recovery signal model for slice 2. Results are similar between slices 2 and 3.

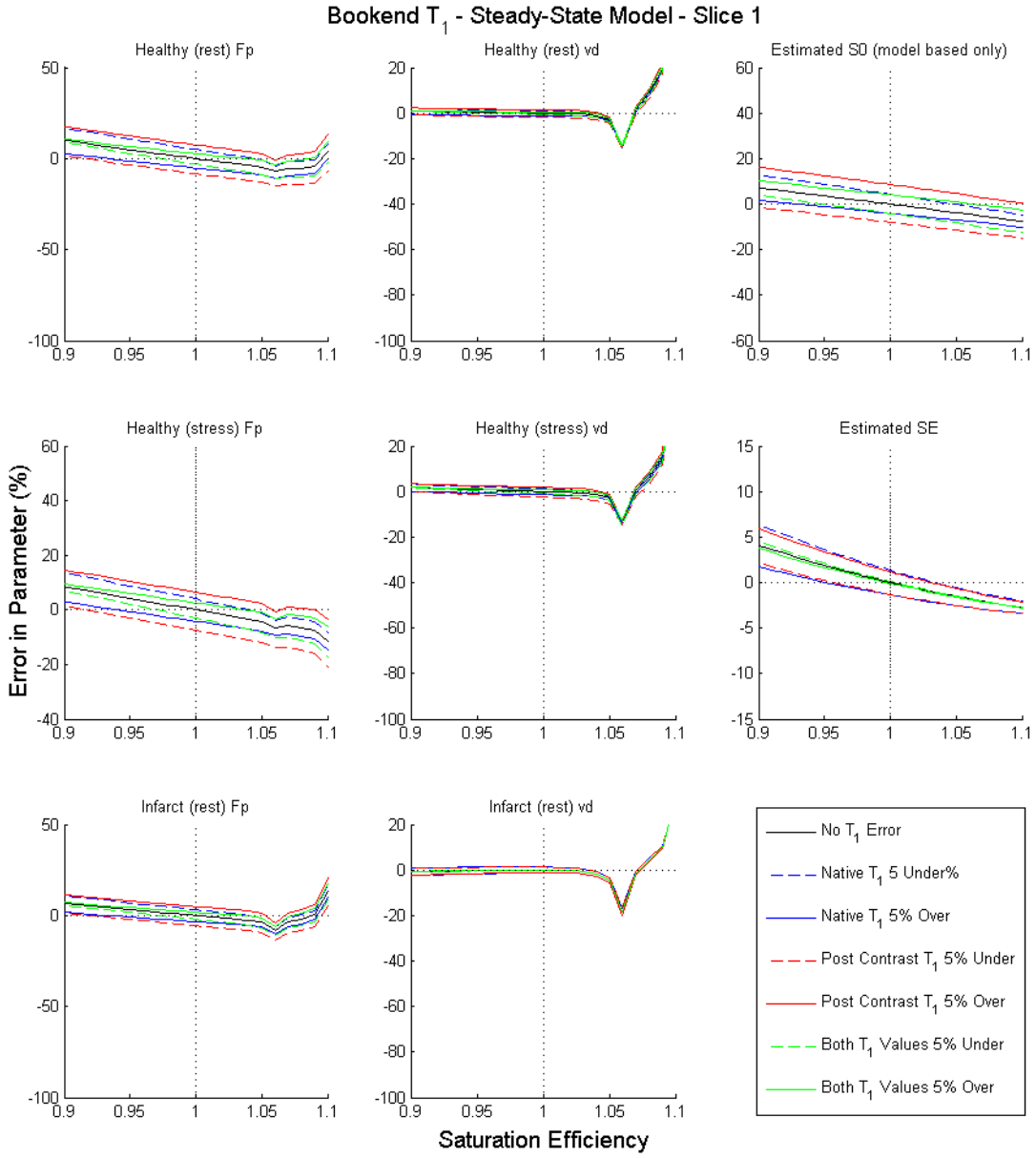

Figure 7-19 – Errors introduced in analysis due to errors in measured T_1 used for model-based correction. Data is for the bookend T_1 based conversion with the steady-state signal model for slice 1.

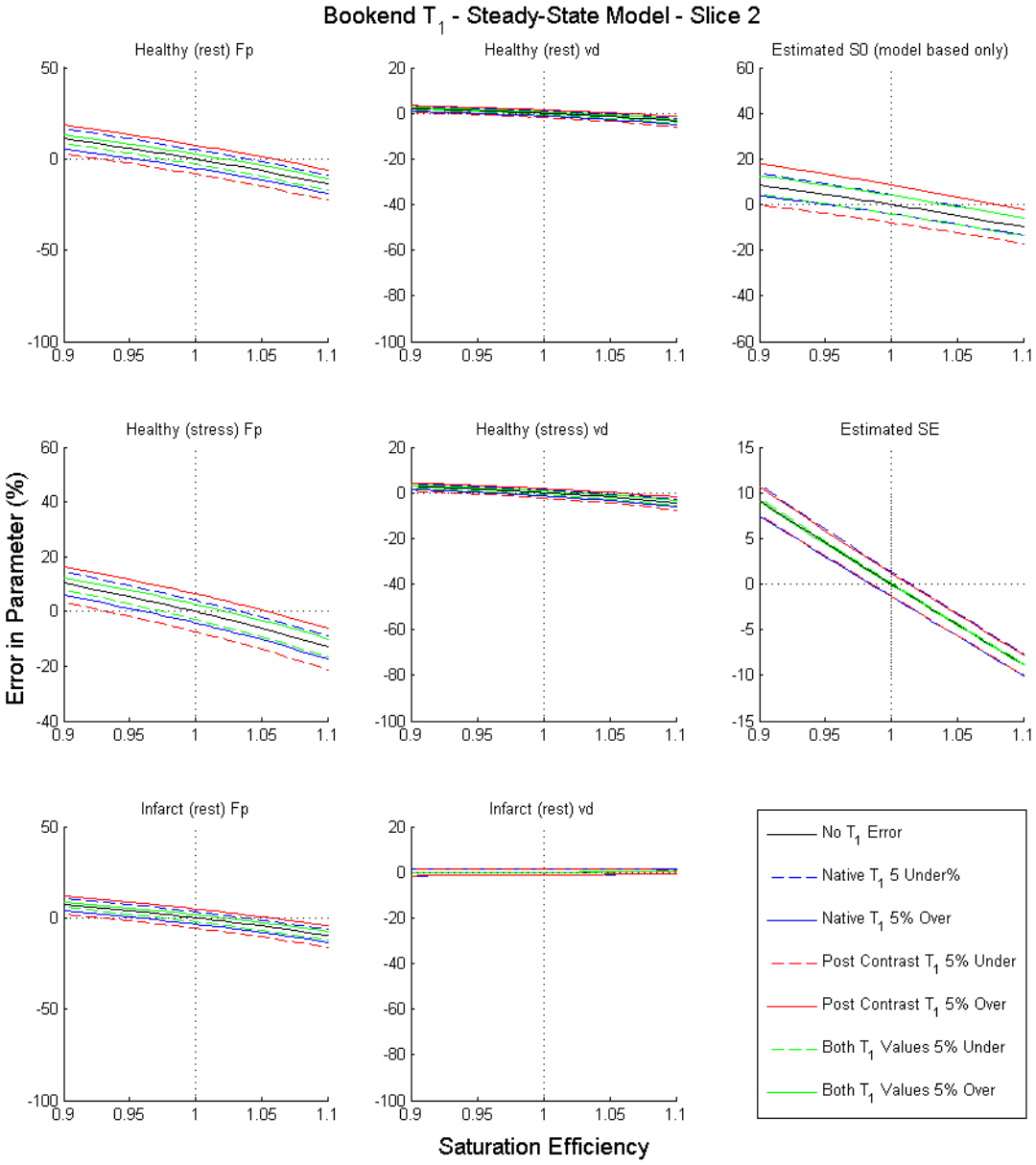

Figure 7-20 – Errors introduced in analysis due to errors in measured T_1 used for model-based correction. Data is for the bookend T_1 based conversion with the steady-state signal model for slice 2. Results are similar between slices 2 and 3.

7.3.1.1 Effect of saturation efficiency and non-linearity correction – PDw based methods

With a 15° readout flip angle signal varied substantially in the early phases of the proton density weighted sequence simulation due to residual T_1 weighting. Analysis failed for the standard acquisition simulation with both models as a positive native T_1 could not be estimated that described the signal after this variation in both the SR and PDw sequences. Reducing the readout flip angle to

further reduce T_1 weighting in the PDw sequence alleviated these problems (Figure 7-21 and Figure 7-22, full recovery model, and Figure 7-23 and Figure 7-24 steady-state model). Saturation efficiency dependency was present although typically less than for the bookend T_1 based method. Unlike the T_1 based methods a small bias was present even with ideal saturation efficiency with 4-5% under-estimation of MBF for the full recovery model and a lesser degree of 2-3% over-estimation for the steady-state model.

When combined with dual-sequence acquisition the PDw based correction method yields only small levels of bias at ideal saturation (Figure 7-25, full recovery model, and Figure 7-26, steady-state model). However the method exhibits very strong saturation efficiency dependency and accuracy deteriorates sharply above SE of 1.02 due to signal nulling in the AIF baseline. This occurs at a lower level of over-saturation than for slice 1 in the other methods due to the shorter TS used. As only one slice of short TS data is acquired, and errors arise mostly due to ΔR_1 quantification inaccuracies in the AIF, there is little difference between slices for this method. Furthermore there is little difference between signal models.

Due to the reduced sensitivity, and hence decreased SNR, in the short TS AIF precision in both MBF and v_d estimates is considerably reduced in the dual-sequence approach.

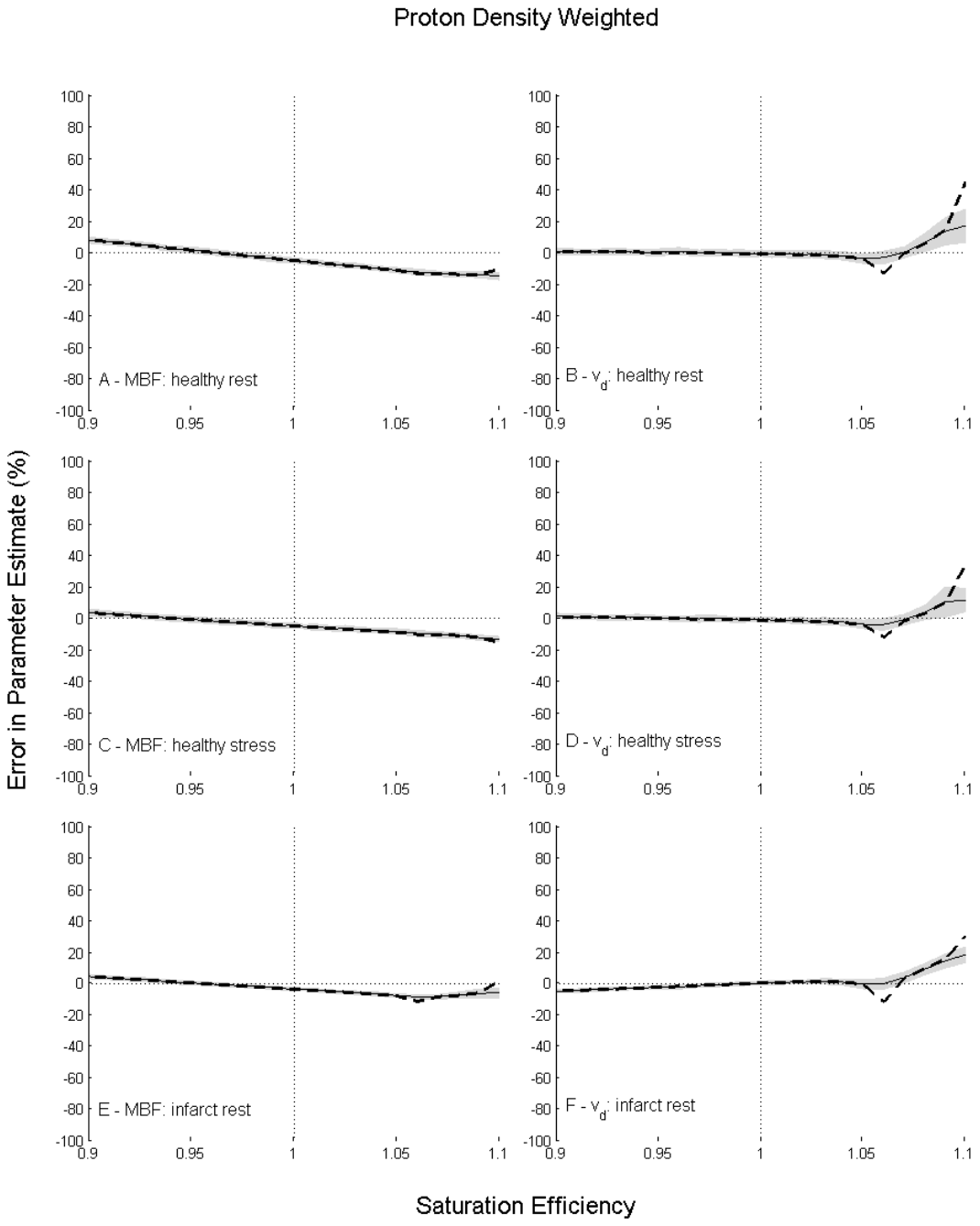

Figure 7-21 - Errors in estimated parameters for healthy myocardium at rest (A – MBF and B – v_d) and stress (C – MBF and D – v_d) and for infarcted myocardium at rest (E – MBF & F – v_d) for deconvolution using proton density weighted image based correction and the full recovery signal model. Dashed lines show results in the absence of noise. Solid lines and shading show mean results +/- one standard deviation for data with noise. Results presented are from slice 1 with 3° flip angle.

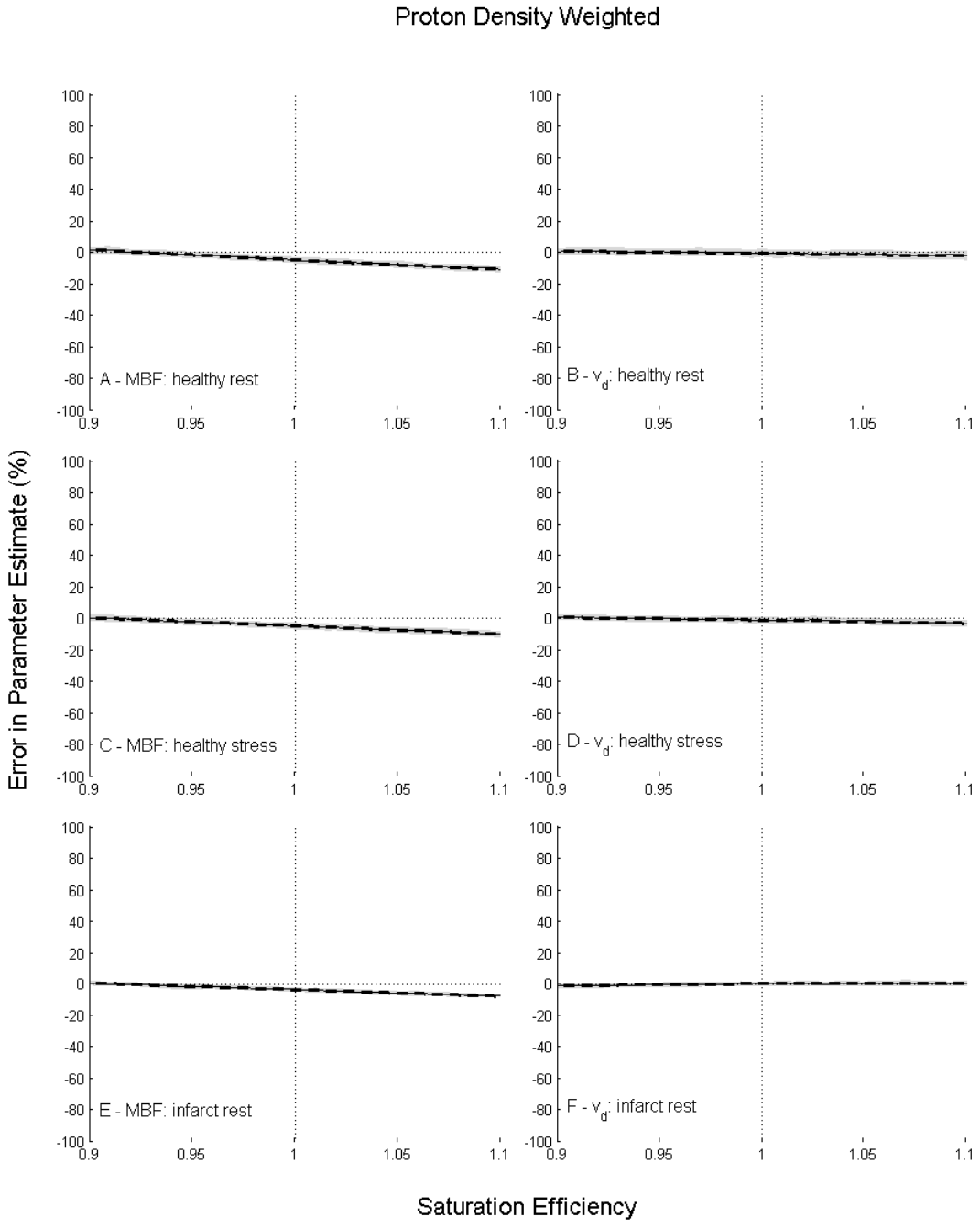

Figure 7-22 - Errors in estimated parameters for healthy myocardium at rest (A – MBF and B – v_d) and stress (C – MBF and D – v_d) and for infarcted myocardium at rest (E – MBF & F – v_d) for deconvolution using proton density weighted image based correction and the full recovery signal model. Dashed lines show results in the absence of noise. Solid lines and shading show mean results +/- one standard deviation for data with noise. Results presented are from slice 2 with 3° flip angle. Results were similar between slices 2 and 3.

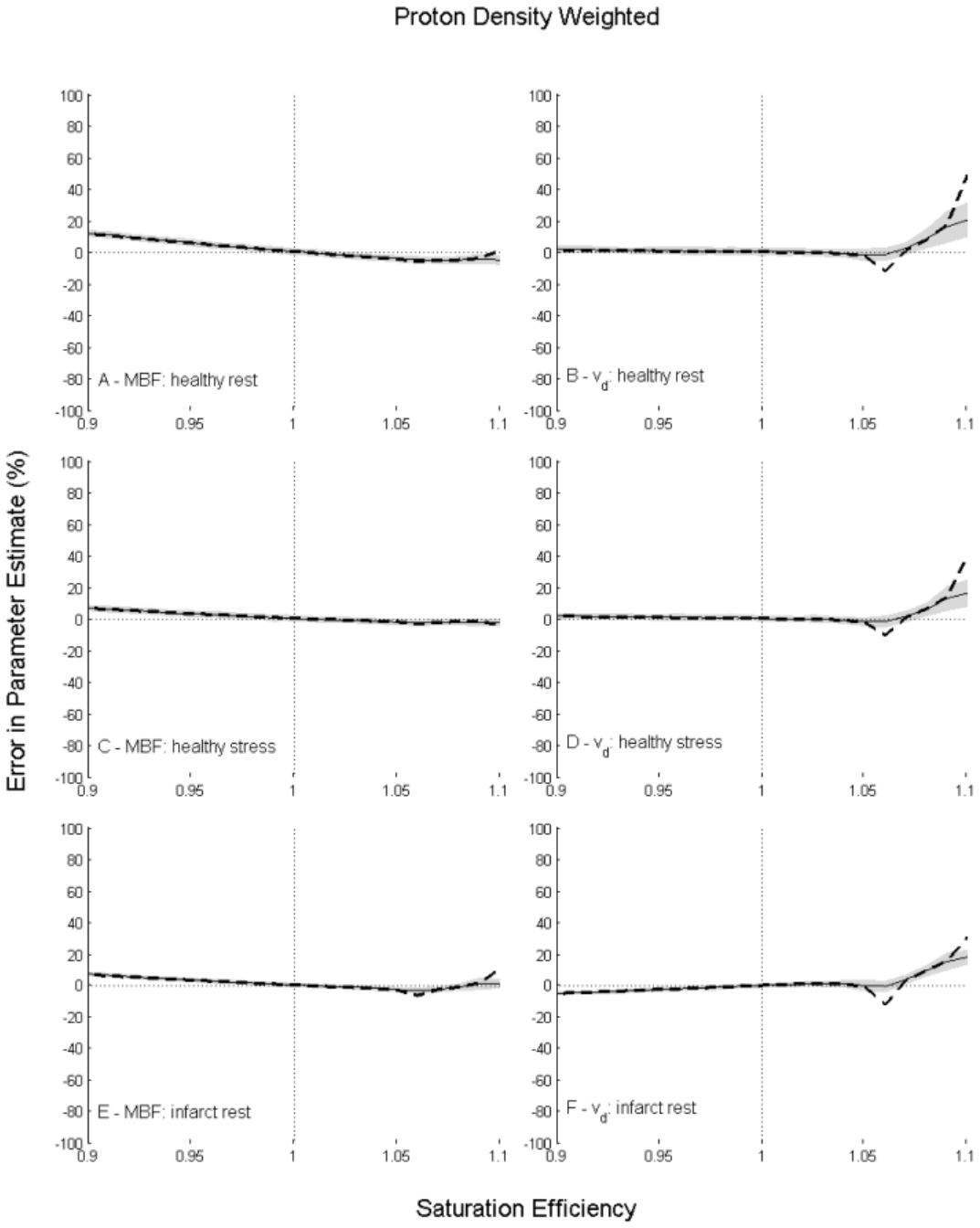

Figure 7-23 - Errors in estimated parameters for healthy myocardium at rest (A – MBF and B – v_d) and stress (C – MBF and D – v_d) and for infarcted myocardium at rest (E – MBF & F – v_d) for deconvolution using proton density weighted image based correction and the steady-state signal model. Dashed lines show results in the absence of noise. Solid lines and shading show mean results +/- one standard deviation for data with noise. Results presented are from slice 1 with 3° flip angle.

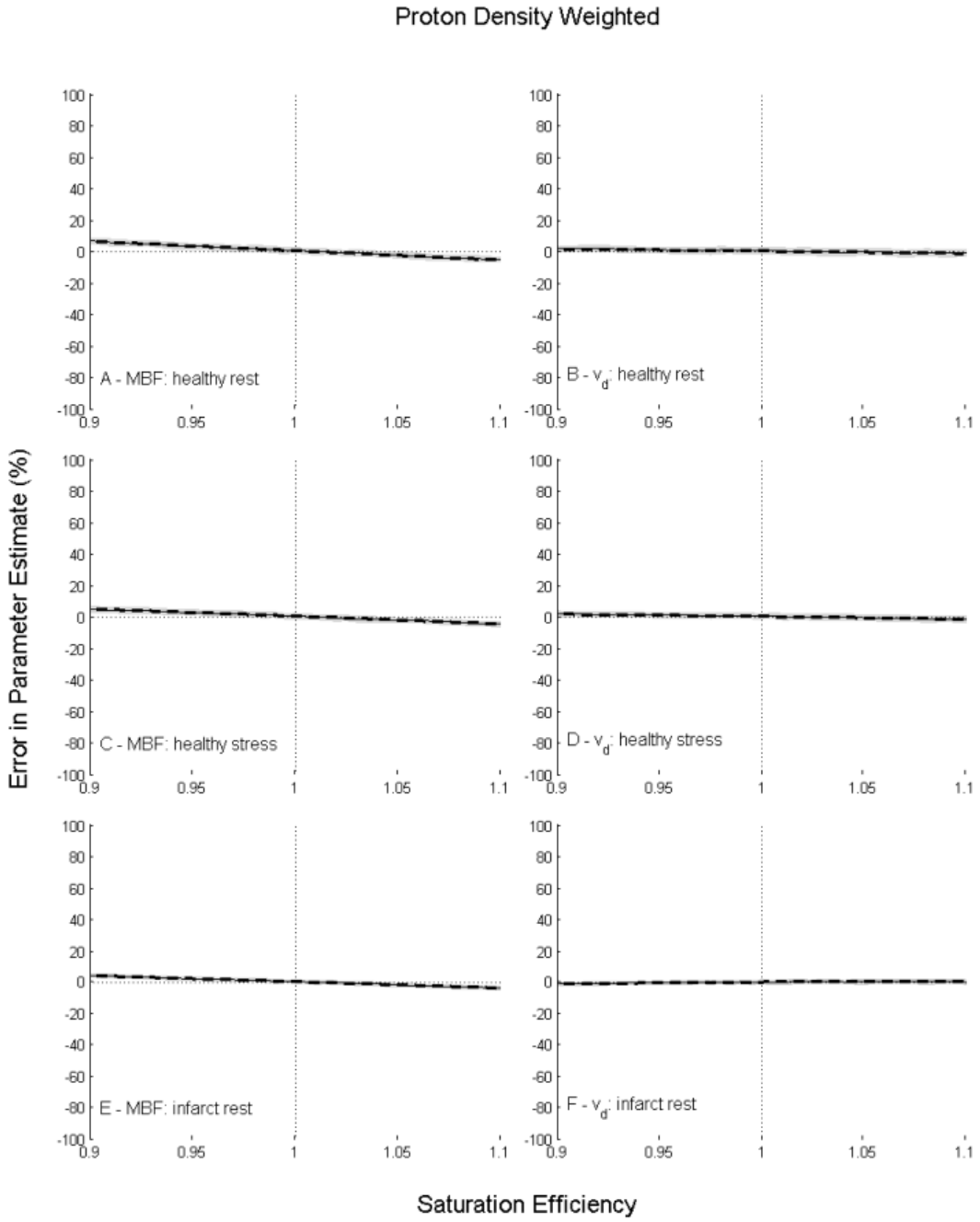

Figure 7-24 - Errors in estimated parameters for healthy myocardium at rest (A – MBF and B – v_d) and stress (C – MBF and D – v_d) and for infarcted myocardium at rest (E – MBF & F – v_d) for deconvolution using proton density weighted image based correction and the steady-state signal model. Dashed lines show results in the absence of noise. Solid lines and shading show mean results +/- one standard deviation for data with noise. Results presented are from slice 2 with 3° flip angle. Results were similar between slices 2 and 3.

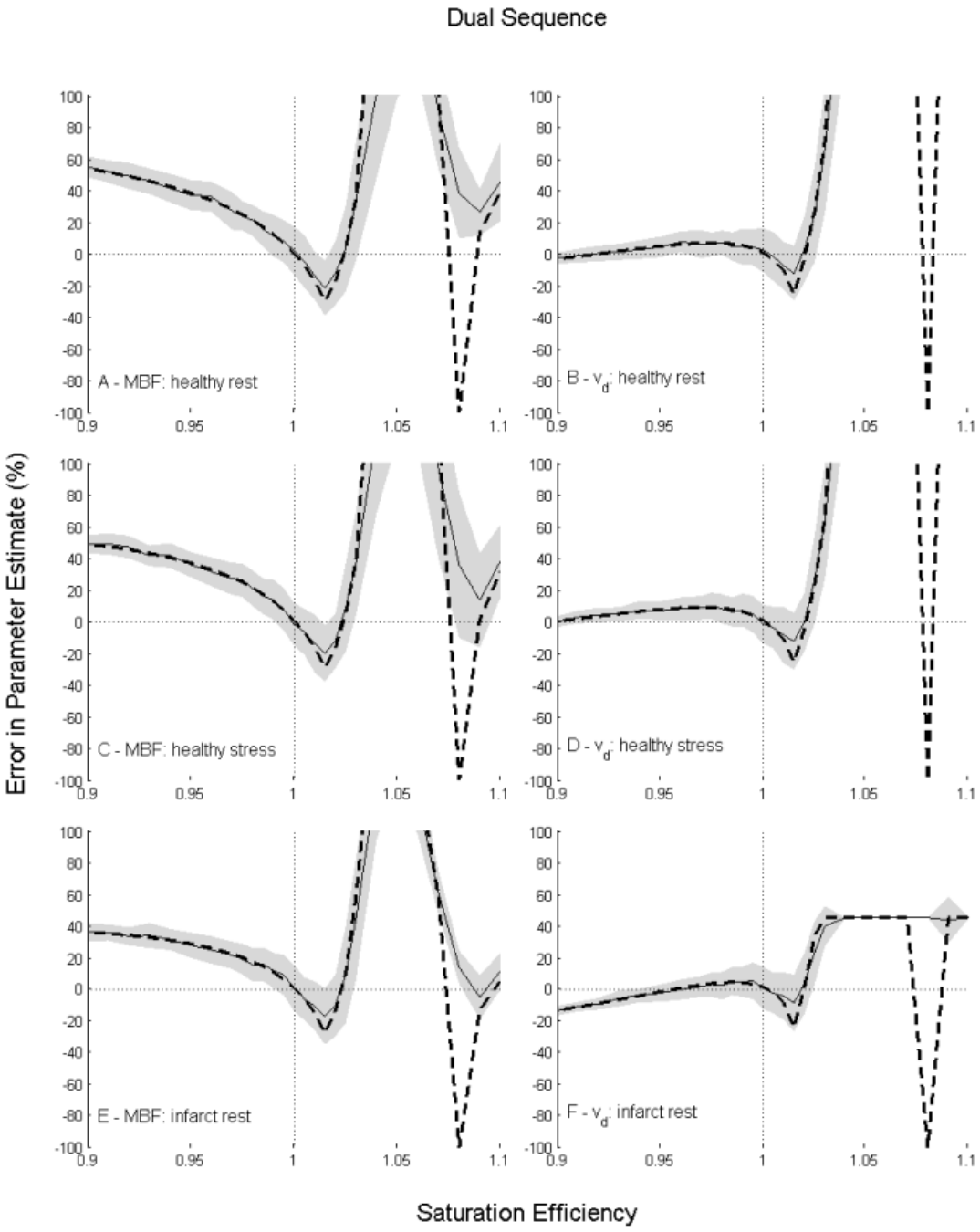

Figure 7-25 - Errors in estimated parameters for healthy myocardium at rest (A – MBF and B – v_d) and stress (C – MBF and D – v_d) and for infarcted myocardium at rest (E – MBF & F – v_d) for deconvolution using the dual-sequence method and the full recovery signal model. Dashed lines show results in the absence of noise. Solid lines and shading show mean results +/- one standard deviation for data with noise. Results presented are from slice 1. Results were similar between all slices.

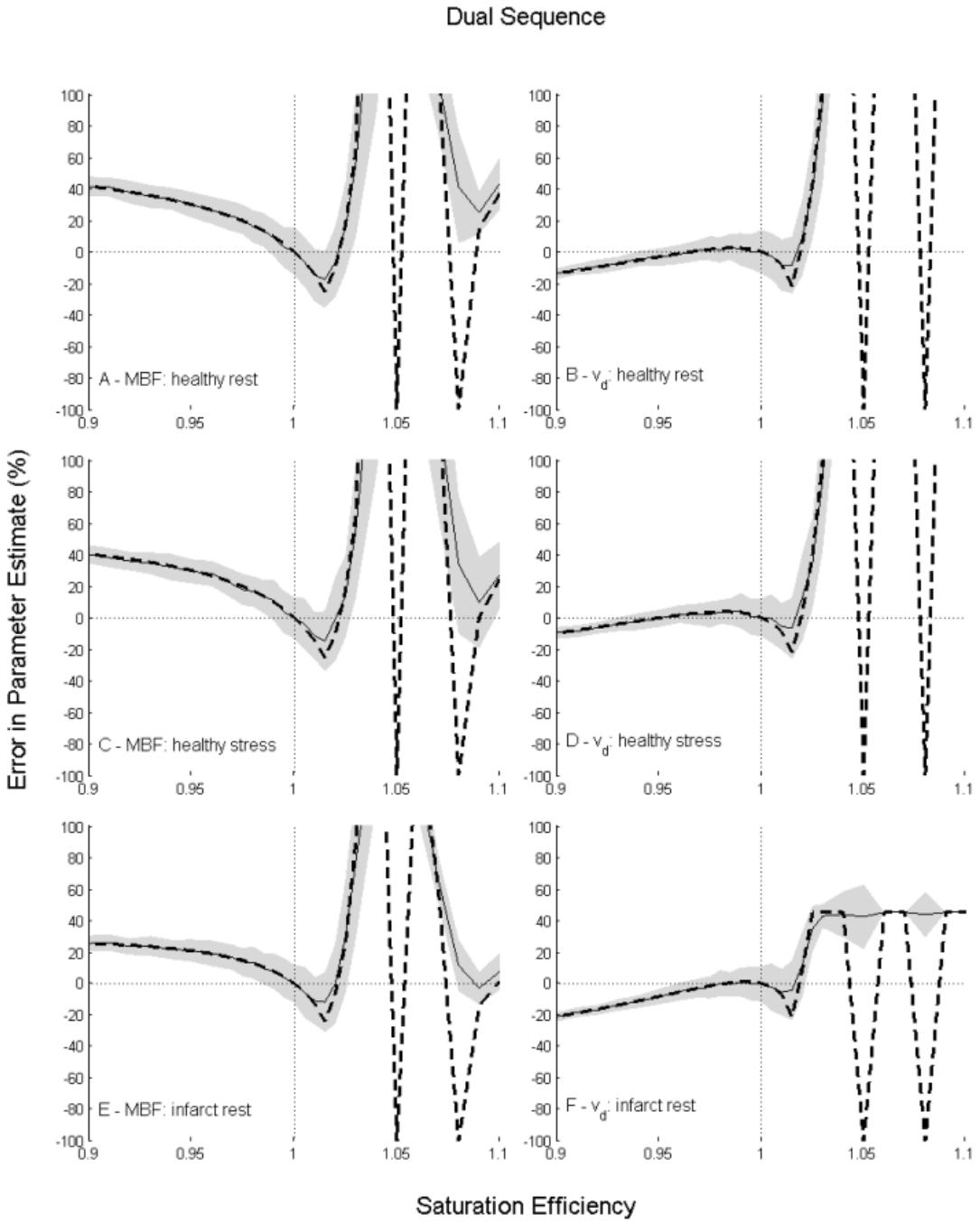

Figure 7-26 - Errors in estimated parameters for healthy myocardium at rest (A – MBF and B – v_d) and stress (C – MBF and D – v_d) and for infarcted myocardium at rest (E – MBF & F – v_d) for deconvolution using the dual-sequence method and the steady-state signal model. Dashed lines show results in the absence of noise. Solid lines and shading show mean results +/- one standard deviation for data with noise. Results presented are from slice 1. Results were similar between all slices.

Results for all methods with ideal saturation and realistic levels of saturation imperfection (SE = 0.975 and 1.025) are compared for healthy resting myocardium in Figure 7-27 and Figure 7-28 (MBF, full recovery and steady-state models) and Figure 7-29 and Figure 7-30 (v_d, full recovery and steady-state models).

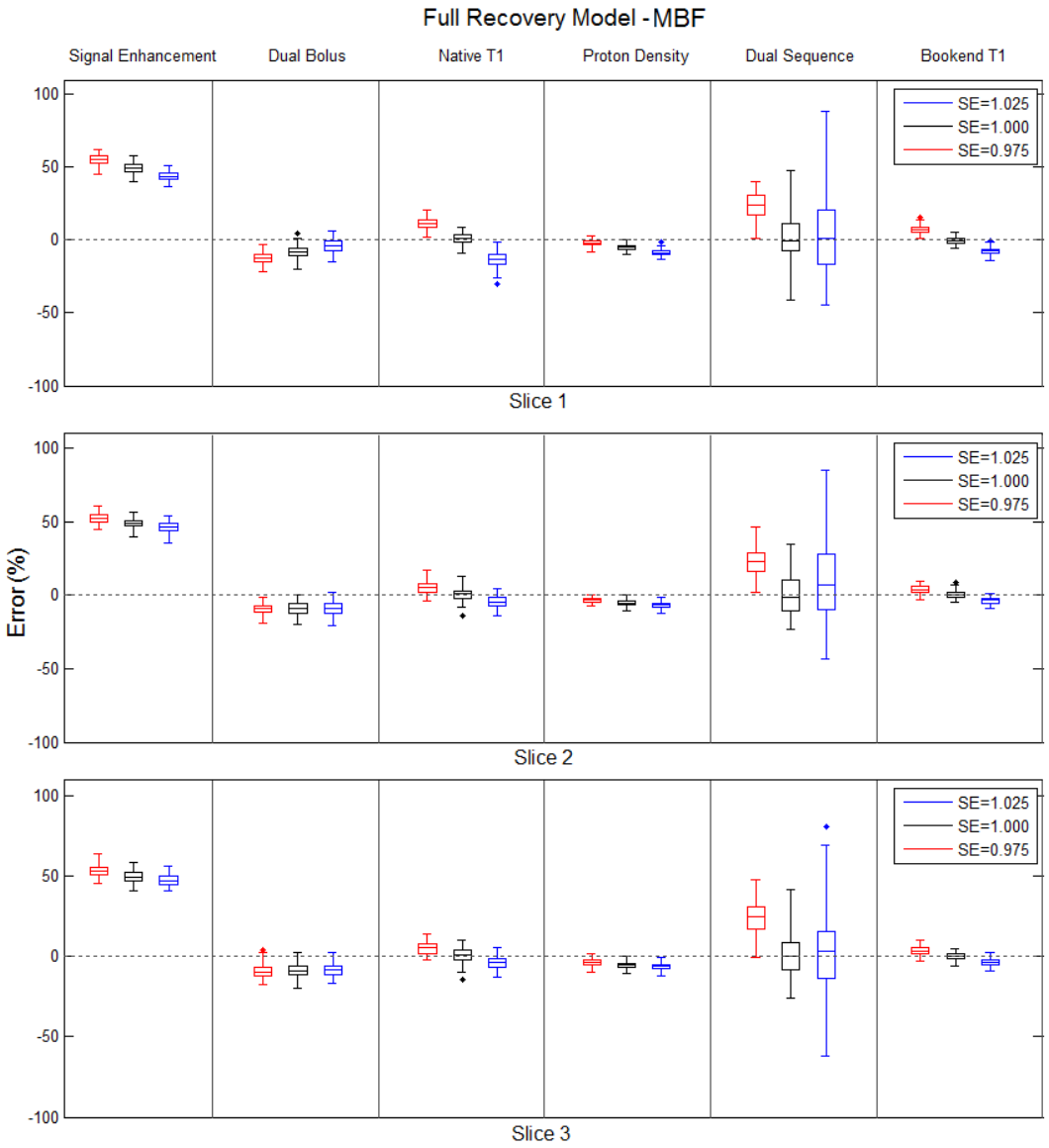

Figure 7-27 - Box-and-whisker plots comparing non-linearity correction methods for realistic levels of saturation efficiency and SNR for resting MBF and normal v_d values. Outliers (individual points) are identified as data more than two times the inter-quartile range above/below the upper/lower quartiles. These results show errors in MBF when the full recovery signal model is used for model based conversions.

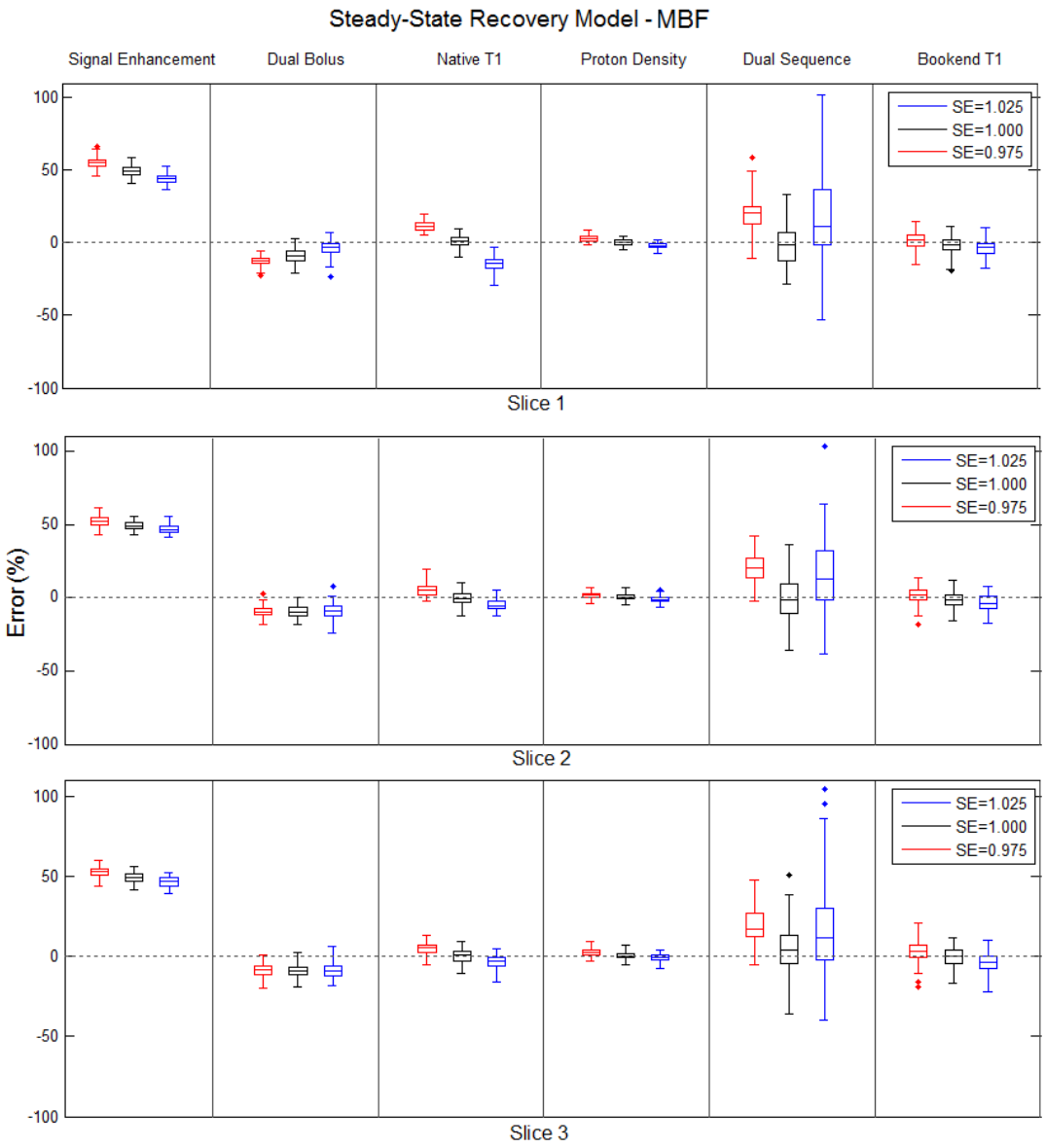

Figure 7-28 - Box-and-whisker plots comparing non-linearity correction methods for realistic levels of saturation efficiency and SNR for resting MBF and normal v_d values. Outliers (individual points) are identified as data more than two times the inter-quartile range above/below the upper/lower quartiles. These results show errors in MBF when the steady-state signal model is used for model based conversions.

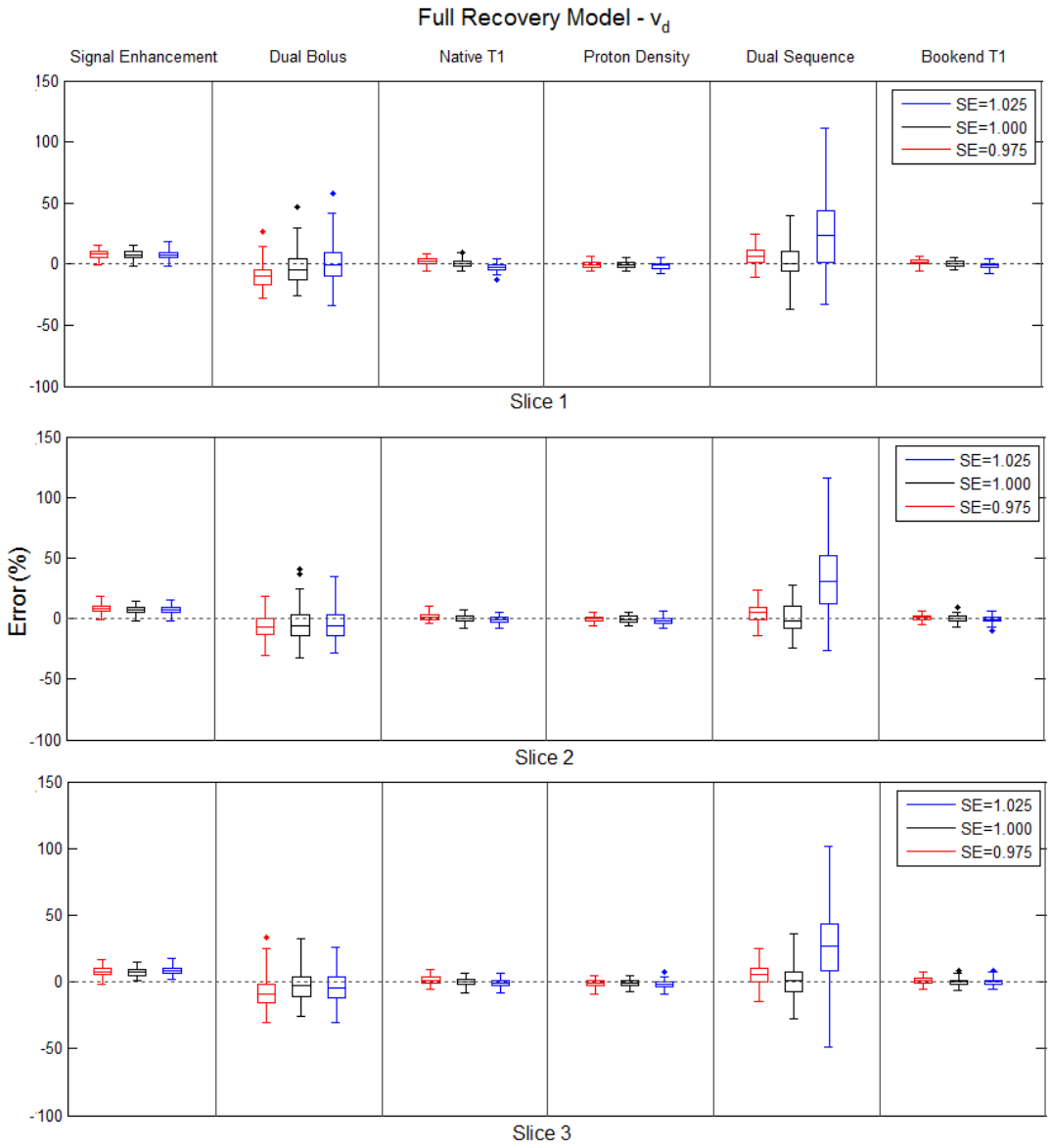

Figure 7-29 - Box-and-whisker plots comparing non-linearity correction methods for realistic levels of saturation efficiency and SNR for resting MBF and normal v_d values. Outliers (individual points) are identified as data more than two times the inter-quartile range above/below the upper/lower quartiles. These results show errors in v_d when the full recovery signal model is used for model based conversions.

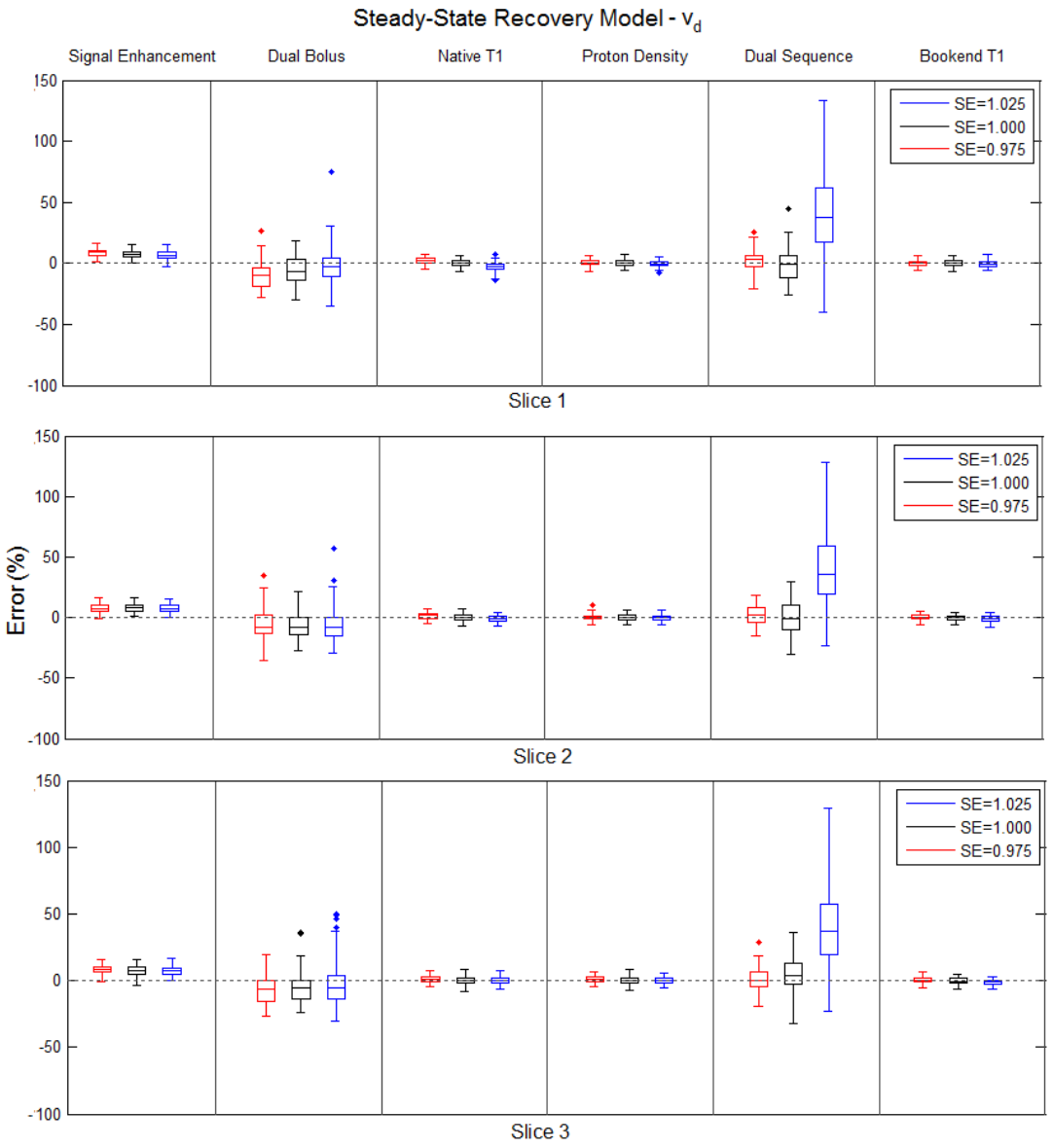

Figure 7-30 - Box-and-whisker plots comparing non-linearity correction methods for realistic levels of saturation efficiency and SNR for resting MBF and normal v_d values. Outliers (individual points) are identified as data more than two times the inter-quartile range above/below the upper/lower quartiles. These results show errors in v_d when the steady-state signal model is used for model based conversions.

7.3.1.2 Effect of Image Noise

Simulations including noise (solid lines and shading in Figure 7-5 to Figure 7-26) showed similar overall patterns to the noise-free simulations. However the

variation in bias around the threshold SE values described above is less sharp. This is due to the asymmetric nature of the Rician noise distribution at low SNR leading to noise induced bias as the threshold value is approached. Inclusion of noise also allows assessment of relative precision of the methods (the vertical extent of the shaded areas is equal to twice the co-efficient of variation), with precision being poorest for dual-bolus due to the reduced CNR in the low-dose AIF and dual-sequence due to the reduced sensitivity in the short TS AIF scan.

7.3.2 Phantom study

IR-SE T_1 values ranged from 224-1941ms and so include the full range of T_1 values typically encountered in clinical T_1 mapping, but do not extend down to the short T_1 values that might be encountered in the blood at peak contrast agent concentration (i.e. at the peak of the first pass of the arterial input function in DCE-MRI). For the simulated AIF the minimum T_1 was 71ms. MOLLI T_1 estimates using the 5s(3s)3s scheme agreed well with IR-SE reference standard T_1 values, with maximum absolute error of 48ms and maximum relative error of 8.6%. The 4s(1s)3s(1s)2s scheme agreed well with both the 5s(3s)3s scheme and IR-SE at short T_1 but showed progressively increased underestimation at longer T_1, with large errors particularly for the gels with T_1>1800ms. This is expected as this scheme is optimised for short T_1 values expected post-contrast, and is not designed to yield accurate T_1 estimates for native tissues or fluids with longer T_1 values. Results are shown in Table 7-2 and Figure 7-31.

TO5 Gel Number	IR-SE T_1 (ms)	MOLLI T_1 (ms)		SR-GE T_1 (ms)
		5s(3s)3s	4s(1s)3s(1s)2s	
1	224	208	201	213
3	343	341	333	343
4	560	512	497	519
6	526	524	519	511
7	774	750	733	738
9	920	907	888	884
10	894	878	864	867
12	1941	1893	449	1919
13	1283	1293	1257	1276
15	1516	1482	1411	1478
17	1674	1661	1513	1629
18	1819	1806	691	1792

Table 7-2 – IR-SE, MOLLI and SR-GE T_1 results.

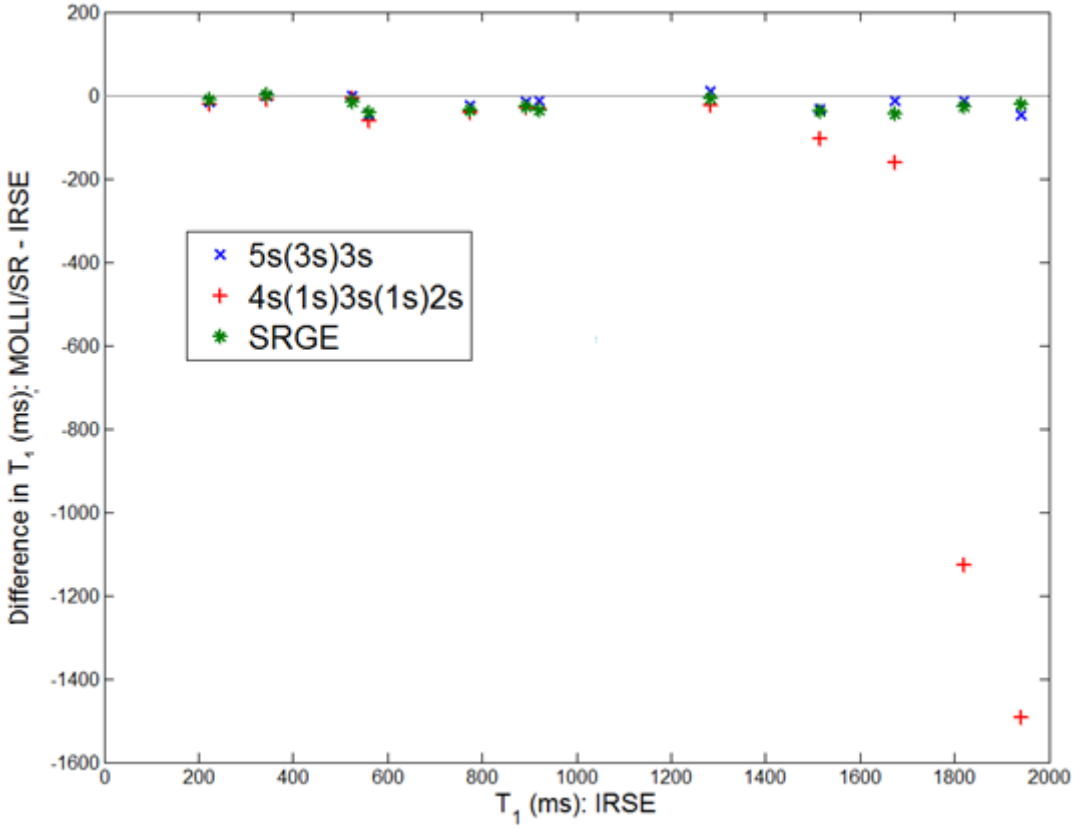

Figure 7-31 - Bland-Altman plot of phantom T_1 values by two MOLLI schemes and SR-GE in comparison to IR-SE. The large errors observed for the 4s(1s)3s(1s)2s scheme at long T_1 are expected is this sequence is designed for use only with contrast enhanced tissues and does not allow for sufficient recovery of longitudinal magnetisation between inversion pulses to accurately quantify the native T_1 values of blood or myocardium.

Fitting Equation 7-13 to SR-GE data (Figure 7-32) yielded a range of saturation efficiency (SE) estimates from 1.0050 to 1.0124 (mean 1.0092, standard deviation 0.0021). T_1 estimates were within 7.4% of IR-SE reference values for all gels (Table 7-2).

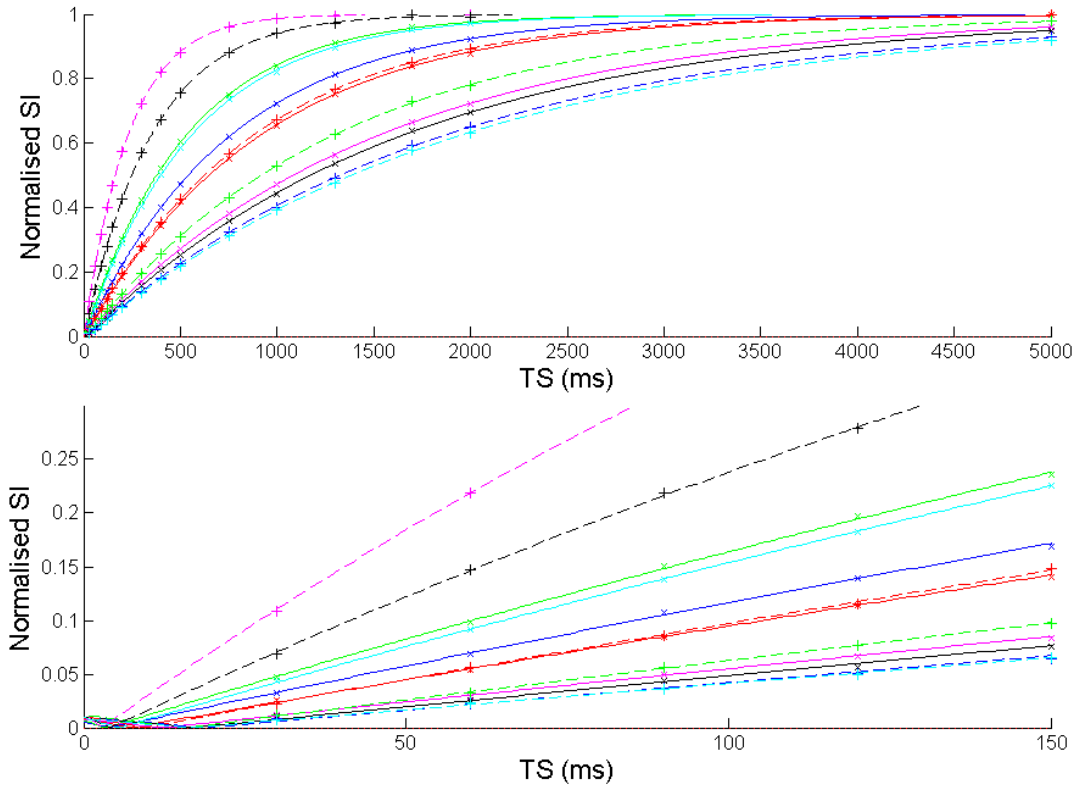

Figure 7-32 – Normalised SR-GE signal intensity (crosses) and model fits (lines) from the phantom study (bottom panel shows zoomed view). Absolute values are plotted and for each gel the fitted curve has a null point at TS>0, indicating over-saturation. For ideal saturation curves would recover from the origin, and for under-saturation curves would not reach the x-axis for TS>0.

The gels with T_1 of 1792ms and 343ms were chosen to represent native and contrast-enhanced blood respectively, as these were closest to the mean values in the volunteer study in the following chapter. In the bookend T_1 method SE was estimated as 1.0174. As shown in Figure 7-33, estimated ΔR_1 (compared to the R_1 of the gel representing native blood) values for the other 10 gels correlated well with MOLLI derived T_1 values across all gels for both methods (R^2>0.97). The gels used to derive S_0 and (for bookend T_1) SE were excluded from the correlation as these necessarily lie on the line of identity.

The agreement was better for the bookend T_1 based method, with a slope of 1.05 and intercept of -0.072s^{-1} compared to 1.69 and -0.173s^{-1} for the native T_1 based method. The value of S_0 estimated using the bookend T_1 based method was 43% higher than for the native T_1 based method.

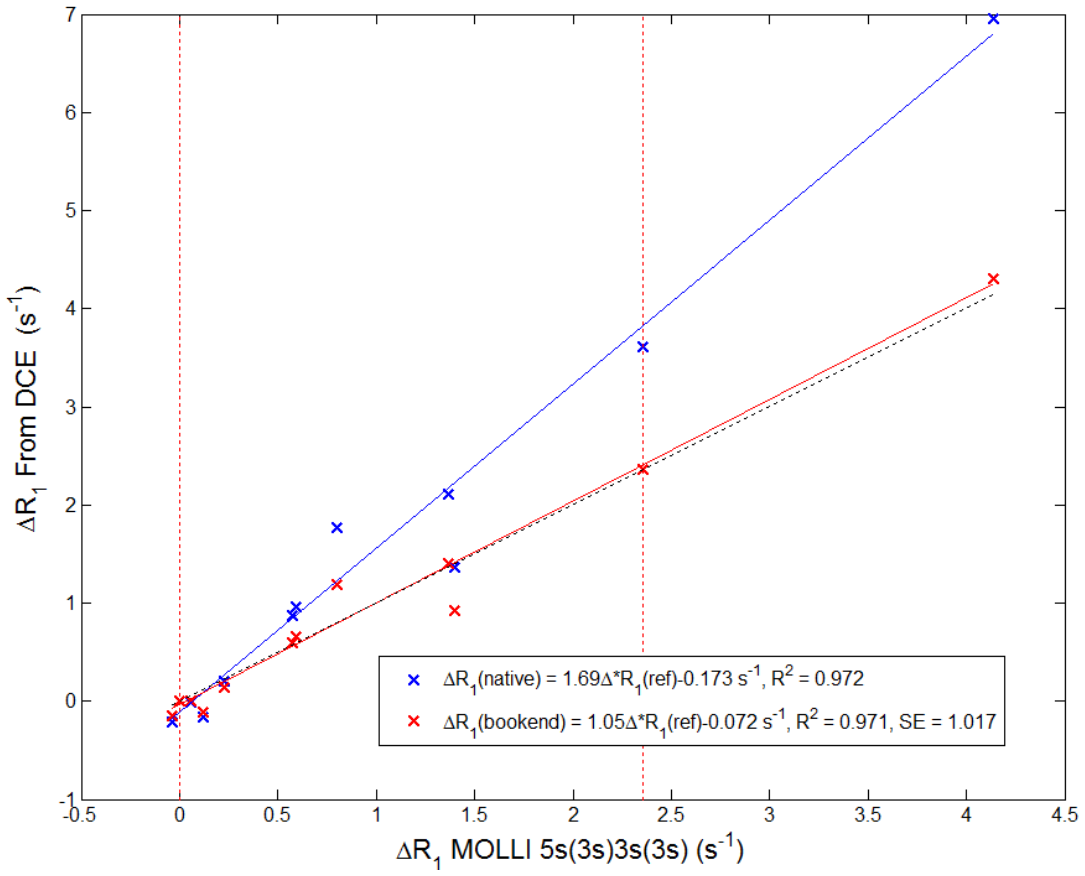

Figure 7-33 – Correlation of ΔR_1 values from data acquired by imaging gels of differing T_1 using a DCE-MRI sequence (estimated using with native (blue) or bookend (red) T_1 based conversion with the full recovery model) to MOLLI T_1 values. The black dashed line shows ideal agreement and the red vertical dashed lines intersect the points used in estimating S_0 and (for bookend T_1) SE. For the native T_1 based approach only the point at ΔR_1=0 was used to constrain the model. The legend shows results of linear fits, and estimated SE for the bookend T_1 based correction.

7.4 Discussion

7.4.1 Signal enhancement based analysis

In accordance with the well-understood effect of signal non-linearity on MBF estimates [54] this study demonstrated that deconvolution of DCE-MRI signal enhancement data without correction for signal non-linearity leads to substantial over-estimation of MBF for the parameters used in this work. Additionally smaller systematic errors were also present in v_d in this study, with overestimation of normal values but underestimation of the elevated v_d value, as well as dependency on the magnitude of errors in both parameters on the saturation efficiency. The difference in behaviour for elevated v_d occurred as the value of the distribution volume, and thus the equilibrium concentration,

exceeded that in blood (the distribution volume fraction of which is 1-hct). Consequently non-linearity effects in the tail of the curves are greater for the myocardial curve than for the AIF at such v_d values. As these errors are well known absolute parameter values derived from quantitative analysis using normal clinical contrast agent doses without non-linearity correction would not normally be reported. As errors arise predominantly due to non-linearity effects in the AIF relative perfusion metrics (such as myocardial perfusion reserve or endocardial to epicardial perfusion ratios) from data uncorrected for signal non-linearity may be reported with lower bias than absolute values (if the AIF is similar or identical for the two sets of data being compared). However, non-linearity effects in the myocardium also contribute to the observed bias to an extent which is dependent on the physiological parameters being measured. Consequently calculating relative rather than absolute parameters will not necessarily completely eradicate such errors.

Reducing the contrast agent dose has been shown to yield lower absolute MBF values by reducing non-linearity effects in the AIF while using a low dose for the AIF and a higher dose to measure the tissue response allows acceptable image contrast for visual analysis to be maintained [105]. However, while this dual-bolus technique affects absolute MBF values it does not necessarily improve diagnostic performance for the detection of CAD [106]. In the simulations in this work this technique has been shown to be partially effective in reducing the magnitude of systematic errors in comparison to a single bolus method, although systematic errors still arise (due to residual non-linearity) and precision is substantially reduced, particularly in $v_{d,}$ due to low SNR in the pre-bolus AIF. Other work has suggested that model-based correction alongside dual-bolus acquisition may further improve accuracy by accounting for non-linearity in the myocardial data [107], however this cannot address the reduction in precision arising from the low SNR in the AIF.

7.4.2 Model-based non-linearity correction

When using model-based correction techniques bias in parameter estimates was typically negligible or small in simulations with ideal saturation pulse performance. However, in a typical myocardial DCE-MRI sequence baseline signal is generated from longitudinal magnetisation which has only recovered to

a small fraction of the equilibrium value. For example, assuming ideal saturation and the parameters used these simulations, baseline signal will be approximately 5% and 10% of S_0 for blood and myocardium respectively in the conventional DCE-MRI series, and smaller for the dual-sequence variant. Consequently a small amount of residual magnetisation after saturation has a substantial impact on baseline SI, as has been previously identified [181]. Results from this study have shown that such biases influence the results of model-based non-linearity correction methods, and consequently the accuracy of quantitative DCE-MRI analysis.

Over- or under-saturation leads respectively to lower or higher baseline signal than ideal saturation. For native T_1 based correction the estimated value of S_0 is directly proportional to the baseline signal, and so these biases propagate into large non-linear errors in estimated ΔR_1 throughout the DCE-MRI series (as illustrated in), and thus also into errors in estimated physiological parameters. For this technique results are identical between the signal models used as the model is only used with an assumed SE value of 1, in which case Equation 7-5 simplifies to Equation 7-4. As the estimated value of S_0 is inversely proportional to the evaluated result of the signal model at baseline T_1 any errors in the measured T_1 value also lead to systematic errors in S_0 and physiological parameters. Underestimation of T_1 (which is generally expected when using MOLLI based sequences, as described in Chapter 5) leads to underestimation of S_0, which leads to underestimation of physiological parameters in most cases. The exception to this is for elevated v_d where the direction of the effect of T_1 errors is reversed (for the same reason as for the reversal of the direction of bias for signal enhancement based).

Differences in behaviour between slices were observed, with greater saturation efficiency dependency for slice 1 than the other slices. This arises because the three slices are acquired contiguously, after which there is a delay prior to the next cardiac cycle. Consequently the time between the saturation pulse for this slice and that from the previous image acquisition is greatest for slice 1, allowing greater recovery of longitudinal magnetisation. The magnetisation is thus greater at the time of the preparation pulse for slice 1. This is discussed further in section 7.4.4.

7.4.2.1 T_1 based methods

Use of the bookend T_1 based technique did reduce saturation efficiency dependency compared to use of native T_1 and baseline signal alone, but to a generally lesser extent than proton density weighted image data for model based correction. However some saturation efficiency dependent bias in MBF and v_d remains with this technique, likely due to limitations of the analytical signal models (note that these residual biases and saturation efficiency dependencies did not occur in the results in the paper published on the initial analysis [1], for which the same model was used for the forwards and backwards simulation as described in the introduction to this chapter). From Figure 7-17 to Figure 7-20 it can be seen that the level of saturation imperfection is underestimated and there are errors in estimated S_0 values. This likely arises due to the fact that assumptions regarding starting magnetisation at the time of magnetisation saturation (of either full-recovery or steady-state prior longitudinal magnetisation) are used in the derivation of the analytical solutions of the signal models which differ to the forward simulations which simulated the magnetisation evolution throughout the full experiment. Consequently even in the simplified simulation study (which neglects effects which would occur in *in vivo* scanning, described in the limitations in section 7.4.6) the models used are not full descriptions of the signal behaviour.

In the phantom study it was estimated using multiple SR-GE images that the RF pulse used slightly over-saturated magnetisation (i.e. resulted in a small fraction of the magnetisation being inverted). Furthermore the T_1 estimates from this experiment agreed well with IR-SE reference results and 5(3s)3 MOLLI supporting the validity of the fits to these data. Over-saturation was also indicated in the bookend T_1 approach when applied to the gels, although a higher level of over-saturation was estimated than in the SR-GE experiment. As described above in the presence of perfect T_1 measurement accuracy deviations of saturation efficiency from ideal are underestimated by the bookend T_1 approach, although biases due to errors in T_1 mapping (as discussed below) may be larger than the errors introduced through limitations of the signal models. As shown in Figure 7-33 estimation of ΔR_1 from the bookend T_1 approach in the gels agreed more closely with those from MOLLI than use of the native T_1 approach, which supports the results of the simulation study.

However for both methods the strength of the linear correlation was very high, with negligible difference between bookend and native T_1 approaches. As a consistent scaling error in ΔR_1 would not lead to errors in estimated parameters from deconvolution of DCE-MRI data (as both the AIF and myocardial curves would be scaled equally) these data do not directly suggest that the bookend T_1 approach would yield more accurate estimates of physiological parameters than the native T_1 approach when estimating physiological parameters. However this experiment was limited by the fact that there were no gels with T_1 as short as would be expected at the peak of the AIF, and so the conversion techniques were not tested across the whole physiologically relevant range.

For the bookend T_1 approach the direction of the influence of errors in native T_1 measurement is reversed in comparison to when only native T_1 and signal is used to constrain the signal model. This is due to the fact that underestimation of native T_1 leads to underestimation of S_0 when SE is constrained to be ideal (in the native T_1 approach), but overestimation when SE is also estimated (in the bookend T_1 approach).

Errors in measurement of post-contrast T_1 affect estimates of S_0 and SE in the opposite direction to errors in native T_1, and have a larger influence. Biases due to consistent under or overestimation of both native and post-contrast T_1 were thus in the same direction, but of lower magnitude, than when errors were simulated in post-contrast T_1 alone.

Unlike for the native T_1 based approach, where ideal saturation is assumed, Equation 7-4 and Equation 7-5 are not equivalent in this approach and so differences in results are present between signal models as well as slices. In general bias is lower at non-ideal saturation efficiency for the steady-state signal model. However for the full recovery model precision is better and the sensitivity to errors in T_1 measurement is reduced. Consequently the preferred choice of model may depend on the expected performance of the saturation pulse being used, with the full recovery model preferred when the pulse is expected to have near-ideal performance but the steady-state model preferred to reduce saturation efficiency dependency where consistent near-ideal saturation pulse performance might not be expected.

It should be noted that the potential use of SE values representative of over-saturation in the signal modelling, which the bookend T_1 based method introduces, raises the potential of systematic biases due to errors when performing optimisation processes with non-monotonic function. As discussed in appendix 3 (section Chapter 7) such errors are not expected to affect the validity or interpretation of the results of this thesis. However the potential for such errors should be considered when applying this technique under different conditions, for example in combination with a dual-sequence acquisition.

7.4.2.2 Proton density weighted image based methods

When simulated with the same 15° readout flip angle as the DCE-MRI sequence the PDw based technique was not successful, due to the effects of substantial residual T_1 weighting in the PDw signal data. In the presence of this T_1 weighting real, positive T_1 values could not be estimated throughout the acquired DCE data with either signal model. This was resolved when using a reduced flip angle to further reduce T_1 weighting beyond removing the saturation pulse. However use of a very low flip angle will reduce SNR in the proton density weighted images and further work is required to determine the optimal sequence parameters to minimise T_1 weighting while maintaining sufficient SNR. In these results saturation efficiency dependency was lower than for both T_1 based approaches. However, unlike the T_1 based approaches small systematic bias was present when perfect saturation efficiency was simulated. Although SE is not estimated in the PDw based technique the signal models are not only used under the assumption of perfect saturation. The model is also used with SE=0 for the PDw sequence. For the latter Equation 7-4 and Equation 7-5 are not identical, so differences between models exist for this technique with lower bias for the steady-state signal model. Precision was similar between models, and comparable to that of the bookend T_1 based method with the full recovery signal model.

The PDw based technique was substantially less sensitive to imperfect saturation than the native T_1 method, despite the methods following exactly the same procedure after baseline T_1 is determined. As the former uses a two-point baseline T_1 estimate (which would be expected to be less accurate than an

independent optimised T_1 mapping sequence) this may seem counter-intuitive. This observation can, however, be explained by examining the error sources.

With the native T_1 method over-saturation leads to underestimation of S_0 (Figure 7-15 and Figure 7-16, top-right panels and Table 7-3 below). As S_0 defines the signal model for conversion of signal data to ΔR_1 it is this error which leads to strong saturation efficiency dependency in the final physiological parameter estimates. If the independent T_1 measurement is inaccurate the strong saturation efficiency dependence remains but the biases are shifted.

For the PDw based method the baseline T_1 estimate is estimated using the SR perfusion sequence and a PDw variant. As the baseline SR signal is strongly dependent on saturation efficiency so too is the estimated baseline T_1. However in the subsequent step of estimating S_0 from the same biased baseline signal and the T_1 estimate these errors largely cancel out. Therefore physiological parameter estimates for this technique are substantially less saturation efficiency dependent than for the native T_1 based method.

Data exemplifying this is shown below. The second row of Table 7-3 shows relative baseline signal intensity for native blood in slice 1 of a standard SR sequence. In this a negative correlation between SE and signal exists. The following three rows show data used in the PDw based method. Firstly signal intensity from the PDw series (3° flip angle). This is independent of SE as this sequence does not use the saturation pulse. The fourth row shows T_1 values estimated as a first step of the PDw based correction technique. These are derived from the previous two rows, and exhibit a positive correlation with SE due to the variation in baseline SR signal intensity. Finally for this method the fifth row shows the estimated value of S_0 that is subsequently derived from the estimated T_1 value and the baseline SR sequence signal intensity. As can be seen the biases largely cancel out yielding low SE dependence in S_0. For the native T_1 method however (bottom two rows), where the T_1 estimate is SE independent, the SE dependency of the baseline SR signal propagates into S_0.

Saturation Efficiency	0.98	1	1.02
SR baseline relative signal (S/S_0)	0.0050	0.0045	0.0040
PDw relative signal (S/S_0)	0.0483	0. 0483	0. 0483
PDw method - Estimated T_1 (ms)	1457	1620	1822
PDw method - Estimated S_0	0.9351	0.9351	0.9351
Native T_1 method - Accurate T_1 (ms)	1736	1736	1736
Native T_1 method - Estimated S_0	1.1086	1.0000	0.8923

Table 7-3 – Example intermediate data for PDw image and native T_1 based correction methods (both for slice 1 using the full recovery signal model). Ground truth native T_1 and S_0 values were 1736ms and 1.

Even under conditions of ideal saturation the estimated T_1 values in the PDw based method exhibit bias, and consequently so do S_0 values. This arises because limitations in signal models remain for the PDw sequence (see appendix 2, section 7.7.1). The full recovery model over-estimates signal for long T_1 as it does not account for signal saturation while the steady-state model is accurate only once the steady-state is achieved. However even for the latter the steady-state is still being approached during the limited duration of the baseline data acquisition. Use of the steady-state model resulted in lower bias in S_0 for ideal saturation, but stronger SE dependence.

Following determination of S_0 the signal model is defined and R_1 is estimated for each dynamic phase. Figure 7-34 shows the signal models derived from the above examples graphically. As the differences in S_0 are negligible for the PDw method the lines overlie each other. For the native T_1 method however the curves for the different SE values diverge substantially.

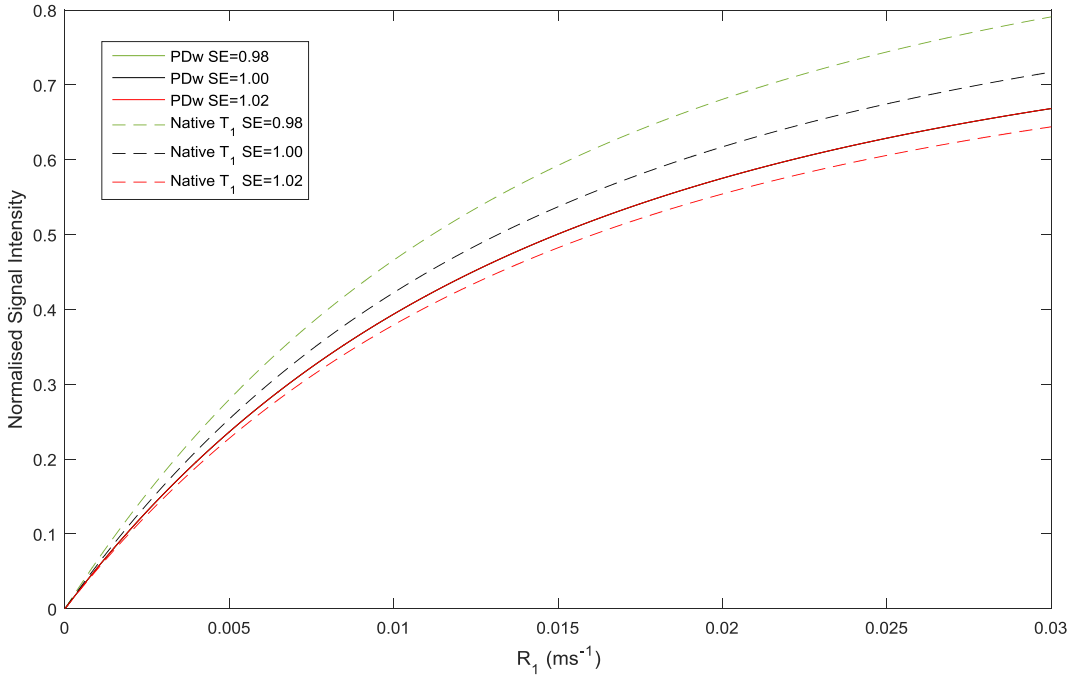

Figure 7-34 – Signal models derived from the results of Table 7-3. The S_0 values for the PDw method are very similar so the three curves are not visibly distinguishable on this plot.

Divergence of the models alone does not determine the differences in estimated ΔR_1 values, as differences in SE will also affect the signal intensities acquired throughout the DCE series. Table 7-4 shows R_1 values that would be estimated for the baseline and peak concentration values in blood, and the corresponding ΔR_1, for each example case described in Table 7-3.

Saturation Efficiency	0.98	1	1.02
SR baseline blood relative signal (S/S_0)	0.0050	0.0045	0.0040
SR peak-contrast blood relative signal (S/S_0)	0.0634	0.0629	0.0625
PDw method - baseline blood R_1 (s^{-1})	0.687	0.617	0.549
PDw method - peak-contrast blood R_1 (s^{-1})	16.760	16.483	16.214
PDw method - peak blood ΔR_1 (s^{-1})	16.073	15.866	15.665
Native T_1 method - baseline blood R_1 (s^{-1})	0.576	0.576	0.576
Native T_1 method - peak-contrast blood R_1 (s^{-1})	11.729	14.171	18.245
Native T_1 method - peak blood ΔR_1 (s^{-1})	11.153	13.595	17.669

Table 7-4 – Estimated R_1 and ΔR_1 values for blood in the scenarios exemplified in Table 7-3. Without noise and with perfect saturation the native T_1 method performs ideally, so the values in the bottom 3 rows of the SE=1 column also reflect the ground truth values.

The values for the native T_1 method at ideal saturation are accurate in this case. Additionally as the model is determined using baseline data the R_1 estimates for that value only are accurate at all SE values. For non-ideal saturation estimates of post-contrast R_1 (and ΔR_1) are biased due to the different S_0 estimates derived above. Due to the bias in S_0 for the PDw method even at ideal

saturation efficiency errors exist for this method throughout. However while the latter exhibits substantial variation in both baseline and post-contrast R_1 estimates the ΔR_1 estimates exhibits less saturation efficiency dependency than in the native T_1 based correction. As for errors in S_0, the absolute errors in ΔR_1 are substantially lower when using the steady-state model for the PDw method.

Dual-sequence

When PDw based correction is used with the dual-sequence acquisition technique the systematic bias at ideal saturation is reduced compared to the results of the PDw based method without dual-sequence acquisition. This is potentially due to further reduced residual T_1 weighting in the PDw data, for which the sequence has a reduced number of readout pulses in the low spatial resolution sequences. However, the short TS in the interleaved sequence leads to reduced SNR in the AIF and consequently precision is substantially poorer for this technique compared to single acquisition strategies. Additionally the short TS leads to very high saturation efficiency dependency as a given degree of saturation imperfection will lead to a greater proportional difference in baseline signal than for the conventional DCE series.

7.4.2.3 Over-saturation threshold

The dual-sequence technique completely breaks down for moderate over-saturation (SE>1.02) as the baseline signal is either nulled or arises from inverted magnetisation above this. Due to this behaviour caution should be adopted when quantifying dual-sequence data if near ideal saturation efficiency cannot be guaranteed. Additionally caution should be adopted if modifications such as use of centric k-space ordering are used to further shorten TS, as this would be expected to further increase the dependence on SE.

Some similar features of sharp changes in results above a threshold over-saturation level can also be observed in results from other techniques. For these the threshold occurs at SE=1.06 for slice 1, as this corresponds to the value at which baseline signal is nulled. For subsequent slices this threshold is not observed in the simulated range of SE values, as the magnetisation prior to saturation is less than for slice 1, due to the shorter delay since the previous saturation pulse. For the same reason the threshold SE value for slice 1 would

be expected to vary with heart rate, with a lower threshold at higher heart rates for which there would be less time for recovery of longitudinal magnetisation prior to the slice 1 saturation pulse.

7.4.3 Influence of image noise

In general image noise can have a biasing effect on baseline SI when the SNR is sufficiently low that the distribution of SI values is asymmetrical. With noise low SI values are, on average, higher than would be predicted in the absence of noise. For the native T_1 based method an increased baseline SI leads to an increased calculated S_0. Conversely an increased baseline SI in the bookend T_1 based method leads to a lower S_0. These deviations can be observed in the presented data (where the continuous line showing mean results from noisy data deviate from the dashed line showing results from noiseless data) for some cases at the highest levels of over-saturation simulated. This only occurs where the SNR becomes very low, as the Rician noise distribution is close to symmetrical for SNR above around 2 [196], and so is more likely to occur either at over-saturation or when using the dual-sequence approach, as in both cases baseline signal intensity is reduced. At higher doses precision in model-based approaches would be expected to initially improve due to increased SNR but then deteriorate due to increased noise sensitivity in the conversion process (due to the reduced SI-[CA] gradient at higher concentration) and preliminary simulations have demonstrated this behaviour [1].

7.4.4 Slice dependence

One previously unexpected finding of this work was the difference in behaviour between slices in the presence of imperfect saturation efficiency, which arises due to the pulse sequence design. In general saturation efficiency dependency is greater for the first slice acquired as the delay between the saturation pulse for that slice and the previous saturation pulse is longer. This allows greater recovery of longitudinal magnetisation prior to magnetisation preparation.

In the simulations only a single heart rate was used (see limitations in section 7.4.6 below), and so the additional “dead-time” at the end of each cardiac cycle was consistent (equal to the simulated cardiac cycle length of one second minus the time required to acquire the three slices of image data). In practice

this will vary both between and within series due to variation in heart rate. In particular at the limiting heart rate at which the acquisition of the three slices completely fills the available time, the saturation pulses would be equally spaced and no differences between slices would be expected, whereas differences would be exacerbated at low heart rates.

In practice where slice ordering and heart rate dependency is expected due to these effects the characteristic behaviour should be considered when interpreting results. However this may not be practical and ideally this effect would be minimised. This could be achieved in part by improvements in saturation pulse efficiency although as discussed in the introduction further development in this area may be limited by energy deposition rate and transmit RF field homogeneity constraints.

A proposed modification of the cardiac perfusion sequence is to automatically adjust image resolution (and thus acquisition duration) based on the subject's heart rate to use all of the available time [197]. Adoption of this strategy would also remove the variations between slices in saturation efficiency dependence for quantitative analysis. This adaptation can only be fully be exploited when the heart rate is perfectly regular, in practice some remaining dead-time would need to be left to allow for potential heart-rate variability throughout the acquisition, and so some residual variation between slices in the saturation efficiency dependency of quantitative DCE-MRI results would be expected. It would also lead to differences in the number of readout pulses per image between DCE-MRI series (for example the increased heart rate at stress would lead to a shorter readout being used). This would affect the image SNR as well as the effect of the readout pulses on the magnetisation recovery, and this difference would need accounting for in model based non-linearity correction techniques

An alternative approach may be to add an additional saturation pulse during the dead time after acquiring the final slice in order to reduce magnetisation recovery prior to magnetisation preparation for the first slice of the subsequent cardiac cycle. While this may reduce saturation efficiency dependence the effect of this additional pulse would need incorporating into model based correction methods and the additional energy deposition would need consideration with respect to patient safety.

7.4.5 Practical implications

Non-linearity in the relationship between contrast agent concentration and MRI signal intensity can lead to substantial bias in the results of quantitative myocardial DCE-MRI analysis. This work has demonstrated that mathematically modelling the non-linear relationship between concentration and signal intensity may avoid this bias for conventional acquisition protocols. Indeed because of the low SNR or high sensitivity to imperfect saturation pulse performance that may affect dual bolus or dual sequence techniques respectively model based correction may be more robust than the dual sampling techniques that have been proposed. Furthermore this may avoid procedural complexity as well as analysis workload as the AIF and myocardial data are obtained from the same images. However appropriate choice of model based method must be used to avoid high sensitivity to saturation pulse efficiency, in particular use of native T_1 based correction should be avoided whereas bookend T_1 or proton density weighted image based correction methods are less susceptible to such errors and can provide higher precision than the dual sampling techniques.
Additionally the technique relies on a mathematical model describing the signal response to contrast agent concentration. Some simplifying assumptions will be required in the definition of this model and, as seen in the results of this work, the choice of equation used affects the accuracy, precision and sensitivity to saturation imperfection of the deconvolution analysis. Of the signal models used in this chapter the full recovery model generally resulted in better precision than the steady-state approximation, and so may be preferable in clinical practice despite the poorer absolute accuracy. Consequently this model was used in the subsequent chapters describing clinical experiments.

Bookend T_1 or proton density weighted image based correction can be recommended as preferable to other non-linearity correction methods on the basis of these results. However the performance of neither is completely ideal and the limitations and details of implementation (such as the signal model used) should be considered when defining myocardial DCE-MRI acquisition and analysis protocols. In particular these two experimental aspects relevant to non-linearity correction should be considered together prospectively when designing such protocols, and their limitations should be considered during interpretation of the study results. The performance of the two recommended methods is

broadly similar, with neither consistently out-performing the other in terms of accuracy and precision. Consequently the choice of technique to use may depend on the specific experimental set-up (including equipment used and expected RF system performance), clinical questions and practicability of inclusion into the scanning protocol.

Finally inaccuracy compared to ground truth and systematic differences between methods are minimised when saturation performance is ideal. Consequently the best preparation pulse available should be used and further work to improve saturation pulse efficiency and reliability is warranted.

7.4.6 Limitations

Several limitations apply to this study. Only a single set of imaging parameters were evaluated whereas sensitivities to various factors will vary between differing implementations of the techniques. The analysis was limited to assessing variation of errors with SE and T_1 measurement accuracy and additional sources of error that were not simulated (e.g. ineffective spoiling, motion and inflow artefact [37], non-uniform sensitivity, slice profile, B_1 inhomogeneity and variations in bolus shape) could influence results. For correction of myocardial data it was assumed that SI differences compared to blood arise solely through differences in T_1. Variations in factors contributing to S_0 (including proton density and coil sensitivity) as well as differences in T_2^* were not included. Similarly the T_2^* shortening effects of contrast agent were not modelled, although this has been shown to be negligible at the short TE values used in DCE sequences [198]. Additionally image data is acquired over a period of time which is of the same order of magnitude as the saturation time. Consequently the effective TS will differ across the spatial frequencies of the image, but for this study the signal intensity was assumed to depend entirely on the zero-spatial frequency data.

Contrast agent relaxivity was assumed to be identical in blood and myocardium and protons in both intra- and extracellular spaces were assumed to experience the effects of the contrast agent equally (i.e. fast water exchange was assumed [41]). While water exchange effects may lead to bias in absolute quantification of DCE-MRI data this would be due to distortion of the tissue response curve. As all methods investigated in this study use the same tissue data we would

thus expect any bias due to water exchange would be expected to be similar across the methods unless water exchange effects were present in the AIF (which would not be expected due to the rapid exchange of water between the plasma and red blood cells [47]).

Simulations were limited to a single set of AIF shape (for rest and stress), native T_1 values, SNR and heart rate, and three sets of physiological parameters using a basic one-compartment model that is a simplified representation of the myocardium (which can be more fully described by two-region models [1, 97]). In practice the AIF shape will vary between patients and between studies (e.g. between rest and stress) due to differences in cardiovascular physiology (both in the peripheral vasculature and in the heart). However in these simulations these differences were neglected and a single AIF shape assumed.

Non-linearity effects may vary with field strength and peak concentrations occurring in the LV blood pool and myocardium and noise induced bias may be more severe at lower SNR, particularly a lower field strengths.

In the phantom study the model based non-linearity correction approaches were approximated by comparing data from different gels in the same field of view, whereas in practice data will be compared from different time points at the same spatial location. Consequently spatial variation in saturation or readout pulse efficiency could have affected the results. Furthermore a gel with T_1 as short as expected at the AIF peak was not included and so future validation studies would ideally include test objects spanning the full range of expected values.

Finally the simulation study assumed each DCE sequence was commenced with no contrast agent present, whereas in clinical protocols multiple contrast agent administrations are common (e.g. when applying the dual-bolus method or when performing DCE under different physiological conditions such as at rest and under stress) and so residual contrast agent from previous administrations will be present for all except the first DCE series.

In view of these limitations the exact behaviour of each method may exhibit substantial dependence on the protocol implemented, equipment used and characteristics of the subject. However the results presented demonstrate

fundamental patterns of behaviour that should be considered when performing quantitative myocardial DCE-MRI.

7.5 Conclusions

Performance characteristics of non-linearity correction methods for myocardial DCE-MRI, including a novel application of bookend T_1 data, have been assessed through simulation and phantom studies. Under ideal conditions non-linear correction techniques have been shown to be effective in reducing or eliminating bias due to signal non-linearity. However, at SNR and SE values consistent with current technology, including optimised saturation pulses, substantial bias or precision degradation may occur.

Various non-linearity correction techniques have been shown to exhibit different performance, including different levels of bias, sensitivity to saturation efficiency imperfection or levels of precision. Consequently potential biases should be considered when comparing quantitative DCE-MRI results from studies using different non-linearity correction methods, protocols or hardware.

In particular high dependence on saturation efficiency has been shown for native T_1 and dual-sequence based methods and so these techniques may be substantially biased unless acquired under conditions where near-ideal saturation pulse performance can be guaranteed

When saturation is not perfect the deviations between signal models and simulations are substantially greater for the interleaved image of the dual-sequence method than for the conventional sequence. The use of a very short saturation time in this manner can thus increase the biases in non-linearity correction arising from use of a limited signal model. With this sequence these can be large even within the range of performance of optimised saturation pulses.

Notably in these simulations the feasibility of model-based conversion of data generated without a dual-acquisition technique (dual-bolus or dual-sequence) has been demonstrated for a simulated protocol. While some systematic errors and saturation efficiency dependency exist in these methods it has been shown

that they can be more accurate and precise than the dual-acquisition approaches, despite the fact that the raw data acquired will be non-linear.

As detailed above the native T_1 based approach is highly sensitive to imperfect saturation efficiency and so is not recommended. Overall either bookend T_1 or PDw based correction methods are thus recommended with the latter approach (using the steady-state signal model) demonstrating the lowest bias, saturation pulse efficiency dependency and slice dependence in these simulations. However evaluation in clinical application is required to determine the impact of factors excluded from this study as discussed in the limitations.

These methods are compared further through *in vivo* study in the following chapter. These results of this chapter have been used to inform the protocols for the following experimental chapters with the exceptions that due to the chronology of the project (section 1.4) the STEMI study did not include PD_w or dual-sequence acquisitions and the hyperoxaemia study used a sub-optimal flip angle for the PD_w sequence. As a sub-optimal PD_w sequence was used for the latter the bookend T_1 based correction was used for clinical studies as discussed in the respective chapters.

Appendices to Chapter 7

7.6 Appendix 1 - Detailed methods for forward signal simulation

This appendix provides a detailed description of the forward simulation process referred to in section 7.2.

7.6.1 Starting condition

To generate signal intensity curves from a T_1-time data set the following process was followed. Magnetisation was described as a 3x1 vector.

Equation 7-14

$$M = \begin{bmatrix} M_x \\ M_y \\ M_z \end{bmatrix}$$

This was assumed to start at equilibrium prior to the first pulse of the first cardiac cycle.

Equation 7-15

$$M_{eq} = \begin{bmatrix} 0 \\ 0 \\ M_0 \end{bmatrix}$$

For the remainder of the sequence the magnetisation was carried forward step-wise from each event (saturation, readout pulse, spoiling or recovery period), including from each cardiac cycle to the next (i.e. the full magnetisation evolution was simulated across the entire DCE-MRI series). The T_1-time data set was discretised into a T_1 value for each cardiac cycle, so the T_1 value used for each event was equal to that at the time of the first saturation pulse.

7.6.2 Events

In the notation below M^+ and M^- refer respectively to the magnetisation vector before and after the corresponding event.

7.6.2.1 Rotation

Rotations of magnetisation were all simulated about the y-axis by multiplication of M_z before the pulse by a 3x3 array, R_y. For flip angle of φ:

Equation 7-16

$$M^+ = R_y M^-$$

$$where\ R_y = \begin{bmatrix} cos\varphi & 0 & sin\varphi \\ 0 & 1 & 0 \\ -sin\varphi & 0 & cos\varphi \end{bmatrix}$$

7.6.2.2 Free recovery/decay

Between pulses recovery of longitudinal magnetisation and decay of transverse magnetisation were simulated by multiplying the magnetisation at the start of the period by the matrix A and adding the vector B. For recovery period of t:

Equation 7-17

$$M^+ = AM^- + BM_0$$

$$where\ A = \begin{bmatrix} e^{-t/T_2} & 0 & 0 \\ 0 & e^{-t/T_2} & 0 \\ 0 & 0 & e^{-t/T_1} \end{bmatrix} and\ B = \begin{bmatrix} 0 \\ 0 \\ 1 - e^{-t/T_1} \end{bmatrix}$$

7.6.2.3 Spoiling

Perfect spoiling was simulated by nulling the two transverse components of the magnetisation:

Equation 7-18

$$M^+ = SM^-$$

$$where\ S = \begin{bmatrix} 0 & 0 & 0 \\ 0 & 0 & 0 \\ 0 & 0 & 1 \end{bmatrix}$$

7.6.3 Scope of events

The effect of each saturation pulse was modelled as a rotation by the effective flip angle of the pulse ($\varphi = \theta = \text{acos}(1\text{-SE})$) followed immediately by perfect spoiling. This was applied for each saturation pulse in the sequence (i.e. three per cardiac cycle) as non-selective saturation pulses are used.

The effect of each readout pulse was modelled as a rotation of the magnetisation about the y-axis by the flip angle of the pulse (φ). Each readout pulse was followed by a recovery period of TR at the end of which perfect spoiling was simulated. The effect of these pulses was only simulated for the slice being simulated, as slice-selective readout pulses are used.

For the dual-sequence approach the effects of the other slice acquired in the same position (following a later saturation pulse) were included when simulating the low-resolution, short TS image, and vice-versa. The AIF scan was interleaved between saturation for and acquisition of the first slice, and was assumed to be in the same physical position as the third slice.

7.6.4 Event timing

7.6.4.1 Standard imaging

Following each saturation pulse one of two options was simulated.

1. If the saturation/readout period did not correspond to the slice being simulated then free recovery was modelled for a single time period, equal in duration to the total duration of the steps below (which equals $TS+TR(N-n_{k0})$). During this period any RF pulses applied would be slice-selective and applied to a different physical location.
2. If the saturation/readout period did correspond to the slice being simulated an initial delay period was simulated of duration equal to $TS-(n_{k0}-1)TR$. There then followed N repetitions of simulation of a readout pulse, recovery for time TR then perfect spoiling. Magnetisation was recorded immediately after application of pulse n_{k0}. At the end of the third saturation/readout period free recovery was simulated for duration equal to the remainder of the cardiac cycle length. The magnetisation at the end of this period was used as the starting magnetisation for the next cardiac cycle.

7.6.4.2 Dual-sequence imaging

For dual-sequence imaging the simulation of signal was identical for slices 1 and 2 as the extra readout pulses were selective to the position of slice 3, and were interleaved into existing dead-time, so did not affect the timing of the other pulses.

When simulating acquisition of either slice 3 or the additional interleaved AIF scan the first saturation/readout period (that used for slice 1 of the high resolution images) was modified to include the extra readout pulses. The initial delay for the interleaved AIF scan was $TS_{DS}-(n_{k0,DS}-1)TR_{DS}$, where the DS subscript indicates the parameters are those corresponding to the interleaved scan. The readout train was then simulated as above for N_{DS} pulses each followed by a delay of TR_{DS} and then spoiling. This was followed by a delay such that the total time between the first two saturation pulses of each cardiac cycle remained as $TS+TR(N-n_{k0})$. Free recovery was simulated between the second and thirst saturation pulses and then after the third saturation pulse a delay, readout train and final delay until the end of the cardiac cycle was simulated for slice three (in the same way as for the standard sequence).

The above process was followed whether simulating the interleaved AIF scan (in which case magnetisation was recorded immediately after application of pulse $n_{k0,DS}$ after the first saturation pulse) or slice three at high resolution (in which case magnetisation was recorded immediately after application of pulse n_{k0} after the third saturation pulse).

7.6.5 Signal simulation

The above process formed a function in Matlab to simulate the longitudinal magnetisation at the time of the application of the readout pulse for the central line of k-space for the slice being simulated. To simulate signal intensity without noise the magnitude of this result was calculated for each cardiac cycle.

To simulate noisy data with a Rician distribution the built in ricernd function in Matlab was used. This function performs the following calculation:

Equation 7-19

$$M_{noisy} = \sqrt{\left(M_{noise-free} + r_1 S\right)^2 + (r_2 S)^2}$$

In the above r_1 and r_2 are random numbers drawn from a normal distribution with mean zero and standard deviation of one, and S is the standard deviation[1] of the noisy signal, as specified in the methods.

7.6.6 Repetition

The above process was repeated separately for each slice (including the interleaved AIF image for the dual-sequence method). Signal was simulated separately for myocardium (in different physiological states) and blood, each with a different T_1-time curve, derived from the concentration-time curves presented in Figure 7-2. When simulating noisy data the process was repeated multiple times (as specified in the methods section of Chapter 7) and each resulting dataset was analysed separately. The resulting physiological parameters were then summarised statistically.

[1] NB Equation 7-19 reflects magnitude reconstruction of MRI images (the positive root is taken), and incorporates the fact that at low SNR the distribution of signal intensity values becomes skewed. M and S approximate the mean and standard deviation of the longitudinal magnetisation at high SNR, where the Rician distribution approximates the Gaussian distribution (and so is approximately symmetrical).

7.7 Appendix 2 - Examination of behaviour of signal models in comparison to forward simulation

As discussed in section 7.2.1 the two analytical signal models used are approximations to the scanning sequences used. The full recovery model was derived by Larsson *et al* [44] for application in myocardial perfusion imaging using an IR sequence whereas SR sequences are now more commonly used. In that derivation ideal performance of the inversion pulse was assumed, as was a starting condition of equilibrium magnetisation prior to each inversion pulse. In the implementation in this thesis the former assumption was relaxed to allow arbitrary magnetisation preparation including ideal or non-ideal saturation.

In practice full recovery will not be achieved whenever there is insufficient time between image acquisitions for effectively complete magnetisation recovery. This would be a concern in the original inversion recovery application. It would also be of concern in non-prepared sequences such as the PDw variant used in this thesis. However it is not a concern for saturation recovery sequences if the preparation is ideal, as the saturation pulse would nulls magnetisation making prior evolution irrelevant. As Larsson's model has been used previously for quantitative myocardial perfusion studies it was included to allow assessment of its performance in the presence of non-ideal saturation pulse performance.

With a regular spacing of image acquisitions and a constant T_1 an analytical model can be derived for the steady-state signal, accounting for incomplete recovery of magnetisation. This was done in work by Kershaw [45] for application in oncological imaging with non-triggered acquisitions in which the effect of each pulse is experienced by all of the spins. In practice this scenario differs to that in the work in this thesis as:

- multi-slice 2D acquisitions are performed with a combination of global and slice-selective RF pulses
- the acquisitions are not spread equally temporally
- the time between successive acquisitions of the same slice varies with natural variation in cardiac cycle length or ECG triggering errors
- T_1 changes due to varying concentrations of contrast agent

Additionally processes such as blood flow or other forms of motion are not accounted for in either of these models.

To account for some of these limitations the relationship between signal intensity and T_1 could be modelled using methods similar to the forward simulations. However this would be computationally demanding as this process would need performing iteratively during optimisation processes to account for temporally varying T_1 in a DCE experiment, and would still neglect additional signal influencing factors.

Given the above considerations it was decided to adopt Kershaw's steady-state model [45] in addition to the full recovery model and to compare their performance. While the steady-state model exhibits the limitations described above it was included to allow comparison of its performance with that of the simpler model, which neglects partial recovery between preparations entirely, but has been used in previous myocardial DCE quantification publications.

In the following sections the characteristics of these two models are examined and compared with forward simulations across the range of conditions and pulse sequence parameters relevant to this chapter. In these figures the data presented is the longitudinal magnetisation relative to the equilibrium value. Relative signal intensity would depend on the magnitude of these values as well as noise contributions.

7.7.1 Conventional saturation recovery sequence

In Figure 7-35 the models are compared to forward simulations for the three acquired slices using the conventional sequence. The simulation results are for the 100^{th} dynamic phase of a series with constant T_1 to approximate the steady-state. This figure extends in both directions beyond the R_1 range encountered in the simulations, through which several key observations can be made.

Models and simulations agree exactly for ideal saturation as prior magnetisation evolution becomes irrelevant when magnetisation is completely nulled. For all SE values the models and simulations converge at high R_1 as longitudinal recovery of magnetisation between preparations becomes close to complete.

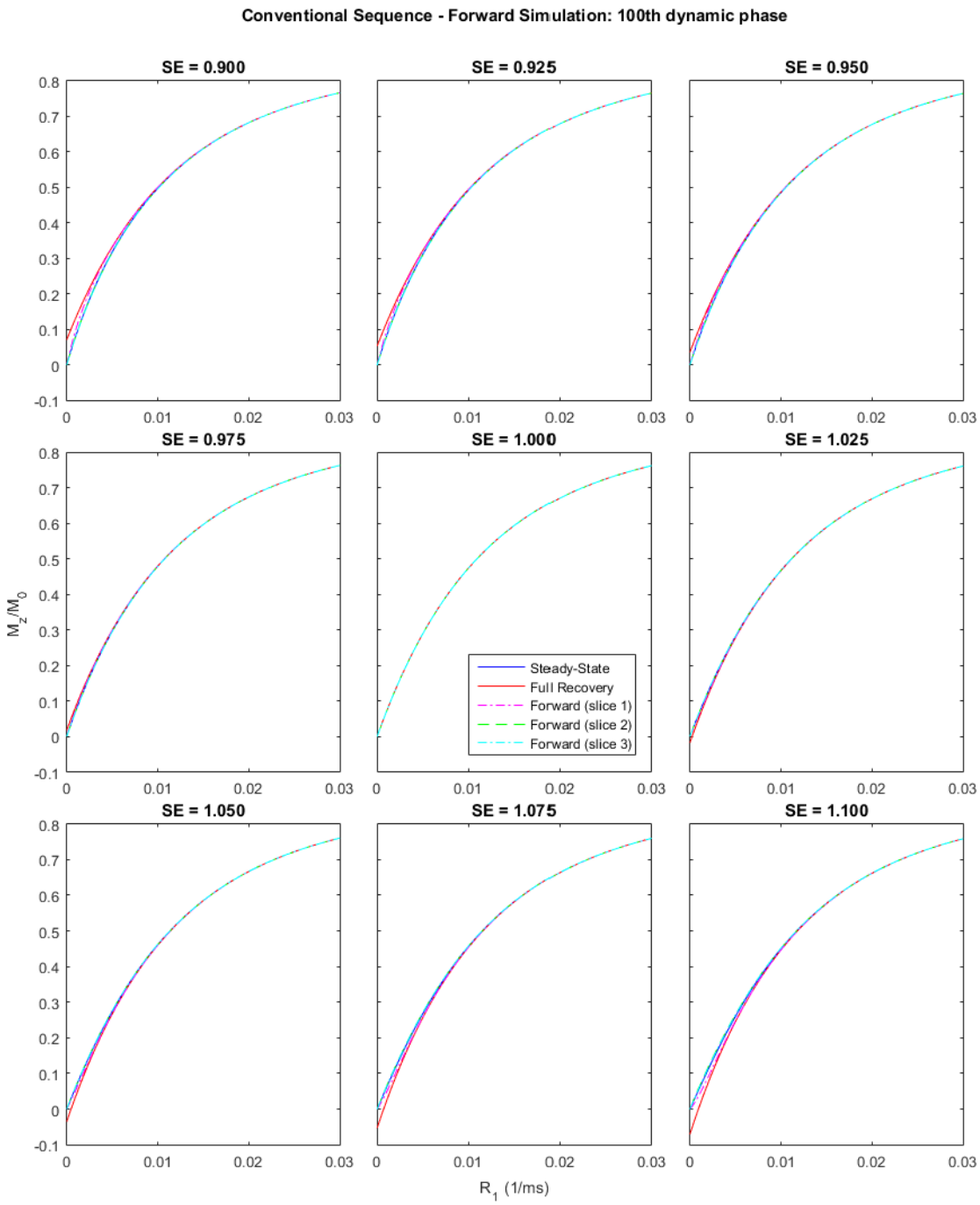

Figure 7-35 – Comparison of analytical models to the approximated steady-state in forward simulations of the conventional SR sequence. At SE = 0 (centre panel) the models and simulations overlie each as prior magnetisation evolution is irrelevant. This is also true for all of the SR data presented in the following three figures.

A key difference between analytical models is that the full recovery version exhibits an SE dependent y-axis intercept whereas the steady-state model and forward simulations consistently exhibit zero or negligible M_z at R_1=0. In the latter two cases repeated RF pulse application with no recovery drives the longitudinal magnetisation to zero in the steady-state.

As the models and simulations converge at high R_1 the following figures show R_1 up to 0.005ms^{-1}, so the divergences can be seen more clearly. Figure 7-36 shows the same data as the previous figure, but only for this narrower range.

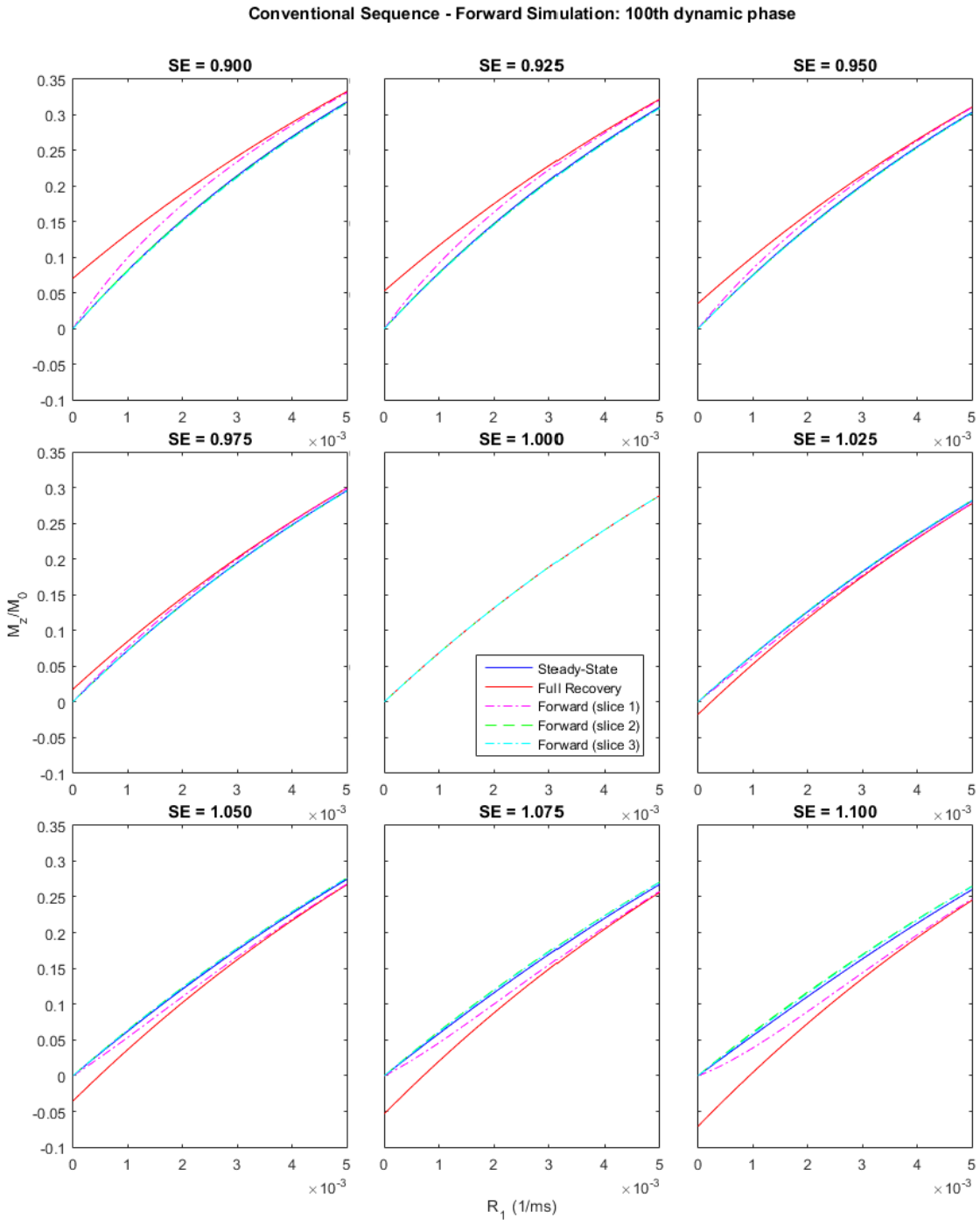

Figure 7-36 – Comparison of analytical models to the approximated steady-state in forward simulations of the conventional SR sequence. This figure is identical to the previous figure, except the x-axis is limited to a narrower range to better show deviations in behaviour.

The steady-state model can be seen to be a close descriptor of the latter slices whereas the behaviour for slice 1 is intermediate to the two models, tending towards the steady-state model at low R_1 and the full recovery model at high R_1.

The data presented so far however shows the results from the 100th dynamic phase in the forward simulation, to approximate the steady-state. In practice the T_1 is changing dynamically so the steady-state may not be achieved. In Figure 7-37 the behaviour for the first dynamic phase is shown, assuming magnetisation was at equilibrium prior to the application of the first pulse. In this case the assumptions of the full recovery model are valid for slice 1, so the results from that slice agree with the full recovery model. For the later slices however the steady-state model is a better descriptor of the behaviour in the simulations as even with non-ideal saturation performance the large effective flip angle of the preparation pulse rapidly drives the system to steady-state.

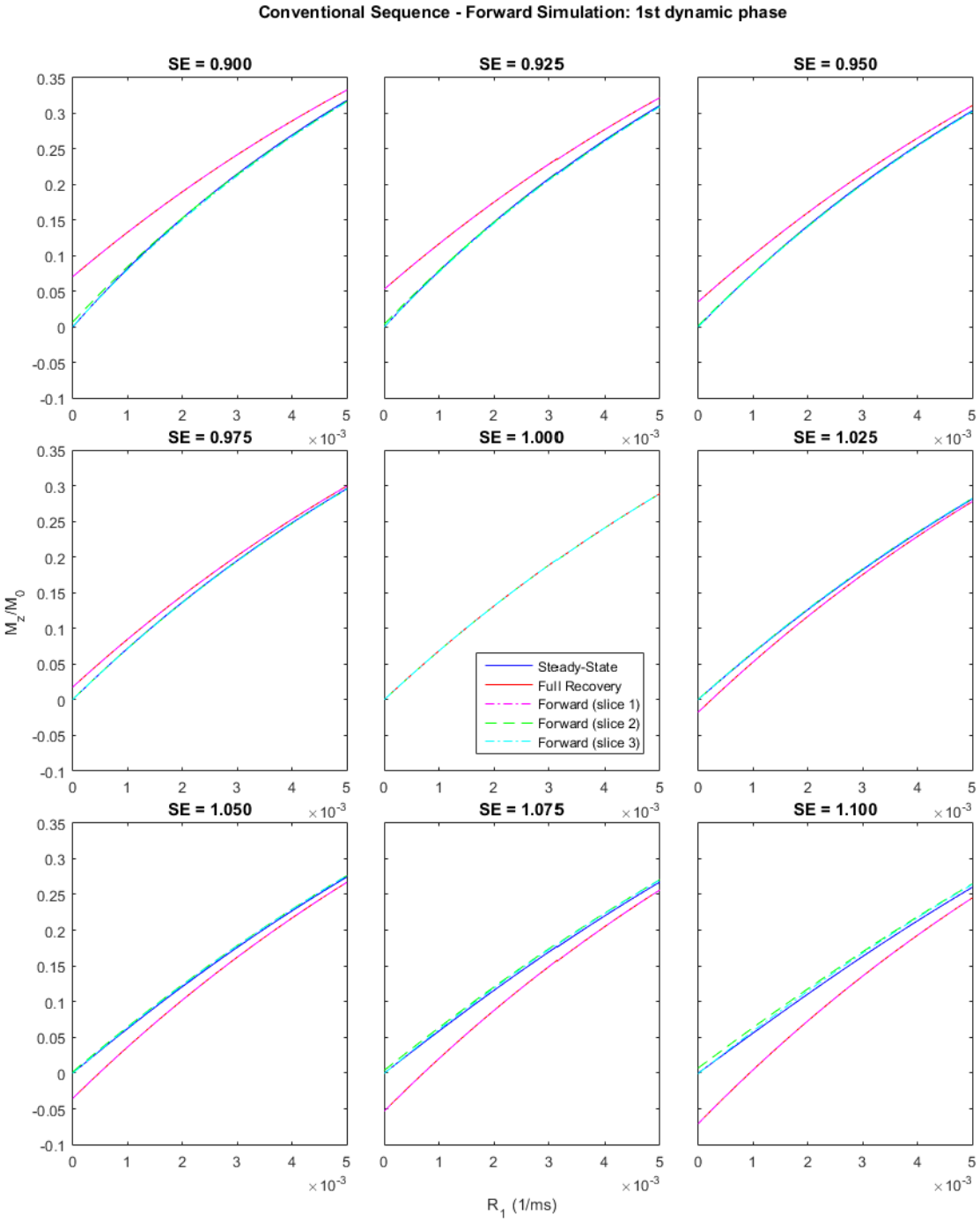

Figure 7-37 – Comparison of analytical models to the first dynamic phase from forward simulations for the conventional SR sequence. The results for slice 1 overlie those for the full recovery model exactly, while those for the latter slices are close to the steady-state model due to the effect of the previous saturation pulse (or pulses).

In summary, the models and simulations converge at high R_1 or with ideal saturation but deviate at low R_1 and poor saturation pulse performance. The steady-state is approached quickly for this sequence, and consequently the steady-state model is generally a close approximation of the signal behaviour for the latter two slices. For the first slice however, the longer delay prior to

preparation leads to divergence from the steady-state model towards the full recovery model at intermediate R_1 values.

7.7.2 Interleaved AIF sequence (dual-sequence)

Figure 7-38 shows behaviour for the interleaved AIF scan. As for the conventional variant both models converge with the simulations at high R_1. Similar to slice 1 in Figure 7-36 the forward simulation matches the steady-state model at zero R_1, and then diverges towards the full recovery model at intermediate R_1 values.

One key difference between this sequence and the conventional sequence is that within the simulated SE range M_z is inverted for a range of low R_1 values (bottom row of Figure 7-38). However this only occurs above the 2-3% oversaturation that might be expected with optimised saturation pulses [180-183]. For high degrees of over-saturation there thus exists a non-monotonic relationship between R_1 and M_z in the forward simulations and steady-state model. Implications of this are discussed in the following appendix (section Chapter 7).

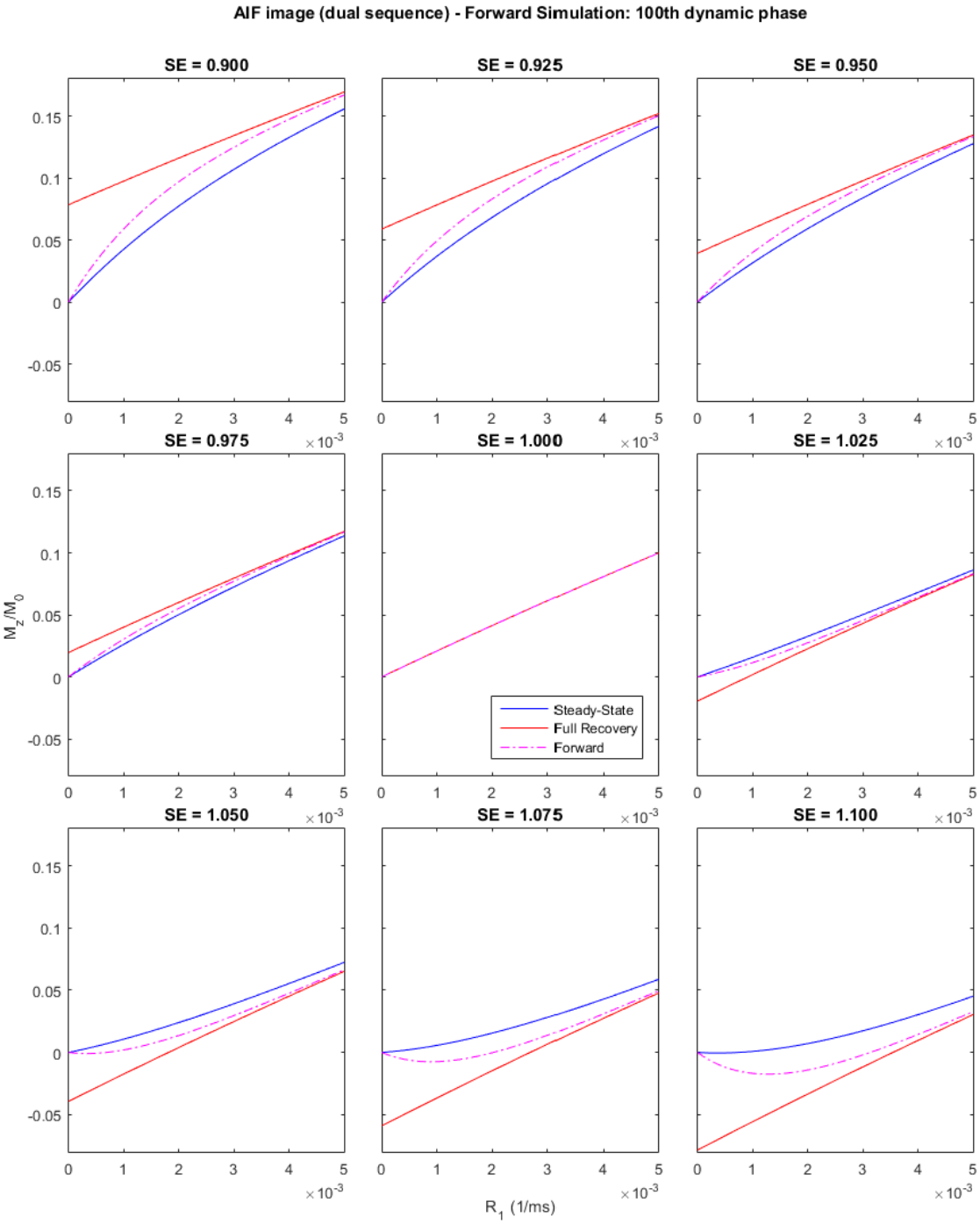

Figure 7-38 – Comparison of analytical models to approximated steady-state from forward simulations for the interleaved AIF sequence. Due to the short saturation times larger relative deviations exist for this sequence than for the conventional sequence.

7.7.1 PDw sequence

Figure 7-39 shows behaviour of the PDw sequence (3° flip angle). While the behaviour over a wide range of R_1 values is shown only pre-contrast behaviour (vertical dashed line) is relevant to the non-linearity correction process.

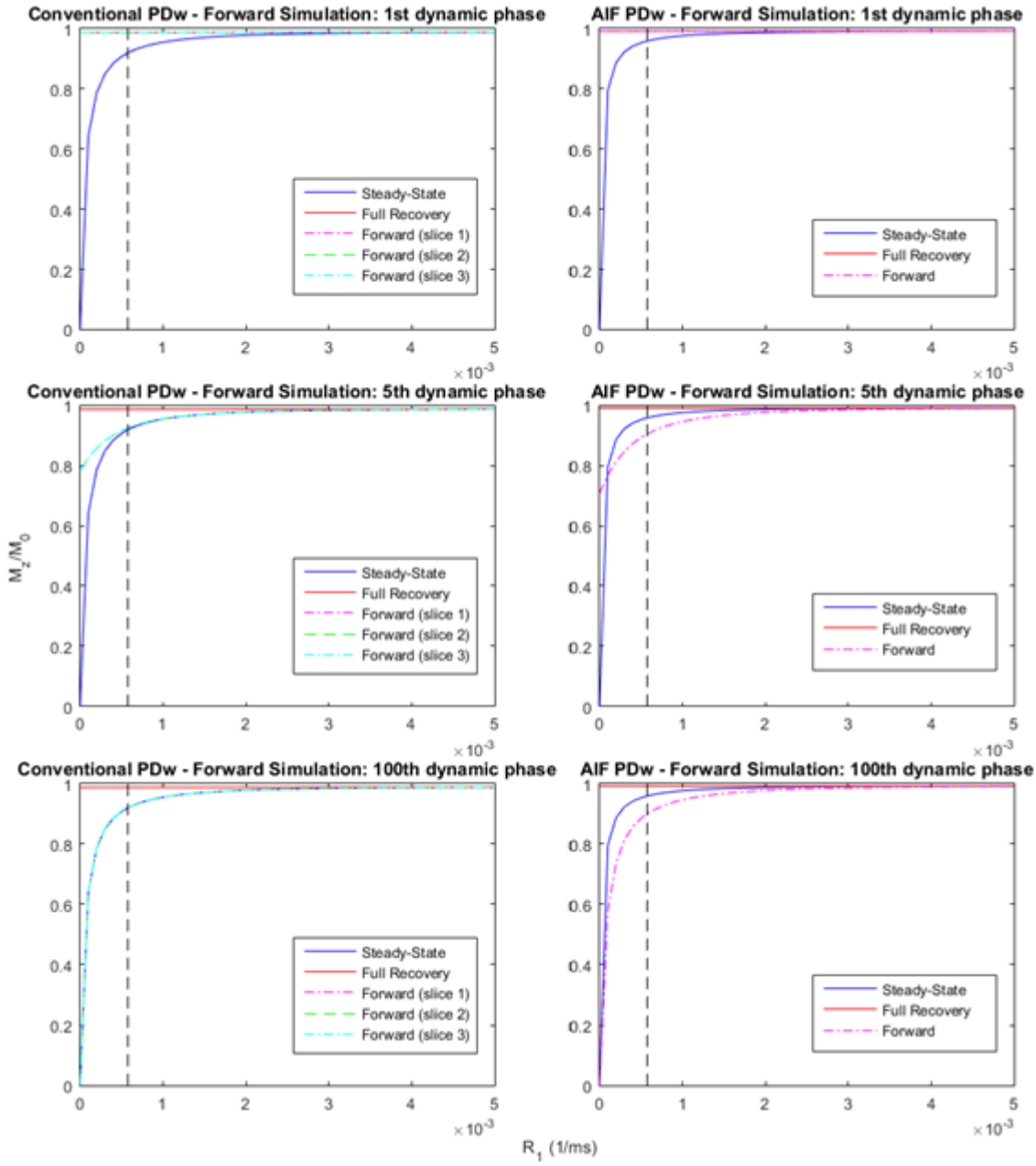

Figure 7-39 – Comparison of analytical models to forward simulations for the 3° flip angle PDw sequence as implemented for the conventional and dual-sequence method. The vertical dashed lines indicate the native R_1 of blood. The top row shows the first dynamic phase while the bottom row shows the 100th, approximating the steady-state. The middle row shows the 5th dynamic phase, at which point the steady-state is still being approached. The three slices of the conventional sequence exhibit identical behaviour to each other and overlie the full-recovery model for the first dynamic phase and the steady-state model for the 100th. For the AIF interleaved sequence the results of the forward simulation for the first dynamic phase overlie the full recovery model.

The full-recovery model describes the behaviour of the forward simulations well for the first dynamic only, but unlike the standard SR sequences this applies for all three slices due to the absence of non-selective pulses in the PDw variant.

By the 100th dynamic phase the steady-state model is a good descriptor of the behaviour for the conventional sequence. However deviations arise for the AIF interleaved image as the analytical model does not include the readout pulses for the co-located full resolution slice.

As discussed previously the SR sequences approach steady-state very rapidly due to the presence of saturation pulses, even where these are not performing ideally. However in the absence of the saturation pulse, and with low readout flip angles, the steady-state is approached much more slowly. As shown in the middle row of Figure 7-39 at the 5th dynamic phase (halfway through the simulated baseline) the steady-state is still being approached for low R_1 values. This approach to steady-state is plotted simulated for the R_1 of native blood and both readout flip angles in Figure 7-40. It can be seen that there is greater variation initially for the higher flip angle, but the variations between phases becomes negligible more quickly (i.e. the steady-state is approached more quickly).

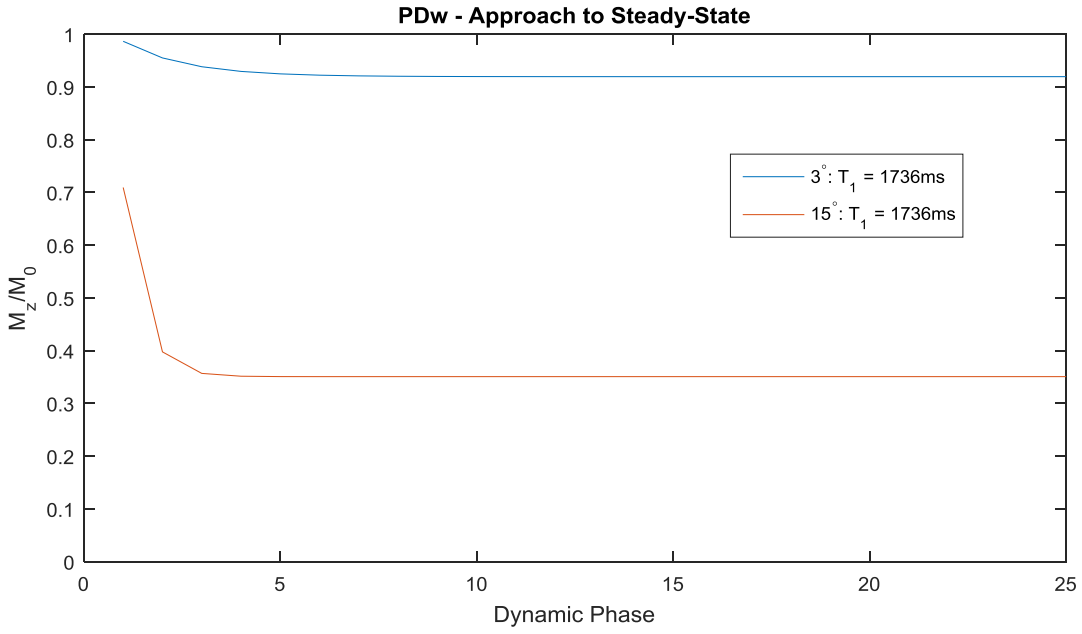

Figure 7-40 – Plots showing the approach to the steady-state for the longest T_1 relevant to the simulation study (that of native blood). Plots are shown for both flip angles simulated.

7.7.2 Justification for signal model choice

The full recovery model was originally implemented for use with inversion recovery sequences. In this scenario large deviations between the model and actual behaviour would be expected due to incomplete recovery between

inversions. With ideal preparation SR sequences are not dependent on prior magnetisation evolution prior, and so the full recovery model would perform better than in its original application. However, in the preceding sections this model is shown to deviate from forward simulations when saturation performance is not ideal, especially at low R_1. The model derived by Kershaw [45] extended the full recovery model to account for both steady-state non-equilibrium magnetisation prior to preparation and arbitrary preparation pulse performance. While the sequences this was derived for differ from those used in myocardial DCE, thus limiting the applicability of the derived model to work in this thesis, it was considered that including reduced longitudinal magnetisation prior to saturation in the model may reduce errors in non-linearity correction.

In the data presented it can be seen that the models and simulations converge for fast longitudinal recovery (high R_1) or ideal saturation (SE = 1) and deviate most substantially for non-ideal saturation at low R_1. In particular larger errors occur for the interleaved AIF scan of the dual-sequence variant, which has a shorter saturation time. At intermediate R_1 values there is inconsistency in which model is a better descriptor of the simulations dependent on the R_1, slice number and progress on the approach to steady state. Similarly deviations exist for the PDw sequence at low R_1. However, in contrast to the SR sequences the steady-state takes several cardiac cycles to approach for this sequence.

In the above sections it can thus be seen that the steady-state model can offer a better descriptor of the signal behaviour compared to the full recovery model in many, but not all, of the scenarios included in the simulation study. Furthermore, it introduces minimal extra complexity and so is readily applicable in practice. Both models were adopted and compared in the assessment of non-linearity correction methods in this chapter. In both cases however further factors (such as motion and heat rate variability) will affect the true behaviour in clinical studies. Consequently it may be possible in future work to derive more detailed models, which may improve accuracy further.

7.8 Appendix 3 - Optimisations with non-monotonic functions

In this appendix issues relating to performing optimisations using a non-monotonic function are discussed, as these are required for the bookend T_1 based non-linearity correction method (see section 7.2.1.3). Two procedures are relevant to this discussion, estimation of SE from baseline and post-contrast data and determination of T_1 throughout the dynamic dataset. These are set out in Equation 7-10 and Equation 7-12, repeated for reference below:

Equation 7-20

$$SE = \underset{0<SE<2}{\arg\min}\left(\left(\frac{\left|f\left(T_{1,baseline}, SE\right)\right|}{\left|f\left(T_{1,post-contrast}, SE\right)\right|} - \frac{SI_{DCE,baseline}}{SI_{DCE,post-contrast}}\right)^2\right)$$

Equation 7-21

$$T_1(t) = \underset{T_1(t)>0}{\arg\min}\left(\left(S_0 \cdot \left|f\left(T_1(t), SE\right)\right| - SI(t)\right)^2\right)$$

Note that while $f(T_1,SE)$ is shown here the same applies when the steady-state model, $g(T_1,SE)$ is used. The issues relate only to the bookend T_1 based method as the models are monotonic for SE = 1 or SE = 0, which are assumed throughout application of the other methods (the latter for PDw sequences).

7.8.1 Determination of saturation efficiency

For determination of SE there is an expectation that in practice the value would be close to ideal (near 1). Consequently this optimisation was initialised with a value of 1, from where the algorithm searched outwards. The model term used in Equation 7-20 (the ratio of results of the signal model with baseline to post-contrast T_1) decreases with increasing SE (and vice versa) in the vicinity of SE = 1 (Figure 7-41). This continues throughout the full range of under-saturation but for over-saturation a null point is reached at the value for which the signal model at baseline (the numerator) would be zero. For the full recovery model this occurs around SE=1.06 for blood. At a higher SE value a singularity is encountered where the post-contrast result (denominator) is zero. The latter however occurs only for SE values substantially outside the simulated range.

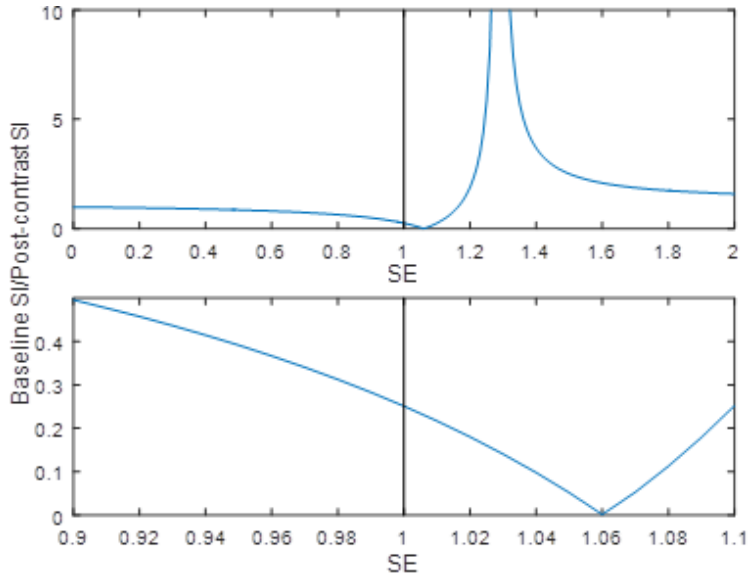

Figure 7-41 – ratio of baseline to post-contrast SI of blood modelled using the full-recovery model and parameters as in Table 7-1. Top: SE=0 to SE=2. Bottom: limited to SE range included in simulations. For the steady-state model the null point and singularity occur at higher SE values.

Given the implementation adopted the algorithm may incorrectly identify a solution from the wrong (low SE) side of the null point in the presence of high levels of over-saturation. The bookend approach should therefore be considered to carry risk of errors if used when over-saturation is potentially high enough that baseline signal is acquired from partially inverted magnetisation. Such cases are unlikely for the SE range expected in practice, although the potential for such errors exists at the upper end of range simulated. It should be noted that the example above is the worst case scenario, the full recovery model. For the steady-state model considerably higher levels of over-saturation are required to yield nulled signal. The smooth variation in bias in estimated SE in the results (Figure 7-17 and Figure 7-18) suggests, however, that such errors did not occur in the simulations. This can be explained by the observation from the results that saturation imperfection is underestimated, and also that even for SE = 1.1 signals generated in forward simulations arise from magnetisation that has recovered past the null point (except slice 1 of the first dynamic phase).

7.8.2 Determination of T_1 from DCE signal intensity

The second occasion where a potentially non-monotonic model is used in an optimisation is in the estimation of T_1 for each time point of the dynamic data, based on the derived signal model from the prior step (Equation 7-21). For the full recovery model the behaviour is non-monotonic for any SE value greater

than 1 (Figure 7-42 - left). The steady-state model differs in that a degree of over-saturation substantially outside the simulated or practically expected range (SE>1.5) is required for non-monotonic behaviour (Figure 7-42 - right). However once this level is reached there are up to three (compared to two for the full-recovery model) R_1 values corresponding to low signal intensities.

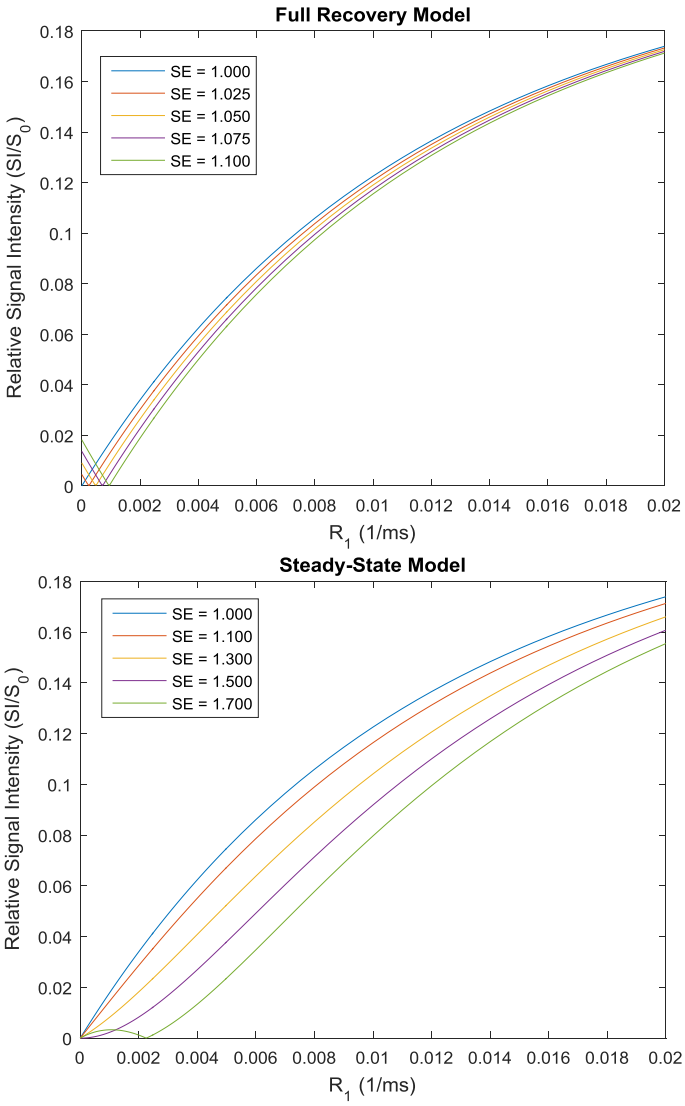

Figure 7-42 – Relative signal intensity variation with R_1 for ideal saturation and various over-saturation values for the full recovery (top) and steady-state (bottom) model. As larger degrees of over-saturation are required for signal nulling in the latter a broader range of SE values is plotted.

In this optimisation there is no clear choice of initialisation value as a wide range of R_1 values are expected throughout the dynamic experiment. Consequently an algorithm implementation which searches over a specified range was chosen rather than one seeded with a starting value.

There is scope for the algorithm to return the wrong R_1 solution if the input signal intensity is within the range exhibiting non-monotonic behaviour, for the

SE value determined in the previous step. Consequently such errors would not be expected with the steady-state model as SE in excess of 1.5 would not be expected. In the worst-case shown above (full recovery model, SE = 1.1) the ambiguous range is $R_1 \leq 0.002$ ms^{-1} (i.e. $T_1 \geq 500$ms). However, as shown in the results the degree of saturation imperfection is underestimated when the bookend T_1 approach is applied with the full recovery model, i.e. the SE value used in the signal model will be closer to 1 than the ground truth input value. The worst-case described above would thus not be encountered and the R_1 range of non-monotonic behaviour will be lower. Indeed for this signal model the highest estimated SE (without noise) for any slice was 1.0221. For this SE value the ambiguous R_1 range is lower than the baseline blood R_1. The corresponding highest signal intensity in the non-monotonic section of the full recovery model is around 25% lower than that of native blood. Consequently even with the addition of realistic noise levels simulated errors arising from the algorithm returning a result from the wrong p of the signal model curve would be unlikely.

7.8.3 Implications for results in this thesis and future work

The bookend T_1 method introduces a requirement to perform optimisations using functions that exhibit non-monotonic behaviour above a threshold SE value. This introduces the potential for errors arising from the optimisation algorithm identifying the incorrect region of the objective function. As described above however such errors are unlikely for the SE range expected in practice.

As a result of the above arguments it is not expected that errors arising from misclassification during optimisation will have affected the validity of findings in this thesis for simulation or practical experiments. However the above discussion does highlight the need to consider the potential impact of the use of non-monotonic models in optimisation steps. Such considerations may be more relevant in different scenarios. For example if the bookend T_1 based method were used with the dual-sequence approach then the potential for such errors would arise at SE values closer to ideal (for the AIF data which, with a shorter TS, requires a lesser degree of over-saturation to lead to signal nulling).

Chapter 8

Volunteer Study - Comparison of Non-Linearity Correction Methods and Contrast Equilibrium MRI

In this chapter a study is described in which DCE-MRI and T_1 data from a cohort of healthy volunteers were acquired and analysed to allow an *in vivo* comparison of the non-linearity corrections methods discussed in the previous chapter.

A subset of data from this study was included in a paper [177] and conference abstract [178] alongside the simulation study described in the previous chapter. Contributions of the individual authors are described at the start of this thesis.

8.1 Introduction

As discussed in Chapter 7 several potential methods exist to account for signal non-linearity in myocardial DCE-MRI. In that chapter these methods were compared through simulation and phantom studies. However such studies are a limited approximation to the full complexity of clinical scanning.

8.1.1 Aims

In this chapter the performance of these signal non-linearity correction methods are assessed *in vivo* by comparing results from model-based deconvolution using a one-compartment model with non-linearity correction methods from the previous chapter applied.

Additionally the T_1 and haematocrit data acquired for this study allows measurement of v_d by contrast-equilibrium MRI, and the results of that analysis are presented in this chapter.

The volunteers were recruited as a healthy comparison group for the hyperoxaemia study discussed in the following chapters. As the primary aim of the work carried out in this chapter was to compare non-linearity correction methods *in vivo* the analysis was limited to the data acquired under conditions

of normoxaemia and analysed using a one-compartment tracer kinetic model to estimate MBF and v_d.

8.2 Methods

8.2.1 Acquisition

30 healthy volunteers were recruited (exclusion criteria were as described in the later clinical study chapters, see section 9.2.1. T_1 and DCE-MRI data were acquired using a clinical 3.0T whole-body scanner (Philips Achieva TX, Philips Healthcare, Best, Netherlands) with a dedicated 32-channel cardiac phased array receiver coil with dual-source radiofrequency-field shimming. All volunteers gave written informed consent and the study was approved by the local research ethics committee. Stress DCE imaging was undertaken during maximal hyperaemia (achieved by 140-210 μg/kg/min adenosine infusion [199]) with an intravenous dual-bolus (0.005/0.05 mmol/kg with the main bolus administered approximately 30 seconds after the pre-bolus) of gadobutrol (Gadovist, Bayer Schering Pharma, Berlin, Germany) administered at 4 ml/s followed by a 20ml saline flush at equal injection rate. Rest DCE-MRI imaging was undertaken at least 15 minutes after stress imaging with the same contrast agent administration protocol. Imaging was performed under normoxaemia and hyperoxaemia (achieved by breathing oxygen through a nasal cannula) in a random order as these volunteers were recruited for the CAD study described in the following chapter. For this chapter analysis is limited to data acquired at normoxaemia.

A dual-sequence series with parameters as in the simulation study (and TE of 1.14 ms, full details in Table 8-1) was acquired over 210 cardiac cycles; implemented using the Philips interleaved scanning capability which allows instantaneous switching between multiple scans. A composite water suppression enhanced through T_1 effects (WET) saturation pulse was used [200]. Prior to the first DCE series a native T_1 map (5s(3s)3s scheme MOLLI) and proton density weighted series (10 cardiac cycles, identical sequence to the

DCE series except without saturation preparation[1]) was acquired. A further saturation prepared DCE series was acquired (10 cardiac cycles) 15 minutes after the final contrast agent administration followed by a contrast enhanced T_1 map (4s(1s)3s(1s)2(s) MOLLI[2]).

Main sequence parameters	
TS	95.94 ms
nk0 (steps to central line of k-space)	11
FA	15°
TR	2.68 ms
TE	1.14 ms
FOV	360x360 mm
Slice Thickness	10mm
Resolution	2.43x2.43 mm
Low T_1 sensitivity sequence parameters	
TS	24.3 ms
nk0 (steps to central line of k-space)	8
FA	15°
TR	2.52 ms
TE	1.14 ms
FOV	360x360 mm
Slice Thickness	10mm
Resolution	5.63x6.27 mm
PDw sequence parameters	
nk0 (steps to central line of k-space)	11
FA	15°
TR	2.68 ms
TE	1.14 ms
FOV	360x360 mm
Slice Thickness	10mm
Resolution	2.43x2.43 mm

Table 8-1 - Imaging parameters for the volunteer study.

[1] N.B. The PDw sequence was performed with the same readout flip angle as the saturation recovery sequence. This is suboptimal and a low flip angle readout would have been preferable but the clinical protocol was finalised prior to the results of Chapter 7 being known (see section 1.4).

[2] N.B. A ShMOLLI scheme may have reduced inaccuracy and heart rate variability in T_1 mapping. However the fitting algorithm for this scheme was not available on the scanner used and so these native and post-contrast enhanced specific schemes were used, as recommended by the scanner manufacturer and in keeping with the results of Chapter 6.

8.2.2 Analysis

Myocardial and LV blood-pool contours were drawn (QMass, Medis, Netherlands), the former covering the full circumferential extent (excluding papillary muscles), on a mid-ventricular slice to extract signal-time data (Figure 8-1).

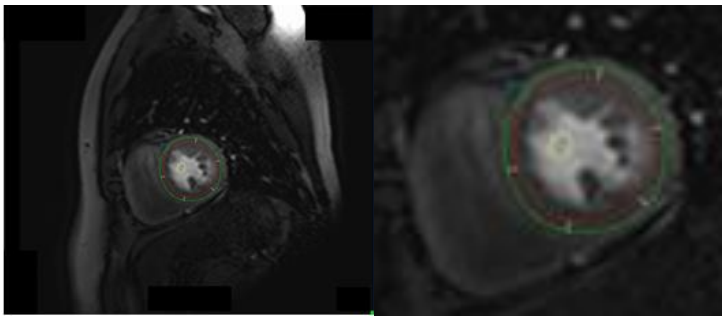

Figure 8-1 – Example contours from the hyperoxaemia volunteer study. Red and green contours show endocardial and epicardial layer contours respectively. The anterior right ventricular insertion point is marked (blue cross) and the myocardium segmented into 6 with equally spaced radial divisions although the full circumferential extent was averaged over these segments for this volunteer study as no focal disease was present. The yellow contour marks the region used for the AIF. Left – full field of view. Right – zoomed section showing left and right ventricles and contours.

8.2.2.1 Non-linearity correction comparison

For comparison of non-linearity correction methods data were analysed using the methods described in the simulation study in the previous chapter (using the full recovery model as this generally yielded higher precision, see section 7.4.5), with physiological parameters estimated using deconvolution constrained by a one-compartment model. Further details of the deconvolution process are described for the clinical studies in the following chapter. Optimisation algorithm parameters were as in section 7.2. A one-compartment model was chosen for this study to allow stable fitting (with few free parameters) and assessment of the impact of the choice of method on estimates of both myocardial blood flow and distribution volume. Deconvolution was performed in the temporal domain using a mono-exponential residue function (Equation 8-1, see section 2.4.1.3).

Equation 8-1

$$R(t) = e^{-F_p t / v_d}$$

8.2.2.2 Contrast equilibrium v_d estimation

In addition to estimation by DCE-MRI, v_d was estimated using contrast equilibrium methods and the native and post-contrast T_1 maps. T_1 and haematocrit values were used to calculate this value using Equation 2-51.

8.3 Results

Of the 30 volunteers recruited 4 withdrew prior to or during scanning. In a further 8 studies an incomplete set of analysable data was acquired due to a combination of factors including injection problems, errors in acquisition, ECG triggering problems or artefacts in T_1 maps. Example data with severe signal variation due to respiratory motion, which can be analysed but will likely have compromised precision, has been presented in Figure 3-4. An example post-contrast T_1 map with fitting errors (apparent in the bimodal distribution of pixel values in the fitted T_1 map) is shown in Figure 8-2. All of the non-linearity methods can thus be compared in 18 studies (9 male (50%), 54±13 years old). No gold standard data were acquired so only relative results can be compared to each other. T_1 values are presented in Table 8-2 along with haematocrit and myocardial v_d calculated using Equation 2-51. Example signal data are presented in Figure 8-3 and example images from selected phases of enhancement in Figure 8-4 (stress) and Figure 8-5 (rest).

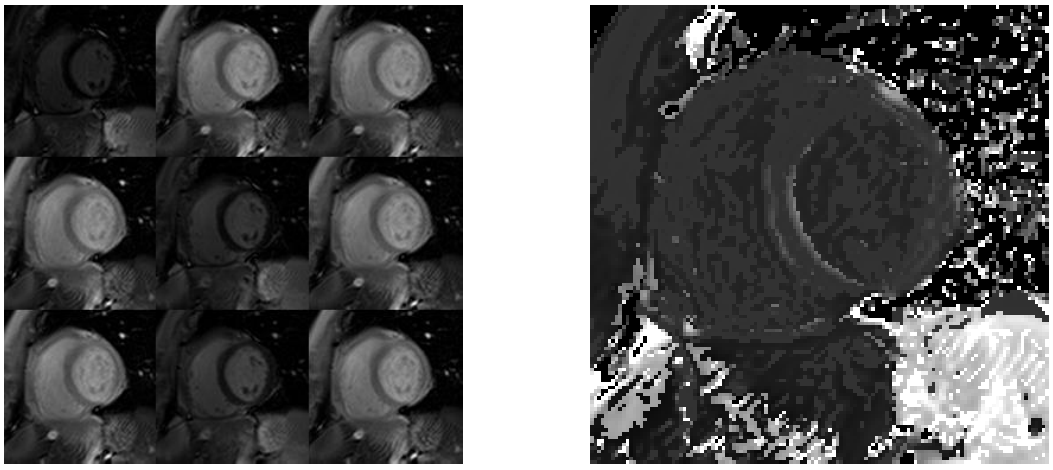

Figure 8-2 – Example post-contrast T_1 map (left: individual images, right: T_1 map) with artefact in the LV and RV blood pool. Images are cropped to the heart.

		Blood T1 (ms)		Myocardial T1 (ms)		
	Hct	Native	Enhanced	Native	Enhanced	ECV (%)
Mean	0.43	1723	280	1179	436	27.7
Std Dev	0.02	138	50	80	55	4.9

Table 8-2 – Haematocrit, T_1 values and ECV from the 18 volunteers.

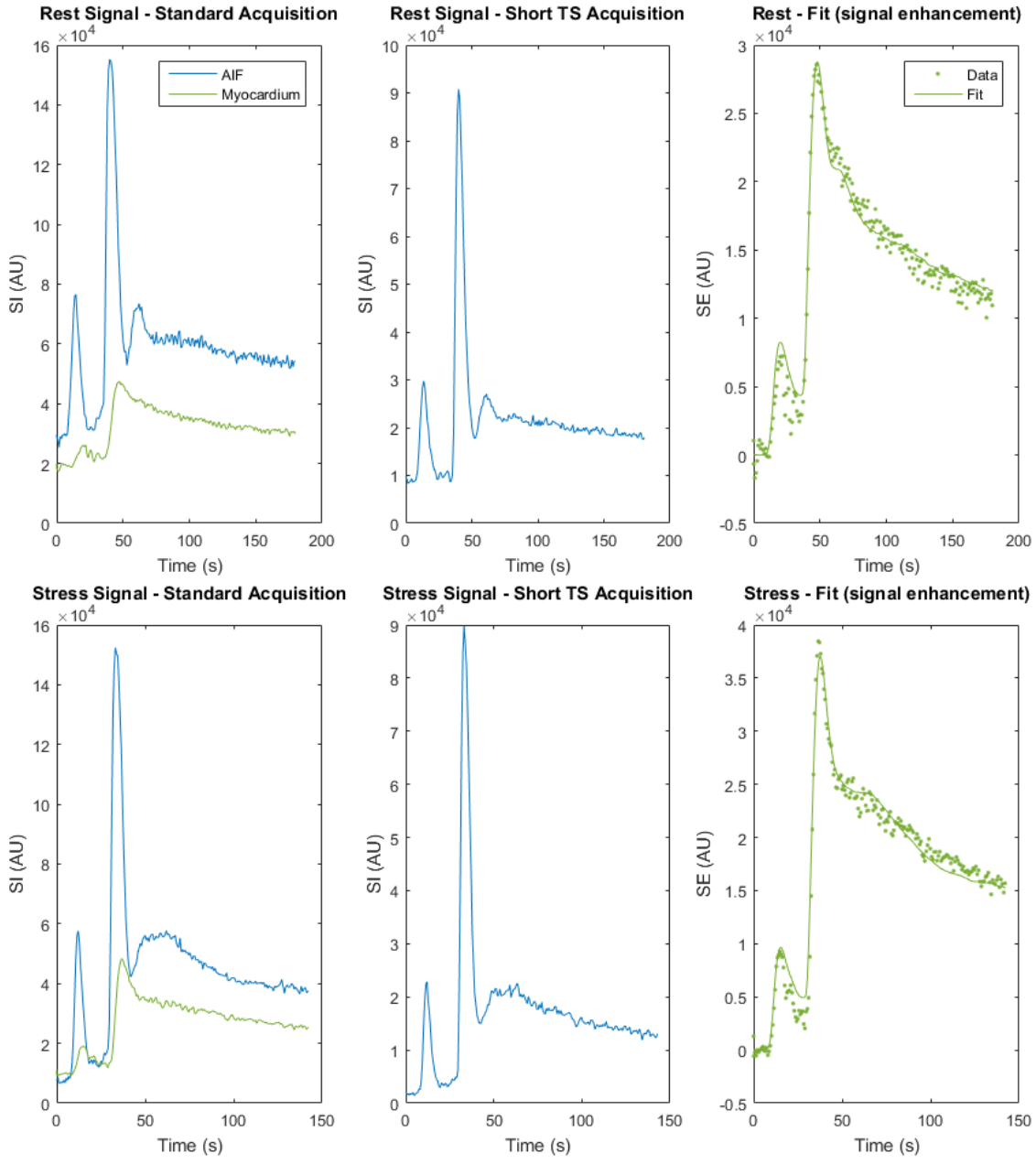

Figure 8-3 – Example signal-time data from one volunteer including one compartment model fits to signal enhancement data.

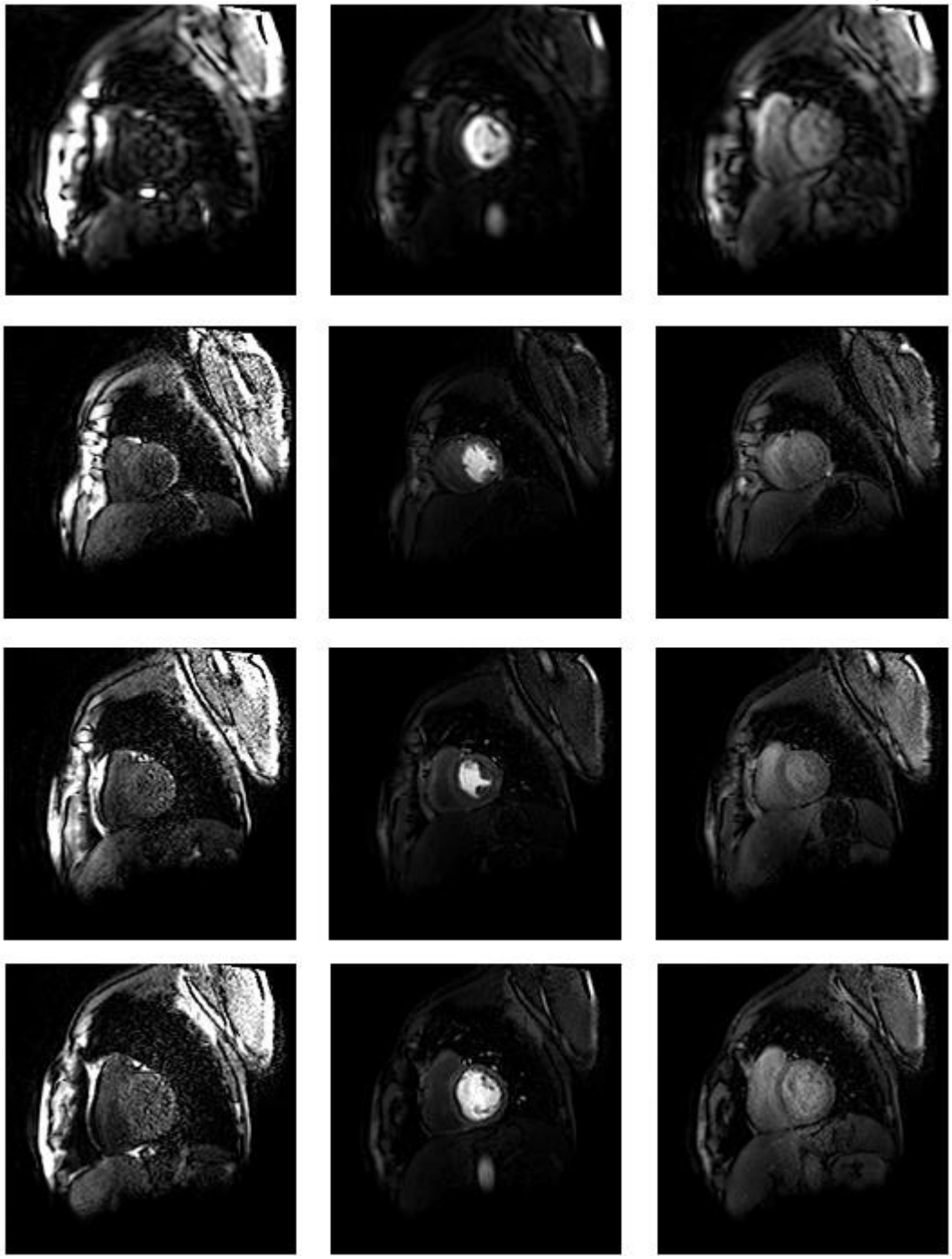

Figure 8-4 – Example stress DCE-MRI images. Top to bottom: interleaved AIF scan (dual-sequence) followed by slices 1-3. Left to right: pre-contrast, peak AIF contrast and approximately 2 minutes post-contrast.

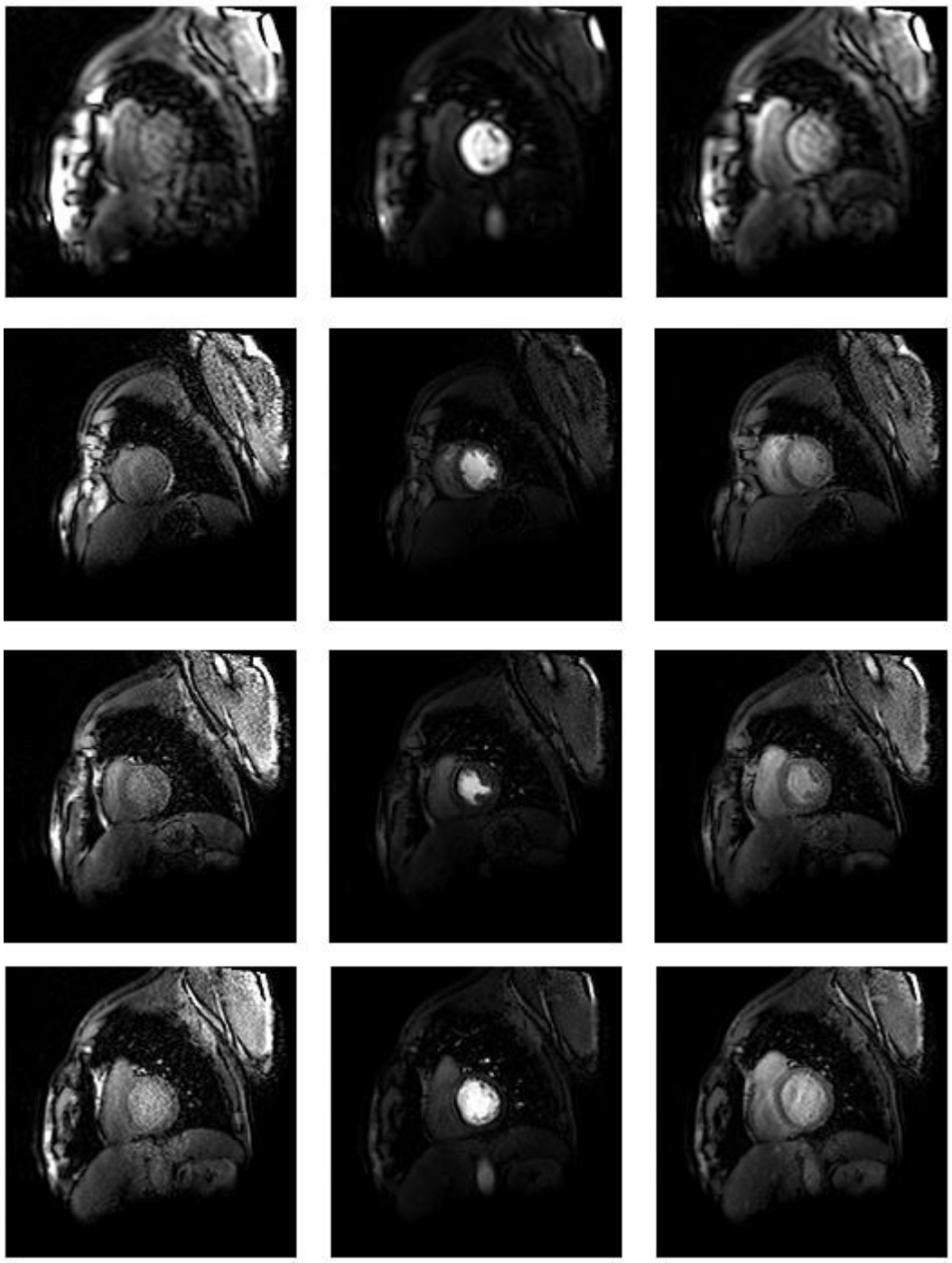

Figure 8-5 – Example rest DCE-MRI images. Top to bottom: interleaved AIF scan (dual-sequence) followed by slices 1-3. Left to right: pre-contrast, peak AIF contrast and approximately 2 minutes post-contrast.

8.3.1 Non-linearity correction comparison

Over-saturation was typically measured using the bookend T_1 based method (SE=1.014±0.014). Non-linearity correction was successful except for native T_1 based correction for which peak signal exceeded estimated S_0 values for two cases in which the bookend T_1 method returned estimates of SE>1.03. Tracer

kinetic model fitting was successful in all but 5 dual-bolus data sets (all rest) in which MBF estimates were stable but estimates of v_d were unstable due to low SNR in the pre-bolus AIF.

Contrary to the simulation results the PDw based conversion was successful with a 15° readout pulse flip angle in these volunteer data. This may be due to differences in signal behaviour *in vivo* compared to the simulation study due to in-flow effects in blood, or other effects not included in the signal simulation.

Systematic differences in mean MBF and v_d were observed between methods (Figure 8-6 and Table 8-3 (MBF) and Table 8-4 (v_d)) with all non-linearity correction methods yielding lower estimates of both parameters than deconvolution of signal enhancement data. Dual-bolus and dual-sequence methods yielded lower MBF estimates than the bookend T_1 and native PDw based methods, while estimates of v_d were lower for the dual-bolus approach compared to the other three methods. Differences in myocardial perfusion reserve were also observed between methods (Table 8-5).

	Stress MBF (ml/min/100 ml)			Rest MBF (ml/min/100 ml)		
Method	Mean	Std Dev	CoV	Mean	Std Dev	CoV
Signal Enhancement	356	96	27%	157	56	36%
Dual Bolus	110	27	25%	43	24	56%
Proton Density Weighted	210	68	32%	86	31	36%
Dual Sequence	124	43	35%	61	16	26%
Native T_1	125	120	96%	62	53	85%
Bookend T_1	210	85	40%	88	37	42%

Table 8-3 – Mean, standard deviation and coefficient of variation for MBF estimates from the different methods.

	Stress v_d (%)			Rest v_d (%)		
Method	Mean	Std Dev	CoV	Mean	Std Dev	CoV
Signal Enhancement	23.4	3.9	17%	23.3	5.2	22%
Dual Bolus	10.2	3.4	33%	12.2	7.5	61%
Proton Density Weighted	20.2	3.7	18%	20.7	7.4	36%
Dual Sequence	14.8	5.5	37%	20.0	8.5	43%
Native T_1	17.6	4.6	26%	17.7	8.4	47%
Bookend T_1	20.1	3.5	17%	20.6	7.1	34%

Table 8-4 – Mean, standard deviation and coefficient of variation for v_d estimates from the different methods.

Method	Mean MPR	Std Dev MPR	CoV MPR
Signal Enhancement	2.51	0.94	37%
Dual Bolus	3.20	1.72	54%
Proton Density Weighted	2.56	0.70	27%
Dual Sequence	2.06	0.50	24%
Native T_1	2.43	1.30	53%
Bookend T_1	2.52	0.69	27%

Table 8-5 – Mean, standard deviation and coefficient of variation for MPR estimates from the different methods.

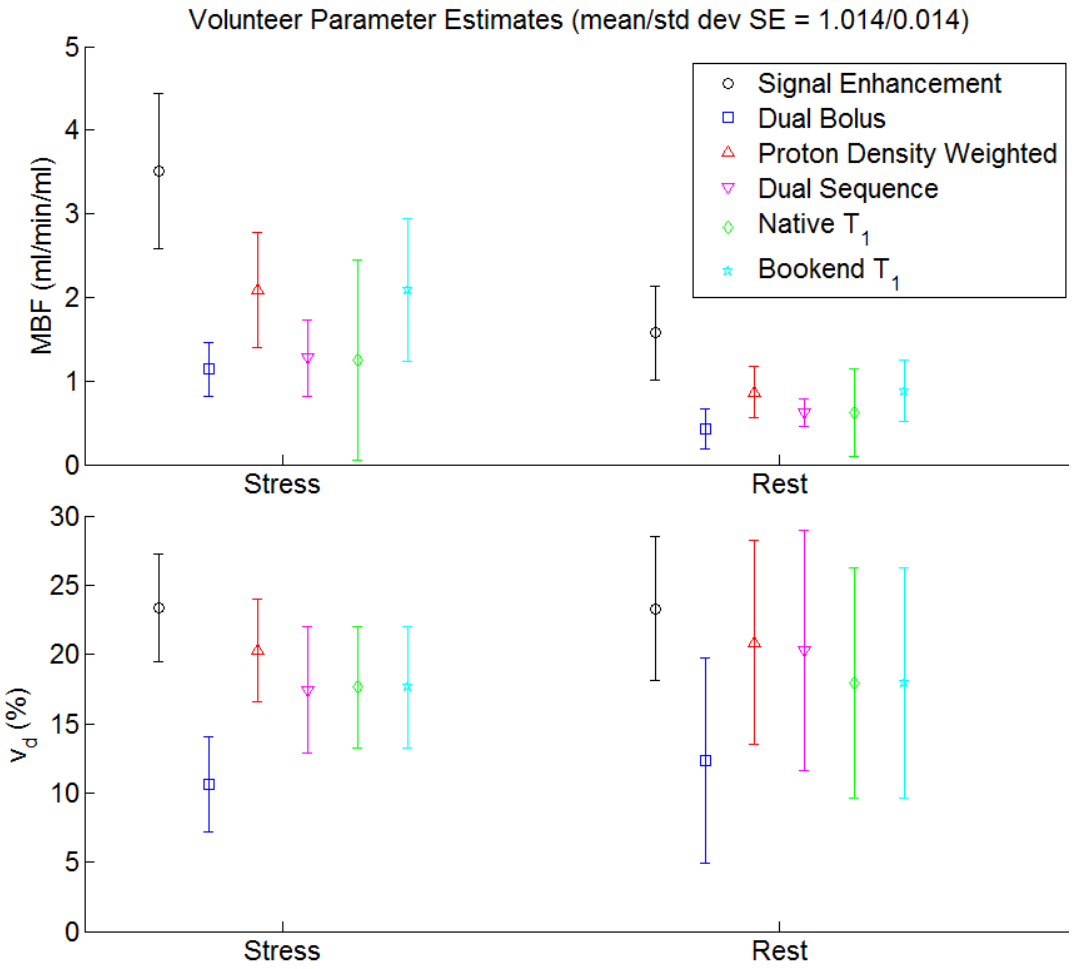

Figure 8-6 - Mean parameter estimates for 18 volunteers (error bars show one standard deviation) showing systematic differences in results dependent on analysis method used. In 2 cases data from the native T_1 based method is excluded as this conversion failed due to peak AIF signal exceeding estimated S_0. These cases had the highest estimated over-saturation (saturation efficiencies of 1.037 and 1.045) by the bookend T_1 based method. Dual-bolus data for resting v_d is based on 13 of the volunteers as in the other 5 the parameter estimate was unstable due to low SNR in the AIF.

As expected adenosine stress leads to a significant increase in MBF, with a myocardial perfusion reserve (MPR = stress MBF/rest MBF) of 2.55 ± 1.08

across all methods. The increased MBF at stress compared to rest was significant (P<0.005, paired t-test) for each non-linearity correction method while there was no significant increase in v_d under adenosine stress (P>0.18 for each method). Estimates of v_d by deconvolution (18.2±5.8% at rest across all methods, 19.9±4.7 excluding dual-bolus) were lower than by contrast equilibrium (27.7±4.9%). For each method this difference was significant (P<0.001).

8.4 Discussion

In the analysis of DCE-MRI data systematic differences in estimates of MBF, MPR and v_d were observed between non-linearity correction methods with closest agreement between model based conversion using proton density weighted image data and bookend T_1 data. The results of the latter were indicative of consistent slight over-saturation, which is in agreement with the phantom study in the previous chapter. The mean result is further from ideal in the volunteers than in the phantom, a result which may in part be due to differences in RF pulse performance between phantom and human scanning. However these SE estimates are also susceptible to error due to potential errors in T_1 measurement and the limitations of the signal model used to estimate SE (which does not fully describe either the pulse sequence used or the effects of motion, which will influence magnetisation evolution) as discussed in the previous chapter.

In estimates of MBF substantial variability between methods was observed in the volunteers, with lowest estimates from the dual-bolus technique and highest when no non-linearity correction was applied (as would be expected due to the expected effect of non-linearity for both techniques). The variability of MBF estimates was greater for native T_1 based conversion (for which 2 cases failed conversion) than other model-based methods, and the results were lower than for bookend T_1 or PDw based conversion, observations which may be expected due to the sensitivity of this method to variations in saturation efficiency and the underestimation of MBF that the simulations predict for this method in the presence of over-saturation.

While the dual-sequence method yielded systematically different results to proton density weighted image and bookend T_1 based correction the precision (coefficient of variation) in MBF and MPR estimates between these methods was comparable. This is not in agreement with the results of the simulation study in Chapter 7 and the reason for this unexpected result is not clear and further investigation is warranted.

Differences between methods persisted when relative blood flow (MPR) was calculated. In particular high estimates of MPR were observed for dual bolus, low estimates for dual sequence and high variability for both dual bolus and native T_1 based correction in comparison to the other methods. For the other methods MPR averaged 2.5, which is slightly lower than reported previously (2.7) for healthy volunteers in pilot work for this PhD [1], although the results in that work were estimated using a shorter DCE-MRI acquisition, native T_1 based non-linearity correction and the distributed parameter model to constrain deconvolution (except for a small number of cases in which that model gave unstable fit results, for which a one-compartment model was used) which tends to give systematically higher stress MBF results (see section 10.3.1.1). Similarly the distributed parameter model yielded unstable results in some cases when applied to this data (as also described in section 10.3.1.1) and so use of this model for this comparison of non-linearity correction methods would have further reduced the numbers available for final analysis. Consequently analysis for this chapter was limited to the simpler one-compartment model.

Variability in these results reflects a combination of genuine variability between subjects and imprecision in the acquisition and analysis methods. Variability in this study was higher than comparable literature, for example coefficient of variation for model-based correction methods (excluding native T_1 as this is known to be very sensitive to saturation efficiency) in this study ranged from 26-42% for MBF and 24-27% for MPR in comparison to 17-22% and 21% respectively in the study reporting quantitative myocardial DCE-MRI results in humans using a dual-bolus approach by Hsu *et al [104]*. This may reflect differences in methods (for example use of a different model, the Fermi function, to constrain deconvolution) as well as genuine differences in perfusion variability in the two studies as the volunteers in the study by Hsu were of a

younger and narrower age range (33±4 compared to 54±13 years) and a different stress agent was used (dipyramidole compared to adenosine).

In practice it may be considered that non-linearity correction is less important when estimating MPR than absolute MBF, as systematic errors which are consistent between stress and rest will cancel out during the calculation of MPR. As discussed in the previous chapter this is partially true, although non-linearity effects in the myocardial data also affect results and so errors will not necessarily completely cancel out. In these results the mean MPR estimated without non-linearity correction is very close to that estimated from the bookend T_1 and PDw based methods, although the variability is slightly higher suggesting that application of an appropriate method of non-linearity correction may improve precision even when only estimating relative values. This could arise due to a combination of the effect of differences between the AIF shape at stress and rest as well as signal non-linearity in the myocardial data. In general while proton density weighted image based correction yielded slightly higher precision in MBF in comparison to bookend T_1 similar precision was found in MPR and v_d between the two methods.

Estimates of v_d were also largest when no non-linearity correction was applied, and in close agreement for PDw and bookend T_1 based conversion. However the differences were lower than for MBF, a result which is consistent with the findings of the simulation study. The dual sequence technique led to largest variability in v_d estimates both between volunteers and between stress and rest, a finding which may reflect the reduced precision of this technique in comparison to the other model-based methods identified in the simulation study.

For the dual bolus technique individual fits were often unstable and mean estimates of v_d were lower than for the other methods. This is likely due to the low SNR of the low dose AIF, as well as the fact that in practice a shorter pre-bolus acquisition is performed than for the main bolus (a difference which was not incorporated into the simulations) so there is less data available beyond the first pass than is present for single bolus methods. Additionally differences in bolus shape were observed between the pre-bolus and main bolus which may also lead to inaccurate parameter estimates. Second pass recirculation peaks were rarely visible and the tail of the AIF often appeared suppressed

(sometimes showing signal lower than baseline) which would not be expected based on the administration of the contrast agent alone. One potential cause of this is the use of the saline flush, which may dilute the blood after the passage of the main bolus. This may lead to the blood T_1 lengthening to values higher than baseline at some time points after the first pass of the contrast agent, particularly for DCE-MRI series completed after a prior contrast agent administration.

In the contrast equilibrium MRI results the mean measured value of 27.7% is comparable to the literature value of 25.4% used for healthy myocardium in the simulation study in the previous chapter [189], although mean v_d and variability was higher (standard deviation of 4.9% in this study compared to 2.5% for the literature value). These differences may reflect age-related increases in v_d which have previously been reported [172] as the mean age in these volunteers was 10 years older than in the reference paper.

The contrast equilibrium estimates were higher than those for all methods (or in the absence) of non-linearity correction for DCE-MRI, particularly for the dual-bolus technique. This overall difference between techniques is not explained by the simulation study and was not observed in previous work [96]. The bias could potentially be due to inaccuracies in the estimates by DCE-MRI due to factors not incorporated into the simulation study, by inaccuracies in the contrast equilibrium MRI results, or a combination of both. One potential source of this discrepancy could be differential impact of water exchange effects (which are described in section 4.3.3.3) which may affect contrast enhanced MRI derived v_d estimates [43]. As DCE-MRI analysis includes data from time periods with higher contrast agent concentrations (at peak enhancement), and thus shorter T_1 values, than for contrast equilibrium MRI such effects may be more substantial for the former. As validation studies have only demonstrated correlation with collagen volume fraction, which is not directly equivalent to v_d, the absolute accuracy, and thus the most accurate technique, cannot be directly determined from such studies.

8.4.1 Limitations

In this study of the 26 volunteers who did not withdraw 8 datasets were excluded from analysis in this chapter. This high exclusion rate arises in part from the fact that only those with a full set of analysable data were included. As each study included two DCE-MRI acquisitions with both dual-bolus administration and dual-sequence acquisition, a late DCE-MRI sequence, two T_1 maps and a pre-contrast proton density weighted sequence this introduced significant scope for acquisition errors to arise. In practice the acquisition problems encountered in each of those 8 volunteers did not necessarily preclude analysis using all of the methods (for example artefact in post-contrast T_1 map only precludes bookend T_1 based correction). However, to allow comparison between methods only results from volunteers for whom a fully analysable data set was acquired were included in this analysis. As described in section 10.3 fewer subjects were thus excluded from the clinical study comparing these volunteers to patients with coronary artery disease.

Additionally the sequence protocol for this study was finalised prior to the results of Chapter 7 being known (see section 1.4). Consequently a sub-optimal sequence with a 15° readout flip angle was used for the proton density weighted sequence. Ideally a lower readout flip angle should be used and clinical data with such a protocol should be acquired and compared to other techniques in future work.

8.5 Conclusions

In this chapter results from contrast equilibrium MRI based v_d estimation and deconvolution of DCE-MRI data with a simple one-compartment tracer-kinetic model have been discussed. The latter has allowed an *in vivo* comparison of the non-linearity correction methods discussed in the previous chapter, in which differences between methods have been observed. These have generally agreed broadly with simulation studies although with some unexplained differences. Practical limitations of the native T_1 model-based or dual bolus techniques which could prevent analysis in some cases (rather than solely leading to bias or precision loss) were identified, with either conversion failures or unstable fits occurring with these techniques.

In addition to the differences between methods of non-linearity correction for DCE-MRI an overall bias in distribution volume estimates between those results and estimates by contrast equilibrium MRI has been identified and potential sources of this bias proposed.

On the basis of these results the conclusions drawn in Chapter 7 have been generally supported with experimental data and model based non-linearity correction using either bookend T_1 or proton density weighted image data can be recommended for clinical studies in place of dual-sampling strategies. However further investigation into the unexpected high precision of MBF by the dual-sequence method is warranted, as is assessment of the proton density weighted image based correction with reduced flip angles to reduce residual T_1 weighting and signal variation. The clinical protocols in the following two chapters were completed prior to and concurrently with the work performed in this and the prior chapter. Consequently a prospective comparison of protocols designed with the findings of this and the preceding chapter would also be beneficial to further support these findings.

Chapter 9

Clinical Study – ST-segment Elevation Myocardial Infarction

In this chapter a clinical study in which analysis of DCE-MRI data from a cohort of patients with ST-segment elevation myocardial infarction (STEMI) is described. Results from the acute visit of the study were presented in a conference abstract [201]. Additionally data on the prognostic value of ECV estimated by contrast equilibrium MRI from this study were presented in conference abstracts [17, 18]. This study was conceived and the protocol finalised prior to the research questions regarding non-linearity correction for this thesis had been developed, and prior to completion of the comparison of T_1 mapping techniques (see section 1.4). Consequently findings from earlier chapters were not available to inform the protocol design and the protocol was not designed to allow comparison of non-linearity correction techniques.

9.1 Clinical background

This chapter discusses a study in which patients were imaged at different stages following STEMI. As discussed in Chapter 2 myocardial infarction occurs when a coronary artery is occluded, restricting perfusion to a region of myocardium and leading to cardiomyocyte necrosis. STEMI is a severe form of myocardial infarction in which one of the major coronary arteries is occluded. Consequently a substantial region of tissue is affected across the full transmural extent of the myocardium. STEMI is typically treated urgently by revascularisation to restore blood flow to the affected myocardial territory. Following infarction and reperfusion there may be oedematous myocardium as well as potentially regions of non-viable infarcted myocardium and microvascular obstruction (MVO) as described in section 2.1.2. Over time regions of oedema and MVO resolve and acutely infarcted myocardium is replaced by non-contractile chronic scar through a process of replacement fibrosis. This pathological process is described in more detail in section 2.1.2.

9.1.1 Distributed parameter model constrained analysis of myocardial DCE-MRI data

In pilot work completed prior to this PhD it was demonstrated that characteristics of healthy myocardium can be measured at rest and adenosine induced stress through analysis of myocardial DCE-MRI data by distributed parameter (DP) model constrained deconvolution [1].

Subsequent studies have focussed on comparing MBF estimates from the DP model to those estimated using other tracer kinetic models [202, 203] in healthy volunteers and patients with CAD. For both studies native T_1 based non-linearity correction was used and reporting of results focussed on MBF and MPR estimates without discussion of the additional parameters derived from the process of deconvolution constrained by this model.

Papanastasiou *et al* [203] compared Fermi and DP estimates at both stress and rest in 8 volunteers and 5 patients. They reported similar MBF results between models at rest, but lower estimates when using the DP model at stress. Similarly Handayani *et al* [202] reported differences between four models (DP, Fermi, extended Tofts and Patlak) at stress only, with highest MBF values from Fermi constrained deconvolution while extended Tofts and Patlak models yielded lower estimates than the DP model.

9.1.2 Aims

The aim of the work described in this chapter was to test the feasibility of bookend T_1 based correction of DCE data to the *in vivo* assessment of human myocardium in a range of healthy and pathological conditions and to investigate differences in tissue physiology in post-infarction myocardium. In particular the study aimed to assess whether perfusion is measurable in regions exhibiting MVO (commonly referred to as “no-reflow”) in qualitative image analysis. These methods were used to assess perfusion and additional physiological parameter differences (including intra- and extra-vascular distribution volumes and the first pass extraction fraction of the contrast agent) in myocardium in a diverse range of pathological states associated with severe myocardial infarction. Importantly these aims were addressed using data acquisition incorporated into a clinically feasible comprehensive CMR protocols.

9.2 Methods

9.2.1 Subjects

Exclusion criteria included contraindications to MRI or administration of gadolinium based contrast agents. Subjects were only recruited if they had none of the following: body-surface area normalised estimated glomerular filtration rate < 30 ml/min/1.73m^2, were pregnant, had any implants or foreign bodies that are contraindicated for MRI at the field strength and conditions used or were too large or heavy for the scanner. All patients gave written informed consent and the study was approved by the local research ethics committee

40 patients who presented with chest pain and were diagnosed with acute STEMI were recruited for this study. All patients were treated by percutaneous coronary intervention within 12 hours of the onset of symptoms and were subsequently recruited to the study. They underwent comprehensive cardiac MRI studies within 3 days of onset of symptoms (acute phase) and at 3-month follow up (chronic phase).

9.2.2 Acquisition protocol

Scan protocols included myocardial DCE-MRI acquired in 3 short-axis slices as well as native and post-contrast MOLLI T_1 maps. Venous blood samples were taken from all patients in order to obtain haematocrit measurements. A conventional DCE-MRI sequence was used, as described in section 3.2.1.

Patients underwent a comprehensive cardiac MRI study including cine MRI, T_2 weighted imaging (T_2w), myocardial tagging, DCE-MRI, early and late gadolinium enhanced imaging (EGE & LGE) and MOLLI T_1 mapping. The DCE-MRI study comprised a dual-bolus administration of contrast agent (0.01/0.1 mmol/kg gadopentetate dimeglumine (Magnevist)) acquired over 210 cardiac cycles. Additional acquisition of DCE-MRI data (with no further contrast administration) over 21 cardiac cycles was performed at 6 and 12 minutes after contrast agent administration. MOLLI (3(3)3(3)5 scheme[1]) T_1 maps were

[1] N.B. This scheme is suboptimal but the clinical protocol was finalised prior to the results of Chapter 6 and findings from the technical literature review in section 4.4 were known (see section 1.4). Additionally comparison of multiple non-linearity techniques was not an aim of this clinical study, and so neither proton density weighted images nor dual-sequence DCE-MRI were included.

acquired pre-contrast and 10 and 15 minutes post-contrast. Deconvolution analysis was performed on the combined data set from the three DCE-MRI series. As these patients were imaged shortly after a severe myocardial infarction imaging was limited to rest only as the physiological stress and discomfort associated with adenosine infusion would not be appropriate in such patients.

Images were evaluated for the presence of artefacts and where possible (i.e. not for DCE-MRI data) acquisitions were repeated if significant artefact was present.

9.2.3 Analysis

9.2.3.1 Contouring

All contouring was performed by a clinical research fellow experienced in cardiac MRI using CVI 42 software (Circle Cardiovascular Imaging, Calgary, Canada)[1]. Regions of infarct, microvascular obstruction and oedema were contoured based on T_2w and LGE images before being transferred to the DCE-MRI images and T_1 maps and adjusted to avoid any regions of artefact. Regions of interest for blood signal and T_1 were drawn in the left ventricular cavity. Figure 9-1 shows example images and contours for a patient with a large region of persistent MVO.

[1] While sample image has been examined by the author of this thesis the primary data thus used for analysis were reports detailing regional signal/T_1 data along with image header information for timing data.

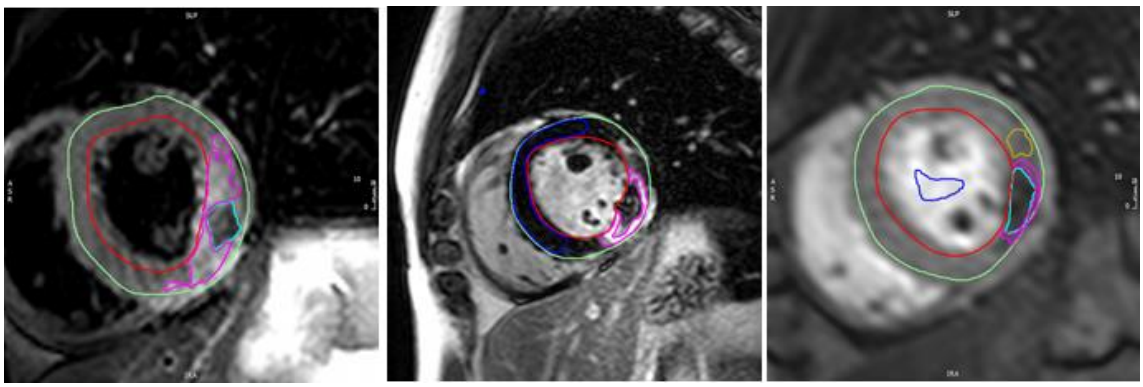

Figure 9-1 - Example images (acute visit) from a patient with persistent MVO and peri-infarct oedema. Left – T_2 weighted image showing contoured bright region which includes infarct and oedema. Centre – LGE image showing contoured bright region of infarct with a core of MVO, also contoured in blue is a region of remote myocardium. Right – DCE-MRI image showing regions used for MVO (cyan), infarct (magenta), peri-infarct oedma (yellow) and left-ventricular blood pool (blue, for AIF). In all images the endocardial and epicardial layers are delineated in red and green respectively.

Figure 9-2 shows example images and contours for a patient with substantial myocardial salvage, that is a large region of bright signal on T_2 weighted images (indicative of tissue that has undergone ischaemia) of which only a small proportion is bright on LGE (indicative of infarction).

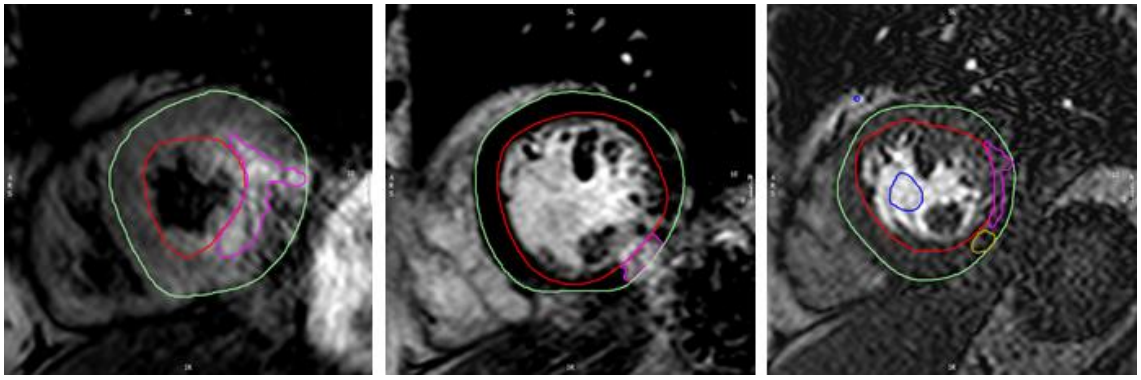

Figure 9-2 - Example images (acute visit) from a patient without MVO and with substantial myocardial salvage. Left – T_2 weighted image showing contoured bright region which includes infarct and oedema. Centre – LGE image showing contoured bright region of infarct which is substantially smaller than the bright region on T_2 weighted imaging. Right – DCE-MRI image showing regions used for infarct (magenta), peri-infarct oedma (yellow) and left-ventricular blood pool (blue, for AIF). In all images the endocardial and epicardial layers are delineated in red and green respectively.

For DCE-MRI contours were initially defined at the phase with peak signal in the blood and then copied to other phases. Inter-phase motion (predominantly due to breathing) was corrected for manually by moving contours rigidly.

Regions of interest were drawn independently at acute and follow-up visits, with oedema and MVO regions drawn only at acute as these pathologies had resolved in all patients by the follow-up study (as exemplified in Figure 9-3). This does have implications regarding the comparison between infarcted regions at the two visits as the regions contoured are not necessarily of the same tissue but are defined based on imaging characteristics at the time of the study. In particular regions of infarct at follow-up will include the regions previously defined as MVO at the acute visit where present. The results of this study should thus be seen as a comparison between acute and sub-acute infarct (which consist of different constituents due to remodelling and fibrotic processes described in section 2.1.2) within patients rather than a direct comparison of the same tissue. An alternative approach would be to transfer contours from the acute visit to the follow-up visit to compare anatomically co-located tissue, although this would need careful registration between visits and may be difficult or impossible if there is substantial remodelling or differences in patient positioning or scan alignment between visits.

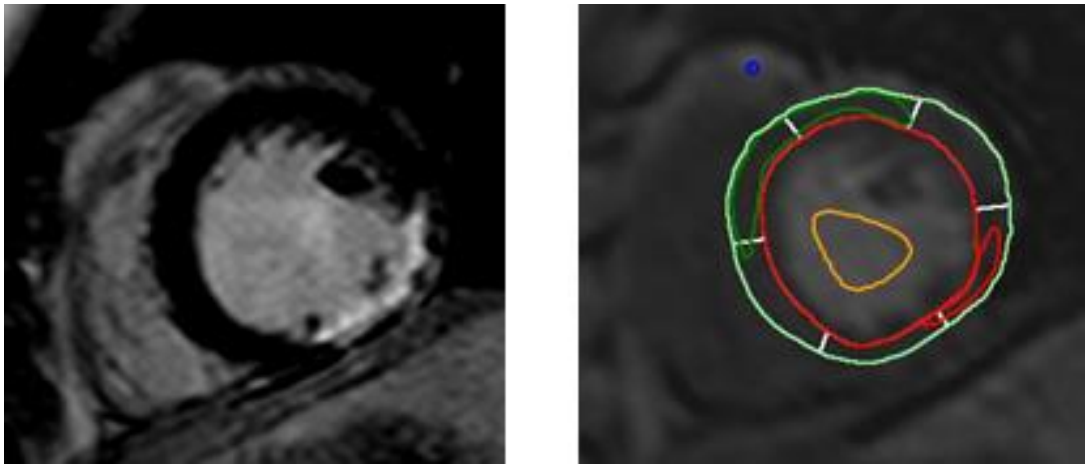

Figure 9-3 – Follow-up images from the same patient and slice location as Figure 9-1. Left – LGE. Right – DCE with contours (infarct in red, remote myocardium in green). Note that in the LGE image the core of MVO is no longer present, nor is the region of slightly enhanced signal in the region contoured as peri-infarct oedema at the first image.

9.2.3.2 Non-linearity correction and conversion to plasma concentrations

For signal non-linearity correction signal-time data were converted to ΔR_1-time data using the bookend T_1 approach (section 7.2.1.3, optimisation algorithm parameters as in section 7.2) and the full recovery signal model (Equation 7-4). S_0 and saturation efficiency were derived for blood within the left-ventricular cavity. Native DCE-MRI signal intensity and T_1 were obtained from the baseline of the DCE-MRI series, prior to contrast agent arrival, and pre-contrast T_1 mapping. To determine the baseline length a point prior to contrast agent arrival was manually identified. The baseline was typically 10-20 cardiac cycles in duration. Post-contrast T_1 was obtained from the 10 minute post-contrast T_1 map. DCE-MRI signal intensity that would be measured at that time was estimated by fitting a bi-exponential function to the tail of the AIF (including data from the initial acquisition, after any re-circulation peaks, and from the two additional 21 phase series) and interpolating the expected signal intensity at the time of the T_1 map (see Figure 9-4 in section 9.3). A bi-exponential model was chosen as Gd-DTPA concentration in blood is expected to decay rapidly in the first few minutes after injection as it distributes to extravascular spaces, followed by a slower decay associated with renal extraction [46].

The AIF can be described in terms of contrast agent concentration in either blood or plasma. For convenience the AIF is scaled by the plasma volume fraction of the blood (1-haematocrit) prior to analysis (Equation 9-1), so that the estimated parameters relate to plasma.

Equation 9-1

$$\mathrm{AIF} = \frac{\Delta R_{1,blood}}{(1 - hct)}$$

9.2.3.3 Deconvolution

Deconvolution was performed using a distributed parameter model with Laplace domain fitting [1]. The fitting process comprised multiple steps performed after non-linearity correction:

Interpolation and bolus arrival estimation

The acquired temporal resolution of the DCE-MRI data is not constant due to variation in cardiac cycle length and occasional missed trigger instances in the ECG synchronisation, and for the STEMI study due to the gaps between the three DCE-MRI series. Prior to transforming data into the Laplace domain the AIF was interpolated onto a regular time grid (with temporal resolution equal to the mean cardiac cycle length) and translated so that the bolus arrival in the AIF and tissue curves were coincident. As described in section 2.4.1.4 a variety of strategies have been proposed to estimate the translation required (the bolus arrival time, BAT). For this study an initial deconvolution using a two compartment exchange model with BAT as an additional free parameter was performed. This model is used for this step as it can be performed using temporal domain calculations (i.e. by directly convolving the AIF and residue function rather than transforming the data into the Laplace domain), thus removing an analytical step. The residue function parameters from this fit are discarded and the AIF translated by the estimated BAT prior to subsequent analysis. By adopting this approach discretisation of BAT estimates (which would occur for the approach where fits with multiple fixed BAT values are used) and the addition of a fifth free parameter in the final fitting process (which would occur in the case of incorporating BAT into the distributed parameter model fit) are both avoided. However, any errors in the estimated BAT value may lead to errors in the subsequent deconvolution analysis [59].

For the STEMI study the gaps in the AIF between DCE-MRI series are also filled by interpolating using a bi-exponential fit to the tail of the AIF, as described in the non-linearity correction section above.

Transformation and multiplication with residue function

In order to avoid time-domain aliasing the calculated tissue response curve must decay to zero (or, practically, negligible levels) by the end of the array [55]. To achieve this the AIF array is padded with zeros after the last measured data point prior to Fourier transformation. Following multiplication in the Laplace domain and inverse Fourier transformation the resulting tissue response curve is then cropped to the length of the valid data for calculation of residuals in comparison to the acquired tissue data. The length of the padding required is

determined by the expected decay constant of the residue function [55]. To allow straightforward calculation of this value the expected decay constant used was that of the adiabatic approach to the tissue homogeneity model, which has a similar decay rate to the distributed parameter model in non-flow-limited tissues [51]. This is k_{ep}, the ratio of the product $E.F_p$ to v_e, for which values from results of the pilot study [1] were used to derive a typical value. To ensure sufficient padding is included for cases with large extracellular volume fractions and low perfusion a substantial margin is applied to this value for zero-padding. In practice the AIF time and signal arrays were padded to the length defined in Equation 9-3.

Equation 9-2

$$PaddedLength = 2^{n+8}$$

$$where\ n = \left\lceil \log_2 \left(N_{AIF} + 6\frac{v_e}{F_p E} \right) \right\rceil$$

$$and\ N_{AIF}\ is\ the\ length\ of\ the\ unpadded\ AIF$$

Following padding the Laplace domain array of frequencies to which the AIF is mapped (s) is calculated centrally around zero with increments as in Equation 9-3.

Equation 9-3

$$\Delta s = \frac{2\pi i}{\max\left(t_{padded}\right)}\ where\ t_{padded}\ is\ the\ padded\ time\ array$$

The tissue response curve is then calculated as the inverse fast Fourier transform of the product of the fast Fourier transform of the padded AIF and the residue function in the Laplace domain (R(s)), as in Equation 9-4.

Equation 9-4

$$\Delta R_{1,myo,modelled} = \bar{\mathcal{F}}\left(F_p \cdot R(s) \cdot \mathcal{F}\left(AIF_{padded}\right)\right)$$

The residue function used is as defined in Equation 9-5, where T_c, T_e and T are the mean transit times in the capillaries, the interstitium and the combined system respectively.

Equation 9-5

$$R(s) = \frac{1 - e^{-s\frac{T + sT_cT_e}{1+sT_e}}}{s}$$

R(s) is not defined for s = 0 as the numerator and denominator both equal zero. R(s=0) is thus replaced with T, which is the limit as s→0 based on l'Hôpital's rule. As the data are discrete the computation is completed in practice using the fast Fourier transform process and following inverse transformation the resulting array is cropped to the length of the original AIF.

Optimisation

The above process of multiplication in the Laplace domain and inverse Fourier transformation is repeated iteratively to identify the optimal set of transit time values and plasma flow to minimise the difference between $\Delta R_{1,myo,modelled}$ and the measured tissue response curve in a least squares sense using the constrained minimisation algorithm *fmincon* in MATLAB (Mathworks, MA, USA). Optimisation algorithm starting guess values were F_p = 0.4 ml/min/ml, T_c = 0.02 min, T_e = 0.19 min, T = 0.25 min (with the value of F_p chosen to match that of the previous chapter and of the mean transit times matching mean results from the pilot study [1]) [1].

Prior to calculation of the residual difference between the modelled and measured myocardial response curves the modelled curve is interpolated back onto the original temporal sampling array. The squared residuals are summed only for samples after arrival of the main contrast agent bolus (identified manually) so that the parameters which best described the response to the main contrast administration are determined.

Parameter interpretation

The deconvolution process yields estimated values of the three mean transit time values (T, T_e and T_c) as well as F_p. From these values PS, ECV, v_e, v_p and

[1] To avoid undefined numbers or invalid solutions lower limits several orders of magnitude lower than realistic values (10^{-6} ml/min/ml (F_p) or 10^{-6} min (T_c, T_e & T)) were used where physical lower limits were zero. Upper limits were infinite. Non-linear constraints were imposed to ensure that calculated values of PS would be positive ($T>T_c$) and that the calculated value of v_d would lie within physical limits of 0-100% ($F_pT<1$).

E are determined as in equations 2-39 to 2-42 [51]. Parameters described above relate to plasma flows and volume fractions. For comparison to literature values or ease of interpretation F_p and v_p can be scaled to myocardial blood flow (MBF) or blood volume (v_b) using the haematocrit (equations 9-6 and 9-7).

Equation 9-6

$$MBF = \frac{F_p}{(1 - hct)}$$

Equation 9-7

$$v_b = \frac{v_p}{(1 - hct)}$$

Fit acceptance

As identified in pilot work the distributed parameter model is sometimes over-parameterised in the case of myocardial DCE data, leading to unstable fitting [1]. Such cases typically manifest as unrealistically high F_p and extremely short T_c being returned from the optimisation process. In such cases a one-compartment model described by two parameters (F_p and T) may adequately describe the data, in which case only blood/plasma flow and total distribution volume can be determined. Distributed parameter model fits with any transit time less than the average temporal resolution (i.e. the mean cardiac cycle length) are identified and where non-physiological parameter estimates are found results are discarded.

Statistical tests

For within study comparisons paired t-tests were applied and significance determined at α=0.05 (with Bonferroni correction applied). Six comparisons were made for each of the 8 physiological parameters so P values less than 0.00104 were thus deemed significant for the respective studies.

9.2.3.4 Contrast equilibrium v_d estimation

In addition to estimation by DCE-MRI v_d was estimated in infarcted and remote myocardium using the native and final post-contrast T_1 data, haematocrit values and Equation 2-51.

9.3 Results

Of the patients recruited 32 (80%) were male and the patients were aged 57±11 years. Mean venous haematocrit was 0.45±0.04 at both visits. Mean v_d derived from contrast equilibrium MRI estimates were 29.8±5.6% and 29.8±6.7% for remote myocardium and 55.7±15.2% and 54.5±19.1% for infarcted myocardium at acute and follow-up visits respectively.

An example AIF including the interpolated data in the tail and the timing of the T_1 maps is shown in Figure 9-4.

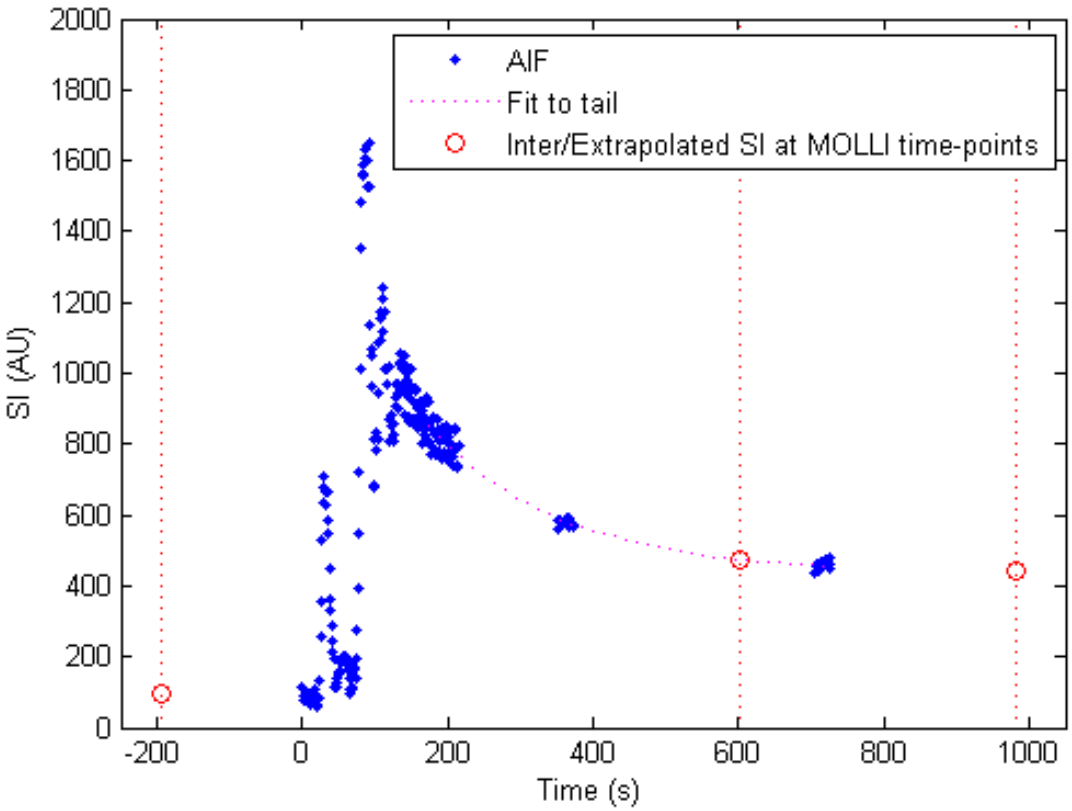

Figure 9-4 - Example AIF. Vertical lines indicate timing of MOLLI acquisitions and red circles indicate the SI used for this time point in saturation correction (derived from the baseline for pre-contrast or from the bi-exponential fit for post-contrast).

9.3.1.1 Fit success

Data was available from acute and follow-up visits from 31 patients. Of these 21 had regions of peri-infarct oedema and 22 had regions of MVO at the acute visit. In the non-linearity correction process saturation efficiency was estimated to be 1.009±0.016. DP model constrained deconvolution gave stable fits for 216/252 analysed regions of interest at visit 1 and 147/173 at follow-up giving an overall success rate of 85%. In all but 4 of the failed fits the estimated value of at least one transit time was less than half of the average cardiac cycle. For 3 of the other cases the optimisation algorithm returned parameter estimates at the upper limit of v_d of 100% (above which is physically non-valid). In the remaining case (a region of peri-infarct oedema) results were excluded due to the estimated F_p value being unusually high (299 ml/min/100 ml) and substantially higher than that estimated by a one-compartment model constrained fit (61 ml/min/100 ml) despite the shortest transit time estimate (T_c = 1.19 s) exceeding the mean cardiac cycle length (1.01 s). A region of oedema in an adjoining slice in the same patient did yield a stable fit using the DP model with a comparable F_p estimate to the one-compartment model and substantially longer T_c (15.54 s) than in the excluded fit.

9.3.1.2 Fitting results

Example myocardial data are presented in Figure 9-5, showing qualitative differences in shape between tissue types. Differences in baseline signal (notably lower signal in the MVO data) arise due to differences in myocardial enhancement from the preceding pre-bolus contrast agent administration. Acute visit results are presented in Table 9-1, follow-up results in Table 9-2 and all results in Figure 9-6.

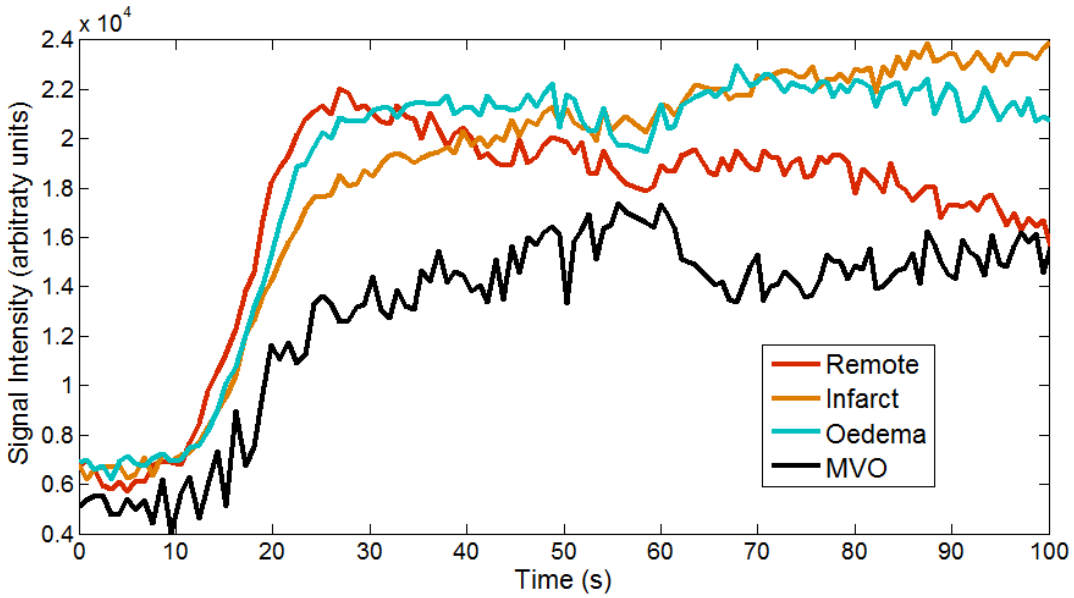

Figure 9-5 – Example myocardial signal-time curves from one patient (cropped to main-bolus administration and first DCE-MRI series).

Acute	Remote (n=72)		Infarct (n=75)		Oedema (n=27)		MVO (n=42)	
	mean	st.dev	mean	st.dev	mean	st.dev	mean	st.dev
F_p (ml/min/100ml)	64.4	32.1	40.1	16.8	44.3	21.7	21.9	23.4
PS (ml/min/100ml)	54.9	47.9	26.9	15.6	29.2	12.4	10.5	8.1
v_e (%)	17.4	4.7	36.2	14.0	26.2	9.7	32.9	12.6
v_p (%)	6.0	3.1	7.7	4.4	7.2	3.0	4.1	2.9
v_d (%)	23.4	5.2	43.9	13.9	33.4	9.6	37.0	13.2
E (%)	54.1	15.2	47.0	13.3	48.7	10.8	43.5	13.9
MBF (ml/min/100ml)	116.8	56.7	73.0	28.9	84.1	43.8	40.2	41.8
v_b (%)	11.0	5.7	14.2	8.3	13.5	5.8	7.7	5.6

Table 9-1 – Results from the STEMI study for the acute visit (n indicates number of regions).

Follow-up	Remote (n=78)		Infarct (n=69)	
	mean	st.dev	mean	st.dev
F_p (ml/min/100ml)	74.4	38.2	50.9	31.1
PS (ml/min/100ml)	71.1	50.7	31.7	23.5
v_e (%)	18.3	5.5	36.1	12.0
v_p (%)	6.7	3.6	8.8	5.1
v_d (%)	25.0	6.0	44.9	12.8
E (%)	58.1	14.7	45.7	15.4
MBF (ml/min/100ml)	130.0	63.7	89.1	52.5
v_b (%)	11.8	6.2	15.3	8.4

Table 9-2 – Results from the STEMI study for the follow-up visit (n indicates number of regions).

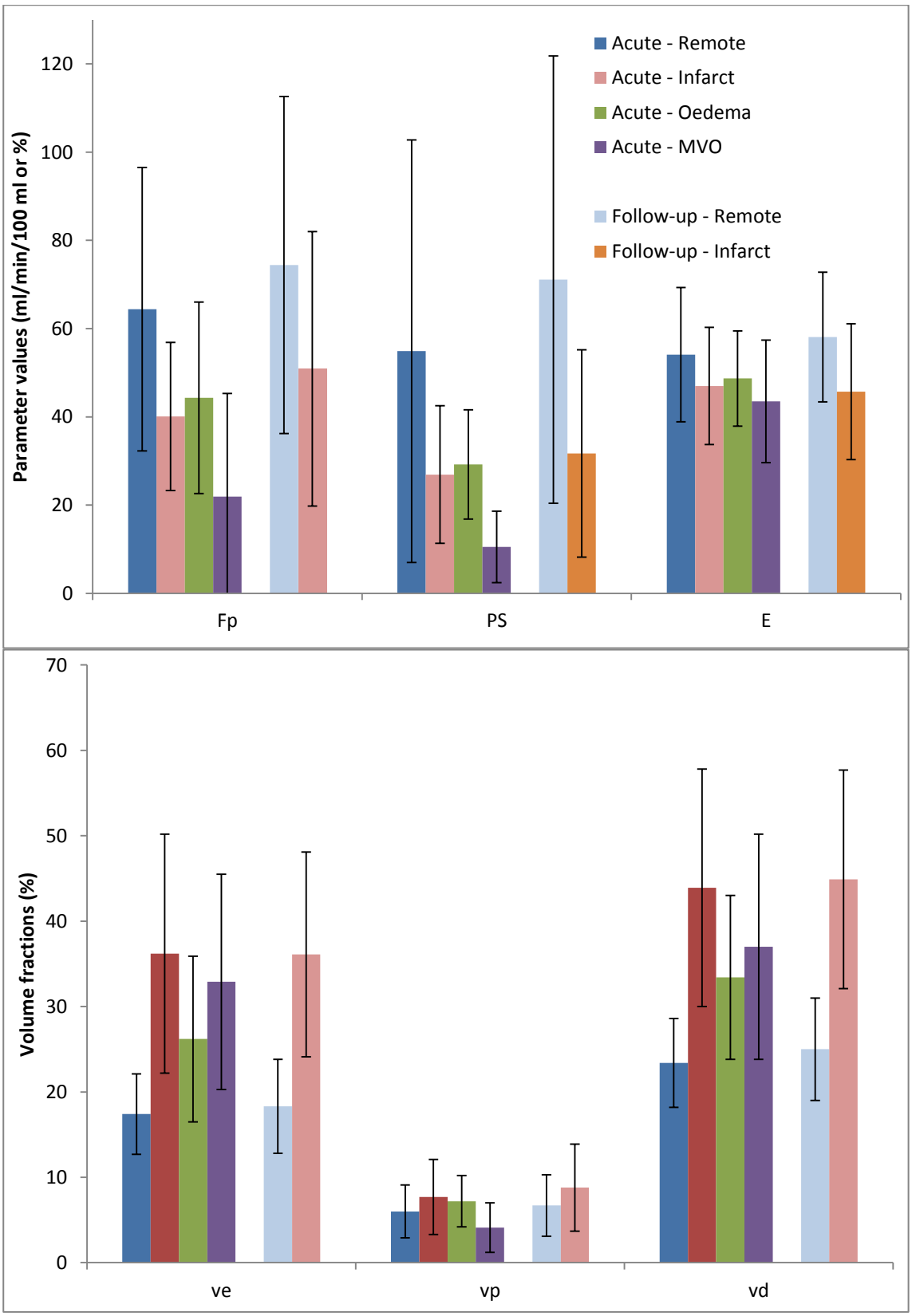

Figure 9-6 – Results from the STEMI study.

Statistical tests

Table 9-3 shows P values from paired t-tests between the various pathological tissue types and remote myocardium at the acute visit and between visits for remote myocardium and infarcted tissue.

	Acute– vs remote			Follow up– vs remote	Follow up vs acute	
	Infarct	Oedema	MVO	Infarct	Remote	Infarct
n	57	23	31	58	60	56
F_p	<0.001	0.022	<0.001	<0.001	0.219	0.037
PS	<0.001	0.027	<0.001	<0.001	0.102	0.205
v_e	<0.001	<0.001	<0.001	<0.001	0.448	0.498
v_p	0.067	0.544	0.090	0.025	0.213	0.298
v_d	<0.001	<0.001	<0.001	<0.001	0.117	0.864
E	0.030	0.946	0.001	<0.001	0.106	0.631
MBF	<0.001	0.018	<0.001	<0.001	0.434	0.097
v_b	0.065	0.585	0.107	0.029	0.408	0.649

Table 9-3 – Paired t-test P values for the STEMI study (n indicates number of regions).

Following Bonferroni correction significant decreases in perfusion metrics (F_p, PS and MBF) are observed in the acute phase in infarcted myocardium and MVO in comparison to remote myocardium along with significant increases in v_e and v_d, but not in v_p. Additionally in MVO, but not infarct, a significant reduction in first-pass extraction fraction (E) is observed. For peri-infarct oedema the increases in v_e and v_d are also significant, but changes in perfusion metrics are not.

At follow-up the reduced perfusion metrics and increased interstitial and total distribution volume fractions remained significant between infarcted and remote myocardium. Additionally the difference in E was significant. However no changes in parameters between the visits were significant after Bonferroni correction, although there was a trend for increased F_p and MBF in the infarct region at follow-up compared to the acute visit.

9.4 Discussion

In this study, as for the phantom work (Chapter 7) and second clinical study (Chapter 10) application of the bookend T_1 based non-linearity correction returned mean estimates of saturation efficiency indicative of slight over-saturation.

In this study significant changes in pathological myocardium in the acute phase of the disease have been observed, with differences between pathological tissue types. Specifically a reduction in perfusion and increase in distribution volume driven by an increased interstitial volume fraction was observed. These changes were measured within 3 days of the infarction and were observed to persist at 3-month follow-up with no significant changes between visits. A trend, which did not reach statistical significance, for increased F_p was observed in the infarct region between visits.

Findings should be interpreted in light of the fact that the two regions are drawn independently at the two visits and so will not necessarily contain the same myocardial tissue. In particular MVO is not observed at 3 month follow-up, so the region of infarct at follow-up will include regions of myocardium classified as MVO at the acute visit. Additionally the composition of tissue that exhibits late gadolinium enhancement will change between the two time points with the initial time point potentially including a mixture of inflammation and hibernating myocardium as well as scar, whereas at the latter point the region would be expected to contain scar only in the form of replacement fibrosis. An alternative analysis method to that employed here would have been to map regions of interest from the acute visit to data from the follow up visit rather than re-drawing contours. However this method could lead to errors due to mis-registration or differences in slice positioning between visits. Furthermore the purpose of this study was to investigate characteristics of the tissue types exhibited that are identified through conventional means (including LGE and T_2 weighted MRI) rather than to determine the development of specific regions of myocardium and so the method employed in this study was deemed more suitable.

While MVO has previously been described as a no-reflow phenomenon this may describe a lack of adequate perfusion despite intervention, rather than a complete absence of flow. This study has shown that in regions of infarct core that do not exhibit late gadolinium enhancement perfusion is substantially reduced, but is present, measurable, and accompanied by elevated v_d.

While parameters measured by DCE-MRI did not change significantly between the two time-points observed it is known that physiological processes are ongoing including the formation of replacement scar in the interstitial space in the infarct region. However as both replacement scar and necrotic cardiomyocytes form regions accessible to extracellular contrast agents the two tissue types may not be readily distinguishable by these methods. This lack of observed difference between phases was also observed in the study by Hopp *et al* [154], although in this study the early data was collected at the sub-acute phase, one week after infarct, and follow-up time was longer (6 months) than in the study described in this chapter.

It has been observed that myocardium remote to infarcted territories may undergo post-infarct remodelling [204] but there is lack of agreement as to whether this involves changes to the extracellular volume fraction, with one study reporting changes in post-contrast T_1 values at both acute and chronic phases of MI [205] but others reporting no difference either in post-contrast T_1 [206] or contrast equilibrium MRI derived ECV [207]. In this study values of v_d from DCE-MRI and from contrast equilibrium MRI were larger in both acute and follow-up visits in STEMI patients compared to the volunteers from the hyperoxaemia study. Furthermore there were differences in perfusion metrics between these two groups. This comparison is discussed further in the following chapter following presentation of the volunteer results.

9.4.1 Limitations

Some limitations apply to this work. Firstly as has been acknowledged in the pilot work fitting with the distributed parameter model yields unstable results in a substantial minority of cases. Consequently care must be taken to identify such fits and exclude results from further analysis. For group comparisons, such as in this work, this could lead to a potential bias if the unstable fits occur predominantly for certain ranges of physiological parameter values.

Furthermore excluding fits reduces the number of data points available for analysis so can lead to reduced statistical power, particularly for paired comparisons when a single unstable fit can preclude valid results from the same subject being included in the final analysis.

Additionally this study did not include comparisons to other forms of analysis including visual and semi-quantitative analysis of DCE-MRI data. Such a comparison may allow the relative diagnostic and prognostic performance of various analysis methods to be performed.

Finally as the bookend T_1 correction method was conceived during analysis of this data the protocol was not optimised for this method as the post-contrast T_1 maps were not acquired close (temporally) to the late DCE-MRI data. Consequently interpolation of the AIF had to be performed and deviations in the true behaviour of the contrast agent distribution and clearance from the bi-exponential pattern assumed in the interpolation may lead to errors in non-linearity correction. This is in contrast to the study in the following chapter for which the protocol was designed prospectively with bookend T_1 based correction planned for.

9.5 Conclusions

In this chapter the clinical feasibility of the use of bookend T_1 based non-linearity correction for quantitative DCE-MRI analysis has been demonstrated through inclusion of the technique in a clinical protocol with patients in the acute phase after STEMI and at 3 month follow-up. For the former similar saturation pulse performance was determined in this clinical study as for the previous experimental chapters.

Additionally clinical findings from analysis of this data analysed using distributed parameter model constrained deconvolution has been presented. These findings are compatible with current understanding of the underlying disease processes. Results at the acute phase of STEMI have demonstrated that measurable perfusion exists in regions of microvascular obstruction, often referred to as exhibiting “no-reflow” after reperfusion, despite the fact that such regions exhibit minimal enhancement on first-pass perfusion. Additionally the

results have shown that while acute and infarcted myocardium are known to be different physiologically and structurally enhancement behaviour using extracellular GBCAs are small and the two tissue types may not be readily distinguishable with such techniques.

Chapter 10

Clinical Study – Hyperoxaemia in Coronary Artery Disease

In this chapter a clinical study is described in which DCE-MRI and T_1 data from cohorts of patients with stable coronary artery disease and healthy volunteers were acquired and analysed.

10.1 Clinical background

This chapter discusses a study designed to investigate the effects of hyperoxaemia on myocardial tissue status and includes patients with stable coronary artery disease (CAD) and a control group of healthy volunteers. Oxygen has been advocated as a therapeutic agent for the management of chest pain although it's effectiveness has been questioned and a recent systematic review has suggested it may potentially have a harmful effect overall [208].

The DCE-MRI component of this study reported in this thesis was part of a larger experimental protocol aiming to gain additional insight into the effect of oxygen on myocardial perfusion. In addition to CMR patients also underwent coronary angiography and invasive coronary physiology assessment.

The data from the volunteer cohort of the hyperoxaemia study was also used for the *in vivo* comparison of non-linearity correction methods in Chapter 8.

10.1.1 Aims

This study aims to extend the work of the previous chapter by testing the feasibility of the bookend T_1 based non-linearity correction in a protocol with multiple DCE-MRI series and to investigate differences myocardial characteristics in a broader range of physiological states than in the previous chapter through inclusion of data acquired under pharmacological stress and hyperoxaemia.

10.2 Methods

10.2.1 Subjects

Exclusion criteria were as for the STEMI study (section 9.2.1). All volunteers and patients gave written informed consent and the study was approved by the local research ethics committee

28 patients with severe stable CAD (coronary luminal stenosis severity >70% identified during routine clinically indicated x-ray angiography performed at the same hospital as the MRI study) were recruited along with 30 age matched healthy volunteers. For this thesis analysis was limited to the 16 patients with severe stenosis in a single major coronary artery (single vessel disease) due to availability of data at the time of analysis. Future analysis will include the remaining patients with multi-vessel disease.

10.2.2 Acquisition protocol

The scan protocol included multiple myocardial DCE-MRI sequences acquired in 3 short-axis slices as well as native and post-contrast MOLLI T_1 maps. Venous blood samples were taken from all patients in order to obtain haematocrit measurements. A dual-sequence variant of the DCE-MRI sequence, as described in section 3.2.1.1, was used.

Patients and volunteers underwent four separate DCE-MRI studies. The first and third studies were performed under maximal hyperaemia induced by infusion of adenosine (stress studies) while the second and fourth were performed at rest. Either the first two or final two studies were performed at hyperoxaemia achieved through inspiration of oxygen through a nasal cannula. The ordering of hyperoxaemia or normoxaemia was randomised. Each study comprised a dual-bolus administration of contrast agent (0.005/0.05 mmol/kg gadobutrol (Gadovist)) acquired over 210 cardiac cycles.

A dual-sequence acquisition (section 3.2.1.1) was performed with a low resolution image interleaved between the saturation pulse and readout train for

the first slice[1]. Additional acquisition of DCE-MRI data (with no further contrast administration) over 10 cardiac cycles was performed at 15 minutes after the final contrast agent administration (late-DCE series). MOLLI T_1 mapping was performed pre-contrast (5s(3s)3s scheme) and after the late-DCE series (4s(1s)3s(1s)2s scheme).

Images were evaluated for the presence of artefacts and where possible (i.e. not for DCE-MRI data) acquisitions were repeated if significant artefact was present.

10.2.3 Analysis

10.2.3.1 Contouring

Regions of interest for left-ventricular myocardium (excluding papillary muscles) were defined manually by drawing endo- and epicardial borders. A reference point was placed at the anterior insertion point of the right-ventricular cavity allowing automated segmentation of the left-ventricle into 6 equal circumferential sectors (QMass, Medis, NL) as demonstrated in section 8.2.2). Data from the mid-slice only (due to time constraints) was analysed for the full circumferential extent for volunteers and on a segmental basis for the patients. Contouring was performed both by a clinical research fellow and by the author of this thesis[2].

Segments were assigned as ischaemic or remote based on the vessel identified as stenosed by angiography and the corresponding perfusion territories defined by the American Heart Association guidelines [209]. However it should be noted that only segments with severe stenosis (as defined in section 10.2.1) were identified as ischaemic, so regions defined as remote to these may still be affected by lesser degrees of coronary artery disease. Summary statistics were calculated for segments with successful fits.

---

[1] N.B. The dual-sequence protocol was used as this protocol was also used for the comparison of non-linearity correction methods described earlier. However the interleaved AIF scan data was not used in this analysis for which the bookend T_1 based correction was applied.

[2] While sample image data, including full studies for those contoured by the author, has been examined by the author of this thesis the primary data thus used for analysis were reports detailing regional signal/T_1 data along with image header information for timing data.

10.2.3.2 Non-linearity correction and conversion to plasma concentrations

Signal non-linearity correction was performed as for the STEMI study (section 9.2.3.2) with native DCE-MRI signal intensity and T_1 obtained from the baseline of the first DCE-MRI series, prior to contrast agent arrival, and pre-contrast T_1 mapping and post-contrast data obtained from the contrast enhanced T_1 map and late DCE-MRI series. As for the STEMI study the baseline was manually identified and was typically 10-20 cardiac cycles in duration.

10.2.3.3 Deconvolution

Deconvolution was performed as for the STEMI study (section 9.2.3.3) with the exception that unlike in that study there was only one DCE-MRI series per-analysis, so interpolation was performed only to convert the data to being on a regular time grid.

Statistical tests

For within study comparisons paired t-tests were applied and significance determined at $\alpha=0.05$ (with Bonferroni correction applied). Four comparisons were made for each of the 8 physiological parameters so P values less than 0.00156 were thus deemed significant for the respective studies. Only a small subset of CAD patients were included to provide preliminary observations on this cohort, and consequently parametric statistical tests were not reported for these data.

10.3 Results

Of the 30 volunteers recruited 4 withdrew prior to or during scanning. Of the remaining subjects 12 (46%) were male and they were aged 54±13 years. Mean venous haematocrit was 0.43±0.03. In 5 cases there were problems with acquisition (3 with ECG triggering problems, 1 with injection problems and 1 with missing data) leaving 21 cases successfully analysed for this study[1].

[1] NB a further 3 volunteers were excluded in the analysis in the previous chapter. These 3 volunteers had acquisition problems or were missing data for sequences required for other non-linearity correction techniques but had all of the data required for the bookend T_1 based conversion successfully acquired.

Of the 16 patients with single vessel disease 1 withdrew and only incomplete data sets were available at the time of analysis for 3 patients. A further case was rejected due to a long delay between the delayed DCE-MRI series and post-contrast T_1 map (> 7 minutes) which would yield inaccurate bookend T_1 based conversion. Of the remaining 11 patients 7 were male (64%) and they were aged 66±12 years). Mean venous haematocrit was 0.44±0.05.

Example DCE-MRI data are shown in Figure 10-1 for a patient and healthy volunteer.

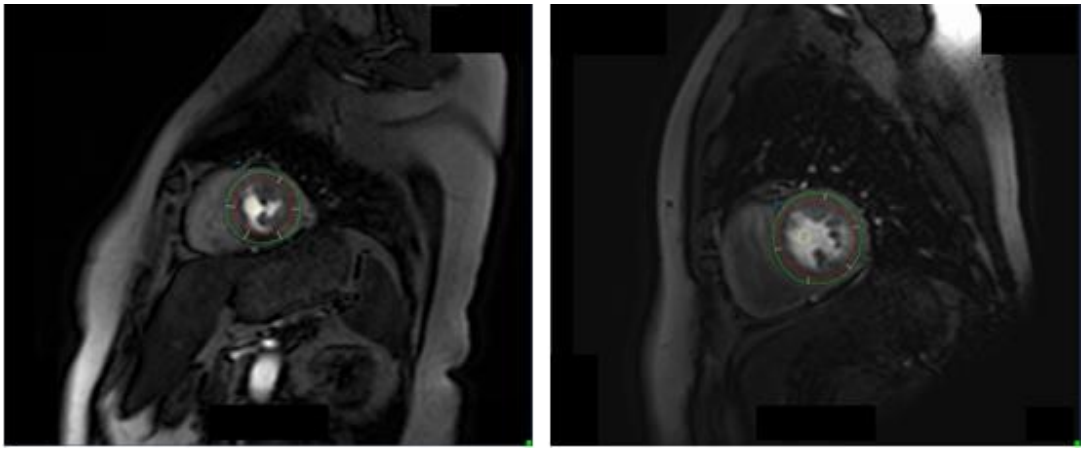

Figure 10-1 – Example DCE-MRI images and contours from the hyperoxaemia study. Left – patient with severe occlusion of the right coronary artery with inferior perfusion defect visible. Right – healthy volunteer image. Images shown are at peak myocardial enhancement.

In the non-linearity correction process saturation efficiency was estimated to be 1.014±0.014 in volunteers, as reported in the previous chapter, and 1.008±0.007 in patients.

10.3.1.1 Volunteers

For volunteers fits were stable for all but one case at rest (hyperoxaemia) and all but two cases at stress (normoxaemia), in which T_c was close to or below half of the temporal resolution. In one additional case at rest under hyperoxaemia the fit was discarded as excessive motion artefacts led to unrealistically high (>50%) estimates of v_e for healthy myocardium. This data is shown in Figure 3-4. In the same volunteer estimates of v_e were normal under the other physiological conditions for which motion artefacts were less apparent.

Results for rest are presented in Table 10-1 and for stress in Table 10-2, and in Figure 10-2. MPR in volunteers was 3.48±1.32 for normoxaemia and 3.74±1.89 for hyperoxaemia. As reported earlier (Table 8-2) contrast equilibrium estimates of v_d were 27.7±4.9%.

Rest	Air (n=21)		O_2 (n=20)	
	mean	st. dev	mean	st. dev
F_p (ml/min/100ml)	50.4	24.3	51.6	23.6
PS (ml/min/100ml)	51.8	35.6	53.2	24.0
v_e (%)	13.9	6.4	16.3	3.8
v_p (%)	7.2	4.9	5.8	2.9
v_d (%)	21.1	7.1	22.1	5.1
E (%)	58.9	19.7	63.1	13.0
MBF (ml/min/100ml)	88.2	40.2	90.5	40.0
v_b (%)	12.5	8.4	10.1	4.3

Table 10-1 – Fitting results for the volunteers in the hyperoxaemia study for data acquired at rest.

Stress	Air (n=19)		O_2 (n=21)	
	mean	st. dev	mean	st. dev
F_p (ml/min/100ml)	186.5	93.2	189.1	117.2
PS (ml/min/100ml)	68.6	29.0	90.7	43.3
v_e (%)	14.8	2.8	14.9	3.4
v_p (%)	7.3	2.4	6.3	1.9
v_d (%)	22.2	4.0	21.2	3.7
E (%)	33.0	10.9	41.6	14.2
MBF (ml/min/100ml)	323.4	149.8	332.8	204.2
v_b (%)	12.8	3.9	10.9	3.2

Table 10-2 – Fitting results for the volunteers in the hyperoxaemia study for data acquired under adenosine induced stress.

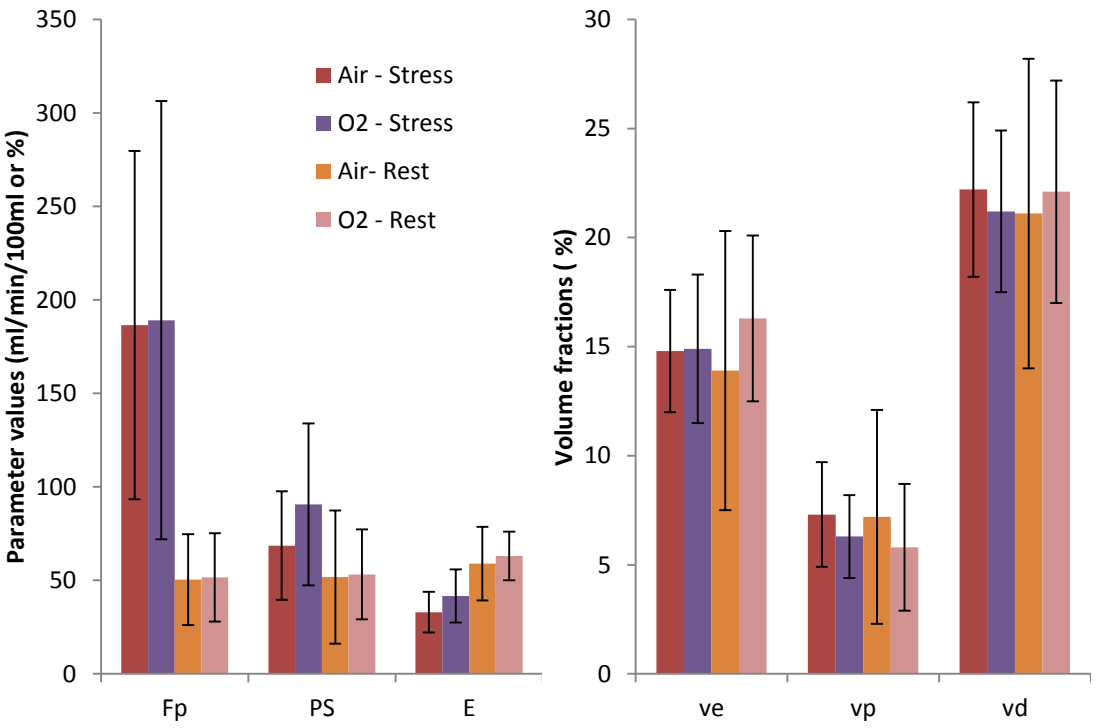

Figure 10-2 – Results from the volunteers in the hyperoxaemia study.

Results of the statistical tests are presented in Table 10-3.

Paired t-tests	Rest Air vs O_2	Stress Air vs O_2	Air Stress vs Rest	O_2 Stress vs Rest
F_p (ml/min/100ml)	0.519	0.941	<0.001	<0.001
PS (ml/min/100ml)	0.632	0.003	0.18	<0.001
v_e (%)	0.313	0.935	0.682	0.189
v_p (%)	0.960	0.105	0.166	0.702
v_d (%)	0.371	0.199	0.598	0.340
E (%)	0.751	0.040	<0.001	0.002
MBF (ml/min/100ml)	0.456	0.895	<0.001	<0.001
v_b (%)	0.946	0.100	0.141	0.670

Table 10-3 – Paired t-test results for the volunteers in the hyperoxaemia study with successful fits for all physiological states.

Stress led to significant increases in MBF for both oxaemia states and in PS for hyperoxaemia (with the relative increase being less than for MBF). The greater relative increase in MBF compared to PS led to decreased E at stress, although

for hyperoxaemia this did not reach significance following Bonferroni correction. Neither oxygenation status nor stress led to significant changes in any distribution volume parameter. Due to the lesser increase in PS with stress for normoxaemia there were trends for hyperoxaemia induced increases in both PS and E at stress but not at rest, although these did not reach statistical significance.

In comparison to the results from the one-compartment (1C) fits performed in the previous chapter estimates of F_p were comparable at rest (mean ± standard deviation $F_p(DP)/F_p(1C) = 1.02\pm0.21$, paired t-test $P=0.51$) although distributed parameter estimates were significantly higher at stress ($F_p(DP)/F_p(1C) = 1.52\pm0.65$, $P<0.001$). The differences in v_d estimates between models were small for both rest ($v_d(DP)/v_d(1C) = 1.02\pm0.03$, $P<0.001$) and stress ($v_d(DP)/v_d(1C) = 1.06\pm0.04$, $P<0.001$), although the estimates were larger from the distributed parameter model in the majority (77/81) of cases. The bias between DCE estimates of v_d and those from contrast equilibrium MRI is thus still present, although slightly reduced, when using this model.

10.3.1.2 Patients

For patients results are presented in Table 10-4 (rest) and Table 10-5 (stress) and Figure 10-3. MPR in ischaemic territories was 1.45±0.66 for normoxaemia and 1.50±0.59 for hyperoxaemia. For remote territories MRP was 1.66±0.47 and 1.97±0.65 respectively. Fits were unstable for 21 of 264 analysed segments (8 rest, 13 stress). Of these 6 were all from one stress series (under hyperoxaemia) for which there were ECG triggering errors, with the remainder due to very short T_c estimates and unrealistically large F_p estimates. With the exception of the case with ECG triggering problems there was at least one successful fit for each combination of stress state, gas breathed and tissue type for each patient.

	Air				O_2			
Rest	Ischaemic (n=11)		Remote (n=11)		Ischaemic (n=11)		Remote (n=11)	
	mean	st.dev	mean	st.dev	mean	st.dev	mean	st.dev
F_p (ml/min/100ml)	47.9	15.6	44.4	13.0	42.1	12.9	44.1	12.0
PS (ml/min/100ml)	60.0	36.8	59.0	34.7	59.8	40.1	55.8	37.4
v_e (%)	17.5	3.7	17.3	4.0	19.1	5.8	18.6	5.2
v_p (%)	4.1	3.8	3.4	2.9	3.0	2.4	3.3	2.7
v_d (%)	21.6	4.2	20.7	4.7	22.1	6.0	21.9	5.2
E (%)	66.6	19.0	68.0	15.1	70.0	17.9	65.6	17.6
MBF (ml/min/100ml)	83.7	24.1	78.0	20.3	73.6	19.3	77.7	18.3
v_b (%)	7.0	6.3	5.9	4.8	5.2	4.3	5.7	4.8

Table 10-4 – Results from patients with single vessel stable coronary artery disease. Results in this table are for the rest studies. The number of cases with stable fit results in at least 1 segment is indicated by n.

	Air				O_2			
Stress	Ischaemic (n=11)		Remote (n=11)		Ischaemic (n=10)		Remote (n=10)	
	mean	st.dev	mean	st.dev	mean	st.dev	mean	st.dev
F_p (ml/min/100ml)	72.1	45.1	79.5	41.5	74.5	41.5	84.7	45.0
PS (ml/min/100ml)	46.0	17.8	48.6	19.5	38.9	15.0	49.8	23.4
v_e (%)	14.6	4.4	14.9	2.7	14.3	3.1	14.2	3.3
v_p (%)	7.4	4.3	6.7	3.2	6.5	2.5	6.8	3.1
v_d (%)	22.0	4.9	21.5	4.0	20.8	4.1	21.0	4.0
E (%)	52.6	22.9	48.8	18.8	44.5	18.2	46.5	14.8
MBF (ml/min/100ml)	126.3	76.0	139.0	67.7	131.3	69.2	148.7	72.5
v_b (%)	13.1	7.2	11.7	5.4	11.6	4.1	12.1	5.2

Table 10-5 – Results from patients with single vessel stable coronary artery disease. Results in this table are for the adenosine stress studies. The number of cases with stable fit results in at least 1 segment is indicated by n.

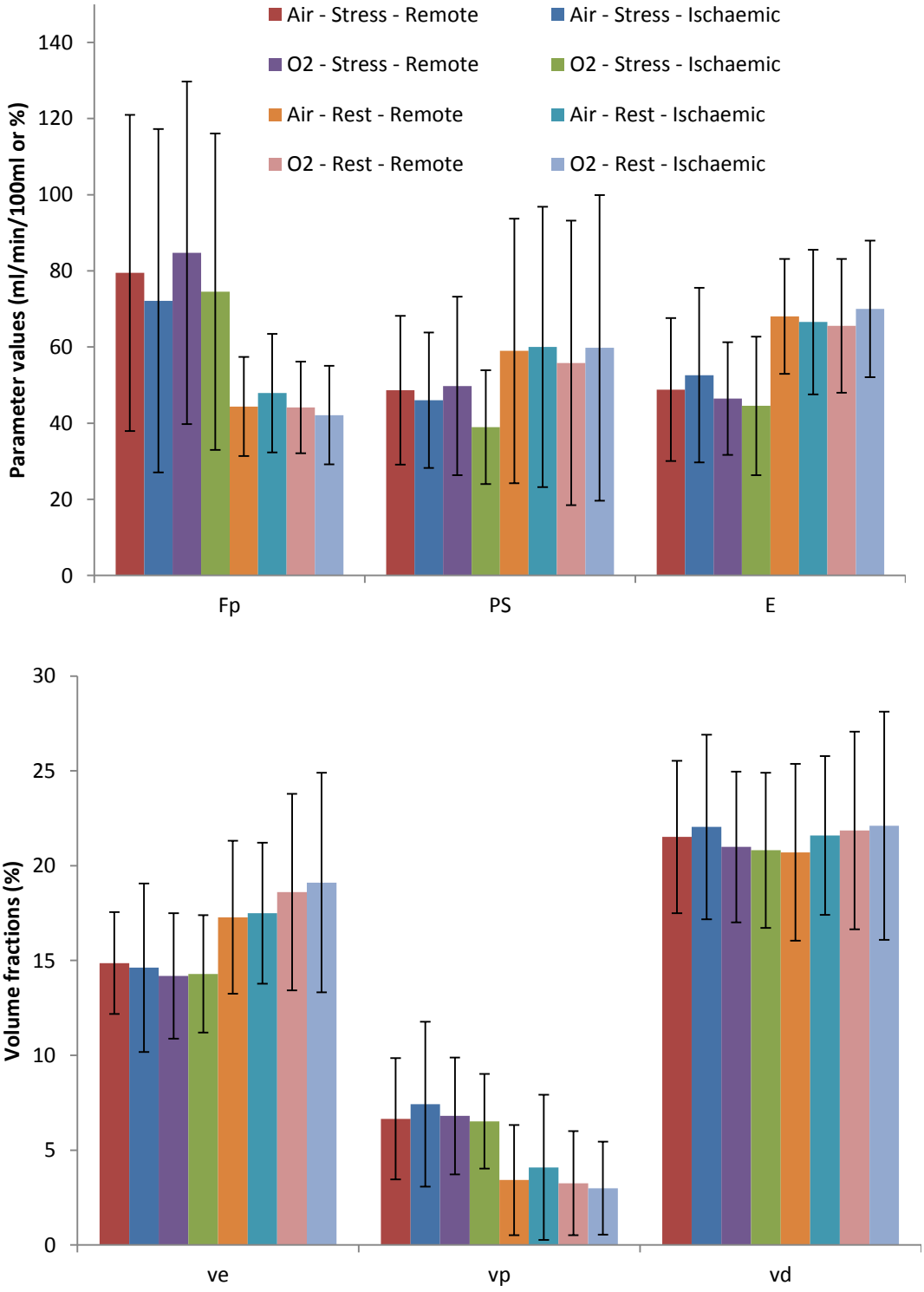

Figure 10-3 – Results from the patients with single vessel stable coronary artery disease in the hyperoxaemia study.

F_p and MBF increase in response to stress in both ischaemic and remote myocardium, but values at stress are substantially lower in both tissue types compared to in healthy volunteers whereas those at rest are only slightly lower. Changes in PS are smaller and show a trend for slight decrease with adenosine

stress for both remote and ischaemic territories (unlike healthy volunteers, for whom PS increased at stress). E is reduced at stress, particularly under hyperoxaemia, for both tissue types. Overall v_d is similar across all states, with a trend for increased v_p and decreased v_e at stress.

10.3.1.3 Myocardial Perfusion Reserve

Myocardial perfusion reserve results are presented in Table 10-6.

	Air		O2	
	mean	st.dev	mean	st.dev
Volunteers	3.14	1.11	3.25	1.75
Patients (ischaemic)	1.54	0.82	1.90	1.06
Patients (remote)	1.89	0.72	1.92	0.90

Table 10-6 – Myocardial perfusion reserve estimates for patients and volunteers from the CAD hyperoxaemia study.

10.4 Discussion

In both patients and volunteers application of the bookend T_1 based non-linearity correction has returned mean estimates of saturation efficiency indicative of slight over-saturation, in line with the findings previous studies both using phantoms (Chapter 7) and STEMI patients (Chapter 9).

The total distribution volume estimates in the volunteer cohort were similar to those reported in the previous chapter using a one-compartment model although slightly higher. Use of the DP model may thus slightly reduce the bias between DCE and contrast equilibrium v_d estimates, although the difference between models is small in comparison to the overall bias and so the other potential sources of error discussed in the previous chapter are still applicable.

In the volunteer study substantially increased MBF was induced by adenosine stress as expected, with smaller increases in PS, and a consequent reduction in E. These findings are in accordance with pilot work [1] although MPR in this study was higher. MPR in these volunteer results was also higher than in the one-compartment model constrained deconvolution results discussed in Chapter 8 due to differences primarily in estimated stress MBF. Hyperoxaemia

did not induce any significant changes in physiological parameters, although there were trends for greater PS and E at stress in comparison to normoxaemia while MBF at stress was similar in the two oxygenation states.

The systematic difference in results between the one compartment and distributed parameter model results raises an issue of appropriate model choice. Ideally a single model would be able to be employed with any acquired data as inspection of each fit result is not practical for routine clinical implementation. In this case the simpler model offers more robust fitting although sacrifices information as fewer parameters are estimated. In the absence of a gold standard measurement it is not possible to assess the relative absolute accuracy of the two models, only bias between them, and this has been seen to be substantial especially for stress MBF. Consequently the two models cannot be used interchangeably even if MBF is the only parameter of interest and other parameters can be discarded. As discussed in the Chapter 11 further developments in acquisition techniques may improve raw data quality. Additionally alternative choices of optimisation strategies may prove more robust and further work is warranted to determine the optimal approach. Developments in either of these areas may allow more robust fitting of the more detailed model in a greater proportion of cases allowing greater depth of information to be gained from DCE-MRI studies. However at present a compromise must be made between this depth of information and reliability of analysis, and the systematic differences between results must be considered when choosing a protocol and also when comparing results between studies.

The volunteer results from rest studies can also be compared to the regions of remote myocardium in the patients with STEMI in the preceding chapter. However this comparison should be made in consideration of the fact that different protocols were employed for the two studies and the volunteers were not matched for age or other demographic parameters with these patients. Any findings should be considered speculative and used only for hypothesis generation. Between these two cohorts the remote myocardium in STEMI patients had higher MBF and PS at both visits than in the volunteers from the hyperoxaemia study. However the first pass extraction fraction was lower in the patients than in the volunteers. Additionally v_d was higher in the patients remote

tissue, and this was driven by higher v_e. These differences may potentially be indicative of diffuse changes to myocardial structure and microvascular permeability in tissue remote to myocardial infarction coupled with compensatory increase in perfusion to remote regions of tissue due to reduced myocardial wall function in the infarcted territories. However these differences may also be due to differences in general myocardial health between these cohorts or systematic differences arising from protocol differences and a prospective study would be required to allow these hypotheses to the tested.

In the subset of CAD patients analysed the adenosine induced relative increase in MBF (MPR) was substantially less in remote myocardium than in the healthy volunteers and the stress MBF was only slightly higher in remote myocardium than in the territories perfused by the severely stenosed artery. This could suggest either less severe degrees of coronary artery disease processes in the vessels not identified as severely stenosed (limiting flow at stress) or compensatory hyperaemia at rest in the remote myocardium. As no clear differences in absolute MBF were apparent between remote and ischaemic myocardium at either rest or stress these preliminary data better support the former hypothesised mechanism of flow limiting disease throughout the coronary vasculature, although a more extensive study would be required to confirm this. MPR in remote territories was similar at normoxaemia and hyperoxaemia. This lack of distinction between ischaemic territories and remote in these patients with severe CAD also raises questions regarding the optimal analysis strategy and whether this should be performed on a per-patient basis or with myocardium segmented into ischaemic and remote territories. The former may provide a better summary of overall ischaemic burden to the patient while the latter may allow heterogeneous disease to be better characterised. Additionally use of larger regions of interest, and consequently improved SNR, may allow more reliable fitting in the case of the former. In order to determine the optimal strategy further study assessing the prognostic accuracy of the potential analysis techniques would be needed, ideally including patients with a broader range of disease severity.

In ischaemic territories MPR was lower at normaoxaemia, although at hyperoxaemia it was similar to the MPR values from the remote regions. This

difference was mostly due to a decrease in resting MBF at hyperoxaemia, rather than an increase in stress values. This may reflect oxygen induced vasoconstriction at rest, although the variability in this measure was high and further evaluation in a larger cohort of patients is required to confirm this observation.

Contrary to the findings in the volunteers there was no clear increase in PS with adenosine stress in either tissue type for these patients, with a trend for a slight decrease observed, particularly for ischaemic segments at hyperoxaemia. Similarly Papanastasiou *et al* reported a lower mean PS value in the perfusion territories of the 7 obstructively stenosed vessels (from 4 patients) at stress than at rest [210]. Along with the observation that MPR was substantially reduced this supports the suggestion that the remote myocardium in these patients does differ to that in healthy volunteers, perhaps reflecting less severe ischaemic heart disease throughout the segments of the ventricle which are not perfused by the artery identified as being severely stenosed.

While differences in perfusion metrics were apparent between patients and volunteers differences in the distribution volume were not (for either ischaemic or remote regions). There is therefore no evidence in this small dataset for remodelling or fibrotic processes at this stage of the disease process in these patients. However, v_e was typically slightly lower in myocardium at stress than at rest, and this was accompanied by a similar but opposing change in v_b leading to no clear change in v_d. A reduction in v_e during vasodilation or capillary recruitment could be explained in part by the resulting increased vascular space occupying part of the previously extravascular-extracellular space. However these findings were from a small number of patients and analysis of a greater number of subjects will be required to further investigate whether these findings are valid. As discussed above resting perfusion may be increased in remote myocardium following infarction as a compensatory mechanism to offset the effect on cardiac output caused by changes in wall motion as a result of infarction. However for these CAD patients (for whom the myocardium is still functioning in ischaemic territories) no evidence of compensatory increases in MBF were observed.

In the volunteers MPR was higher in this analysis, using the distributed parameter model, than in the corresponding bookend T_1 based correction results using the one-compartment model from the previous chapter. As discussed above this was primarily due to higher MBF estimates at stress, and may reflect the fact that the one-compartment model does not adequately describe the structure and physiology of the myocardium at stress leading to inaccuracy in MBF estimates. Conversely at rest, where the extraction fraction is higher, the one-compartment model may adequately describe the acquired data, leading to lower differences in MBF estimates between models.

10.4.1 Limitations

Some limitations apply to this work including those relating to the unstable fitting in some cases and the lack of analysis using semi-quantitative or qualitative methods which also applied to the findings of Chapter 9.

Data analysis was limited to the mid-slice due to time constraints and the labour intensity of image contouring. The segments on this slice were assumed to correlate to the vascular perfusion territories described in the AHA 17 segment model, although in reality there will be variation in anatomy between patients and this idealised models. This may have reduced the apparent difference in results between remote and ischaemic territories compared.

The findings from the patient cohort in the hyperoxaemia study in particular are from a very small number of subjects. Consequently firm conclusions cannot be drawn from these data and they are included as a preliminary indication of potential trends in this clinical setting. Analysis of a larger number of subjects may yield further clarity or insights into the initial findings presented above.

10.5 Conclusions

In this chapter the clinical feasibility of the use of bookend T_1 based non-linearity correction for quantitative DCE-MRI analysis has been further demonstrated through inclusion of the technique in a different clinical protocol to the previous chapter. A key difference between these studies was that this protocol included multiple DCE-MRI experiments for which a single set of pre and post-contrast data were used to estimate saturation efficiency.

Results from analysis of DCE-MRI data for in myocardium of patients with severe coronary artery disease in a variety of physiological states have been presented alongside findings from healthy volunteers in the same states, thus extending the range of physiological conditions examined from those in the previous chapter by including temporary external physiological influences (adenosine stress and oxygen). Volunteer results have been in accordance with pilot data published previously [1]. Results from the small sample of patients with severe single-vessel CAD suggest that there are differences in the myocardium remote to the territory of the stenosed vessel in these patients in comparison to healthy volunteers, potentially due to less severe artherosclerotic disease throughout the heart.

Hyperoxaemia has not been observed to have measurable effect on most parameters, except for a trend to increase permeability-surface area product under adenosine stress which would need further investigation to confirm. The study has raised questions regarding the practical implementation of quantitative myocardial DCE-MRI analysis into routine clinical practice relating to model selection (which can systematically affect results as well as impact upon fitting reliability and depth of information that can be gained) as well as to the optimal strategy for defining regions of interest for best assessing the status of myocardial health in patients. Further work would be required to address both of these issues.

Chapter 11
Conclusions

11.1 Current research

In this thesis key processes in the estimation of absolute physiological parameters from myocardial DCE-MRI have been investigated. This was focussed on correction of the non-linear response of signal intensity to contrast agent concentration. Additionally the performance of commonly proposed MOLLI T_1 schemes that were available on the scanner used for the experimental work were characterised through simulation and phantom studies. Finally the feasibility of applying model based correction using a proposed bookend T_1 based correction in clinically applicable protocols has been demonstrated through application in clinical studies in which differences in tissue properties between myocardium in various states of health and pathology related to ischaemic heart disease have been investigated.

11.1.1 Signal non-linearity correction

In Chapters 7 and 8 simulations along with phantom and volunteer studies were used to assess the performance of various strategies proposed to address the non-linear response of signal intensity in conventional myocardial DCE-MRI sequences to the contrast agent concentration. In this work a novel application of bookend T_1 and signal data to constrain model-based non-linearity correction has been proposed. A similar technique has been used in breast DCE-MRI [185] to address composite errors arising from a variety of sources. To the knowledge of the author this is the first application of these techniques in the context of myocardial DCE-MRI aimed specifically at addressing the error source of imperfect saturation during the magnetisation preparation phase of the imaging sequences.

Use of saturation prepared sequences may be beneficial for quantitative DCE-MRI as an ideal saturation pulse will erase the magnetisation history each time it is applied, thus making modelling of the signal for the sequence more straightforward. This is particularly pertinent for myocardial DCE-MRI where the use of ECG triggering and the natural variability in cardiac cycle length means

that trains of image readout pulses are not generally equally spaced. This benefit of saturation prepared sequences only applies fully when saturation pulse performance is ideal. The work has led to insights into the sensitivity of these model-based conversion techniques to small degrees of saturation imperfection which might be expected even with RF pulses optimised for high performance in cardiac MRI.

To reduce bias due to signal non-linearity effects sampling of the arterial input function that is independent to that of the myocardial response has been proposed. However use of these dual acquisition methods impose technical difficulties on acquisition either through the requirement for more complex contrast agent administration schemes (dual bolus) or the use of non-standard sequences that are not currently readily available (dual-sequence). Additionally analysis is more time consuming as additional contouring is required. While potential advances in areas such as injection pump design and image registration tools may ease some of these burdens the results of this work have generally suggested that appropriate model based correction of signal non-linearity may yield more accurate and precise results than the dual sampling strategies and so may be preferable even if the technical obstacles can be overcome.

Of the model based corrections it has been shown that the three techniques investigated in this thesis (with models constrained by native T_1, proton density weighted image signal intensity or the novel proposal of bookend T_1 data) exhibit differing performance characteristics including differing sensitivity to imperfections in saturation pulse performance. In particular use of native T_1 data alone has been shown to be highly sensitive to imperfect saturation efficiency and its use is thus strongly recommended against unless extremely high saturation efficiency can be guaranteed.

The other two methods demonstrate reduced saturation efficiency dependence for different reasons. Using native proton density weighted image signal intensity rather than native T_1 is inherently less sensitive to saturation pulse performance despite the fact that the assumption in the modelling that saturation efficiency is ideal is maintained. This is due to the fact that while deviations from this assumption lead to substantial errors in estimated values of

R_1 throughout the DCE-MRI experiment the magnitude of the biases are much less variable (with varying contrast agent concentration) than for the native T_1 based approach, and so biases in the changes in R_1 (that are subsequently used for deconvolution analysis) are smaller.

However, when PDw based corrections are applied to dual-sequence data the dependence on saturation efficiency is very high. The shorter saturation time used for the interleaved image leads to greater deviation between the analytical signal models and simulated behaviour. This contributes to substantial biases at levels of saturation pulse performance that may realistically be encountered in clinical practice. Furthermore the possibility that signal may be generated from inverted longitudinal magnetisation is introduced. This adds a further potential error source to the analysis, which would only exist outside the expected saturation pulse performance range for the conventional sequence. Based on these observations and the results of Chapter 7, the dual-sequence method as implemented in this work is therefore not recommended.

Model based correction using either proton density weighted signal or bookend T_1 data with conventional sequences can thus be recommended as clinically feasible and preferable to use of raw signal enhancement, dual sampling techniques or native T_1 based correction. However, neither offer completely ideal performance with both retaining some slight saturation efficiency dependent bias. In this study neither consistently produced higher performance than the other so the choice of method may depend on practical considerations, such as whether the additional data required for either is being acquired already for other uses.

Additionally differences in the signal behaviour between slices in the presence of non-ideal saturation, arising from the irregular temporal spacing of the slices, have been identified. This leads to further practical questions regarding the implementation of these methods in clinical practice and whether modifications to the acquisition scheme could reduce slice-to-slice precision and accuracy variation. As the main difference arises between the first and the latter slices due to the difference in recovery time since the prior saturation pulse a change to the saturation scheme could be applied. One option would be to acquire an additional, unwanted slice first and discard this data. However, that would use

up available scanning time and thus likely impose additional limitations on possible spatial resolution, particularly at high heart rates. A preferable alternative may be to add a further saturation pulse after acquisition of the final pulse. While this would still leave variable recovery time between slices (with heart rate dependence) the overall magnetisation magnitude prior to saturation for the first image slice would be reduced. Further investigation would be needed to assess the impact of such a scheme and potential implications on increased specific absorption rate would need considering.

Overall the optimal choice of method may thus depend on both the performance characteristics of the saturation pulse in use (a limitation of this work is that only one pulse design applied on one scanner was used) as well as the particular requirements for absolute accuracy, precision or insensitivity to saturation efficiency or slice position that apply to the research or clinical question. From the results of the work carried out in this thesis it is therefore not possible to produce a definitive recommendation for either of these two methods. Further work addressing one of the main limitations of this study (the fact that the protocol used for the experimental work used a sub-optimal proton density weighted as the scanning protocols were finalised prior to the results of the simulation study being known, as discussed in section 1.4) may offer further clarity as to which method, if either, could be recommended as generally preferred.

The complexity of the results of this analysis highlights a general limitation of model-based conversion techniques. For ideal performance a complete signal model fully describing the scenario in clinical scanning is required. This requires detailed knowledge of the scan protocol and in practice is unlikely to be possible. Models of sufficient simplicity for practical implementation require assumptions to be imposed and do not account for the numerous additional factors which affect signal intensity (motion being a potential key factor). Knowledge of the assumptions included in the signal model, and the potential effects of deviations from these assumptions is thus required to understand the potential biases which may arise through use of these techniques. Signal enhancement based methods are also susceptible to such biases, but are simpler to analyse and in some scenarios (particularly where relative, rather

than absolute, parameters are reported) may offer sufficient accuracy and precision to answer clinical questions. The choice of a method for non-linearity correction in a myocardial DCE-MRI protocol is thus not a straightforward one and will depend on the requirement of the particular study.

11.1.2 T_1 mapping in quantitative CMR

Since myocardial T_1 mapping became practical in a clinical setting, largely prompted by the introduction of the MOLLI sequence [7] as well as subsequent modifications and alternative approaches, it has become a widely used tool as discussed in Chapters 4 and 5. Use of T_1 data for signal non-linearity correction in DCE-MRI is only one of the applications for this technique; with both individual T_1 maps and T_1 map derived estimates of extracellular volume fraction having demonstrated clinical utility. Consequently understanding of the limitations of these techniques is required. Chapter 6 investigates this for MOLLI and a selection of proposed shortened variants through both simulation and phantom studies, and the results support existing literature [176, 189] demonstrating that such shortened schemes can offer not only improved clinical acceptability through reduced breath-hold durations but also improved performance compared to the originally proposed methods. Efforts to characterise the performance of such techniques are ongoing through large multi-centre, multi-vendor studies including those using volunteer cohorts [14] and phantom studies (such as the T_1 Mapping and ECV Standardisation (T1MES) study which is commencing at the time of writing).

11.1.3 Myocardial characteristics in ischaemic disease

In Chapters 9 and 10 the techniques discussed and evaluated throughout this thesis were brought together to be applied in two clinical studies. Through these studies myocardium in a wide range of both healthy and pathological physiological states was evaluated. The results of these studies demonstrated that quantitative myocardial DCE-MRI is sensitive to the changes in myocardium that exist between these states, and provide insight into the disease processes occurring in ischaemic heart disease.

Anticipated differences in myocardial physiology were demonstrated in these data, including substantially increased v_d in reperfused infarcted myocardium

and reduced MPR in ischaemic territories in patients with severe CAD. Additionally peri-infarct oedema and regions of MVO where characterised at the acute phase, the former having MBF and v_d intermediate to that in remote and infarcted myocardium and the latter having elevated v_d and substantially reduced, but still measurable, perfusion. In the CAD study substantial differences between myocardium remote to the territory perfused by the severely stenosed vessel and that in healthy volunteers was observed, most notably substantially reduced perfusion reserve. This likely reflects less severe disease in the other coronary arteries or in the microvasculature throughout the left-ventricular myocardium.

By measuring additional parameters beyond blood flow and total distribution volume fraction further insights can also be gained from these data, such as changes to the first pass extraction fraction and the relative contributions of intra- and extravascular regions to the total distribution volume fraction. For example the relative responses of MBF and PS to stress have been shown to be different, with a reduction in E under stress in all tissue types tested. While adenosine stress was not included in the STEMI study differences in E between remote and pathological tissue were observed, with a significantly lower value in regions of MVO and infarct at 3-month follow up, and a trend for a lower value in acute infarct. In patients with severe CAD a trend for decreased PS at stress was observed (contrasting with an increase for healthy volunteers), which has been observed elsewhere [210] but for which a physiological mechanism is not clear. This was most apparent in ischaemic territories under conditions of hyperoxaemia. However it should be noted that these are small studies and evaluation in larger cohorts would be required to confirm the preliminary findings of these analyses.

The work in this thesis has demonstrated that distributed parameter model constrained deconvolution of myocardial DCE-MRI data can be successfully extended beyond the application in healthy volunteers reported in pilot work [1] and into studies assessing pathological myocardium. Importantly the studies have shown that such data can be acquired through protocols that can be applied in a clinical setting as part of a comprehensive CMR protocol.

Overall quantitative myocardial DCE-MRI is a complex, multi-step process requiring careful monitoring of the acquisition and analysis process to yield robust results. While limitations within several of these steps have been identified and assessed, both in this thesis and elsewhere, the technique can provide estimates of physiological data which may be of clinical value. This can either be on an individual patient basis (for example in assessing myocardial health and response to therapy) or on a group basis for developing understanding of myocardial disease processes without the need for invasive procedures. There remain several areas in which further research and development may either improve the accuracy, precision or robustness of these techniques, or potentially allow estimation of further physiological characteristics. Some of these potential areas are discussed below.

Finally through this work an additional bias between distribution volumes measured using DCE-MRI to those from contrast equilibrium MRI was identified, with the latter yielding higher results. This bias was not predicted through simulation work and the source remains to be identified. One possible source of this bias is water exchange effects. As discussed below further investigation in this area is warranted as this may not only improve accuracy of estimates of physiological parameters conventionally derived from contrast enhanced MRI but also potentially provide additional data of potential clinical interest.

11.2 Future related research directions

Owing to the limitations discussed above further work is required to allow such techniques to be applied routinely and in a fully automated process without the need for user input. Several areas which may facilitate this remain open for development and further research in this field is warranted. This includes, but is not limited to, the areas described below.

11.2.1 Signal model derivation

In this thesis non-linearity correction techniques were compared using two previously proposed signal models. One which assumed full recovery between each image acquisition [44] and a second which accounted for a reduction in steady-state magnetisation due to repeated acquisition [45]. However, as

described in Chapter 7, both were limited approximations of the sequences used in this work. Section 7.7 shows the deviations that exist between both models and the forward simulations. These are largest for the interleaved image of the dual-sequence method, and this method exhibited very strong biases even with only slight saturation imperfection. Derivation and use of analytical signal models more completely describing the imaging sequences may allow an improvement in accuracy to be achieved in any of the model based non-linearity correction techniques.

11.2.2 Motion correction

A major bottleneck in the analysis of myocardial DCE-MRI data is the correction for motion between cardiac cycles, particularly when image acquisition is performed over an extended period of time beyond that for which a breath-hold is feasible. Manual motion correction is labour intensive and is susceptible to human error. Advances in robust, automated motion correction will facilitate more rapid analysis of myocardial DCE-MRI data and accelerate future research in this field. Such advances may also lead to a shift in preference for how breathing instructions are given during perfusion studies. Commonly a breath-hold is performed during the first pass followed by free gentle breathing. However this may lead to a sharp intake of breath during the study and so robust motion correction may allow gentle free-breathing throughout. However for any motion correction applied to two-dimensional imaging it must be remembered that only in-plane, and not through-plane, motion can be corrected.

11.2.3 Acquisition improvements – resolution, noise and anatomical coverage

The experimental protocols described in this thesis utilised 3-slice, 2D acquisition to provide short-axis views of the myocardium at different anatomical positions. Consequently the coverage of the myocardium is incomplete, with the most basal and apical parts of the left ventricle not imaged, as well as regions between the slices. Furthermore the acquisition of 2D data results in the fact that motion correction (manual or automatic) can account only for in-plane motion. Advancements in 3D myocardial DCE-MRI acquisition techniques may

allow whole heart coverage allowing assessment of all of the myocardium of the left-ventricle, as well as allowing correction for motion in all directions.

For any MRI acquisition compromises must be made between signal to noise ratio (SNR), spatial resolution and temporal resolution. Due to the constraints imposed by the combination of cardiac and respiratory motion this is particularly true for myocardial DCE-MRI.

Using the acquisition protocols in this study spatial resolution of around 2.4 mm in-plane and 10mm through plane is possible with adequate SNR and a short enough temporal footprint to allow 3 slices to be acquired for most heart-rates encountered clinically. While this resolution is sufficient for assessment of whole myocardial status or for large regions of interest, spatial resolution can be a limiting factor when assessing small regions of interest. In particular partial volume effects may be a concern for small regions of focal disease or when assessing myocardium close to the endocardial or epicardial surfaces. Analysis is thus limited to the left ventricle, where the myocardium is thickest, and may be limited in conditions which lead to thinning of the myocardial wall (such as dilated cardiomyopathy).

Advances in MRI technology or acquisition techniques may lead to improved SNR, which may yield more robust fitting or allow improved spatial resolution. This may allow more robust analysis, particularly of small regions of interest, and may potentially allow analysis of data from other chambers of the heart with thinner myocardial wall thicknesses. This may also allow estimation of transmural variation in derived parameters which may prove clinically valuable, as transmurality of infarct area has established very high prognostic value [31]. However, as discussed in an abstract [17] arising from the STEMI study discussed in Chapter 9[1] assessment of severity rather than extent of infarct may better predict functional recovery and so in the case of quantitative assessment transmurality assessment may not prove as important as in qualitative assessment of contrast enhanced myocardial MRI for post-infarction prognostication.

[1] The author of this thesis was a co-author on this abstract but the work contained within does not form part of this thesis.

11.2.4 Water exchange effects

The analysis in this thesis has assumed that water exchange between regions of the myocardium is fast in comparison to the longitudinal magnetisation relaxation rates. At high concentrations of contrast agent this assumption may not be valid. This may impact upon the accuracy of parameter estimates, potentially explaining differences between DCE and contrast equilibrium derived v_d values identified in Chapter 8. Further research could elucidate the significance of such effects and allow for correction for water exchange effects where required. Additionally incorporating water exchange into the analysis process may provide additional, potentially clinically useful, physiological information as changes is tissue properties will affect water residence times.

11.2.5 Effect of saline flush

Differences in AIF shape between pre-bolus and main bolus, which cannot be explained by the understanding of the administration of the contrast agent alone, were often observed in experimental dual-bolus data in the work carried out in this thesis. It has been hypothesised that this could be due to the saline flush administered immediately after the contrast agent bolus. Further experimental work may provide further insights into the effect of the saline on the acquired signal data and consequential effects on quantitative analysis.

11.2.6 Deconvolution – model selection and robust fitting

Several decisions must be made when designing analysis processes, including the choice of tracer-kinetic model (where used) and implementation details. The latter include a range of choices including whether to perform analysis in the temporal or frequency domain and the choice of optimisation algorithm (least-squares based or otherwise) along with the parameters determining the start point and termination of the optimisation. Ideally analysis would be insensitive to such workflow decisions. However in practice, and especially in cases where fitting can be unstable such as when using models with higher numbers of physiological parameters, different analysis strategies can potentially yield substantially different results. Further research is thus required to identify optimal analysis strategies to improve the robustness of parameter estimates and to avoid use of data from failed fits to inform clinical decisions.

Additionally strategies which circumvent the requirement for measurement of the AIF, for example blind AIF estimation or estimation of the AIF using reference tissues have been proposed [211-214] both for myocardial DCE-MRI quantification and for other tissues. While not investigated in this thesis these methods could potentially avoid some of the issues introduced by the need to quantify relative concentrations across the full range encountered in blood pool. However their use and description in the literature has so far been limited and deconvolution using study specific measured AIF data (as performed in this thesis) remains the most reported method for quantitative analysis of myocardial DCE-MRI data.

11.2.7 Clinical studies and application

In this work small studies are presented in a limited range of pathological tissue states. Further studies could provide more robust conclusions relating to the ischaemic processes probed in this work or insights into other pathologies not investigated in this thesis. In particular application to cardiomyopathies characterised by diffuse tissue changes may allow identification of disease processes before clinical manifestation or before they are identifiable through visual analysis of imaging data, and additionally these techniques may have value in the monitoring of the response of the myocardium to therapy.

11.3 Conclusions

Despite the limitations described above the methods described in this thesis can provide measures of physiological tissue status not measurable using conventional analysis techniques. The comparison of non-linearity strategies and proposal of the novel application of bookend T_1 data to perform this provide evidence which may be used to improve the robustness of myocardial DCE-MRI quantification, particularly when estimating absolute rather than relative values. Furthermore the feasibility of applying these methods in clinical studies using standard, commonly available, imaging sequences has been demonstrated.

Application of the distributed parameter model in this project has allowed measurement of parameters beyond the conventional analysis of myocardial blood flow from DCE-MRI data and total extracellular volume fraction from contrast equilibrium MRI data. Application of these methods in both volunteers

and patients has allowed preliminary insights to be gained into the physiology of left-ventricular myocardium both in health and in a variety of pathological states.

However there remain several questions open as to the optimal acquisition and analysis methods (which should be considered in combination, not isolation) as well as technical obstacles which limit the applicability of these techniques in routine practice. Further development and refinement of these techniques is thus needed to provide a robust methodology that can both be readily applied and provide reliable, robust results. Furthermore for more widespread adoption of the technique the analysis workload must be acceptable for the investment in staff time required to be justified against the clinical information gathered. Without robust motion correction the contouring required for this technique is highly time consuming and thus ongoing development in motion correction strategies could greatly ease the application of quantitative DCE-MRI in both research and clinical practice. Automation of this step in the process, as well as contouring, quantitative analysis and presentation of results could significantly enhance the applicability of the method, particularly if integrated with routine clinical workflow by integration with commercial scanner software.

Should these hurdles be overcome the technique could provide further insights into understanding of disease processes through application the research realm while the diagnostic or prognostic value must also be proven before the technique can find routine application in the assessment of individual patients to inform clinical decision making.

References

1. Broadbent D, Biglands J, Larghat A, Sourbron S, Radjenovic A, Greenwood J, Plein S, Buckley D: **Myocardial blood flow at rest and stress measured with dynamic contrast-enhanced MRI: Comparison of a distributed parameter model with a fermi function model.** *Magn Reson Med* 2013, **70:**1591-1597.
2. Pennell D, Sechtem U, Higgins C, Manning W, Pohost G, Rademakers F, van Rossum A, Shaw L, Yucel K: **Clinical indications for cardiovascular magnetic resonance (CMR): Consensus Panel report.** *Eur Heart J* 2004, **25:**1940-1965.
3. Wilke N, Jerosch-Herold M, Stillman AE, Kroll K, Tsekos N, Merkle H, Parrish T, Hu X, Wang Y, Bassingthwaighte J: **Concepts of myocardial perfusion imaging in magnetic resonance imaging.** *Magn Reson Q* 1994, **10:**249-286.
4. Wilke N, Kroll K, Merkle H, Wang Y, Ishibashi Y, Xu Y, Zhang J, Jerosch-Herold M, Muhler A, Stillman A, et al: **Regional myocardial blood volume and flow: First-pass MR imaging with polylysine-Gd-DTPA.** *Journal of magnetic resonance imaging : JMRI* 1995, **5:**227-237.
5. Kim R, Chen E-L, Lima Jo, Judd R: **Myocardial Gd-DTPA Kinetics Determine MRI Contrast Enhancement and Reflect the Extent and Severity of Myocardial Injury After Acute Reperfused Infarction.** *Circulation* 1996, **94:**3318-3326.
6. Kim RJ, Fieno DS, Parrish TB, Harris K, Chen EL, Simonetti O, Bundy J, Finn JP, Klocke FJ, Judd RM: **Relationship of MRI delayed contrast enhancement to irreversible injury, infarct age, and contractile function.** *Circulation* 1999, **100:**1992-2002.
7. Messroghli D, Radjenovic A, Kozerke S, Higgins D, Sivananthan M, Ridgway J: **Modified Look-Locker inversion recovery (MOLLI) for high-resolution T1 mapping of the heart.** *Magn Reson Med* 2004, **52:**141-146.
8. McDiarmid A, Swoboda P, Erhayiem B, Ripley D, Kidambi A, Broadbent D, Higgins D, Greenwood J, Plein S: **Single bolus versus split dose gadolinium administration in extra-cellular volume calculation at 3 Tesla.** *Journal of Cardiovascular Magnetic Resonance* 2015, **17:**6.
9. McDiarmid A, Higgins D, Broadbent D, Ripley D, Swoboda P, Kidambi A, Erhayiem B, Musa T, Dobson L, Garg P, et al: **Split dose versus single bolus gadolinium administration in ecv calculation at 3 Tesla CMR.** *Journal of Cardiovascular Magnetic Resonance* 2015, **17:**P257.
10. McDiarmid A, Broadbent D, Higgins D, Swoboda P, Kidambi A, Ripley D, Erhayiem B, Al Musa T, Dobson L, Greenwood J, Plein S: **The effect of changes to MOLLI scheme on T1 mapping and extra cellular volume calculation in healthy volunteers with 3 tesla cardiovascular magnetic resonance imaging.** *Quantitative imaging in medicine and surgery* 2015, **5:**503-510.
11. McDiarmid A, Swoboda P, Erhayiem B, Lancaster R, Lyall G, Broadbent D, Dobson L, Musa T, Ripley D, Garg P, et al: **Athletic Cardiac Adaptation in Males Is a Consequence of Elevated Myocyte Mass.** *Circulation: Cardiovascular Imaging* 2016, **9:**e003579.
12. Biglands J, Ripley D, Broadbent D, Higgins D, Swoboda P, McDiarmid A, Garg P, Plein S, Buckley D: **A comparison of dual-bolus and dual-**

sequence quantitative myocardial perfusion techniques. *Journal of Cardiovascular Magnetic Resonance* 2015, **17:**P50.
13. Broadbent D, Higgins D, Ferreira V, Liu A, Marini C, Kramer C, Plein S, Neubauer S, Piechnik S: **Pilot Data on Inter-Centre and Inter-Vendor Comparison of MOLLI and ShMOLLI T1 Mapping Variants at 3T.** In *Joint Annual Meeting ISMRM-ESMRMB; Milan, Italy*. 2014: 2449.
14. Dabir D, Child N, Kalra A, Rogers T, Gebker R, Jabbour A, Plein S, Yu C, Otton J, Kidambi A, et al: **Reference values for healthy human myocardium using a T1 mapping methodology: results from the International T1 Multicenter cardiovascular magnetic resonance study.** *Journal of Cardiovascular Magnetic Resonance* 2014, **16:**69.
15. Kidambi A, Biglands J, Higgins D, Ripley D, Zaman A, Broadbent D, McDiarmid A, Swoboda P, Musa T, Erhayiem B, et al: **Susceptibility-weighted cardiovascular magnetic resonance in comparison to T2 and T2 star imaging for detection of intramyocardial hemorrhage following acute myocardial infarction at 3 Tesla.** *Journal of Cardiovascular Magnetic Resonance* 2014, **16:**86.
16. Kidambi A, Biglands J, Higgins D, Ripley D, Zaman A, Broadbent D, McDiarmid A, Swoboda P, Musa T, Erhayiem B, et al: **Clinical validation of susceptibility-weighted cardiovascular magnetic resonance in comparison to T2 and T2* imaging for detection of intramyocardial hemorrhage following acute myocardial infarction.** *Journal of Cardiovascular Magnetic Resonance* 2015, **17:**P117.
17. Kidambi A, Motwani M, Uddin A, Ripley D, McDiarmid A, Swoboda P, Broadbent D, Musa T, Erhayiem B, Leader J, et al: **Myocardial extracellular volume estimation by CMR predicts functional recovery following acute myocardial infarction.** *Journal of Cardiovascular Magnetic Resonance* 2015, **17:**Q63.
18. Kidambi A, Motwani M, Uddin A, Ripley D, McDiarmid A, Swoboda P, Broadbent D, Musa T, Erhayiem B, Leader J, et al: **125 Myocardial Extracellular Volume Estimation by Cardiovascular Magnetic Resonance Predicts Functional Recovery Following Acute Myocardial Infarction.** *Heart* 2015, **101:**A72-A72.
19. Broadbent D, Kidambi A, Biglands J: **Cardiovascular Magnetic Resonance Physics for Clinicians.** In *CMR Pocket Guides* (Herzog B, Greenwood J, Plein S eds.): EACVI (CMR Section); 2015.
20. Greenbaum RA, Ho SY, Gibson DG, Becker AE, Anderson RH: **Left ventricular fibre architecture in man.** *Br Heart J* 1981, **45:**248-263.
21. Bassingthwaighte JB, Yipintsoi T, Harvey RB: **Microvasculature of the dog left ventricular myocardium.** *Microvasc Res* 1974, **7:**229-249.
22. Roberts J, Wearn J: **Quantitative changes in the capillary-muscle relationship in human hearts during normal growth and hypertrophy.** *Am Heart J* 1941, **21:**617-633.
23. Archie J: **Myocardial oxygen transport. The interrelationship of coronary blood flow, oxygen diffusion and capillary recruitment.** *J Surg Res* 1978, **25:**200-210.
24. Botvinick E: **Current Methods of Pharmacologic Stress Testing and the Potential Advantages of New Agents.** *J Nucl Med Technol* 2009, **37:**14-25.

25. Nesto R, Kowalchuk G: **The ischemic cascade: Temporal sequence of hemodynamic, electrocardiographic and symptomatic expressions of ischemia.** *The American journal of cardiology* 1987, **59:**C23-C30.
26. Mewton N, Liu CY, Croisille P, Bluemke D, Lima J: **Assessment of myocardial fibrosis with cardiovascular magnetic resonance.** *J Am Coll Cardiol* 2011, **57:**891-903.
27. Klug G, Mayr A, Schenk S, Esterhammer R, Schocke M, Nocker M, Jaschke W, Pachinger O, Metzler B: **Prognostic value at 5 years of microvascular obstruction after acute myocardial infarction assessed by cardiovascular magnetic resonance.** *Journal of Cardiovascular Magnetic Resonance* 2012, **14**.
28. Bekkers S, Yazdani S, Virmani R, Waltenberger J: **Microvascular Obstruction.** *J Am Coll Cardiol* 2010, **55:**1649-1660.
29. Braunwald E, Kloner RA: **Myocardial reperfusion: a double-edged sword?** *J Clin Invest* 1985, **76:**1713-1719.
30. de Waha S, Desch S, Eitel I, Fuernau G, Zachrau J, Leuschner A, Gutberlet M, Schuler G, Thiele H: **Impact of early vs. late microvascular obstruction assessed by magnetic resonance imaging on long-term outcome after ST-elevation myocardial infarction: a comparison with traditional prognostic markers.** *Eur Heart J* 2010, **31:**2660-2668.
31. Choi KM, Kim RJ, Gubernikoff G, Vargas JD, Parker M, Judd RM: **Transmural extent of acute myocardial infarction predicts long-term improvement in contractile function.** *Circulation* 2001, **104:**1101-1107.
32. Mahrholdt H, Wagner A, Parker M, Regenfus M, Fieno D, Bonow R, Kim R, Judd R: **Relationship of contractile function to transmural extent of infarction in patients with chronic coronary artery disease.** *J Am Coll Cardiol* 2003, **42:**505-512.
33. Schuijf JD, Shaw LJ, Wijns W, Lamb HJ, Poldermans D, de Roos A, van der Wall EE, Bax JJ: **Cardiac imaging in coronary artery disease: differing modalities.** *Heart (British Cardiac Society)* 2005, **91:**1110-1117.
34. Hashemi RH, Bradley WG, Lisanti CK: *MRI: The Basics.* Updated Third Edition edn: Lippincott Williams & Wilkins; 2012.
35. McRobbie DW, Moore EA, Graves MJ, Prince MR: *MRI from Picture to Proton.* 2nd edn: Cambridge University Press; 2007.
36. Ridgway J: **Cardiovascular magnetic resonance physics for clinicians: part I.** *Journal of Cardiovascular Magnetic Resonance* 2010, **12:**71.
37. Garpebring A, Wirestam R, Östlund N, Karlsson M: **Effects of inflow and radiofrequency spoiling on the arterial input function in dynamic contrast-enhanced MRI: A combined phantom and simulation study.** *Magn Reson Med* 2011, **65:**1670-1679.
38. Preibisch C, Deichmann R: **Influence of RF spoiling on the stability and accuracy of T1 mapping based on spoiled FLASH with varying flip angles.** *Magn Reson Med* 2009, **61:**125-135.
39. Yarnykh V: **Optimal radiofrequency and gradient spoiling for improved accuracy of T1 and B1 measurements using fast steady-state techniques.** *Magn Reson Med* 2010, **63:**1610-1626.

40. Donahue K, Burstein D, Manning W, Gray M: **Studies of Gd-DTPA relaxivity and proton exchange rates in tissue.** *Magn Reson Med* 1994, **32:**66-76.
41. Donahue KM, Weisskoff RM, Burstein D: **Water diffusion and exchange as they influence contrast enhancement.** *J Magn Reson Imaging* 1997, **7:**102-110.
42. Donahue KM, Weisskoff RM, Chesler DA, Kwong KK, Bogdanov AA, Mandeville JB, Rosen BR: **Improving MR quantification of regional blood volume with intravascular T1 contrast agents: accuracy, precision, and water exchange.** *Magn Reson Med* 1996, **36:**858-867.
43. Coelho-Filho O, Mongeon F-P, Mitchell R, Moreno H, Nadruz W, Kwong R, Jerosch-Herold M: **Role of transcytolemmal water-exchange in magnetic resonance measurements of diffuse myocardial fibrosis in hypertensive heart disease.** *Circulation Cardiovascular imaging* 2013, **6:**134-141.
44. Larsson H, Fritz-Hansen T, Rostrup E, Søndergaard L, Ring P, Henriksen O: **Myocardial perfusion modeling using MRI.** *Magn Reson Med* 1996, **35:**716-726.
45. Kershaw L: **Measuring microvascular physiology using quantitative magnetic resonance imaging.** University of Manchester, School of Medicine; 2008.
46. Weinmann HJ, Brasch RC, Press WR, Wesbey GE: **Characteristics of gadolinium-DTPA complex: a potential NMR contrast agent.** *Am J Roentgenol* 1984, **142:**619-624.
47. Koenig S, Spiller M, Brown R, Wolf G: **Relaxation of water protons in the intra- and extracellular regions of blood containing Gd(DTPA).** *Magn Reson Med* 1986, **3:**791-795.
48. Boudreau RJ, Burbidge S, Sirr S, Loken MK: **Comparison of the biodistribution of manganese-54 DTPA and gadolinium-153 DTPA in dogs.** *Journal of nuclear medicine : official publication, Society of Nuclear Medicine* 1987, **28:**349-353.
49. Prato F, Wisenberg G, Marshall T, Uksik P, Zabel P: **Comparison of the Biodistribution of Gadolinium-153 DTPA and Technetium-99m DTPA in Rats.** *J Nucl Med* 1988, **29:**1683-1687.
50. Coelho-Filho O, Shah R, Mitchell R, Neilan T, Moreno H, Simonson B, Kwong R, Rosenzweig A, Das S, Jerosch-Herold M: **Quantification of Cardiomyocyte Hypertrophy by Cardiac Magnetic Resonance.** *Circulation* 2013, **128:**1225-1233.
51. Sourbron SP, Buckley DL: **Tracer kinetic modelling in MRI: estimating perfusion and capillary permeability.** *Phys Med Biol* 2012, **57:**R1.
52. Parker G, Roberts C, Macdonald A, Buonaccorsi G, Cheung S, Buckley D, Jackson A, Watson Y, Davies K, Jayson G: **Experimentally-derived functional form for a population-averaged high-temporal-resolution arterial input function for dynamic contrast-enhanced MRI.** *Magn Reson Med* 2006, **56:**993-1000.
53. Gerber B, Raman S, Nayak K, Epstein F, Ferreira P, Axel L, Kraitchman D: **Myocardial first-pass perfusion cardiovascular magnetic resonance: history, theory, and current state of the art.** *Journal of Cardiovascular Magnetic Resonance* 2008, **10:**18.

54. Jerosch-Herold M: **Quantification of myocardial perfusion by cardiovascular magnetic resonance.** *Journal of Cardiovascular Magnetic Resonance* 2010, **12:**57.
55. Garpebring A, Ostlund N, Karlsson M: **A novel estimation method for physiological parameters in dynamic contrast-enhanced MRI: application of a distributed parameter model using Fourier-domain calculations.** *IEEE Trans Med Imaging* 2009, **28:**1375-1383.
56. Jerosch-Herold M, Wilke N, Stillman AE: **Magnetic resonance quantification of the myocardial perfusion reserve with a Fermi function model for constrained deconvolution.** *Med Phys* 1998, **25:**73-84.
57. Kershaw L, Buckley D: **Precision in measurements of perfusion and microvascular permeability with T1-weighted dynamic contrast-enhanced MRI.** *Magn Reson Med* 2006, **56:**986-992.
58. Cheong LH, Koh TS, Hou Z: **An automatic approach for estimating bolus arrival time in dynamic contrast MRI using piecewise continuous regression models.** *Phys Med Biol* 2003, **48:**N83.
59. Natsume T, Ishida M, Kitagawa K, Nagata M, Sakuma H, Ichihara T: **Theoretical considerations in measurement of time discrepancies between input and myocardial time–signal intensity curves in estimates of regional myocardial perfusion with first-pass contrast-enhanced MRI.** *Magn Reson Imaging* 2015, **33:**1059-1065.
60. Al Jaroudi W, Iskandrian A: **Regadenoson: A New Myocardial Stress Agent.** *J Am Coll Cardiol* 2009, **54:**1123-1130.
61. Messroghli D, Bainbridge G, Alfakih K, Jones T, Plein S, Ridgway J, Sivananthan M: **Assessment of regional left ventricular function: accuracy and reproducibility of positioning standard short-axis sections in cardiac MR imaging.** *Radiology* 2005, **235:**229-236.
62. Kramer C, Barkhausen J, Flamm S, Kim R, Nagel E: **Standardized cardiovascular magnetic resonance (CMR) protocols 2013 update.** *Journal of Cardiovascular Magnetic Resonance* 2013, **15:**91.
63. Motwani M, Maredia N, Fairbairn T, Kozerke S, Greenwood J, Plein S: **Assessment of ischaemic burden in angiographic three-vessel coronary artery disease with high-resolution myocardial perfusion cardiovascular magnetic resonance imaging.** *European heart journal cardiovascular Imaging* 2014, **15:**701-708.
64. Johnston D, Liu P, Lauffer R, Newell J, Wedeen V, Rosen B, Brady T, Okada R: **Use of Gadolinium-DTPA as a Myocardial Perfusion Agent: Potential Applications and Limitations for Magnetic Resonance Imaging.** *J Nucl Med* 1987, **28:**871-877.
65. de Roos A, Doornbos J, van der Wall EE, van Voorthuisen AE: **MR imaging of acute myocardial infarction: value of Gd-DTPA.** *Am J Roentgenol* 1988, **150:**531-534.
66. Biglands J, Radjenovic A, Ridgway J: **Cardiovascular magnetic resonance physics for clinicians: part II.** *Journal of Cardiovascular Magnetic Resonance* 2012, **14:**66.
67. Flett A, Hayward M, Ashworth M, Hansen M, Taylor A, Elliott P, McGregor C, Moon J: **Equilibrium contrast cardiovascular magnetic resonance for the measurement of diffuse myocardial fibrosis: preliminary validation in humans.** *Circulation* 2010, **122:**138-144.

68. Fedele F, Montesano T, Ferro-Luzzi M, Di Cesare E, Di Renzi P, Scopinaro F, Agati L, Penco M, Serri F, Vitarelli A, Dagianti A: **Identification of viable myocardium in patients with chronic coronary artery disease and left ventricular dysfunction: Role of magnetic resonance imaging.** *Am Heart J* 1994, **128:**484-489.
69. Finn P, Nael K, Deshpande V, Ratib O, Laub G: **Cardiac MR imaging: state of the technology.** *Radiology* 2006, **241:**338-354.
70. Ordovás K, Reddy G, Higgins C: **MRI in nonischemic acquired heart disease.** *Journal of magnetic resonance imaging : JMRI* 2008, **27:**1195-1213.
71. Ordovas K, Higgins C: **Delayed contrast enhancement on MR images of myocardium: past, present, future.** *Radiology* 2011, **261:**358-374.
72. Karamitsos T, Francis J, Myerson S, Selvanayagam J, Neubauer S: **The role of cardiovascular magnetic resonance imaging in heart failure.** *J Am Coll Cardiol* 2009, **54:**1407-1424.
73. Pennell D: **Cardiovascular Magnetic Resonance.** *Circulation* 2010, **121:**692-705.
74. Jellis C, Martin J, Narula J, Marwick T: **Assessment of nonischemic myocardial fibrosis.** *J Am Coll Cardiol* 2010, **56:**89-97.
75. Kellman P, Arai A: **Cardiac imaging techniques for physicians: Late enhancement.** *Journal of magnetic resonance imaging : JMRI* 2012, **36:**529-542.
76. Kim R, Wu E, Rafael A, Chen E-L, Parker M, Simonetti O, Klocke F, Bonow R, Judd R: **The Use of Contrast-Enhanced Magnetic Resonance Imaging to Identify Reversible Myocardial Dysfunction.** *N Engl J Med* 2000, **343:**1445-1453.
77. Peel S, Morton G, Chiribiri A, Schuster A, Nagel E, Botnar R: **Dual Inversion-Recovery MR Imaging Sequence for Reduced Blood Signal on Late Gadolinium-enhanced Images of Myocardial Scar.** *Radiology* 2012, **264:**242-249.
78. Stirrat J, Joncas S, Salerno M, Drangova M, White J: **Influence of phase correction of late gadolinium enhancement images on scar signal quantification in patients with ischemic and non-ischemic cardiomyopathy.** *Journal of Cardiovascular Magnetic Resonance* 2015, **17:**66.
79. Diesbourg L, Prato F, Wisenberg G, Drost D, Marshall T, Carroll E, O'Neill B: **Quantification of myocardial blood flow and extracellular volumes using a bolus injection of Gd-DTPA: Kinetic modeling in canine ischemic disease.** *Magn Reson Med* 1992, **23:**239-253.
80. Kety S: **The theory and applications of the exchange of inert gas at the lungs and tissues.** *Pharmacol Rev* 1951, **3:**1-41.
81. Kellman P, Arai A: **Imaging sequences for first pass perfusion --a review.** *Journal of Cardiovascular Magnetic Resonance* 2007, **9:**525-537.
82. Larsson H, Stubgaard M, Søndergaard L, Henriksen O: **In vivo quantification of the unidirectional influx constant for Gd-DTPA diffusion across the myocardial capillaries with MR imaging.** *Journal of magnetic resonance imaging : JMRI* 1994, **4:**433-440.
83. Tong C, Prato F, Wisenberg G, Lee T, Carroll E, Sandler D, Wills J: **Techniques for the measurement of the local myocardial extraction**

efficiency for inert diffusible contrast agents such as gadopentate dimeglumine. *Magn Reson Med* 1993, **30:**332-336.
84. Tong C, Prato F, Wisenberg G, Lee T, Carroll E, Sandler D, Wills J, Drost D: **Measurement of the extraction efficiency and distribution volume for Gd-DTPA in normal and diseased canine myocardium.** *Magn Reson Med* 1993, **30:**337-346.
85. Burstein D, Taratuta E, Manning W: **Factors in myocardial "Perfusion" imaging with ultrafast MRI and Gd-DTPA administration.** *Magn Reson Med* 1991, **20:**299-305.
86. Atkinson DJ, Burstein D, Edelman RR: **First-pass cardiac perfusion: evaluation with ultrafast MR imaging.** *Radiology* 1990, **174:**757-762.
87. Larsson HB, Fritz-Hansen T, Rostrup E, Søndergaard L, Ring P, Henriksen O: **Myocardial perfusion modeling using MRI.** *Magn Reson Med* 1996, **35:**716-726.
88. Vallée JP, Sostman HD, MacFall JR, Wheeler T, Hedlund LW, Spritzer CE, Coleman RE: **MRI quantitative myocardial perfusion with compartmental analysis: a rest and stress study.** *Magn Reson Med* 1997, **38:**981-989.
89. Tofts PS, Brix G, Buckley DL, Evelhoch JL, Henderson E, Knopp MV, Larsson HB, Lee TY, Mayr NA, Parker GJ, et al: **Estimating kinetic parameters from dynamic contrast-enhanced T(1)-weighted MRI of a diffusable tracer: standardized quantities and symbols.** *Journal of magnetic resonance imaging : JMRI* 1999, **10:**223-232.
90. Vallée JP, Lazeyras F, Kasuboski L, Chatelain P, Howarth N, Righetti A, Didier D: **Quantification of myocardial perfusion with FAST sequence and Gd bolus in patients with normal cardiac function.** *Journal of magnetic resonance imaging : JMRI* 1999, **9:**197-203.
91. Nielsen G, Fritz-Hansen T, Dirks C, Jensen G, Larsson H: **Evaluation of heart perfusion in patients with acute myocardial infarction using dynamic contrast-enhanced magnetic resonance imaging.** *Journal of magnetic resonance imaging : JMRI* 2004, **20:**403-410.
92. Flacke S, Fischer S, Lorenz C: **Measurement of the Gadopentetate Dimeglumine Partition Coefficient in Human Myocardium in Vivo: Normal Distribution and Elevation in Acute and Chronic Infarction.** *Radiology* 2001, **218:**703-710.
93. Pereira R, Prato F, Sykes J, Wisenberg G: **Assessment of myocardial viability using MRI during a constant infusion of Gd-DTPA: Further studies at early and late periods of reperfusion.** *Magn Reson Med* 1999, **42:**60-68.
94. Pack N, Dibella E, Wilson B, McGann C: **Quantitative myocardial distribution volume from dynamic contrast-enhanced MRI.** *Magn Reson Imaging* 2008, **26:**532-542.
95. Jerosch-Herold M, Swingen C, Seethamraju RT: **Myocardial blood flow quantification with MRI by model-independent deconvolution.** *Med Phys* 2002, **29:**886-897.
96. Jerosch-Herold M, Hershberger RE, Broberg C: **Estimation of the Myocardial Extracellular Volume Fraction from Dynamic Contrast-Enhancement Measurements and Comparison with Partition Coefficient Measurements.** In *Proceedings of the 17th Scientific Meeting & Exhibition ISMRM; Hawaii, USA*. 2009: 1743.

97. Pack N, DiBella E: **Comparison of myocardial perfusion estimates from dynamic contrast-enhanced magnetic resonance imaging with four quantitative analysis methods.** *Magn Reson Med* 2010, **64:**125-137.
98. Hsu B: **PET tracers and techniques for measuring myocardial blood flow in patients with coronary artery disease.** *Journal of biomedical research* 2013, **27:**452-459.
99. Handayani A, Triadyaksa P, Dijkstra H, Pelgrim GJ, van Ooijen P, Prakken N, Schoepf J, Oudkerk M, Vliegenthart R, Sijens P: **Intermodel agreement of myocardial blood flow estimation from stress-rest myocardial perfusion magnetic resonance imaging in patients with coronary artery disease.** *Invest Radiol* 2015, **50:**275-282.
100. Biglands J, Magee D, Sourbron S, Plein S, Greenwood J, Radjenovic A: **Comparison of the Diagnostic Performance of Four Quantitative Myocardial Perfusion Estimation Methods Used in Cardiac MR Imaging: CE-MARC Substudy.** *Radiology* 2014.
101. Biglands J, Magee D, Boyle R, Larghat A, Plein S, Radjenović A: **Evaluation of the effect of myocardial segmentation errors on myocardial blood flow estimates from DCE-MRI.** *Phys Med Biol* 2011, **56:**2423-2443.
102. Cernicanu A, Axel L: **Theory-based signal calibration with single-point T1 measurements for first-pass quantitative perfusion MRI studies.** *Acad Radiol* 2006, **13:**686-693.
103. Christian T, Rettmann D, Aletras A, Liao S, Taylor J, Balaban R, Arai A: **Absolute Myocardial Perfusion in Canines Measured by Using Dual-Bolus First-Pass MR Imaging.** *Radiology* 2004, **232:**677-684.
104. Hsu L-Y, Rhoads K, Holly J, Kellman P, Aletras A, Arai A: **Quantitative myocardial perfusion analysis with a dual-bolus contrast-enhanced first-pass MRI technique in humans.** *J Magn Reson Imaging* 2006, **23:**315-322.
105. Köstler H, Ritter C, Lipp M, Beer M, Hahn D, Sandstede J: **Prebolus quantitative MR heart perfusion imaging.** *Magn Reson Med* 2004, **52:**296-299.
106. Groothuis J, Kremers F, Beek A, Brinckman S, Tuinenburg A, Jerosch-Herold M, van Rossum A, Hofman M: **Comparison of dual to single contrast bolus magnetic resonance myocardial perfusion imaging for detection of significant coronary artery disease.** *Journal of magnetic resonance imaging : JMRI* 2010, **32:**88-93.
107. Hsu L-Y, Kellman P, Arai A: **Nonlinear myocardial signal intensity correction improves quantification of contrast-enhanced first-pass MR perfusion in humans.** *J Magn Reson Imaging* 2008, **27:**793-801.
108. Gatehouse P, Elkington A, Ablitt N, Yang G-Z, Pennell D, Firmin D: **Accurate assessment of the arterial input function during high-dose myocardial perfusion cardiovascular magnetic resonance.** *J Magn Reson Imaging* 2004, **20:**39-45.
109. Sánchez-González J, Fernandez-Jiménez R, Nothnagel N, López-Martín G, Fuster V, Ibañez B: **Optimization of dual-saturation single bolus acquisition for quantitative cardiac perfusion and myocardial blood flow maps.** *Journal of Cardiovascular Magnetic Resonance* 2015, **17:**21.
110. Kim D, Axel L: **Multislice, dual-imaging sequence for increasing the dynamic range of the contrast-enhanced blood signal and CNR of**

myocardial enhancement at 3T. *Journal of magnetic resonance imaging : JMRI* 2006, **23:**81-86.
111. Kholmovski E, DiBella E: **Perfusion MRI with radial acquisition for arterial input function assessment.** *Magn Reson Med* 2007, **57:**821-827.
112. Chen D, Sharif B, Dharmakumar R, Thomson L, Bairey Merz N, Berman D, Li D: **Improved quantification of myocardial blood flow using highly constrained back projection reconstruction.** *Magn Reson Med* 2014, **72:**749-755.
113. Ge L, Kino A, Griswold M, Mistretta C, Carr J, Li D: **Myocardial perfusion MRI with sliding-window conjugate-gradient HYPR.** *Magn Reson Med* 2009, **62:**835-839.
114. Arheden H, Saeed M, Higgins C, Gao D-W, Bremerich J, Wyttenbach R, Dae M, Wendland M: **Measurement of the Distribution Volume of Gadopentetate Dimeglumine at Echo-planar MR Imaging to Quantify Myocardial Infarction: Comparison with 99mTc-DTPA Autoradiography in Rats1.** *Radiology* 1999, **211:**698-708.
115. Thornhill R, Prato F, Wisenberg G, White J, Nowell J, Sauer A: **Feasibility of the single-bolus strategy for measuring the partition coefficient of Gd-DTPA in patients with myocardial infarction: independence of image delay time and maturity of scar.** *Magn Reson Med* 2006, **55:**780-789.
116. Schelbert E, Testa S, Meier C, Ceyrolles W, Levenson J, Blair A, Kellman P, Jones B, Ludwig D, Schwartzman D, et al: **Myocardial extravascular extracellular volume fraction measurement by gadolinium cardiovascular magnetic resonance in humans: slow infusion versus bolus.** *Journal of Cardiovascular Magnetic Resonance* 2011, **13:**16.
117. Salerno M, Janardhanan R, Jiji R, Brooks J, Adenaw N, Mehta B, Yang Y, Antkowiak P, Kramer C, Epstein F: **Comparison of methods for determining the partition coefficient of gadolinium in the myocardium using T1 mapping.** *Journal of magnetic resonance imaging : JMRI* 2012, **38:**217-224.
118. Kawel N, Nacif M, Zavodni A, Jones J, Liu S, Sibley C, Bluemke D: **T1 mapping of the myocardium: intra-individual assessment of post-contrast T1 time evolution and extracellular volume fraction at 3T for Gd-DTPA and Gd-BOPTA.** *Journal of Cardiovascular Magnetic Resonance* 2012, **14:**26.
119. Milanesi M, Barison A, Positano V, Masci P, De Marchi D, Marinelli L, Hardy C, Foo T, Landini L, Lombardi M: **Modified cine inversion recovery pulse sequence for the quantification of myocardial T1 and gadolinium partition coefficient.** *Journal of magnetic resonance imaging : JMRI* 2013, **37:**109-118.
120. Kawel N, Nacif M, Zavodni A, Jones J, Liu S, Sibley C, Bluemke D: **T1 mapping of the myocardium: Intra-individual assessment of the effect of field strength, cardiac cycle and variation by myocardial region.** *Journal of Cardiovascular Magnetic Resonance* 2012, **14:**27.
121. Judd R, Atalay M, Rottman G, Zerhouni E: **Effects of Myocardial Water Exchange on T1 Enhancement during Bolus Administration of MR Contrast Agents.** *Magn Reson Med* 1995, **33:**215-223.

122. Judd R, Reeder S, May-Newman K: **Effects of water exchange on the measurement of myocardial perfusion using paramagnetic contrast agents.** *Magn Reson Med* 1999, **41:**334-342.
123. Wacker CM, Bock M, Hartlep AW, Beck G, van Kaick G, Ertl G, Bauer WR, Schad LR: **Changes in myocardial oxygenation and perfusion under pharmacological stress with dipyridamole: assessment using T*2 and T1 measurements.** *Magn Reson Med* 1999, **41:**686-695.
124. Higgins D, Ridgway J, Radjenovic A, Sivananthan M, Smith M: **T1 measurement using a short acquisition period for quantitative cardiac applications.** *Med Phys* 2005, **32:**1738-1746.
125. Look DC, Locker DR: **Time Saving in Measurement of NMR and EPR Relaxation Times.** *Rev Sci Instrum* 1970, **41:**250-251.
126. Freeman AJ, Gowland PA, Mansfield P: **Optimization of the ultrafast Look-Locker echo-planar imaging T1 mapping sequence.** *Magn Reson Imaging* 1998, **16:**765-772.
127. Deichmann R, Haase A: **Quantification of T1 values by SNAPSHOT-FLASH NMR imaging.** *Journal of Magnetic Resonance (1969)* 1992, **96:**608-612.
128. Scheffler K, Hennig J: **T1 quantification with inversion recovery TrueFISP.** *Magn Reson Med* 2001, **45:**720-723.
129. Messroghli D, Plein S, Higgins D, Walters K, Jones T, Ridgway J, Sivananthan M: **Human myocardium: single-breath-hold MR T1 mapping with high spatial resolution--reproducibility study.** *Radiology* 2006, **238:**1004-1012.
130. Messroghli D, Greiser A, Fröhlich M, Dietz R, Schulz-Menger J: **Optimization and validation of a fully-integrated pulse sequence for modified look-locker inversion-recovery (MOLLI) T1 mapping of the heart.** *Journal of magnetic resonance imaging : JMRI* 2007, **26:**1081-1086.
131. Nacif M, Turkbey E, Gai N, Nazarian S, van der Geest R, Noureldin R, Sibley C, Ugander M, Liu S, Arai A, et al: **Myocardial T1 mapping with MRI: Comparison of look-locker and MOLLI sequences.** *Journal of magnetic resonance imaging : JMRI* 2011, **34:**1367-1373.
132. Shao J, Rapacchi S, Kim-Lien N, Hu P: **Myocardial T1 mapping at 3.0 tesla using an inversion recovery spoiled gradient echo readout and bloch equation simulation with slice profile correction (BLESSPC) T1 estimation algorithm: FLASH-MOLLI with BLESSPC T1 Mapping.** *J Magn Reson Imaging* 2016, **43:**414-425.
133. Marks B, Mitchell DG, Simelaro JP: **Breath-holding in healthy and pulmonary-compromised populations: effects of hyperventilation and oxygen inspiration.** *Journal of magnetic resonance imaging : JMRI* 1997, **7:**595-597.
134. Lee J, Liu S, Nacif M, Ugander M, Han J, Kawel N, Sibley C, Kellman P, Arai A, Bluemke D: **Myocardial T1 and extracellular volume fraction mapping at 3 tesla.** *Journal of Cardiovascular Magnetic Resonance* 2011, **13:**75.
135. Kellman P, Arai A, Xue H: **T1 and extracellular volume mapping in the heart: estimation of error maps and the influence of noise on precision.** *Journal of Cardiovascular Magnetic Resonance* 2013, **15:**56.
136. Piechnik S, Ferreira V, Dall'Armellina E, Cochlin L, Greiser A, Neubauer S, Robson M: **Shortened Modified Look-Locker Inversion recovery**

(ShMOLLI) for clinical myocardial T1-mapping at 1.5 and 3 T within a 9 heartbeat breathhold. *Journal of cardiovascular magnetic resonance* 2010, **12**.
137. Piechnik S, Ferreira V, Lewandowski A, Ntusi N, Banerjee R, Holloway C, Hofman M, Sado D, Maestrini V, White S, et al: **Normal variation of magnetic resonance T1 relaxation times in the human population at 1.5T using ShMOLLI.** *Journal of Cardiovascular Magnetic Resonance* 2013, **15:**13.
138. Fontana M, White S, Banypersad S, Sado D, Maestrini V, Flett A, Piechnik S, Neubauer S, Roberts N, Moon J: **Comparison of T1 mapping techniques for ECV quantification. Histological validation and reproducibility of ShMOLLI versus multibreath-hold T1 quantification equilibrium contrast CMR.** *Journal of Cardiovascular Magnetic Resonance* 2012, **14:**88.
139. Song T, Stainsby J, Ho V, Hood M, Slavin G: **Flexible cardiac T1 mapping using a modified look–locker acquisition with saturation recovery.** *Magn Reson Med* 2012, **67:**622-627.
140. Xue H, Greiser A, Zuehlsdorff S, Jolly M-P, Guehring J, Arai A, Kellman P: **Phase-sensitive inversion recovery for myocardial T1 mapping with motion correction and parametric fitting.** *Magn Reson Med* 2013, **69:**1408-1420.
141. Chow K, Flewitt J, Green J, Pagano J, Friedrich M, Thompson R: **Saturation recovery single-shot acquisition (SASHA) for myocardial T 1 mapping : SASHA for T 1 Mapping.** *Magn Reson Med* 2014, **71:**2082-2095.
142. Roujol S, Weingärtner S, Foppa M, Chow K, Kawaji K, Ngo L, Kellman P, Manning W, Thompson R, Nezafat R: **Accuracy, precision, and reproducibility of four T1 mapping sequences: a head-to-head comparison of MOLLI, ShMOLLI, SASHA, and SAPPHIRE.** *Radiology* 2014, **272:**683-689.
143. Weingärtner S, Akçakaya M, Basha T, Kissinger K, Goddu B, Berg S, Manning W, Nezafat R: **Combined saturation/inversion recovery sequences for improved evaluation of scar and diffuse fibrosis in patients with arrhythmia or heart rate variability: Improved Imaging of Scar/Fibrosis.** *Magn Reson Med* 2014, **71:**1024-1034.
144. Fitts M, Breton E, Kholmovski E, Dosdall D, Vijayakumar S, Hong K, Ranjan R, Marrouche N, Axel L, Kim D: **Arrhythmia insensitive rapid cardiac T1 mapping pulse sequence.** *Magn Reson Med* 2013, **70:**1274-1282.
145. Stanisz G, Odrobina E, Pun J, Escaravage M, Graham S, Bronskill M, Henkelman M: **T1, T2 relaxation and magnetization transfer in tissue at 3T.** *Magn Reson Med* 2005, **54:**507-512.
146. Goldfarb J, Mathew S, Reichek N: **Quantitative breath-hold monitoring of myocardial gadolinium enhancement using inversion recovery TrueFISP.** *Magn Reson Med* 2005, **53:**367-371.
147. Reiter U, Reiter G, Dorr K, Greiser A, Maderthaner R, Fuchsjäger M: **Normal diastolic and systolic myocardial T1 values at 1.5-T MR imaging: correlations and blood normalization.** *Radiology* 2014, **271:**365-372.
148. Pereira R, Prato F, Wisenberg G, Sykes J: **The determination of myocardial viability using Gd-DTPA in a canine model of acute**

myocardial ischemia and reperfusion. *Magn Reson Med* 1996, **36:**684-693.
149. Pereira R, Prato F, Lekx K, Sykes J, Wisenberg G: **Contrast-enhanced MRI for the assessment of myocardial viability after permanent coronary artery occlusion.** *Magn Reson Med* 2000, **44:**309-316.
150. Karamitsos T, Neubauer S: **The prognostic value of late gadolinium enhancement CMR in nonischemic cardiomyopathies.** *Current Cardiology Reports* 2013, **15**.
151. Kuruvilla S, Adenaw N, Katwal A, Lipinski M, Kramer C, Salerno M: **Late gadolinium enhancement on cardiac magnetic resonance predicts adverse cardiovascular outcomes in nonischemic cardiomyopathy: a systematic review and meta-analysis.** *Circulation Cardiovascular imaging* 2014, **7:**250-258.
152. Klein C, Nekolla S, Balbach T, Schnackenburg B, Nagel E, Fleck E, Schwaiger M: **The influence of myocardial blood flow and volume of distribution on late Gd-DTPA kinetics in ischemic heart failure.** *Journal of magnetic resonance imaging : JMRI* 2004, **20:**588-594.
153. Selvanayagam J, Jerosch-Herold M, Porto I, Sheridan D, Cheng A, Petersen S, Searle N, Channon K, Banning A, Neubauer S: **Resting Myocardial Blood Flow Is Impaired in Hibernating Myocardium.** *Circulation* 2005, **112:**3289-3296.
154. Hopp E, Bjørnerud A, Lunde K, Solheim S, Aakhus S, Arnesen H, Forfang K, Edvardsen T, Smith H: **Perfusion MRI at rest in subacute and chronic myocardial infarct.** *Acta Radiol* 2013, **54:**401-411.
155. Jerosch-Herold M, Sheridan D, Kushner J, Nauman D, Burgess D, Dutton D, Alharethi R, Li D, Hershberger R: **Cardiac magnetic resonance imaging of myocardial contrast uptake and blood flow in patients affected with idiopathic or familial dilated cardiomyopathy.** *American journal of physiology Heart and circulatory physiology* 2008, **295**.
156. Jacquier A, Kallifatidis A, Guibert N, Giorgi R, Falque C, Thuny F, Croisille P, Clarysse P, Maurel B, Flavian A, et al: **Assessment of myocardial partition coefficient of gadolinium (λ) in dilated cardiomyopathy and its impact on segmental and global systolic function.** *Journal of magnetic resonance imaging : JMRI* 2014, **40:**1336-1341.
157. Treibel T, White S, Sado D, Hasleton J, Flett A, Herrey A, Hausenloy D, Moon J: **Not all LGE is the same. Scar contrast volume of distribution is lower in HCM than in infarction.** *Journal of Cardiovascular Magnetic Resonance* 2012, **14:**O95.
158. Ellims A, Iles L, Ling L, Hare J, Kaye D, Taylor A: **Diffuse myocardial fibrosis in hypertrophic cardiomyopathy can be identified by cardiovascular magnetic resonance, and is associated with left ventricular diastolic dysfunction.** *Journal of Cardiovascular Magnetic Resonance* 2012, **14:**76.
159. Ho C, Abbasi S, Neilan T, Shah R, Chen Y, Heydari B, Cirino A, Lakdawala N, Orav J, González A, et al: **T1 Measurements Identify Extracellular Volume Expansion in Hypertrophic Cardiomyopathy Sarcomere Mutation Carriers With and Without Left Ventricular Hypertrophy.** *Circulation: Cardiovascular Imaging* 2013, **6:**415-422.

160. Brouwer W, Baars E, Germans T, de Boer K, Beek A, van der Velden J, van Rossum A, Hofman M: **In-vivo T1 cardiovascular magnetic resonance study of diffuse myocardial fibrosis in hypertrophic cardiomyopathy.** *Journal of Cardiovascular Magnetic Resonance* 2014, **16:**28.
161. Broberg C, Chugh S, Conklin C, Sahn D, Jerosch-Herold M: **Quantification of diffuse myocardial fibrosis and its association with myocardial dysfunction in congenital heart disease.** *Circulation Cardiovascular imaging* 2010, **3:**727-734.
162. Flett A, Sado D, Quarta G, Mirabel M, Pellerin D, Herrey A, Hausenloy D, Ariti C, Yap J, Kolvekar S, et al: **Diffuse myocardial fibrosis in severe aortic stenosis: an equilibrium contrast cardiovascular magnetic resonance study.** *European Heart Journal – Cardiovascular Imaging* 2012, **13:**819-826.
163. Neilan T, Coelho-Filho O, Shah R, Feng J, Pena-Herrera D, Mandry D, Pierre-Mongeon F, Heydari B, Francis S, Moslehi J, et al: **Myocardial Extracellular Volume by Cardiac Magnetic Resonance Imaging in Patients Treated With Anthracycline-Based Chemotherapy.** *The American journal of cardiology* 2013, **111:**717-722.
164. Tham E, Haykowsky M, Chow K, Spavor M, Kaneko S, Khoo N, Pagano J, Mackie A, Thompson R: **Diffuse myocardial fibrosis by T1-mapping in children with subclinical anthracycline cardiotoxicity: relationship to exercise capacity, cumulative dose and remodeling.** *Journal of Cardiovascular Magnetic Resonance* 2013, **15:**48.
165. Rao A, Shah R, Garg R, Abbasi S, Neilan T, Perlstein T, Di Carli M, Jerosch-Herold M, Kwong R, Adler G: **Aldosterone and myocardial extracellular matrix expansion in type 2 diabetes mellitus.** *The American journal of cardiology* 2013, **112:**73-78.
166. Khan JN, Wilmot EG, Leggate M, Singh A, Yates T, Nimmo M, Khunti K, Horsfield M, Biglands J, Clarysse P, et al: **Subclinical diastolic dysfunction in young adults with Type 2 diabetes mellitus: a multiparametric contrast-enhanced cardiovascular magnetic resonance pilot study assessing potential mechanisms.** *European heart journal cardiovascular Imaging* 2014.
167. Coelho-Filho O, Shah R, Neilan T, Mattos Souza J, Jose C, Carlos F, Lindemberg da Mota S-F, Martins de Oliveira P, Severino E, Jerosch-Herold M, Petrucci O: **Characterization of both myocardial extracellular volume expansion and myocyte hypertrophy by CMR in heart transplantation recipients without active rejection: implications for early cardiac remodeling.** *Journal of Cardiovascular Magnetic Resonance* 2015, **17:**O75.
168. Parnham S, Gleadle J, Leong D, Grover S, Bradbrook C, Woodman R, De Pasquale C, Selvanayagam J: **Myocardial perfusion is impaired in asymptomatic renal and liver transplant recipients: a cardiovascular magnetic resonance study.** *Journal of Cardiovascular Magnetic Resonance* 2015, **17:**56.
169. Banypersad S, Sado D, Flett A, Gibbs S, Pinney J, Maestrini V, Cox A, Fontana M, Whelan C, Wechalekar A, et al: **Quantification of myocardial extracellular volume fraction in systemic AL amyloidosis: an equilibrium contrast cardiovascular magnetic resonance study.** *Circulation Cardiovascular imaging* 2013, **6:**34-39.

170. Thuny F, Lovric D, Schnell F, Bergerot C, Ernande L, Cottin V, Derumeaux G, Croisille P: **Quantification of Myocardial Extracellular Volume Fraction with Cardiac MR Imaging for Early Detection of Left Ventricle Involvement in Systemic Sclerosis.** *Radiology* 2014, **271:**373-380.
171. Edwards N, Moody W, Yuan M, Hayer M, Ferro C, Townend J, Steeds R: **Diffuse interstitial fibrosis and myocardial dysfunction in early chronic kidney disease.** *The American journal of cardiology* 2015, **115:**1311-1317.
172. Liu C-Y, Liu Y-C, Wu C, Armstrong A, Volpe G, van der Geest R, Liu Y, Hundley W, Gomes A, Liu S, et al: **Evaluation of Age-Related Interstitial Myocardial Fibrosis With Cardiac Magnetic Resonance Contrast-Enhanced T1 Mapping.** *J Am Coll Cardiol* 2013, **62:**1280-1287.
173. Neilan T, Coelho-Filho O, Shah R, Abbasi S, Heydari B, Watanabe E, Chen Y, Mandry D, Pierre-Mongeon F, Blankstein R, et al: **Myocardial extracellular volume fraction from T1 measurements in healthy volunteers and mice: relationship to aging and cardiac dimensions.** *JACC Cardiovascular imaging* 2013, **6:**672-683.
174. Miller C, Naish J, Bishop P, Coutts G, Clark D, Zhao S, Ray S, Yonan N, Williams S, Flett A, et al: **Comprehensive Validation of Cardiovascular Magnetic Resonance Techniques for the Assessment of Myocardial Extracellular Volume.** *Circulation: Cardiovascular Imaging* 2013.
175. Christophe de Meester de R, Bouzin C, Lazam S, Boulif J, Amzulescu M, Melchior J, Pasquet As, Vancraeynest D, Pouleur A-C, Vanoverschelde J-L, Gerber B: **Histological Validation of measurement of diffuse interstitial myocardial fibrosis by myocardial extravascular volume fraction from Modified Look-Locker imaging (MOLLI) T1 mapping at 3T.** *Journal of Cardiovascular Magnetic Resonance* 2015, **17:**48.
176. Kellman P, Hansen M: **T1-mapping in the heart: accuracy and precision.** *Journal of Cardiovascular Magnetic Resonance* 2014, **16:**2.
177. Broadbent DA, Biglands JD, Ripley DP, Higgins DM, Greenwood JP, Plein S, Buckley DL: **Sensitivity of quantitative myocardial dynamic contrast-enhanced MRI to saturation pulse efficiency, noise and t1 measurement error: Comparison of nonlinearity correction methods.** *Magn Reson Med* 2016, **75:**1290-1300.
178. Broadbent D, Biglands J, Ripley D, Plein S, Buckley D: **Comparison of non-linearity correction methods for quantitative myocardial perfusion MRI.** *Journal of Cardiovascular Magnetic Resonance* 2015, **17:**P45.
179. Utz W, Niendorf T, Wassmuth R, Messroghli D, Dietz R, Schulz-Menger J: **Contrast-dose relation in first-pass myocardial MR perfusion imaging.** *J Magn Reson Imaging* 2007, **25:**1131-1135.
180. Kim D, Gonen O, Oesingmann N, Axel L: **Comparison of the effectiveness of saturation pulses in the heart at 3T.** *Magn Reson Med* 2008, **59:**209-215.
181. Kim D, Oesingmann N, McGorty K: **Hybrid adiabatic-rectangular pulse train for effective saturation of magnetization within the whole heart at 3 T.** *Magn Reson Med* 2009, **62:**1368-1378.

182. Kim D, Cernicanu A, Axel L: **B0 and B1-insensitive uniform T1-weighting for quantitative, first-pass myocardial perfusion magnetic resonance imaging.** *Magn Reson Med* 2005, **54:**1423-1429.
183. Chow K, Kellman P, Spottiswoode B, Nielles-Vallespin S, Arai A, Salerno M, Thompson R: **Saturation pulse design for quantitative myocardial T 1 mapping.** *Journal of Cardiovascular Magnetic Resonance* 2015, **17:**84.
184. Cron GO, Santyr G, Kelcz F: **Accurate and rapid quantitative dynamic contrast-enhanced breast MR imaging using spoiled gradient-recalled echoes and bookend T(1) measurements.** *Magn Reson Med* 1999, **42:**746-753.
185. Cron G, Kelcz F, Santyr G: **Improvement in breast lesion characterization with dynamic contrast-enhanced MRI using pharmacokinetic modeling and bookend T1 measurements.** *Magn Reson Med* 2004, **51:**1066-1070.
186. Pintaske J, Martirosian P, Graf H, Erb G, Lodemann K-P, Claussen C, Schick F: **Relaxivity of Gadopentetate Dimeglumine (Magnevist), Gadobutrol (Gadovist), and Gadobenate Dimeglumine (MultiHance) in human blood plasma at 0.2, 1.5, and 3 Tesla.** *Invest Radiol* 2006, **41:**213-221.
187. Pintaske J, Martirosian P, Graf H, Erb G, Lodemann K-P, Claussen C, Schick F: **Erratum - Relaxivity of Gadopentetate Dimeglumine (Magnevist), Gadobutrol (Gadovist), and Gadobenate Dimeglumine (MultiHance) in human blood plasma at 0.2, 1.5, and 3 Tesla.** *Invest Radiol* 2006, **41:**869-869.
188. Mehta A, Hoffbrand V: *Haematology at a glance.* 4th edn. Sussex, UK: Wiley Blackwell; 2014.
189. Kellman P, Wilson J, Xue H, Bandettini W, Shanbhag S, Druey K, Ugander M, Arai A: **Extracellular volume fraction mapping in the myocardium, part 2: initial clinical experience.** *Journal of Cardiovascular Magnetic Resonance* 2012, **14:**64.
190. Fritz-Hansen T, Rostrup E, Larsson H, Søndergaard L, Ring P, Henriksen O: **Measurement of the arterial concentration of Gd-DTPA using MRI: A step toward quantitative perfusion imaging.** *Magn Reson Med* 1996, **36:**225-231.
191. Fritz-Hansen T, Hove J, Kofoed K, Kelbaek H, Larsson H: **Quantification of MRI measured myocardial perfusion reserve in healthy humans: A comparison with positron emission tomography.** *J Magn Reson Imaging* 2008, **27:**818-824.
192. Husso M, Sipola P, Kuittinen T, Manninen H, Vainio P, Hartikainen J, Saarakkala S, Töyräs J, Kuikka J: **Assessment of myocardial perfusion with MRI using a modified dual bolus method.** *Physiol Meas* 2014, **35:**533-547.
193. Su M-Y, Lee B-C, Wu Y-W, Yu H-Y, Chu W-C, Tseng W-Y: **Perfusion of residual viable myocardium in nontransmural infarct zone after intervention: MR quantitative myocardial blood flow measurement.** *Radiology* 2008, **249:**820-828.
194. Cheng A, Pegg T, Karamitsos T, Searle N, Jerosch-Herold M, Choudhury R, Banning A, Neubauer S, Robson M, Selvanayagam J: **Cardiovascular Magnetic Resonance Perfusion Imaging at 3-Tesla**

for the Detection of Coronary Artery Disease. *J Am Coll Cardiol* 2007, **49:**2440-2449.
195. Lerski RA, de Certaines JD: **Performance assessment and quality control in MRI by Eurospin test objects and protocols.** *Magn Reson Imaging* 1993, **11:**817-833.
196. Gudbjartsson H, Patz S: **The rician distribution of noisy mri data.** *Magn Reson Med* 1995, **34:**910-914.
197. Ripley D, McDiarmid A, Kidambi A, Uddin A, Swoboda P, Musa T, Erhayiem B, Bainbridge G, Greenwood J, Plein S, Higgins D: **Patient adaptive maximal resolution magnetic resonance myocardial stress perfusion imaging.** *Journal of magnetic resonance imaging : JMRI* 2015.
198. Kellman P, Aletras A, Hsu L-Y, McVeigh E, Arai A: **T2* measurement during first-pass contrast-enhanced cardiac perfusion imaging.** *Magn Reson Med* 2006, **56:**1132-1134.
199. Karamitsos T, Ntusi N, Francis J, Holloway C, Myerson S, Neubauer S: **Feasibility and safety of high-dose adenosine perfusion cardiovascular magnetic resonance.** *Journal of Cardiovascular Magnetic Resonance* 2010, **12:**66.
200. Ogg RJ, Kingsley RB, Taylor JS: **WET, a T1- and B1-Insensitive Water-Suppression Method for in Vivo Localized 1H NMR Spectroscopy.** *Journal of Magnetic Resonance, Series B* 1994, **104:**1-10.
201. Broadbent D, Kidambi A, Plein S, Buckley D: **Quantitative Dynamic Contrast Enhanced MRI in Acute ST-Elevated Myocardial Infarction: Blood Flow, Microvascular Permeability and Interstitial Volume in Infarct and Peri-Infarct Edema.** In *Proceedings of the 23rd Scientific Meeting & Exhibition ISMRM; Toronto, Canada*. 2015: 517.
202. Handayani A, Triadyaksa P, Dijkstra H, Gert J, van Ooijen P, Prakken N, Schoepf J, Oudkerk M, Vliegenthart R, Sijens P: **Intermodel agreement of myocardial blood flow estimation from stress-rest myocardial perfusion magnetic resonance imaging in patients with coronary artery disease.** *Invest Radiol* 2015, **50:**275-282.
203. Papanastasiou G, Williams M, Kershaw L, Dweck M, Alam S, Mirsadraee S, Connell M, Gray C, MacGillivray T, Newby D, Semple S: **Measurement of myocardial blood flow by cardiovascular magnetic resonance perfusion: comparison of distributed parameter and Fermi models with single and dual bolus.** *Journal of Cardiovascular Magnetic Resonance* 2015, **17:**17.
204. St. John Sutton M, Sharpe N: **Left Ventricular Remodeling After Myocardial Infarction.** *Circulation* 2000, **101:**2981-2988.
205. Chan W, Duffy S, White D, Gao X-M, Du X-J, Ellims A, Dart A, Taylor A: **Acute Left Ventricular Remodeling Following Myocardial Infarction.** *JACC: Cardiovascular Imaging* 2012, **5:**884-893.
206. Messroghli D, Walters K, Plein S, Sparrow P, Friedrich M, Ridgway J, Sivananthan M: **Myocardial T1 mapping: application to patients with acute and chronic myocardial infarction.** *Magn Reson Med* 2007, **58:**34-40.
207. Ugander M, Oki A, Hsu L-Y, Kellman P, Greiser A, Aletras A, Sibley C, Chen M, Bandettini P, Arai A: **Extracellular volume imaging by magnetic resonance imaging provides insights into overt and sub-clinical myocardial pathology.** *Eur Heart J* 2012.

208. Cabello J, Burls A, Emparanza J, Bayliss S, Quinn T: **Oxygen therapy for acute myocardial infarction.** *The Cochrane database of systematic reviews* 2013, **8**.
209. American Heart Association Writing Group on Myocardial S, Registration for Cardiac I, Cerqueira M, Weissman N, Dilsizian V, Jacobs A, Kaul S, Laskey W, Pennell D, Rumberger J, et al: **Standardized Myocardial Segmentation and Nomenclature for Tomographic Imaging of the Heart.** *Circulation* 2002, **105:**539-542.
210. Papanastasiou G, Williams M, Alam S, Dweck M, Mirsadraee S, Gray C, Connell M, MacGillivray T, Newby D, Semple S: **Assessing the reliability of DP and Fermi estimates in single and dual bolus cardiac MR perfusion imaging.** *Journal of Cardiovascular Magnetic Resonance* 2014, **16:**P347.
211. Fluckiger J, Benefield B, Harris K, Lee D: **Absolute quantification of myocardial blood flow with constrained estimation of the arterial input function: Quantification of MBF With Constrained Estimation.** *J Magn Reson Imaging* 2013, **38:**603-609.
212. Fluckiger J, Schabel M, Dibella E: **Model-based blind estimation of kinetic parameters in dynamic contrast enhanced (DCE)-MRI.** *Magn Reson Med* 2009, **62:**1477-1486.
213. Schabel M, Fluckiger J, DiBella E: **A model-constrained Monte Carlo method for blind arterial input function estimation in dynamic contrast-enhanced MRI: I. Simulations.** *Phys Med Biol* 2010, **55:**4783.
214. Kratochvíla J, Jiřík R, Bartoš M, Standara M, Starčuk Z, Taxt T: **Distributed capillary adiabatic tissue homogeneity model in parametric multi-channel blind AIF estimation using DCE-MRI.** *Magn Reson Med* 2016, **75:**1355-1365.